Connect Store: A fully coupled 3D model of ice flow, calving, subglacial hydrology and ice-ocean interactions applied to Store Glacier, Greenland

This thesis is submitted 09.07.2020 for the degree of Doctor of Philosophy

Samuel James Cook

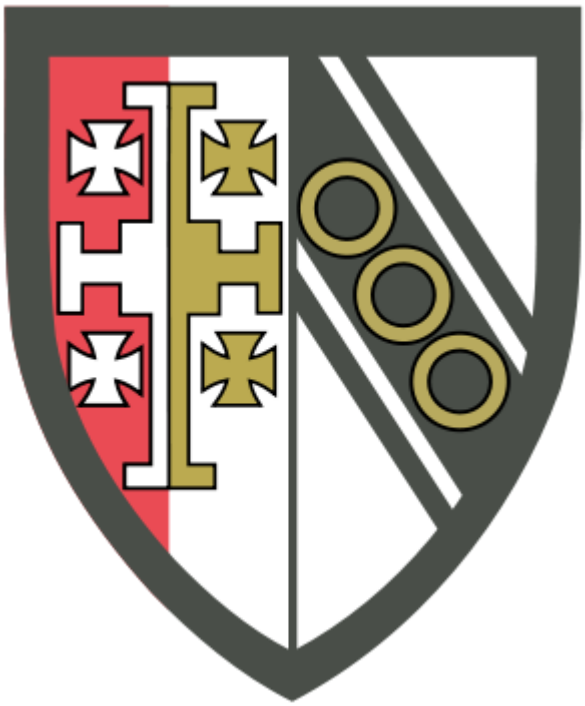

Selwyn College

Declaration

I hereby declare that except where specific reference is made to the work of others, the contents of this dissertation are original and have not been submitted in whole or in part for consideration for any other degree or qualification in this, or any other university. This dissertation is my own work and contains nothing which is the outcome of work done in collaboration with others, except as specified in the text and Acknowledgements. This dissertation does not exceed the length limits prescribed by the Degree Committee for the Faculty of Earth Sciences and Geography.

Samuel Cook

June 2020

Abstract

Title: Connect Store: A fully coupled 3D model of ice flow, calving, subglacial hydrology and ice-ocean interactions applied to Store Glacier, Greenland

Name: Samuel Cook

This dissertation uses the 3D, finite-element, full-Stokes, open-source model Elmer/Ice to investigate the coupled dynamics of the ice-calving-subglacial-hydrology-plume system at Store Glacier, a large, fast-flowing tidewater outlet glacier on the west coast of Greenland. Understanding these large outlet glaciers is critical to being able to accurately predict the future evolution of the Greenland Ice Sheet.

This study therefore presents a three-week record of calving activity at Store Glacier, gathered in July 2017 using a terrestrial radar interferometer. This record is the longest and most detailed yet produced for a Greenlandic tidewater glacier and shows the complex and time-varying nature of calving at Store Glacier.

In parallel, an uncoupled model of subglacial hydrology and plume melting at the calving front is developed within the Elmer/Ice framework and applied to Store Glacier to investigate seasonal differences in hydrology. Overall, the dynamic nature and key role of the subglacial hydrological system of Store is made clear, with little modelled relationship between surface melt and plume melt, owing to the storage capacity of the intervening subglacial system. The model is compared to available observations, which suggest that it is providing a realistic picture of the subglacial hydrology of Store Glacier.

Finally, a fully coupled model of ice flow, calving, subglacial hydrology and plume melting is presented and applied to Store Glacier, being validated against the observed calving dataset. This represents the first time a fully coupled simulation of a tidewater glacier anywhere has been undertaken. The model qualitatively reproduces the validation dataset well, but under-estimates it quantitatively. The coupled model allows demonstration of the dynamics of the coupled ice-hydrology-calving system, showing that hydrology-induced velocity changes are the key large-scale calving control, and that channelisation inland is greatly suppressed when two-way ice-hydrology coupling is included. It also makes clear that, while the terminus appears to be able to channelise fully under high melt, this is not the case farther inland, mirroring the situation observed in land-terminating regions of the Greenland Ice Sheet.

Acknowledgements

'Utúlie'n aurë! Aiya Eldalië ar Atanatári, utúlie'n aurë!'

'Auta i lómë!'

So spoke Fingon and so replied his host in misplaced hope not long before getting bludgeoned to death by Balrogs as the armies of the Eldar and the Edain were nearly wiped out by the machinations of Morgoth. Notwithstanding the unfortunate consequences, which I can hope to avoid, the sentiment seems appropriate: The Day has indeed finally come and the Night is passing. Sméagol is free. A new Age dawns and much is changed. The Road goes ever on and on, but this stage is over.

It has indeed been a long road, and I have come as I could, though not in the manner I perhaps envisaged nearly four years ago. For general PhD advice and keeping me on the academic straight and narrow, my supervisors, Poul Christoffersen and Joe Todd, deserve a great deal of thanks. Joe, I'd still be struggling to run anything in Elmer without you. I'd also like to thank Donald Slater for putting up with my inability to model plumes correctly for several months. If that part of the model produces anything like a sensible answer, it's down to you. And more generally, all my co-authors deserve my thanks for pointing out when I'm being an idiot or letting me use their hard-won data. I should also mention Olivier Gagliardini and Thomas Zwinger for dealing with occasional inane questions from me on Elmer/Ice. In return, I promise all this code will get on the repository soon! NERC also should be mentioned for throwing 3.5 years of money at me – hopefully, they think it was worth it.

I should, of course, thank everyone at SPRI for putting up with my idiosyncrasies and creating such a welcoming place to work. Though I do question your decision to keep feeding me with jigsaw puzzles, without which I'd have finished this thing months ago. In particular, my fellow PhD students, Becky, Tom, Rob, Peter, Henry and Morgan for sharing the Road with me and for being so abysmal at crosswords that I had to do them all; and Charlie and John for not laughing at what I'm sure is my grammatically inferior German.

All work and no play makes Jack an incredibly dull boy, though, so I'd like to thank, in no particular order, the Cambridge Tolkien Society (and apologise to the Oxford Tolkien Society for Knowing Too Much About Tolkien), the Cambridge University Quiz Society, the Cambridge University Science-Fiction and Fantasy Society, the Badmintime crew, Quizzy's Rascals and other sundry friends outside the echo chamber of glaciology for keeping me sane.

Finally, I'd like to thank my parents and my sister (and my brother-in-law – it's still weird that I have to call you that, Henry) for just Being There. Even if I'm fairly certain I never really explained properly what I'd spent four years doing.

Finally, finally, I'd like to thank you, the reader, for reading this. I apologise that it's really dull, but it seems that humorous footnotes and tangential flights of fancy aren't *de rigueur* in academic writing. So you'll just have to make do with dry description of the World's Most Complex Functioning Glacier Model™[1]. Sorry.

[1] Description correct at time of writing for given values of 'World', 'Complex' and 'Functioning'.

'*The only thing we know for sure is that Stonehenge is a terraforming device built by aliens from another dimension.'*

Jacob*, Stonehenge Apocalypse*

Or, possibly, a deep Descartes-esque reflection on the contingency of knowledge derived from computer models.

Contents

List of Figures

List of Tables

List of Equations

List of Symbols

Roman Symbols

a	Constant
A	Rheological constant of ice multiplied by an order one geometrical factor
A_s	Sliding coefficient
C	Friction coefficient
D_w	Water depth
g	Acceleration due to gravity
H_{float}	Critical flotation thickness
h	Sheet thickness
h_r	Typical bedrock bump height
J_0	Initial cost function
J_{reg}	Regularised cost function
J_{tot}	Total cost function
L	Latent heat of fusion of water
l_r	Typical horizontal spacing of cavities
m	Constant
n	Constant (typically ≈3)
N	Effective pressure
P_i	Ice overburden pressure
P_w	Water pressure
q	Constant (typically ≈1)
S	Maximum bed slope of glacier
S_c	Channel cross-sectional area
u_b	Basal velocity
u_H	Horizontal component of modelled velocity
u_H^{obs}	Horizontal component of observed velocity
w	Cavity opening rate
w_c	Channel opening rate
v	Cavity closure rate

v_c Channel closure rate

Z Elevation

Z_b Basal elevation

Z_{sl} Sea level

Greek Symbols

α_p Inversion parameter

β Basal sliding coefficient

Γ Number of data points

Γ_b Lower limit for regularised cost function

Γ_s Lower limit for initial cost function

λ Regularisation parameter

λ_w Wavelength

Ξ Potential energy dissipated per unit length

Π Sensible heat change of water

ρ_i Density of ice

ρ_w Density of water

τ_b Basal stress

ϕ Hydraulic potential

χ Basal sliding term

1. Introduction

'It's the job that's never started as takes longest to finish'

-Sam, The Lord of the Rings, Book 2, Ch. VII

The IPCC (Stocker et al., 2013) have demonstrated that the mean annual earth surface temperature has warmed by 0.85°C since 1880, on average. This warming has been particularly concentrated at the poles, with the Arctic, for example, showing an average of 1.2°C of warming since 1913 (Najafi et al., 2015). This degree of warming had already caused the Greenland Ice Sheet's (GrIS) mass balance to drop to -243 ± 18 Gt a^{-1} by 2009 (Csatho et al., 2014), with a recent increase to -269 ± 51 Gt a^{-1} for 2011-14 (McMillan et al., 2016), though this has since slowed to -217 ± 32 Gt a^{-1} in 2013-17 (Shepherd et al., 2019). One of the main culprits behind this increasing mass loss is an acceleration in so-called "fast" outlet glaciers, as demonstrated for three of the largest: Jakobshavn Isbrae, Kangerdlugssuaq and Helheim by Howat et al. (2011).

The mechanisms behind these accelerations vary – for Kangerdlugssuaq and Helheim, in the south-east of the GrIS, which exhibited a rapid acceleration 2004-05 before slowing and stabilising since, the culprit seems to have been a combination of enhanced surface melting, warm water intrusion into their terminal fjords (linked to a weak NAO) and strong katabatic winds (Christoffersen et al., 2012). Together, these factors led to basal lubrication, increased ice-front melting through stronger turbulent meltwater plumes mixing in warm fjord water, and loss of backstress from the sikussak, which was either melted by the warm water or removed by the winds (Christoffersen et al., 2012). This suggests the acceleration is episodically-caused by a particular set of climatic circumstances, but, on the basis that the regional climate is projected to become warmer and cloudier (IPCC, 2020), these may recur more frequently. Equally, as Enderlin et al. (2014) suggest, the rapid synchronous retreat in the south-east may have been due to unpinning from bedrock highs, so that there is little potential for further acceleration in the region. Until favourable conditions for retreat should repeat, it remains unclear how far this is the case.

This shows how different parts of the GrIS are responding differently to the same overall forcing, highlighting the importance of local and regional factors in determining ice response (Csatho et al., 2014). Jakobshavn Isbrae, by contrast with the south-east, after an initial acceleration starting in 1998, has maintained its fast flow, accelerating at 5-7% per year over 2004-2007 (Joughin et al., 2012), though there has been a recent slowdown linked to colder ocean temperatures (Khazendar et al., 2019), though whether this continues is uncertain (Joughin et al., 2020). This seems to have been due to a loss of buttressing when the ice tongue collapsed in 1998/99, together with dynamic processes, which suggests that the acceleration may be long-term (Joughin et al., 2012). This is

supported by the fact the Jakobshavn sits in a long and deep trough, which it seems likely it will have to retreat to the head of before being able to fully stabilise (Joughin et al., 2012). Joughin et al. (2012) suggest this may take up to a century, with the current rapid flow pertaining in the meantime, though they do find that there seems to be limited potential for further acceleration. Whether the current slowdown is maintained or proves temporary remains to be seen.

It is therefore clear that much further work needs to be undertaken to understand the GrIS, particularly its fast-flowing glaciers. More recent work by Enderlin et al. (2014) has shown that only 15 of Greenland's (fast) outlet glaciers, including the little-studied Koge Bugt and Ikertivaq South in second and fourth, respectively, account for around 77% of the mass loss since 2000, with the top four accounting for 50% alone. It can therefore be seen that understanding the behaviour of fast glaciers is critical to being able to accurately predict the future evolution of the GrIS.

Given the IPCC (Stocker et al., 2013) envisage a range of climate scenarios, which, between them, predict 0.3-4.8°C of further warming globally by 2100, with the Arctic continuing to warm faster than the global mean, there is undeniably the potential for these glaciers to accelerate further, leading to greater mass loss from the GrIS. The GrIS alone contains enough ice to raise global sea levels by over 7 m (Gregory et al., 2004; Stocker et al., 2013), so, should fast glaciers continue to accelerate, sea levels could rise by more than the current extreme IPCC (Stocker et al., 2013) predictions of around 1m by 2100. It is thus vitally important to understand how these glaciers will continue to react to the changing climate and to be able to predict how they might change further in the future.

This PhD proposes that this broad aim would be achieved through the development and application of multiple numerical models. This is particularly important as many of the processes controlling fast glacier motion take place at the bed or the calving front, both areas that are very difficult, if not impossible, to observe or otherwise study. This PhD consequently aims to produce and validate an accurate simulation of an entire fast-flowing tidewater glacier system in Greenland. This would allow the GrIS's contribution to sea-level rise to be better-constrained and would refine projections for the remainder of the century, allowing optimal mitigation strategies to be implemented in at-risk areas.

This thesis is split into seven chapters. This first chapter has provided the rationale behind this PhD project whilst the second will give an overview of relevant literature, situating it more precisely within contemporary glaciology. Chapter 3 will expand on the aims, objectives and methods of the project; and Chapters 4-6 will present the work undertaken to meet these aims. Chapter 4 will present a dataset of observed calving at the study site, which will provide the basis for model validation; Chapter 5 will detail findings from an uncoupled version of the fully-coupled model; and Chapter 6 will present results from the fully-coupled model. Finally, Chapter 7 will present a

synthesis of the PhD and will include validation of the fully coupled model by comparison to the dataset described in Chapter 4.

1.1. Aims

As discussed throughout this dissertation, the complex and inaccessible nature of tidewater glacier systems makes them particularly suited to a numerical-modelling approach. However, numerical modelling is not necessarily useful without being validated against an independent set of observations. Taking all these considerations into account led me to develop the following three broad aims for this thesis:

1. Develop a fully coupled model of Store Glacier including ice flow, calving, subglacial hydrology and proglacial plumes in one simulation to allow modelling of hydrological controls on ice flow and how these also influence calving and plume-induced frontal melting
2. Apply this model to Store Glacier to gain insights into how hydrological changes affect glacier dynamics and how this might change in the future at a real glacier
3. Characterise the calving behaviour of Store Glacier using high-resolution radar observations, thereby also providing a dataset that can be used to validate the model

The first two aims are the primary concern of Chapters 3, 5 and 6; the third aim is the focus of Chapter 4, as well as Sections 3.6 and 6.6.

1.2. Study Site

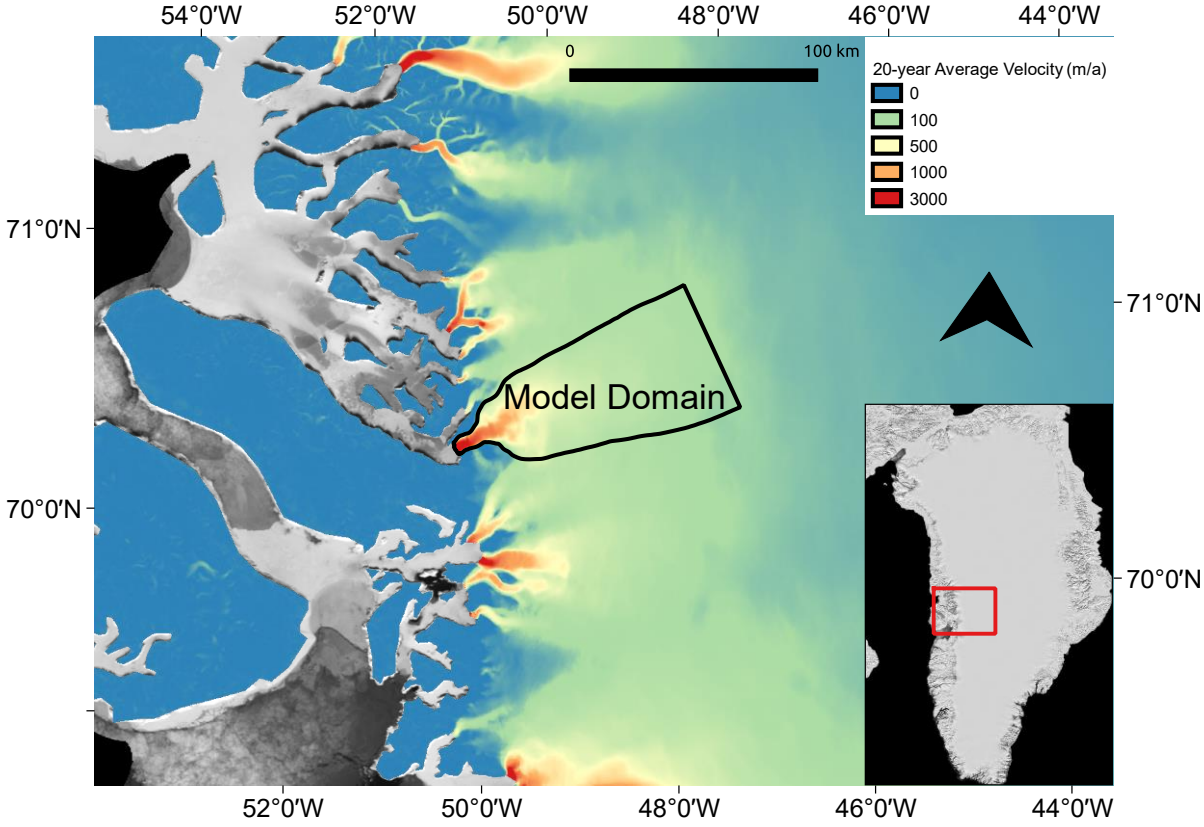

Figure 1 – Location of Store (inset) and model domain. Background shows the 20-year velocity average from the MEaSUREs dataset (Joughin et al. 2016, 2018).

Store Glacier (Store; *Sermeq Kujalleq*), one of the largest tidewater outlet glaciers on the west coast of Greenland (70.4°N, 50.55°W), flows into Ikerasak Fjord (*Ikerasaup Sullua*) at the southern end of the Uummannaq Fjord system (Figure1). The calving front is 5 km wide, with surface velocities reaching up to 6600 m a^{-1} (Joughin et al., 2018), and is pinned on a sill making the terminus position relatively stable despite the trunk of the glacier flowing through a deep trough extending to nearly 1000m below sea level (Rignot et al., 2015). With no observed retreat since 1985 (Catania et al., 2018), the glacier represents a stable Greenland outlet glacier and is an ideal target for modelling studies aiming to understand such glaciers (e.g. Morlighem et al., 2016; Todd et al., 2018; Todd and Christoffersen, 2014; Xu et al., 2013), hence its use as the study site for this thesis.

2. Literature Review

'*Less welcome did the Lord Denethor show me then than of old, and grudgingly he permitted me to search among his hoarded scrolls and books*'

-Gandalf, The Lord of the Rings, Book 2, Ch. II

This chapter provides an overview of the relevant theory and literature underpinning this dissertation. Section 2.1 deals with the theoretical basis of tidewater glaciers and key components of the tidewater-glacier system; Section 2.2 gives further detail on the modelling of tidewater glaciers; and Section 2.3 provides some context for the use of the radar interferometer outlined in Chapter 4.

2.1. The Tidewater Glacier System

Tidewater glaciers are particularly complex glacier systems, as they are subject to the full range of glacial processes applicable to their land-terminating cousins, but also to an extensive additional set of processes resulting from the immersion of their fronts in seawater. This section considers the theoretical basis of and current literature on the three components of the tidewater-glacier system most relevant to this thesis: subglacial hydrology (Section 2.1.1), meltwater plumes (Section 2.1.2) and calving (Section 2.1.3).

2.1.1. Subglacial Hydrology

The study of glacial hydrology – i.e. how liquid water moves over, through and under a glacier or ice sheet – has long been an active field of research. The structure and behaviour of the hydrological system is important on all glaciers through its effect on velocity, but assumes additional importance for tidewater glaciers due to its role in driving freshwater plumes at the calving front. It is thus crucial that it be explicitly modelled in a full simulation of a tidewater glacier. This section gives an overview of the relevant theory underpinning the current understanding of subglacial hydrology, with plumes covered separately in Section 2.1.2.

Liquid water at the base of an ice mass, from whatever source (surface melt due to temperature, basal melt due to friction and geothermal heat, etc.), has a major impact on the motion of the overlying ice. Once at the base, water will flow according to the hydraulic potential gradient, which is a function of slope and pressure (Shreve, 1972). This flow will happen in one of two kinds of system: an efficient, channelised system, as first proposed by Röthlisberger (1972) and developed by Nye (1976); or an inefficient, distributed system, often in the form of a series of linked cavities (Lliboutry, 1968).

For present purposes, the central difference between the two systems is how they react contrastingly to increasing inputs of water. The state of the subglacial hydrological system is determined by two factors: ice creep acting to close up cavities and channels, which is a function of the ice overburden pressure; and melting by release of latent energy from water contained within the system acting to expand them (Röthlisberger, 1972). For a channelised system, the generally high volume-to-surface-area ratio means that, as discharge increases, melt increases at a greater rate than ice creep, resulting in reduced water pressure within the system and more water therefore flowing into the growing channels, following the hydrological gradient (Röthlisberger, 1972). For a distributed system, on the other hand, the volume-to-surface-area ratio is much lower, with water spread thinly across a wide area of the bed, meaning that closure tends to outweigh expansion (Walder, 1986). Therefore, as discharge increases, so too does water pressure.

It is also possible for a distributed system to morph into a channelised one – as water pressure increases, melt can start to outpace ice creep in the larger cavities or conduits, forming embryonic channels that can then start to grow as pressure drops and water is sucked in (Kamb, 1970). This process has been observed on many alpine-type glaciers as a consequence of higher melt with the onset of the melt season, with the reverse happening as melt starts to tail off again with the return of colder temperatures (e.g. Rippin et al., 2003; Schuler et al., 2004; Willis et al., 2009).

These pressure-related differences drive the impact of the subglacial hydrology on the motion of the overlying ice mass. This is because the degree of sliding that the ice is subject to largely depends on the effective pressure (N):

$$N = P_i - P_w \tag{1}$$

Where P_i is the ice overburden pressure and P_w is the water pressure. Various sliding laws have been proposed to attempt to capture this mathematically and link basal stress to basal velocity, but none has so far proven entirely satisfactory (Cuffey and Paterson, 2010). The simplest, Weertman-type sliding laws take the form of:

$$\tau_b = C u_b^{m-1} u_b \tag{2}$$

where τ_b is basal stress, C is a friction coefficient, u_b is the basal velocity and m is a constant. Such sliding laws take no account of subglacial hydrology, so are not considered further here. More complex, physically-based Coulomb-type sliding laws are instead more appropriate. These take the form of Gagliardini et al. (2007):

$$\tau_b = SN\left[\frac{\chi u_b^{-n}}{(1+a\chi^q)}\right]^{\frac{1}{n}} u_b$$

(3)

Where

$$a = \frac{(q-1)^{q-1}}{q^q}$$

(4)

And

$$\chi = \frac{u_b}{S^n N^n A_s}$$

(5)

Where S is a constant equal to the maximum bed slope of the glacier, n is a constant, typically equal to 3, q is a constant, typically equal to 1, and A_s is the sliding coefficient. Whilst such laws are more physically-based, they still require the determination of poorly constrained parameters, so are more difficult to implement in numerical models than a simple Weertman-type sliding law.

As is clear from Eq. (3), the lower N is, the more the ice overburden pressure is being borne by the water present subglacially, and thus the lower the friction and the smoother the bed (more water means smaller obstacles will be submerged, reducing drag). If P_w reaches or exceeds P_i (i.e. N drops to 0), a phenomenon known as hydraulic jacking (Iken, 1981; Iken and Bindschadler, 1986), the ice may be lifted entirely off its bed and achieve very high sliding velocities.

A logical consequence of the above is that sliding is favoured by increasing discharge in a high-pressure, distributed subglacial drainage system, whereas a low-pressure, channelised system will tend to limit the degree to which sliding is promoted. At the most basic level, a distributed system also spreads water more widely across the bed, leading to greater lubrication generally. Understanding which kind of system is active at any one time beneath a glacier is therefore critical in being able to predict its behaviour. It is, of course, entirely possible to have a mix of both kinds of system active beneath any one glacier, and these two idealised states should be regarded more as end-members of a spectrum of subglacial drainage systems, with most real systems falling somewhere between them.

It is also necessary to be able to model when one type of system will transition into the other. As stated above, there is ample evidence from land-terminating valley glaciers of a hydrological switch,

where an initially distributed system evolves into a channelised one under the influence of higher discharges at the start of the melt season, before returning to a distributed state with the end of the melt season and a drop in discharge. The consequence of this is that these glaciers usually show a spring velocity peak, as pressures spike in the distributed system, before velocities drop again as the channelised system takes over and reduces P_w once more (Mair et al., 2001, 2003). Therefore, to some extent, the glacier self-regulates, such that the impact of hydrology on velocity at an annual scale is small.

However, this 'Spring Event' pattern requires there to be sustained high melt discharges to force the subglacial drainage system to begin channelising. If high discharges are more episodic, the distributed system will not channelise, as the necessary levels of latent heat availability will not be maintained to overcome ice creep (Schoof, 2010). This means that each discharge event will be accompanied by an increasing P_w and consequent velocity spike (Schoof, 2010).

This is particularly relevant to Greenland, where the thicker ice compared to valley glaciers impedes the formation of channels, as P_i and, thus, creep is higher (Dow et al., 2014; Meierbachtol et al., 2013). This is doubly true for fast, tidewater outlet glaciers, as the higher velocities also promote ice creep. It might therefore be expected that distributed systems and the potential for attendant high P_w and velocity might persist except in the face of very high melt. It has been demonstrated that the sudden drainage of a supraglacial lake can lead to short-term, local velocity peaks (Das et al., 2008), as would be expected in a distributed system. The general picture of how the hydrological system of the GrIS is reacting to increased discharges as melt intensifies and what this means for velocity is, however, less clear.

The current consensus is that, for land-terminating portions of the GrIS (Davison et al., 2019) and, more tentatively, for the ablation area in general (Nienow et al., 2017), that what could be termed the 'valley-glacier hydrological model' holds true. Several studies in the south-west of the ice sheet, both direct observations through boreholes (e.g. Andrews et al., 2014; Chandler et al., 2013; Meierbachtol et al., 2013) and remotely-sensed records of surface velocity (e.g. Bougamont et al., 2014; Sole et al., 2013; Sundal et al., 2011; Tedstone et al., 2013, 2015; van de Wal et al., 2015) support this position. Other studies that suggested a positive correlation between velocity and surface melt for this region (e.g. Palmer et al., 2011; Zwally et al., 2002) seem attributable to a late-season rainstorm that overwhelmed a subglacial drainage system that had now decayed back to a distributed state (Doyle et al., 2015).

There is also some suggestion that a third component needs to be added to this classic model to fully explain the observed velocity patterns (Hoffman et al., 2016), principally that late-summer and early-

winter velocities are considerably lower than late-winter velocities (e.g. Sole et al., 2013; Tedstone et al., 2015; van de Wal et al., 2015; Zwally et al., 2002), even though the channelised system should collapse back to a distributed state within a few days (Dow et al., 2014; Sole et al., 2013). This would take the form of a very weakly-connected and largely inactive region of the bed, which is gradually dewatered over the course of a melt season by increased connectivity under higher pressures, such that, at the end of the melt season, water pressure over the whole bed is lower than at the start (and thus basal friction is higher), lowering velocity (Hoffman et al., 2016). This weakly-connected system would then be recharged over several years (different areas may be tapped in different years, depending on the process of channel formation), priming the system for a new melt season (Hoffman et al., 2016).

However, it is debatable whether the valley-glacier hydrological model holds true for areas further inland, with thicker ice and reduced melt. Even in idealised conditions, Dow et al. (2014, 2015) were unable to produce realistic channels in the accumulation area in a numerical model, unless P_w was continuously at least 90% of P_i, which implies very high, constant discharges. Several studies have also shown no evidence for channelisation and the associated velocity decreases beyond a few tens of kilometres from the margin (e.g. Chandler et al., 2013; Doyle et al., 2014; Meierbachtol et al., 2013). This suggests that, in the short term at least, subglacial channelised systems are likely to be restricted to the margins of the GrIS, which may lead to more velocity spikes further inland as the distributed system is confronted with higher melt.

For marine-terminating areas and tidewater glaciers, where the addition of marine processes complicates the picture, the situation is even less clear, not helped by a relative paucity of studies on these complex environments. The generally thicker ice and faster velocity of tidewater glaciers compared to land-terminating ones make drilling boreholes to investigate the subglacial drainage system much harder; indeed, only two studies (Doyle et al., 2018; Lüthi et al., 2002) have so far reported results of borehole investigations on tidewater glaciers, finding, at Store, persistently high water pressures in an active distributed drainage system 30 km inland in the case of Doyle et al. (2018). The outflow of water into the submarine environment also severely hinders the use of dye-tracing techniques, meaning traditional hydrological-system investigations are less applicable to the tidewater setting. Despite these difficulties, it is obvious that there is a great heterogeneity of responses across the GrIS to climate forcing and hydrology (Csatho et al., 2014), which suggests that one simple hydrological model is unlikely to be applicable everywhere, but, as stated above, disentangling the effect of hydrological changes from that of oceanic changes remains difficult and is an area that requires more study. Instead, much work on the hydrology of tidewater glaciers has

focussed on its role in driving meltwater plumes at the calving front, which is discussed in the next section.

However, recent advances in the modelling and observation of subglacial hydrology promise to help resolve this issue. Seismic interferometry and polarisation is starting to be used as a tool to observe the subglacial drainage system (Vore et al., 2019; Zhan, 2019) and has successfully been applied to a surging tidewater glacier, revealing mostly distributed drainage in a network of transverse basal crevasses (Zhan, 2019). This being said, seismic observational campaigns require the installation and maintenance of expensive equipment – two broadband seismometers maintained for 12 years for Zhan (2019) – so modelling remains the main solution for extensive investigation of the subglacial hydrology of tidewater glaciers.

The maturity of the field is demonstrated by the undertaking of the first Subglacial Hydrological Model Intercomparison Project (SHMIP) (de Fleurian et al., 2018), which, for the first time, allowed the relative performance of several different hydrological models to be assessed. Modelling studies of subglacial hydrology have proliferated recently (e.g. Banwell et al., 2013; de Fleurian et al., 2014, 2018; Flowers, 2015; Hewitt et al., 2012; Hoffman et al., 2016; Schoof, 2010; Werder et al., 2013; Dow et al., 2019), but, so far, these models have been applied largely to land-terminating catchments in Greenland or elsewhere, where validation is easier due to the availability of better observations of the hydrological system. This is important, because these models often rely on several parameters for which the appropriate value is not known and/or poorly constrained, so validation needs to be undertaken to ensure the modelled system is, as far as possible, in accordance with realistic glacier behaviour. There is, though, no fundamental reason why these models should not also function effectively in a tidewater setting, as undertaken in this thesis.

The main division between subglacial hydrological models is between those that model channels explicitly (e.g. Werder et al., 2013) and those that do not (e.g. de Fleurian et al., 2014). The latter continuum models use layers of different hydrological conductivity to simulate inefficient and efficient components of the subglacial drainage system, with drainage switching between the two layers depending on some criterion, whilst the former explicitly grow efficient channels when sufficient water accumulates locally in the inefficient sheet layer. Continuum models are computationally less expensive, but the lack of explicit channel modelling can make them over-simplified for some environments or applications (de Fleurian et al., 2018), particularly when investigating complex dynamic feedbacks. The lack of explicit channels also makes them less suitable for driving models of freshwater plumes at the calving front, so this thesis takes the more computationally expensive route, and uses a model with explicit channel growth.

2.1.2. Meltwater Plumes

All the water that accumulates at the base of a glacier eventually flows out of the system via the land- or marine-terminating margins. On land, this leads to the formation of one or more proglacial streams, but, for tidewater glaciers, this water is instead discharged at the grounding line (if the terminus is floating) or, more often, at the base of the calving front (if the terminus is grounded), straight into the fjord waters. This fresh meltwater, despite often being colder than the oceanic fjord water, is less dense, which means that it forms turbulent plumes that rise along the calving face until they reach either neutral buoyancy or the surface (Jenkins, 2011).

The turbulence of these plumes means that they mix in a large amount of the surrounding fjord water and bring it into contact with the terminus face, promoting melting (Jenkins, 2011; Slater et al., 2016). Without plumes, the ice face is to some extent protected from contact with the fjord water by a thin layer of very cold water formed as it begins to melt; plumes disrupt this layer and allow greater interaction between the warmer fjord waters and ice face (Jenkins, 2011). Larger plumes can, in fact, mix in so much fjord water that they rapidly lose any meltwater characteristics, and tend to rise well above neutral buoyancy due to their inertia (Carroll et al., 2015). Large plumes can therefore usually be easily-spotted from the surface due to the gaps they create in the ice mélange adjacent to the calving face, being effectively upwellings of warmer water by the time they reach the (near-)surface (Carroll et al., 2015; Slater et al., 2017). Smaller plumes, meanwhile, tend to be trapped at depth by mid-column stratification maxima, betraying no visible surface signature (Carroll et al., 2015). If there is a thick surface meltwater layer in the fjord, however, the increased stratification of the water column can lead to even large plumes not reaching the surface (De Andrés et al., 2020).

Theoretically, the degree of melting attributable to these plumes is dependent on the magnitude of the discharge at their origin point, as larger plumes contain more energy and can mix in more fjord water. The melting rate this actually translates to in practical terms is uncertain, due to the difficulties in obtaining observations at the calving front, but modelling work suggests large plumes can be responsible for melt rates of 3 m d^{-1} or more in their immediate vicinity (Fried et al., 2015; Slater et al., 2018; Xu et al., 2013). However, whilst this is very high, when averaged over the entire ice face, it is almost negligible compared to ice velocity and calving. The contribution of plumes to overall melting at the ice front instead seems to depend very heavily on the structure of the near-terminus subglacial drainage system (Slater et al., 2015, 2018). If this is heavily channelised, there will be a few large plumes at the outlets of the major channels, which will lead to strong melting immediately above them, but much of the ice face will be unaffected by plume activity. If, instead,

the system is more distributed, there will be many much smaller plumes, which will produce lower melt rates than a larger plume, but will affect a much larger proportion of the ice face (Slater et al., 2015, 2017; Fried et al., 2015). In this more distributed case, the total melt rate contributed by plumes can be five times higher than in the case of a single, much larger plume (Slater et al., 2015).

This shows the importance of explicitly modelling the configuration of the subglacial drainage system at the terminus – not only for its own sake, but also to ensure plumes are correctly specified. The current balance of evidence for tidewater glaciers suggests that the near-terminus drainage system is more distributed than would be expected based on land-terminating glaciers. On Kangerlussuup Sermia in western Greenland, Fried et al. (2015) found one large outlet and several smaller outlets at the calving front; the smaller outlets being responsible for 85% of the plume-induced melting. Slater et al. (2017), meanwhile, demonstrated a similar situation for Kangiata Nunata Sermia, also on the west coast of the GrIS, by showing that, if all melt were concentrated into one large plume, this would have been visible at the surface for much longer than plumes were. The inference is that the meltwater was being split between multiple, smaller plumes. The reasons behind this apparent tendency towards more distributed near-terminus drainage systems are unclear, but are most likely related to the high velocities present in these regions, which increase the closure rate of channels by creep, making them unstable (Slater et al., 2017). The region of low hydraulic potential behind the front of tidewater glaciers would also likely favour more distributed drainage (Vore et al., 2019). Observations by Jackson et al. (2017) at Kangerlussuup Sermia in West Greenland also show a plume inconsistent with traditional axisymmetric, conical plume theory; instead a sheet-like wall plume upwelling from a low, broad outlet of around 200 m in width provides a better fit. Not only therefore does the structure of the subglacial drainage system need to be taken into account, but the morphology of the outlets can also play an important role in determining the resulting melt at the calving front. Overall, though, the literature shows plumes are clearly a key driver of melt and calving at tidewater glacier fronts in Greenland (Wagner et al., 2019).

Plumes are therefore an important part of the tidewater-glacier system, hence their inclusion in this thesis. However, studying them is challenging. By their nature, plumes are dynamic and observable signals can be ephemeral. From the surface, only plumes sufficiently large to disrupt the surface of the fjord are visible, where they can be observed by UAV (Jouvet et al., 2018) or time-lapse imagery (How et al., 2018). Only particularly persistent plumes will be reliably visible in satellite imagery, with its longer repeat times (e.g. Schild et al., 2016). Gaining sub-surface observations of plumes is especially difficult due to the hazardous nature of the calving-front environment, which makes bringing in boats with sonar capability or similarly equipped AUVs complicated. Depending on ice conditions, access to the calving front may not even be possible, meaning a reliable, long-term

measurement campaign is virtually impossible; such observations as we do have are, by necessity, episodic (Chauché et al., 2014; Stevens et al., 2016). One innovative solution to this problem was the use of instrumented ringed seals by Everett et al. (2018) to study plumes in Kongsfjorden, Svalbard, but such animal-based techniques are not always available and are inherently unpredictable and unreproducible.

Consequently, for similar reasons to subglacial hydrology, computer-based numerical modelling of plumes has become a major avenue of investigation. These studies all use models based on buoyant plume theory (BPT) (Jenkins, 2011; Slater et al., 2016) to simulate the initial discharge of freshwater and subsequent turbulent mixing, and resulting melting of the plume thus formed. Whilst BPT does provide a sound physical basis for plume modelling, it does require the determination of several parameter values, which, in the calving-front setting, are virtually impossible to accurately measure, presenting a similar problem to that seen for models of subglacial hydrology. Validation needs to be undertaken in some manner to ensure the modelled plumes exhibit realistic behaviour. Laboratory experiments (e.g. Ezhova et al., 2018) can provide some insight and help constrain some parameter values, but it is also likely that the 'real' parameter values vary from location to location, meaning that validation remains necessary. This is further underlined by recent observations at two tidewater glaciers, one in Alaska and one in Greenland, that show that submarine melting is up to two orders of magnitude greater than that predicted by BPT and models based on it (Sutherland et al., 2019; Wagner et al., 2019); clearly, therefore, plume modelling, whilst useful, requires further development.

2.1.3. Calving

The most obvious difference between land-terminating and tidewater glaciers is the presence of a calving front at the latter. Calving is an important mass-loss process in Greenland, being responsible for 40% of current ice loss from the GrIS (Mouginot et al., 2019), but it is also a process that is difficult to study, owing to the dangerous nature of the calving-front environment and the unpredictable nature of the process, and also complex to model, as knowledge of micro-scale ice characteristics is ideally required.

At the most fundamental level, calving occurs when a fracture intersects the ice surface at two or more points. Larger, full-thickness calving events are the result of a single fracture intersecting the surface and base of the ice, completely isolating a portion of the front. Smaller events happen when the fracture intersects the calving front and one of the surface or base. Therefore, any change in the glacier system that promotes fracture propagation will ultimately increase calving event frequency; any change that supresses fractures will likewise reduce calving event frequency.

Of particular relevance is the complex relationship between ice thickness, effective pressure, buoyancy and ice velocity (Cuffey and Paterson, 2010). A thinning at the terminus from whatever cause acts to reduce effective pressure (Eq. (1)), as the ice overburden pressure drops whilst water pressure remains constant. This is because water pressure at the terminus of tidewater glaciers is mainly controlled by the depth of the fjord, which is constant on the timescale of interest here. Therefore, velocity increases, as the reduced effective pressure decreases friction at the bed. The increase in velocity increases strain rates and hence (extensional) stress, promoting fracture growth and leading to greater calving; it also leads to further thinning of the glacier, as the increased ice export is not necessarily balanced by increased accumulation. The increased thinning feeds back into the loop summarised above; the increased calving event frequency can lead to terminus retreat.

At the same time, the impact of buoyancy needs to be considered: the termini of tidewater glaciers are exposed to buoyant forces as the ice 'wants' to float. These buoyant forces create a rotational moment acting on the calving front, with the pivot at the grounding line, greatly promoting basal crevasse growth as the terminus attempts to spring upwards. Whether the terminus actually floats is determined by the critical flotation thickness for seawater (Cuffey and Paterson, 2010):

$$H_{float} = \frac{\rho_w}{\rho_i} D_w = 1.14 D_w \quad (6)$$

Where H_{float} is the critical flotation thickness, ρ_w is the density of seawater, ρ_i is the density of ice and D_w is the water depth (in m). In other words, if the ice thickness is less than 1.14 times the water depth at the terminus, the terminus will float unless the glacier geometry forces it to remain grounded, putting it in a position of superbuoyancy. Therefore, if thinning occurs at the terminus such that it drops below the critical flotation thickness, catastrophic calving can take place as the increasing buoyancy forces gain the upper hand. This feeds in to the set of processes discussed above, and can lead to further retreat. All these processes work in reverse, so an initial thickening at the terminus can lead to a suppression of calving through reversing the same set of mechanisms.

Calving can also be promoted by the presence of meltwater plumes at the front. The high melt rates that plumes can produce lead to localised higher melt rates that can cut notches into the calving front, creating a set of headlands and bays (Todd et al., 2019). The reduced lateral support provided to the headlands makes these more vulnerable to calving, as the headlands are under greater stress and present a smaller width of ice for any fracture to penetrate through. If plumes occur near the slower-flowing margins of the ice, recent work has suggested they can melt back through the compressive arch that stabilises the entire front of the glacier, leading to large-scale calving across

the entire front with consequent dynamic effects (Cowton et al., 2019); plumes nearer the centre, where flow is faster, are unlikely to achieve melt rates higher than the velocity of the glacier, so any ice they melt is ice that would soon have calved anyway (Benn and Åström, 2018; Cowton et al., 2019). Plumes can also contribute to undercutting of the terminus, leading to an unsupported overhang that is similarly also primed for calving (O'Leary and Christoffersen, 2013).

This entire set of interlinked processes is chiefly mediated by the effective pressure at the bed of the ice and one of the main factors determining this is the state of the subglacial hydrological system. As discussed in Section 2.1.1, a more channelised drainage system will have lower water pressures and thus higher effective pressures than a distributed system. Changes in the structure of the subglacial hydrological system can therefore counteract or enhance variations in effective pressure occasioned by thinning or thickening of the overlying ice. These changes are also themselves mediated by both changes in ice thickness and velocity. As an example, thinner ice will make channel formation easier, which could increase effective pressure. At the same time, the thinner ice will directly reduce effective pressure, increasing velocity and making channel formation harder. Which side of the equation dominates is dependent very much on the glacier geometry. Therefore, it is necessary to consider all these components of the tidewater-glacier system together.

Whether changes in the calving event frequency through the above mechanisms lead to retreat or advance depends on the rate of calving versus the ice velocity (Cuffey and Paterson, 2010). If the calving rate is less than the ice velocity, the terminus will advance and vice versa. A stable calving front therefore implies that calving rate and ice velocity are equal. A significant role is also played by the geometry of the glacier and fjord bed. If a retreating glacier is retreating into deeper water, the water pressure at the base will tend to increase, reducing effective pressure, increasing velocity and exacerbating calving and dynamic thinning, all of which will tend to lead to further retreat (Rignot et al., 2016). If the glacier is instead retreating upslope, the reverse will be true, tending to limit the amount of retreat. Advance follows a similar pattern – advance downslope into deeper water is rendered difficult; advance upslope into shallower water is encouraged. These patterns are further modulated by the change in width of the fjord as the glacier advances or retreats along it. Retreat into a narrowing fjord will concentrate the ice, increasing thickness and making it more firmly grounded, which will limit the retreat. Retreat into a widening fjord will instead lead to the ice spreading out, thinning it and leading to further retreat.

The fjord geometry is also a key factor in determining how exposed tidewater glacier termini are to warm ocean water, which is often the initial trigger for thinning and retreat (Rignot et al., 2012; Seale et al., 2011; Wood et al., 2018). Warmer water is generally present at depths below a few

hundred metres, so a shallow sill at the fjord mouth or along its length is an effective barrier that protects the glacier from the higher melt rates and potential retreat the warmer water can produce (Rignot et al., 2016). These local topographical factors are thought to be the main reason neighbouring and ostensibly similar tidewater glaciers in Greenland can display very different reactions to the same forcing (Csatho et al., 2014; Mouginot et al., 2015; Rignot et al., 2016).

This dependence on local factors is particularly relevant to one way of conceptualising the calving front of tidewater glaciers: as a self-organised critical system seeking to reach the attractor of equilibrium in its phase space (Åström et al., 2014). Actually reaching the attractor is impossible, so the calving front oscillates around it, and is therefore in a state of permanent over- or under-shoot. In an undershot state, the calving front will advance incrementally, with many small calving events; in an overshot state, it will retreat rapidly with large calving events. Perturbations to the system move the position of the attractor, so a system that was in undershoot can suddenly find itself in overshoot and vice versa, with concomitant effects on its behaviour. Consequently, the stable position of any given calving front is highly dependent on local conditions and on small changes in these conditions.

The foregoing discussion makes it clear that calving is the result of a complex interplay of processes, which further adds to the difficulty of studying it. Attempts to model calving ideally model it explicitly in 3D, by considering the propagation of individual fractures (Åström et al., 2013), but such models are very computationally expensive and unsuitable for wider coupled simulations. Therefore, modelling calving has focused on 2D simulations (Todd and Christoffersen, 2014) or on developing some sort of simple parameterisation for inclusion in 3D models, often related to some combination of water depth, ice thickness and glacier width (Benn et al., 2017a; Benn and Åström, 2018), but these inevitably fail to capture the full complexity and dynamism of calving. More recent attempts have used stress concentrations within 3D continuum models as a proxy for fracture propagation and have achieved some success as a middle ground between acceptable computational expense and realism (Todd et al., 2018, 2019). However, there is still a dearth of studies that attempt to model calving as part of a fully coupled tidewater-glacier system, providing the gap that this thesis seeks to address.

2.2. Modelling Tidewater Glaciers

Numerical modelling has been touched on in Section 2.1 for the individual components of the tidewater-glacier system, but this section aims to give a brief overview of why it is a particularly applicable method to the whole system, as well as reviewing progress in the field. Section 2.2.1

provides additional detail on the use of inversion techniques within numerical modelling, as the use of such methods forms part of Chapters 3, 5 and 6.

Computer-based modelling of glaciers has been a major tool within the field since it was first developed in the 1970s, with the first 3D model presented by Mahaffy (1976). As computing power has increased in the intervening forty years, the sophistication and complexity of glaciological computer modelling have followed, with recent studies investigating ice at all scales from individual glaciers (Favier et al., 2014; Gillet-Chaulet et al., 2016; Larour et al., 2014; Morlighem et al., 2016; Shapero et al., 2016; Solgaard et al., 2018) and ice shelves (Khazendar et al., 2015) to entire ice sheets (e.g. Arthern et al., 2015; Fürst et al., 2016; Gillet-Chaulet et al., 2012; Stevens et al., 2018). Much work has also been undertaken on the theoretical basis of modelling of all kinds (e.g. Ahlkrona et al., 2016; Gong et al., 2016; Maxwell et al., 2008; Mcnabb et al., 2012; Mosbeux et al., 2016; Passalacqua et al., 2016; Petra et al., 2012; Truffer, 2004) and on comparing the performance of different models in the same situation to establish the effect of model bias on results and which models perform best in which situations (e.g. De Fleurian et al., 2018; Favier et al., 2014; Gagliardini et al., 2016; Gladstone et al., 2017; Mosbeux et al., 2016; Pattyn et al., 2012; Zhang et al., 2017).

Earlier modelling studies mainly used simplifications or approximations of the Navier-Stokes equations to reduce the computing load, such as the Shallow Ice Approximation (SIA) or Shallow Shelf Approximation (SSA) (e.g. Rutt et al., 2009), both of which are valid in some cases, but are known to perform poorly in environments where it is important to consider the full 3D stress balance, such as the terminus region of tidewater glaciers (Gagliardini et al., 2013; Morlighem et al., 2010). The greater availability of computing power, however, means that full-Stokes, 3D models of tidewater glaciers are now feasible and capable of producing more accurate results in these complex environments (e.g. Favier et al., 2014; Morlighem et al., 2010, 2016; Gong et al., 2018)

The reason for this effusion of modelling studies is that computer modelling allows glaciologists to overcome some of the issues inherent in the discipline. To begin with, it is the only practical way to produce predictions about how a given ice mass is likely to change in the future, which is essential to understanding the impacts of global warming and projecting sea-level rise over the coming decades and centuries (e.g. Liu et al., 2017; Luo et al., 2016; Price et al., 2011; Stocker et al., 2013). On a similar note, it allows hindcasting, i.e. studying the evolution of ice masses in past glacial cycles (e.g. Bougamont et al., 2015; Evans et al., 2009; Hubbard, 1999; Kleman et al., 1997; Stokes and Tarasov, 2010), which also allows validation of the model by applying it to a situation with a known outcome. These possibilities mean that modelling also gives us the capacity to conduct ‘What if?’ experiments,

which can be of great use in understanding glacial dynamics and the range of possible glaciological outcomes where the inputs are uncertain (e.g. Gillet-Chaulet et al., 2012; Stocker et al., 2013).

On a different note, modelling also allows gaps in observations to be filled in, given that the largely remote-sensing-based observational record inevitably contains lacunae due to satellite orbits, cloud, and instrument malfunction. It also allows data to be generated for regions that cannot be observed, either due to remoteness (e.g. the Polar holes present in many satellite orbits that limit the number of observations available; not that these necessarily affect tidewater glaciers as much as the interior of the ice sheets) or to access issues (e.g. the calving front or the bed of the glacier).

Numerical modelling is therefore particularly applicable to tidewater glaciers, being able to handle such complex environments and help resolve the lack of observations available for many aspects of these important systems, providing the methodological direction for this thesis, which is detailed further in Chapter 3. As should be obvious from Section 2.1, the dynamics of tidewater glaciers are chiefly the result of the interplay of the evolution of several systems: the ice and fjord geometry, the subglacial hydrology and calving, so modelling such glaciers ideally requires explicit incorporation of all these systems.

2.2.1 – Inversion-based Modelling

One of the particular advantages of modelling referred to in Section 2.2, above, is that it can facilitate the study of areas of the glacier that are not amenable to direct observation. This is particularly relevant to tidewater glaciers, where many of the key processes take place at the bed and the calving front. Both of these environments are very difficult to study otherwise – the bed is buried beneath several hundred metres of ice and the calving front is extremely difficult and dangerous to approach, as well as having the same problem of inaccessibility for the part below the waterline. Therefore, computer modelling is the only practical way of investigating these two crucial zones.

One especial modelling technique is of relevance here: that of using inversions. This refers to the practice of taking an easily-observable surface quantity (e.g. surface velocity) and using this to work out an inobservable parameter (e.g. the basal friction coefficient). This method was first applied to glaciology by MacAyeal (1993) and has become increasingly popular in recent years as computing power has grown, with many studies seeking to invert for parameters such as basal friction (e.g. Arthern et al., 2015; Gillet-Chaulet et al., 2012; Shapero et al., 2016; Solgaard et al., 2018) or viscosity (e.g. Khazendar et al., 2015; Petra et al., 2012).

To undertake an inversion, a model requires two components: a forward model and an inverse model. The forward model solves the Navier-Stokes equations and the inverse model uses this to calculate values for the variable that is being inverted for. There are several different approaches used to perform this inversion, but the most popular and the one that is used in this thesis is the control method (also called the adjoint method), as used by MacAyeal (1993). Regardless of the method used, the inverse model iterates towards a field of the inverted-for quantity that reproduces the observed surface quantity. There are an infinite number of possible solutions that could fulfil this requirement, so any inverse method requires some sort of optimisation criterion that allows a particular solution to be chosen (Truffer, 2004).

For the control method, a cost function to minimise the mismatch between the observed surface values and the modelled values is used to choose the best-possible solution. This approach is detailed in Gillet-Chaulet et al. (2012) and Gagliardini et al. (2013) and is summarised here. The initial cost function, J_0, is calculated as:

$$J_0 = \int_{\Gamma_s} \frac{1}{2}(|u_H| - |u_H^{obs}|)^2 \, d\Gamma \tag{7}$$

Where u_H is the horizontal component of the modelled velocity and u_H^{obs} is the observed velocity, both in m a^{-1}. J_0 is not always minimised strictly with respect to the inverted-for parameter, but is often minimised with respect to some power function of it to avoid negative values and to produce smoother output.

J_0 is also usually subject to some form of regularisation to promote a smoother output at the expense of solutions that produce unphysical rapid variations, which also aids model convergence. This is often Tichonov regularisation (e.g. Konovalov, 2012) and adds a J_{reg} term to J_0 to give a new cost function, J_{tot}. J_{reg} is defined as:

$$J_{reg} = \int_{\Gamma_b} \frac{1}{2}\left(\frac{d_{\alpha_p}}{d_x}\right)^2 + \left(\frac{d_{\alpha_p}}{d_y}\right)^2 d\Gamma \tag{8}$$

Where α_p is the parameter being inverted for. The combined cost function, J_{tot}, is thus:

$$J_{tot} = J_0 + \lambda J_{reg} \tag{9}$$

Where λ is a parameter that can be tuned to define the balance between mismatch between the modelled and observed velocities (J_0) and smoothness (J_{reg}). The optimal value of λ, which varies for each domain, may be found by using the L-curve method (e.g. Gillet-Chaulet et al., 2012; Konovalov, 2012). This consists of plotting a graph of J_0 against J_{reg} for a range of values of λ, giving a characteristic 'L' shape, the corner of which is the optimal value of λ that gives the best compromise between mismatch and smoothness. However, the resulting L curve will often have more than one corner, making interpretation subjective, and, in practice, a range of possible lambda values will provide a satisfactory output.

It should also be mentioned that it is theoretically possible to invert for multiple parameters at once – for example, it would be useful to better constrain the viscosity field through an ice mass, as well as the basal friction coefficient – but this imposes far larger demands on computational resources, is complex to implement, and reduces the accuracy of the individual inversions (Petra et al., 2012), so will not be considered further here.

2.3. Observations of Tidewater Glaciers from Radar Interferometry

Whilst modelling is the main focus of this thesis and is an area that has seen rapid progress in recent years, one key challenge is obtaining observations with which the increasingly complex models can be validated. The number of inputs required means that most obvious datasets (e.g. surface velocity, mass balance or elevation change) have already been used in the modelling process, certainly if inversions are undertaken, so are not appropriate to use for validation, meaning other datasets need to be considered. One major recent advance in this area is the use of terrestrial radar interferometers (TRIs). TRIs are becoming increasingly used in glaciological research as a means of obtaining high-resolution datasets, both in space and time, of the terminus of tidewater glaciers. TRIs typically operate in the Ku band (λ_w = 1.75 cm) and have one transmission antenna and two receive antennae, so can be used to derive change over time, i.e. velocity, by feature-tracking successive images obtained from the same receive antenna (e.g. Cassotto et al., 2018; Voytenko et al., 2017; Xie et al., 2016), and change over space, i.e. DEMs/topography, by comparing simultaneous images from each receive antenna (e.g. Cassotto et al., 2018; Walter et al., 2020). Spatial resolutions of 0.75 m in range and 8 m at 1 km distance in azimuth are typically achievable (Cassotto et al., 2018), whilst temporal resolution can be as high as one observation per minute (Walter et al., 2020). This makes TRIs a very useful instrument for observing short-term calving-front processes related to calving and expressed as precursory velocity changes or displacement (Voytenko et al., 2017; Xie et al., 2016), as well as the form and distribution of calving events themselves (Cassotto et al., 2018; Walter et al., 2020).

The main consideration with using TRIs is being able to find a suitable deployment position – on a stable substrate, facing the calving front and within a few kilometres of it – and, given the instrument's sensitivity, to protect it as far as possible from interference due to natural conditions or human activity. One solution is to encase the instrument in a radome (Xie et al., 2016), but siting the instrument in a sheltered spot away from generators or drilling equipment is sufficient.

TRIs do come with several challenges, however: they are large, bulky, expensive instruments that require round-the-clock power, which often means the use of generators that further add to the instruments' expense. The amount of data generated – about 100 GB per day at a 3-minute temporal resolution – also imposes heavy data storage requirements. Poor siting of the instrument can lead to unsatisfactory datasets and the eventual processing of the raw radar data to produce useful datasets is computationally expensive. Despite this, TRIs provide one of the few possible means of obtaining datasets that can be used to independently validate numerical models, as well as unparalleled spatiotemporal resolution.

3. Modelling Framework, Code Development and TRI Method

'[R]emote upon the edge of sight, and beyond the count of leagues, he glimpsed a mountain, rising beyond his mind's reach into a shining cloud, and at its feet a long surf glimmering. And even as he strained to hear the sound of those far waves, and to see clearer that distant light, the note ended[.]'
-Of Tuor and His Coming to Gondolin, Unfinished Tales

This chapter sets out the suite of modelling developments that underpins Chapters 5 and 6, as well as the methods used to derive the radar interferometry dataset described in Chapter 4. Section 3.1 describes the overall modelling problems that needed to be solved to provide context for Sections 3.2-3.5, with methodological details on the three main avenues of model development provided in Sections 3.2 (3D hydrological modelling), 3.3 (dual-mesh simulations) and 3.4 (interfacing with a plume model). Section 3.5 details additional code developments undertaken outside the main model-development avenues, but which were necessary to the functioning of the fully coupled model. The radar processing methods are then presented in Section 3.6.

3.1. Nature of the Problem

Modelling tidewater glaciers requires consideration of several processes absent from land-terminating glaciers, due to the presence of water at the glacier terminus. Two of the most obvious are calving and proglacial freshwater plumes fed by subglacial discharge at depth in the fjord. Whilst models exist for individual components of the tidewater-glacier system, e.g. Slater et al. (2016) for plumes, Werder et al. (2013) for subglacial hydrology, and Todd et al. (2018) for calving, there has been little attempt to integrate them until now. Such attempts as there have been (e.g. Vallot et al., 2017, 2018) have avoided coupling the different components and adopted an off-line approach, where each model runs separately and feeds its output to another component. This is because coupling the different components within one simulation, particularly coupling the subglacial hydrology to glacier dynamics, can lead to prohibitively long model run times, owing to the complexity of the resulting set up. In addition, the not-insignificant technical difficulties in getting several originally disparate model elements not necessarily first written in the same programming language to communicate effectively so that the right output goes to the right input at the right time can represent a substantial technical challenge.

The approach I adopted here to address the first aim of this dissertation was to develop the model within the Elmer/Ice modelling suite (Gagliardini et al., 2013); a suite of open-source, 3D, full-Stokes, finite-element modelling software. This presented two main advantages: firstly, previous work by Joe Todd (Todd et al., 2018; Todd and Christoffersen, 2014) meant that a coupled calving-ice-flow model was already available. Secondly, an initial version of Mauro Werder's Glacier Drainage System

(GlaDS) (Werder et al., 2013) subglacial hydrology model had just been introduced to the suite, but was only functional for 2D simulations and some (not all) 3D simulations. The key challenges to solve were consequently:

1. Adapt the existing GlaDS code to produce a subglacial hydrological model that worked correctly in all 3D simulations.
2. Work out an approach that allowed calving and subglacial hydrology to interact and run successfully in the same simulation.
3. Develop a new plume model or adapt an existing one, and work out how to integrate this with the other components of the simulation.

The remainder of this chapter provides methodological details on how each of these issues were resolved. Section 3.2 considers 3D hydrology; Section 3.3 deals with coupling calving and subglacial hydrology; and Section 3.4 details the set-up of the plume model.

3.2. 3D Hydrology

3.2.1. The GlaDS Subglacial Hydrology Model

GlaDS functions by simulating a sheet of water at the ice-bed interface, with the model variables being defined at nodes on an unstructured triangular mesh (Figure 2) as is usual within Elmer/Ice. This sheet represents the inefficient distributed component of a subglacial drainage system. It also models efficient channels explicitly, which are formed on the edge elements of the mesh (Figure 2) where the sheet becomes locally thick enough to sufficiently melt the overlying ice. Whether large cavities that lead to high sheet thicknesses open is determined ultimately by the balance between basal sliding (the opening term) and viscous creep related to effective pressure and, ultimately, ice thickness (the closing term). Inefficient drainage is therefore the default model, with efficient drainage only appearing when the inefficient system becomes sufficiently water-filled, at which point the efficient channels can capture water from the inefficient sheet, potentially leading to a reduction in flow in the inefficient network. The channels then evolve independently of the sheet, with opening primarily determined by melt caused by viscous dissipation of heat from water flowing within the channel and closure again determined by viscous creep related to effective pressure and ice thickness. Channels can therefore further expand or collapse back to zero cross-sectional area (in which case the model removes them), depending on the subsequent evolution of the hydrological system.

The edge elements on which channels are formed are otherwise little-used in Elmer/Ice and caused repeated problems throughout the code development phase, as detailed further in Sections 3.3 and 3.4. The difference between the two types of variable is shown in Figure 2.

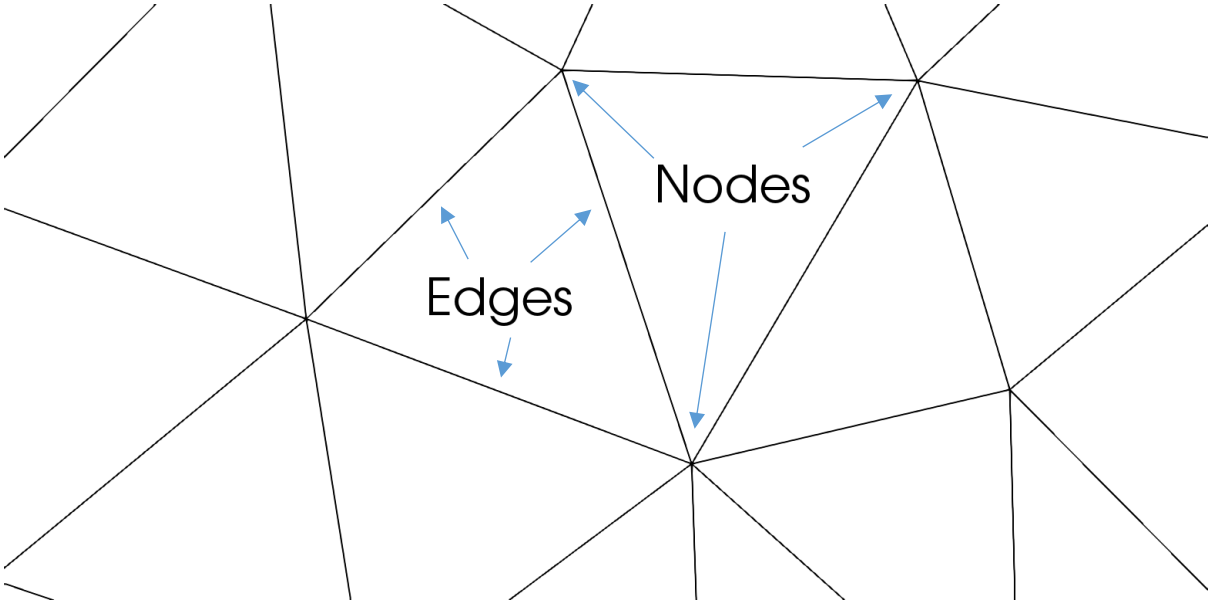

Figure 2 – Mesh example showing nodes (where most model variables are defined) and edges (where channels are allowed to form).

Full mathematical details on the functioning of the GlaDS model are available in Werder et al. (2013), with additional details on its functioning within Elmer/Ice in Gagliardini and Werder (2018). These are not presented here, as none of the work I conducted for this dissertation involved modifying the existing core of the model, or introducing new mathematical capabilities. However, the critical equations for sheet-channel transition and subsequent channel evolution are shown (Eq. (10)-(13)), as these are relevant to the discussion in Chapter 6. All are adapted from Werder et al. (2013).

Cavities that form at the ice-bed interface and whose size and presence determine the sheet thickness and, ultimately, where channels nucleate, open according to:

$$w = \begin{cases} \frac{u_b(h_r - h)}{l_r} & if\ h < h_r \\ 0 & otherwise \end{cases} \quad (10)$$

Where w is the opening rate, u_b is the basal velocity, h_r is the typical bedrock bump height (a model parameter – see Chapter 5 for the value used in this thesis), h is the sheet thickness, and l_r is the typical horizontal cavity spacing.

Cavities then close by:

$$v(h, N) = Ah|N|^{n-1}N$$

(11)

Where v is the closing rate, h is the sheet thickness, A is the rheological constant of ice multiplied by an order one geometrical factor, and N is the effective pressure.

The opening rate of channels is given by:

$$w_c = \frac{\Xi - \Pi}{\rho_i L}$$

(12)

Where Ξ is the potential energy dissipated per unit length, Π is the sensible heat change of the water, and L is the latent heat of fusion of water. Ξ depends chiefly on the volume of water in the channel (if one already exists) and in the sheet within a user-defined distance of the potential or actual channel (i.e. the edge element; this parameter is also described in Chapter 5), and therefore on local sheet thickness. Π then likewise chiefly depends on discharge in the channel and in the surrounding sheet, as well as the local hydraulic and elevation potentials.

The rate of channel closure, finally, is described by:

$$v_c(S_c, N) = AS_c|N|^{n-1}N$$

(13)

Where S_c is the channel cross-sectional area.

3.2.2. Internally Extruded Simulation

The original version of GlaDS adapted for Elmer/Ice by Olivier Gagliardini from Werder et al. (2013) only functioned within a 2D simulation, or in 3D if an externally extruded 3D mesh was used (i.e. the model was provided with a 3D mesh *ab initio*). This was problematic, because the calving model implemented in Elmer/Ice relies on internal extrusion of a provided 2D footprint mesh to create a 3D mesh as part of the simulation. Therefore, it was necessary to adapt GlaDS to work in this case.

Making GlaDS function correctly for 3D internally-extruded simulations was achieved with some bug fixes within the mesh generation section (`MeshUtils.F90`) of the Elmer/Ice source code related to ensuring correct generation and preservation of edge elements on the 3D mesh. This allowed GlaDS to run smoothly on the basal boundary of an internally extruded 3D mesh, making it possible to move on to the next step in the modelling process.

3.3. Coupling Calving and Hydrology

The version of GlaDS I started working with was already set up to allow two-way coupling between it and ice flow. GlaDS requires as inputs both the velocity of the ice and the ice normal stress at the bed, ensuring coupling from the ice to the hydrology. Coupling in the other direction is undertaken using the effective pressure calculated by GlaDS as an input for a Coulomb sliding law (in `USF_Sliding.F90`) of the form detailed in Section 2.1.1. A further coupling link is provided by the use of the basal water pressure calculated by GlaDS as the water pressure variable in `ProjectCalving.F90`, which uses it to work out the extent of basal crevassing; as high-pressure water in basal crevasses and the associated hydrofracturing is a key factor in crevasse propagation. Whilst this overall simple framework was essentially set from the start, implementing it within a coupled calving-hydrology model run required the resolution of some deeper incompatibilities between GlaDS and the existing calving code, as detailed in Sections 3.3.1-3.3.3.

3.3.1. Dual Meshes

The primary issue with coupling GlaDS to the existing calving functionality within Elmer/Ice was related to the way the model used meshes. The calving solver (specifically `Calving3D.F90`) proceeds by detecting a calving event, remeshing the model domain minus the area that has just calved, and then interpolating all model variables from the old, pre-calve mesh to the new, post-calve mesh. This approach was unproblematic for the nodal variables, but could not handle the edge-defined channel variables. One possibility was to attempt to modify the interpolation routines to function with edge variables, but this was rejected owing to inherent issues. When the remeshed post-calve mesh is generated, the nodes and edges all move slightly compared to the pre-calve mesh. For nodal variables representing a continuous field, interpolation is then straightforward, as the nodal values are simply adjusted slightly to give the same field; for edge variables, which do not represent a continuous field, it is not obvious how values should be re-assigned to the new set of edges in a manner that will produce a set of values consistent with the pre-calve values.

Therefore, I took the decision to adopt a dual-mesh approach. All variables related to ice flow and calving are defined, as usual, on an internally extruded 3D mesh that can be deformed and remeshed using the existing calving code. GlaDS, meanwhile, runs on a separate, static 2D mesh representing the basal boundary of the 3D ice mesh. Adopting this approach avoided the fundamental issue of interpolating edge variables between pre- and post-calve meshes, but then required interpolation of necessary input and output variables between the ice and GlaDS meshes, as well as working out a method to represent the moving calving front on the GlaDS mesh. These two areas of code development are detailed further in Sections 3.3.2 and 3.3.3, respectively. Several

bugs within the existing calving code relating to how it dealt with remeshing when different variables were run at different timesteps and when not all variables needed to be considered for interpolation also had to be addressed as part of this dual-mesh approach, leading to minor fixes across several parts of the source code, principally `Calving3D.F90` and `CalvingRemesh.F90`.

3.3.2. Interpolation – `CalvingHydroInterp.F90`

As described in Section 3.3.1 above, two sets of variables need to be interpolated between the ice mesh and the GlaDS mesh: the ice variables required as inputs to GlaDS, and the GlaDS variables required to feed back to the ice mesh to ensure two-way coupling. This is achieved with a new solver (`CalvingHydroInterp.F90`) that allocates all the necessary storage and pointers for the interpolated variables. This solver then performs the interpolation using a version of `InterpVarToVar.F90` I modified to allow interpolation between meshes differing in resolution, extent and dimension, and then seeks to clean up any interpolation artefacts. The solver will also add variables to the main GlaDS mesh that have been read in from rasters, such as the surface runoff. Finally, it interpolates and conserves the temperature residual variable from the ice mesh to the GlaDS mesh, the reasons for which are discussed in Section 3.5.1.

The main issue here, which requires further discussion, is the nature of the interpolation artefacts. As the GlaDS mesh is usually at a higher resolution than the ice mesh, simple interpolation often leads to a few artefacts along the lateral and inflow boundaries, where an obviously erroneous value is assigned to some boundary elements and/or nodes. This is particularly problematic for the ice normal stress variable, where lateral boundary nodes were occasionally assigned values of 0. This then meant that GlaDS interpreted these areas as having very low hydraulic potentials, turning them into preferred sites for water accumulation and channel formation, despite their location under thick ice tens of kilometres inland. This diverted water from the calving front and also often led to numerical instabilities. The solver resolves this issue by, after interpolation, checking for 0 values of ice normal stress in grounded areas of the GlaDS mesh (ungrounded areas are discussed in Section 3.3.3) and simply copying in a non-zero value from one of the other nodes in the same element (or the average of the non-zero values if the element has multiple non-zero additional nodes). If all nodes in the element have 0 ice normal stress, the average ice normal stress value for the partition is used, plus a constant (set to equal 3 MPa for Store, based on a sensitivity analysis). I consider this simplification valid, because it only affects a very small number of nodes per simulation, the ice normal stress field does not vary sharply, and because these affected nodes are not hydrologically important and just need to be prevented from turning into unphysical sinks by being assigned a sufficiently high ice normal stress value.

3.3.3. Ungrounded Areas and the Calving Front

The other key issue that coupling GlaDS and the calving code presented was how to represent the moving calving front of the ice mesh on the GlaDS mesh and how to handle ungrounded areas from a hydrological point of view. The first step to resolving these two linked issues was to ensure the static GlaDS mesh covered a larger footprint than the dynamic ice mesh. Calving-front retreat could be accommodated within the existing mesh, but the possibility of advance required that the GlaDS mesh extended some distance beyond the front of the initial ice mesh. The next step, implemented as part of `CalvingHydroInterp.F90`, was to interpolate the mask of grounded and ungrounded areas produced by `GroundedSolver.F90` from the ice mesh to the GlaDS mesh. The mask marks grounded nodes as '1', the grounding line as '0' and ungrounded nodes as '-1'. Interpolation, however, leads to values in-between these three categories being created around the grounding line, so the solver, post-interpolation, rounds all values to the nearest integer to restore the tripartite division of values. This leads to some minor distortion of the grounding line, but this would be unavoidable with any form of interpolation. Any errors are then cleaned up by `CalvingHydroInterp.F90` that, post-interpolation, sets any areas where the ice normal stress is equal to 0 to be ungrounded. Given the correction routines for ice normal stress detailed in the previous section, this condition is only true on the area of the GlaDS mesh extending in front of the calving front, so functions as an effective mask here.

Interpolation also, again, tends to create artefacts on the lateral margins of the model domain farther inland, which, in this case, manifest themselves as small ungrounded areas. I remove these by forcing all nodes on the GlaDS mesh more than a certain distance inland from the calving front, as determined by the distance (the default is 10 km) from a user-specified reference point, to be grounded. I also apply a boundary condition to the lateral margins forcing any ungrounded nodes to be grounded (grounding-line nodes remain unchanged). This does mean that the lateral margins of the area of the GlaDS mesh extending beyond the front of the ice mesh are also grounded, but this is dealt with using boundary conditions, as described below.

The interpolation of the grounded mask therefore provides a method for GlaDS to keep track of where the calving front is and adjust its functioning appropriately. I therefore needed to decide how best to deal with these ungrounded areas. There are two kinds of ungrounded areas produced by the model:

- Those connected to the wider fjord (here, represented by those connected to the ungrounded area of the GlaDS mesh sitting beyond the front of the ice mesh).
- Those unconnected to the fjord, i.e. isolated ungrounded patches.

For the former, physically, it is reasonable to assume that there is effectively no subglacial hydrology of the kind able to be modelled by GlaDS. Any water reaching these areas has left the grounded subglacial drainage system modelled by GlaDS and entered some kind of fjord-connected sub-ice cavity where it will form a freshwater plume rising up the ice front (discussed further in Section 3.4). For the latter, this is not true, as these ungrounded patches are essentially large cavities within a subglacial drainage system containing many other cavities, so modelling of hydrological processes should continue in these areas. Therefore, I implemented modifications to `GlaDSCoupledSolver.F90` to set all hydrological variables except water pressure to 0 in ungrounded areas. These are reinforced by conditional boundary conditions that also force no hydrology in ungrounded areas and which prevent the growth of channels on all boundary edge elements, mitigating the forced groundedness of the lateral mesh boundaries. Water pressure in ungrounded areas, meanwhile, is set to the hydrostatic pressure, i.e.:

$$P_w = abs(Z_b \rho_w g) \tag{14}$$

Where Z_b is the basal elevation, which is negative below sea level (and therefore negative in any ungrounded areas at Store, hence the abs() function). This ensures basal crevasses can still open as normal in ungrounded areas and is also more physically realistic.

This solution does, however, require discrimination between fjord-connected ungrounded areas, where this approach is appropriate, and isolated ungrounded patches, where it is not. If this distinction is not made, isolated ungrounded patches become unphysical sinks of water, as GlaDS cannot model drainage into and out of such areas. This distinction is achieved using a validity mask (`GMValid.F90`), based on `BasalMelt3D.F90`, which assigns a value of 1 to the mask in all ungrounded areas connected to the fjord; everywhere else it is set to 0. Therefore, ungrounded areas with non-zero values for the mask variable (and which are therefore connected to the fjord) have all hydrological variables set to 0 and are ignored by GlaDS, whilst those with 0 for the mask variable (and which are therefore isolated ungrounded patches) are treated as if they were grounded and thus continue to have hydrological processes modelled in them.

3.4. Interfacing with a Plume Model

The final component of the fully coupled model that needed to be developed was the addition of a model to simulate proglacial freshwater plumes at the calving front. The input for these plumes comes from the channel flux and sheet discharge variables in GlaDS; the plume model then calculates melt rates that are applied to the calving front, making a further link in the model. The

plume model itself is described in Section 3.4.1, with the wrapper routine that interfaces with the wider Elmer code set out in Section 3.4.2.

3.4.1. The Plume Model – `PlumeSolver.F90`

The plume model I implemented in Elmer/Ice is a version of that presented in Slater et al. (2016). It is a 1D Ordinary Differential Equataion (ODE) model that takes an input discharge and models the resulting plume, including the melt rates that are extracted and applied to the calving front. The model relies on the public-domain ODEPack library of ODE solvers written in FORTRAN 77 and which I modified slightly to allow them to compile with the Elmer FORTRAN compiler, which uses the FORTRAN 90 standard. Work is ongoing to write an ODE solver within Elmer, but remains to be completed.

The model is set up to simulate a sheet-style plume, rather than a conical plume (Jenkins, 2011), as this plume geometry is a better fit for the limited available observations of plume outlets at tidewater glaciers (Fried et al., 2015; Jackson et al., 2017). These observations suggest many low, broad outlets, rather than discrete, fully channelised outlets, hence my decision to move forward with sheet plumes.

3.4.2. Model Set-Up – `PlumeSolver.F90`

The wrapper subroutine that provides inputs to the plume model and extracts the outputs is based on one initially written by J. Todd to model fixed, conical plumes with prescribed melt rates. All this functionality is maintained, but I undertook a substantial expansion of this skeleton to allow fully dynamic modelling of plumes estimated from theory and not simply the conical shapes used by Todd et al. (2018).

The overall strategy adopted by the solver is to simulate a dynamically evolving continuous sheet plume along the entire calving front, avoiding any requirement for the user to specify plume locations or melt rates. Initially, all the nodes on the grounding line on the GlaDS mesh are identified using the interpolated grounded mask, as these nodes are where the plumes will form. Each of these GlaDS nodes is then assigned to the nearest grounding-line node on the ice mesh, as this is the mesh where the melt rates need to be applied. Of course, the nearest grounding-line node on the ice mesh will likely be in a different partition to the GlaDS-mesh grounding-line node under consideration, so the solver is forced to consider each GlaDS-mesh grounding-line node one-by-one and communicate among all partitions to find the one that contains the nearest ice-mesh grounding-line node.

The solver then discards the GlaDS-mesh grounding-line nodes too far inland, i.e. those that sit on the grounding line surrounding an isolated ungrounded patch. It does this by considering two parameters: the mesh resolution at the terminus, provided as a solver option, and the distance from the target node to the nearest node with a non-zero value for the basal melt rate. As discussed in Section 3.3.3, this variable, calculated in the same way as the validity mask created by `GMValid.F90`, works effectively as a mask for ungrounded areas connected to the wider fjord and those not. If the distance from the target GlaDS-mesh grounding-line node to the nearest ice-mesh grounding-line node is greater than 500 m **and** the distance from the target node to the nearest node with a non-zero basal melt rate is greater than 110% of the mesh resolution at the terminus, the node is considered to be on an isolated ungrounded patch and is ignored. Any valid grounding-line node should have a neighbouring node with a non-zero basal melt rate, so there should be one within the distance defined by the mesh resolution at the terminus. The 500 m distance criterion is a threshold appropriate for Store, given the distribution of ungrounded areas found at the terminus, but may need changing for other settings.

The discharge available to form plumes at each valid GlaDS-mesh grounding-line node is then calculated from the sum of sheet discharge at that node and channel flux in the edges flowing towards it. If multiple GlaDS nodes are assigned to the same ice node, their discharges are summed. The solver then reads in the ambient conditions, i.e. the temperature and salinity profile of the fjord water, from a data file and passes this information and the discharge to the plume model, which runs for every ice-mesh grounding-line node with non-zero discharge. The plume model can handle non-vertical calving fronts, but the current implementation assumes vertical calving fronts. Non-vertical fronts are relevant on ice shelves and where extensive ungrounded areas exist, but this is not the case at Store. The plume model also requires a set of depths to evaluate the plume at; for convenience, these are the depths at which salinity and temperature are defined.

Once the plume model has run for every relevant node, it constructs a 2D array of plume melt rates, with depth below sea level as one axis and distance along the calving front as the other. The latter is calculated by working out the major axis of the front – i.e. is it primarily oriented in the x (East-West) or y (North-South) direction – and then ordering the ice-mesh grounding-line nodes by the relevant co-ordinate. This simplification is unproblematic for fairly straight calving fronts with uncomplicated grounding lines, as is the case at Store, but may need modification for more convoluted fronts and grounding lines. To apply the plume melt rates to the calving front, the solver then loops through all nodes on the frontal boundary of the ice mesh and interpolates a melt rate from the 2D array based on the node's position. First, the solver finds which two plume nodes the target node falls between, and then linearly interpolates the melt rate in each plume at the depth of the target node. The

solver then linearly interpolates between the two melt values depending on the horizontal position of the target node. If the target node is off one end of the plume list, i.e. it is at one margin of the calving front and not between two plumes, Gaussian decay from the nearest plume is applied. The resulting melt rate is then applied as ablation on the frontal boundary of the ice mesh.

3.5. Other Code Development

This section details three other areas of code development that were necessary to ensure the coupled model functioned correctly, but fell outside of the main set of problems. Section 3.5.1 describes the user function that handles the source term for GlaDS – i.e. how much water is going into the hydrological system – Section 3.5.2 details how the coupled model simulations can be restarted, and Section 3.5.3 summarises modifications made to the code to avoid numerical instabilities.

3.5.1. Water Input – `USF_SourceCalcCalving.F90`

GlaDS requires a water source term, which, for a glacier, is going to come primarily from meltwater (direct rainfall is not considered in this model, but could be easily added if required). This can be runoff from surface melt that has reached the subglacial drainage system through crevasses and moulins at the surface, or it can be meltwater produced at the base or internally due to heating from friction or strain and the geothermal heat flux. To include both these terms and have them update dynamically, I wrote a user function, `USF_SourceCalcCalving.F90`. This function has two switches that allow the user to specify whether to include surface and/or basal melt. Surface melt input is taken from a named variable, which will usually be a raster of surface runoff (from RACMO data in this dissertation) loaded in separately (direct rainfall could therefore be included simply by adding precipitation values to the raster). All runoff is assumed to travel straight to the bed at the site of production; in other words, no supraglacial routing is performed. Given the scale of the model domain, the resolution of the runoff data (typically 1km by 1km), and the focus on the influence of hydrology on calving processes, this is a reasonable simplifying assumption, as transport distance in the supraglacial network is typically over relatively short distances (Smith et al., 2015) before it is intercepted by a moulin or crevasse.

Basal and strain melt is calculated from the temperature residual produced by the TemperateIce solver (`TemperateIce.F90`). As the upper temperature limit is set at the pressure melting point (PMP), this residual records the amount of excess heat removed by the solver to keep the system at or below that limit. Or, to put it another way, the amount of energy that would have gone into melting the surrounding ice. This residual is interpolated on to the GlaDS mesh by

`CalvingHydroInterp.F90`, which also ensures that energy is conserved, as simple interpolation will lead to the creation of energy, assuming the GlaDS mesh is at a finer resolution than the ice mesh. The user function then calculates the amount and location of melt that the residual would generate and adds it to the surface melt term to get the total input to the subglacial drainage system at each node on the GlaDS mesh.

3.5.2. Restarting Hydrological Simulations – **`HydroRestart.F90`**

The default Elmer/Ice behaviour is, if multiple meshes are being used in a simulation and a restart is requested, to attempt to restart all variables on all meshes. This is not appropriate in this case for two reasons. Firstly, for any simulation initialising the hydrology, but using a restart for the ice mesh variables, there are simply no restart files for the GlaDS mesh. Secondly, the additional GlaDS meshes associated with the two secondary GlaDS solvers and with any solvers that are reading in variables destined for the primary GlaDS mesh never need to be restarted, so disabling the default behaviour reduces processing time. Therefore, I modified `ElmerSolver.F90` and `ModelDescription.F90` to change the default behaviour to only restarting the primary model mesh, which will always be the ice mesh. I also added an option to allow users to vary this if desired with a new keyword in the simulation section of the SIF. I then wrote a new solver, `HydroRestart.F90`, that replicates the behaviour of the standard Elmer restart routine and associates the right GlaDS variables with the right mesh to ensure a smooth restart.

3.5.3. Model Stability

One final issue encountered as part of modelling development was a tendency for GlaDS to generate numerical instabilities that manifested as unphysical sheet thicknesses (on the order of 10^{10} m or higher), leading to runaway channel growth and eventual production of infinite values that crashed the model run. Some of these were due to the ice normal stress artefacts on lateral boundaries described in Section 3.3.2, so removing these improved the simulations. Others, however, were the product of channels in the finest-resolution mesh areas (where the resolution is 100 m) growing to channel areas greater than the distance between mesh elements and consequently causing issues. Therefore, I modified GlaDSCoupledSolver.F90 to limit channel cross-sectional area to 10000 m^2 and sheet thickness to 100 m to prevent any instabilities from propagating and precipitating a crash. Sheets of over a few metres in thickness are unphysical, so the 100 m limit should have no impact on 'normal' model functioning, whilst, assuming a semi-circular channel, 10000 m^2 equates to a channel with a diameter of ~160 m, which allows channels of the right order-of-magnitude to form, based on limited observations (Jackson et al., 2017), without permitting them to reach problematic dimensions.

3.6. Radar Interferometry

This section describes the data processing method used to derive the calving record of Store presented in Chapter 4.

3.6.1. Radar Data Processing

The terrestrial radar interferometer (TRI) used to collect the observations reported in Chapter 4 was a Gamma Remote Sensing Ground-based Portable Radar Interferometer II (GPRI-II). This is a Ku-band (17.2 GHz; λ=1.75 cm), real-aperture, yaw-rotating instrument that is capable of measuring surfaces up to 16 km away with a range resolution of 0.75 m and an azimuthal resolution proportional to slant range with a ratio of 8:1000 (i.e., an azimuthal resolution of 8 m at 1 km distance) (Werner et al., 2008). The instrument has one transmit and two receive antennas, the receivers being spaced 25 cm apart, allowing both temporal change (velocity) and spatial change (topography) to be measured. The former is achieved by comparing images from the same antenna taken at two different times; the latter, used here, by comparing images from both antennae taken at the same time. The exact instrument set-up used in this thesis is described in Section 4.3.2; the rest of this section describes in detail the data processing undertaken following acquisition of data from the TRI.

I used the interferogram record from the TRI, processed using the Gamma software suite, to generate a sequence of DEMs from which a record of calving events at Store could be extracted. Topography was calculated following the method of Strozzi et al. (2012), with the resulting DEMs being resampled to a 10m by 10m resolution and reprojected to Cartesian co-ordinates. As the measurements from each receiver antenna are contemporaneous, no atmospheric or phase displacement corrections are needed (Strozzi et al., 2012). Inspection of the resulting record revealed significant phase breaks and changes in orientation of the TRI over the course of the observation period, which I ascribe to periods of high winds buffeting the instrument. I identified four stable periods, covering the vast majority of the three-week record (18 out of 21 days), within which orientation and instrument biases were constant. Rotations were applied to each phase to ensure alignment of DEMs, as set out in Table 1.

Table 1 – Stable phases and applied rotations to ensure alignment. Times are in local time.

Name	Start	End	Rotation
Phase 1	18:25 05/07/17	07:18 14/07/17	0
Phase 2	19:06 14/07/17	23:36 18/07/17	-10°
Phase 3	14:06 21/07/17	01:03 26/07/17	-3°
Phase 4	01:09 26/07	11:01 27/07/17	0

Initially, I interpolated the DEMs to fill gaps, but further investigation of the files showed that this created substantial interpolation artefacts in areas of radar shadow and poor radar return. Unfortunately, this included the entire southern half of the terminus of Store, from which returns throughout the record were extremely patchy, making analysis of it impossible. I ascribe this to a overly acute viewing angle and obstruction by protruding parts of the terminus of Store. I therefore restrict the analysis in Chapter 4 to the northern embayment of the calving front (marked on Figure 4) and avoid interpolation, as problematic artefacts were still created in the northern half of the front. This decision means some calving events may be split into several smaller events by no-data pixels, but I considered this to be preferable to detecting phantom calving events. I also observed significant jump discontinuities in DEM elevation values, which I deleted from the record before differencing was undertaken to leave a consistent set of DEMs within each of the phases identified in Table 1. Images were deleted based on their mean value, with images with means deviating significantly from a baseline established from the majority mean range within each phase being removed.

The lack of reliable returns from large swathes of the calving front and viewing area also meant correcting the DEMs against a stable ground control point was essentially impossible, as there were no suitable points to use. However, the remaining DEMs are consistent within each phase, so relative height changes can be measured with confidence, which is sufficient for the detection of calving events, so I did not pursue a solution to this issue.

3.6.2. Detecting Calving Events

The remaining DEMs were then differenced within each phase, though no differencing was undertaken across different phases. Calving events were then extracted. First, a front mask for each phase was produced based on the position of the calving front within each phase, such that other areas of the image were masked out. The position of the calving front within the unmasked area for each DEM was then digitised using a Sobel filter. Valid calving events were then identified as negative changes in elevation of more than 10 m. Additionally, I required them to have at least one pixel on the digitised calving front and for the entire event to fall within the unmasked area. As a further quality-control step, events of 3 or fewer pixels were filtered out. These steps filtered out noise and avoided detection of negative elevation changes produced by serac collapse inland or iceberg movement or disintegration in the proglacial fjord. Areal determination was conducted pixel-wise, with contiguous areas of pixels meeting the above criteria being considered as single events.

Finally, the volume of each event was calculated by multiplying the area of each pixel by the elevation change, producing a record of subaerial calving volumes and frequencies for the northern half of Store's terminus.

4. The Observed Calving Behaviour of Store Glacier

'Behold the snow, and the cunning work of frost!'

-Ilúvatar, Ainulindalë, The Silmarillion

This chapter presents results describing the observed calving behaviour of Store derived from the radar interferometry dataset using the methods detailed in Chapter 3. This dataset is used for model validation in Chapter 7.

The work presented in this chapter has been submitted for consideration and is currently under review by the *Journal of Geophysical Research: Earth Surface*, and, as such, the text of this chapter is taken directly from the submitted manuscript. A methods section is therefore included, which summarises the more detailed method presented in Chapter 3 and provides detail on the exact experimental set-up used. S. Cook gathered and processed the dataset with guidance from M. Truffer. Analysis was performed solely by S. Cook. A. Abellan and T. Chudley provided, respectively, the time-lapse and UAV data referred to in this chapter. S. Cook wrote the manuscript with supervision and guidance from P. Christoffersen, and all co-authors participated in reviewing and editing the final submission. The reference for the manuscript (available on ESSOAr) is: Cook, S., Christoffersen, P., Truffer, M., Chudley, T. R. and Abellan, A.: Calving of a large Greenlandic tidewater glacier has complex links to meltwater plumes and mélange, preprint, 2020. doi: 10.1002/essoar.10502452.1.

4.1. Abstract

Calving and solid ice discharge into fjords account for approximately half of the annual net ice loss from the Greenland Ice Sheet, but these processes are rarely observed. To gain insights into the spatio-temporal nature of calving, we use a terrestrial radar interferometer to derive a three-week record of 8,026 calving events from Store Glacier, including the transition between a mélange-filled and ice-free fjord. We show that calving event frequency doubles across this transition and that the interferometer record is in good agreement with volumetric estimates of calving losses from contemporaneous UAV surveys. We report significant variations in calving activity over time, which obfuscate any simple power-law relationship. While there is a statistically significant relationship between surface melt and the number of calving events, no such relationship exists between surface melt and the volume of these events. Similarly, we find a 70% increase in the number of calving events in the presence of visible meltwater plumes, but only a 3% increase in calving volumes. While calving losses appear to have no clear single control, we find a bimodal distribution of iceberg sizes due to small sections of ice breaking off the subaerial part of the front and large capsizing icebergs

forming by full-thickness failure. Whereas previous work has hypothesised that tidewater glaciers can be grouped according to whether they calve predominantly by the former or latter mechanism, our observations indicate that calving here inherently comprises both, and that the dominant process can change over relatively short periods.

4.2. Introduction

Tidewater glaciers in Greenland drain 88% of the Greenland ice sheet (GrIS) (Rignot and Mouginot, 2012). Ice discharge due to calving from these glaciers is currently responsible for 40% (0.33 mm a^{-1}) of GrIS annual net mass loss (global sea-level rise) (Mouginot et al., 2019). While increasing surface melt and runoff act to reduce the solid ice discharge due to the thinning it causes, tidewater glaciers are discharging more ice into the ocean (King et al., 2018). Therefore, understanding how calving occurs and its relationship to other processes in the tidewater-glacier system becomes of central importance in forecasting the evolution of the GrIS in the coming decades and century.

Calving is an important glaciological process in tidewater environments in which glaciers discharge ice into fjords and coastal seas. It occurs when extensional stresses at the terminus produce fractures that intersect the calving front from either the surface or the base of the glacier (Benn et al., 2017a, 2017b). Calving is governed by the flow of the glacier and its setting as well as environmental processes that can increase stresses at the terminus, such as buoyancy, surface melting or submarine melt undercutting (Benn et al., 2017a; Benn and Åström, 2018). As such, calving is a highly complex process that happens with little detectable warning based on small changes in one or more of the controlling variables (Åström et al., 2013; Benn et al., 2017b).

Calving at tidewater glaciers, due to this unpredictable nature, is therefore a difficult process to observe directly, meaning that obtaining information about overall rates or controls, which could allow the development of simple calving parameterisations, is challenging. Conventional remote-sensing does not offer sufficient temporal resolution, with satellites typically providing images a few days apart and even more recent techniques such as Unmanned Aerial Vehicles (UAVs) several hours apart (Chudley et al., 2019; van Dongen et al., 2019; Jouvet et al., 2017). Time-lapse cameras, whilst having sufficient temporal resolution, produce 2D imagery that is not easily converted into 3D volumes of calving events (How et al., 2018; Mallalieu et al., 2017; Vallot et al., 2019). Terrestrial laser scanning has been used (Pętlicki and Kinnard, 2016; Podgórski et al., 2018), but repeat surveys with this technique are problematic due to the large quantity of data in each survey, as well as the significant logistical effort required. Continuous and detailed datasets on calving behaviour at tidewater glaciers are thus lacking, yet understanding this process is crucial to better prediction of tidewater-glacier behaviour and consequent sea-level rise.

Modelling calving to this end has progressed rapidly in recent years (e.g. Benn and Åström, 2018; Todd et al., 2018), but the lack of continuous and detailed observational datasets makes it difficult to validate such models. In this study, we therefore use a real-aperture terrestrial radar interferometer (TRI) (Chapuis et al., 2010; van Dongen et al., 2019; Strozzi et al., 2012; Voytenko et al., 2017; Xie et al., 2019), located 1 km from the front of Store Glacier (Store) to produce a directly observed, near-continuous, 3-week record of calving events for a major Greenlandic outlet glacier. The high resolution of this technique, both spatially and temporally, allows us to characterise 8,026 calving events in terms of size and frequency, while exploring the effect of different environmental factors.

4.3. Methods

4.3.1. Study site

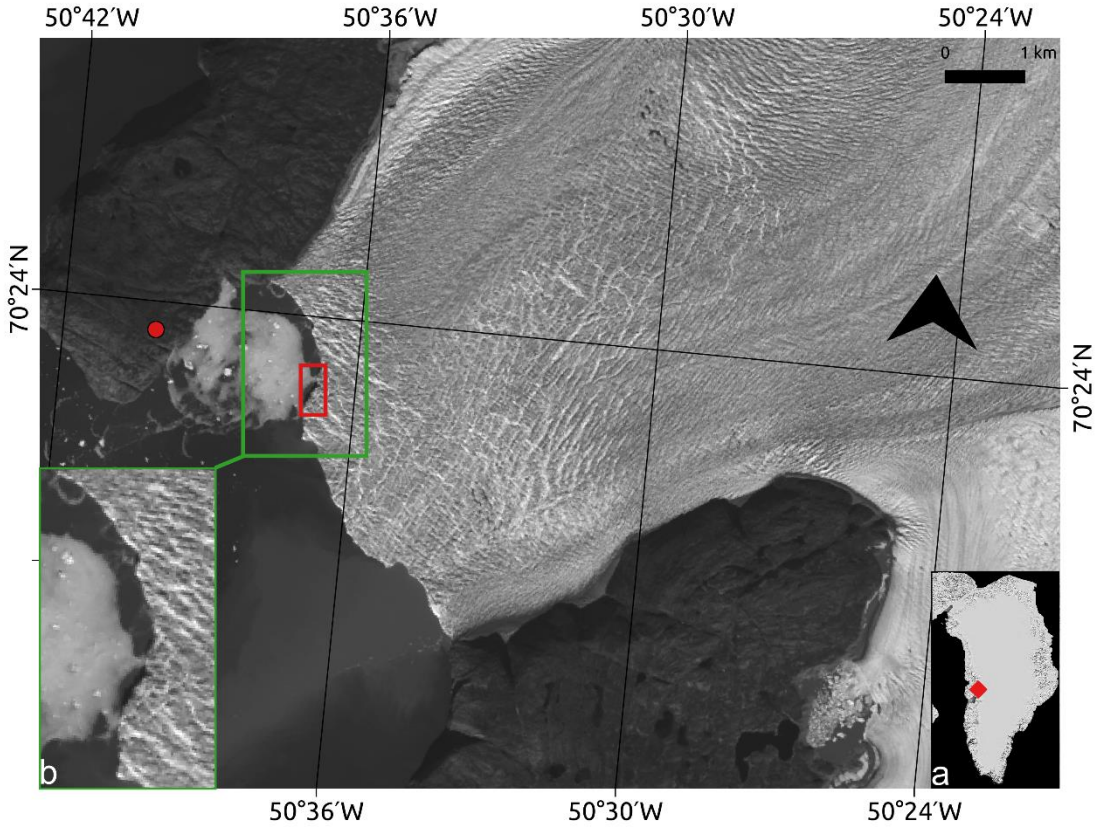

*Figure 3 – Location of Store Glacier (inset **a**) and location of TRI (red circle). The study area is outlined in green (inset **b**). The red rectangle represents the area zoomed in on in Figures 5 and 6. Background image from Landsat.*

Store Glacier (*Sermeq Kujalleq*) (70.4° N 50.6° W, Figure 3), referred to here as Store, is one of the largest tidewater outlet glaciers on the west coast of Greenland. The glacier discharges around 12 Gt annually into Ikerasak Fjord (Rignot et al., 2016) in the southern end of Uummannaq Bay. The calving

front of Store is 5 km wide, with surface velocities reaching up to 6600 m a^{-1} (Joughin et al., 2018), and is located at a lateral constriction in the fjord on top of a basal pinning point, making the terminus position relatively stable (Todd et al., 2019) with no observed retreat since 1985 (Catania et al., 2018). This stability makes it an ideal target for developing calving models (e.g. Morlighem et al., 2016; Todd et al., 2018; Todd and Christoffersen, 2014; Xu et al., 2013) and for observing tidewater-glacier processes in a 'natural', i.e. unperturbed setting. However, behind this pinning point, Store sits in a deep trough that could condition it for rapid retreat should the front be pushed back from the pinning point (Aschwanden et al., 2019). This means Store is additionally interesting, as it may provide information on the transition from a stable calving front to a retreating calving front in the future.

4.3.2. Radar set-up

The TRI used in this study was a Gamma Remote Sensing Ground-based Portable Radar Interferometer II (GPRI-II). This is a Ku-band (17.2 GHz, λ_w=1.75 cm), real-aperture, rotating instrument that has a range of up to 16 km with a range resolution of 0.75 m and an azimuthal resolution proportional to slant range with a ratio of 8:1000 (i.e., an azimuthal resolution of 8 m at 1 km distance) (Werner et al., 2008). The instrument has one transmit and two receive antenna, spaced 25 cm apart, allowing measurement of spatio-temporal change in calving-front dynamics. Velocity can be computed by comparing images from the same antenna taken at two different times; topography, used here, by comparing images from both antennae taken at the same time.

The GPRI-II was located about 1 km from the glacier terminus on the northern side of the fjord, on a rocky promontory overlooking the calving front (Figure 4). A Canon EOS 750D time-lapse camera was also installed next to it. The TRI was set to scan at a repeat interval of 3 minutes for 21 days, between 18:25 on the 5th and 11:01 on the 26th July 2017.

Figure 4 – Set-up of the TRI overlooking the calving front of Store.

4.3.3. Radar data processing

We used the interferogram record from the TRI, processed using the Gamma software suite, to generate a sequence of digital elevation models (DEMs) from which a record of calving events at Store could be extracted. Topography, which can be computed from the difference in path lengths between the transmitting and receiving antennas, which is related to the measured interferometric phase and wavelength of the radar, was calculated following the method of Strozzi et al. (2012), with the resulting DEMs being resampled to a 10m by 10m resolution and reprojected to Cartesian co-ordinates. As the measurements from each antenna are simultaneous, no atmospheric or phase displacement corrections are needed (Strozzi et al., 2012). Inspection of the resulting record revealed a small number of significant phase breaks and changes in orientation of the TRI over the course of the observation period, which we ascribe to periods of high winds buffeting the instrument. We identified four stable periods, covering the majority of the three-week record (18 out of 21 days), within which orientation and instrument biases were constant. Rotations were applied to each period to ensure alignment of DEMs, as set out in Table 2.

Table 2 – Stable periods and applied rotations to ensure alignment. Times are in local Greenland time WGST).

Name	Start	End	Rotation
Period 1	18:25 05/07/17	07:18 14/07/17	0
Period 2	19:06 14/07/17	23:36 18/07/17	-10°
Period 3	14:06 21/07/17	01:03 26/07/17	-3°
Period 4	01:09 26/07	11:01 27/07/17	0

To identify calving events, we difference consecutive DEMs produced at each timestep within the above periods (Table 2). Initially, we interpolated the DEMs to fill gaps, but this created substantial interpolation artefacts in areas of radar shadow and poor radar return. We therefore avoid interpolation and restrict our analysis to the northern embayment of the calving front (inset **b.** in Figure 3), as the southern embayment was frequently obstructed through the study period by the protruding terminus of Store Glacier, and did not generate good-quality radar returns. This decision means some calving events may be split into several smaller events by no-data pixels, but means that we avoid false positive events. Where DEMs showed anomalous differences (tens of metres of change or more in static surfaces) in elevation values, they were deleted from the record before differencing was undertaken, to leave a consistent set of DEMs within each of the periods identified in Table 2.

Although no ground control was reliably available within the viewing angle, we have confidence in the data as the remaining DEMs, when considered consecutively, do not show decorrelation within each period. Relative height changes can thus be reliably measured, which is sufficient for our purpose, so we did not pursue a solution to this issue.

To identify calving events, the remaining DEMs were then differenced within each period, though no differencing was undertaken across different periods. Calving events were then extracted. First, a mask of the ice front position for each period was produced, leaving the area around the calving front, where calving events would be detected, unmasked. The position of the calving front within the unmasked area for each DEM was then digitised using a Sobel filter. Valid calving events were identified as negative changes in elevation of more than 10 m with at least one pixel on the digitised calving front and entirely within the unmasked area. Additionally, events of 3 pixels or fewer in area were filtered out. These steps filtered out noise and avoided detection of negative elevation changes produced by serac collapse inland or iceberg movement or disintegration in the proglacial fjord. The area of each event was then calculated by summing up the number of contiguous DEM pixels meeting the above criteria.

Finally, the volume of each event was calculated by multiplying the area of each pixel by the elevation change, producing a record of subaerial calving volumes and frequencies for the northern half of Store's terminus. This method therefore imposes a minimum detectable calving event size of 4000 m^3, so smaller events are not part of the analysis in this paper. To support the time-series data, we compare it to total daily surface melt from the Store drainage basin from RACMO 2.3p2 data (van Wessem et al., 2018). We also manually examine the TRI footage to determine when the majority of the northern side of the calving front and fjord were mélange-covered and when at least one plume was visible in the area. Counts and volumes of ice-covered and ice-free periods, and of plume-visible and plume-absent periods, were subsequently standardised to enable direct comparison.

4.4 UAV and time-lapse data

For comparison and validation, we combine TRI data from Store with DEMs produced photogrammetrically with a 20 cm resolution from contemporaneous UAV surveys. Overlapping imagery was captured using a Sony α6000 camera mounted on a Skywalker X8 2m fixed-wing UAV. Flights were flown at an altitude of ≈450 m a.g.l., targeting a ground sampling distance of ≈11 cm, a forward overlap of 80%, and a sidelap of 60%. 3D models were produced using Structure-from-Motion with Multi-View Stereo (SfM-MVS) photogrammetry using Agisoft Metashape software. Models were geolocated via aerial triangulation using a L1 carrier-phase GPS receiver mounted on the UAV, post-processed kinematically against a bedrock-mounted GPS base station. For a full

outline of the methods, see Chudley et al. (2019). We use DEMs produced from flights over the calving front at 2017-07-12 at 22:00 and 2017-07-13 at 10:00 WGST. Calving volumes were calculated by differencing the two DEMs, manually delineating the calved area and then multiplying the area of each pixel by the elevation change. Volumes are uncorrected for advance in the position of the glacier front, as the high temporal sampling rate makes this quantity negligible compared to ice loss.

In addition, we used time-lapse camera images taken at 5-minute intervals throughout the field season, including the 12 hour period separating the two UAV surveys.

4.5. Results

4.5.1. Comparison of TRI with UAV and time-lapse data

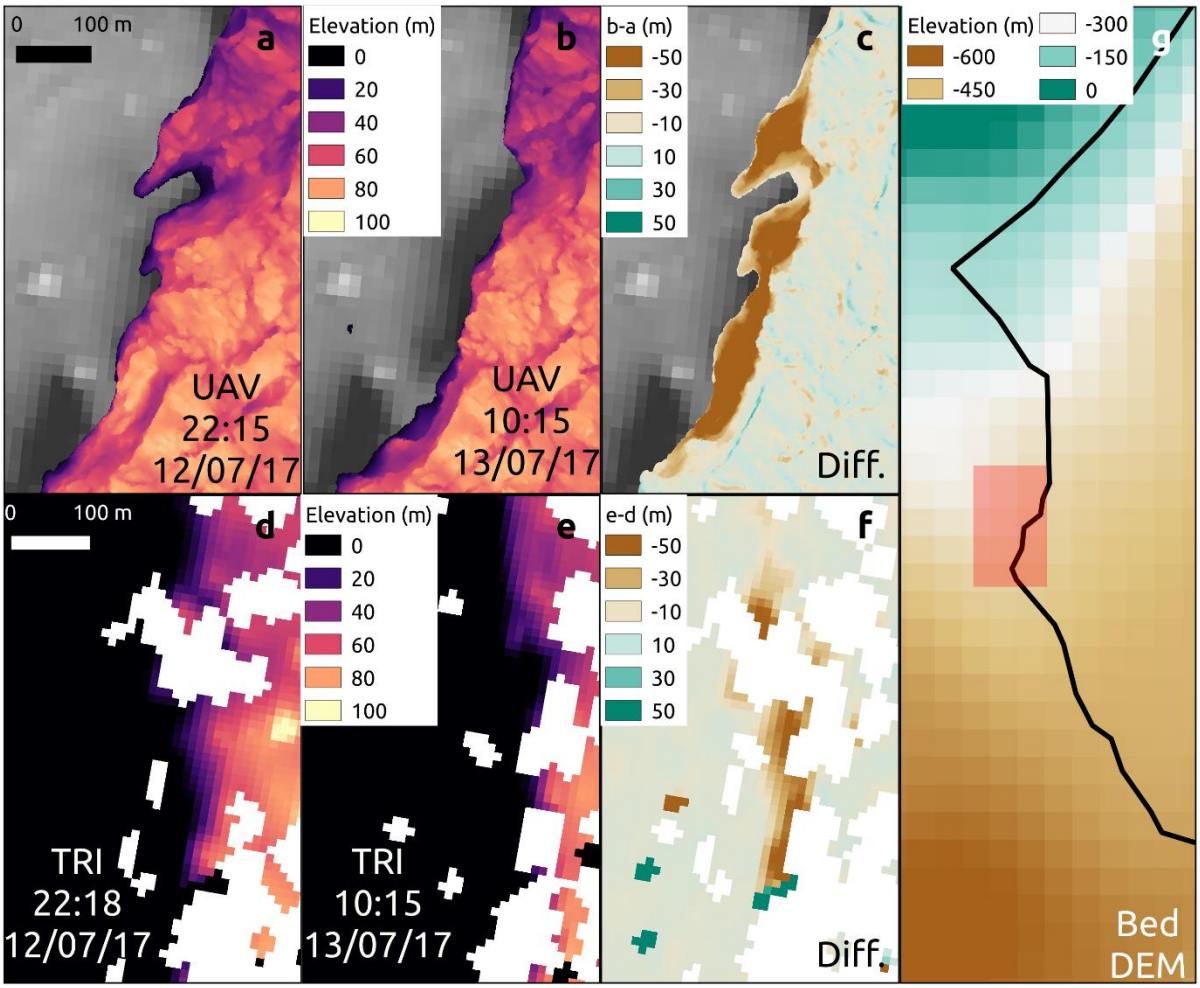

*Figure 5 – Comparison of calving loss detection across UAV and TRI datasets. Panels **a** and **b** show a large-scale calving loss from UAV-derived DEMs acquired across a 12-hour period; panel **c** shows the difference between panels **a** and **b**. Panels **d** and **e** show the same calving loss on TRI-derived DEMs; panel **f** shows the difference between panels **d** and **e** Panel **g** shows*

the location of the calving at the front of Store (red box) and the bed DEM (see Chapter 5 for its derivation) used in volume calculations. The black line is the approximate outline of the calving front of Store.

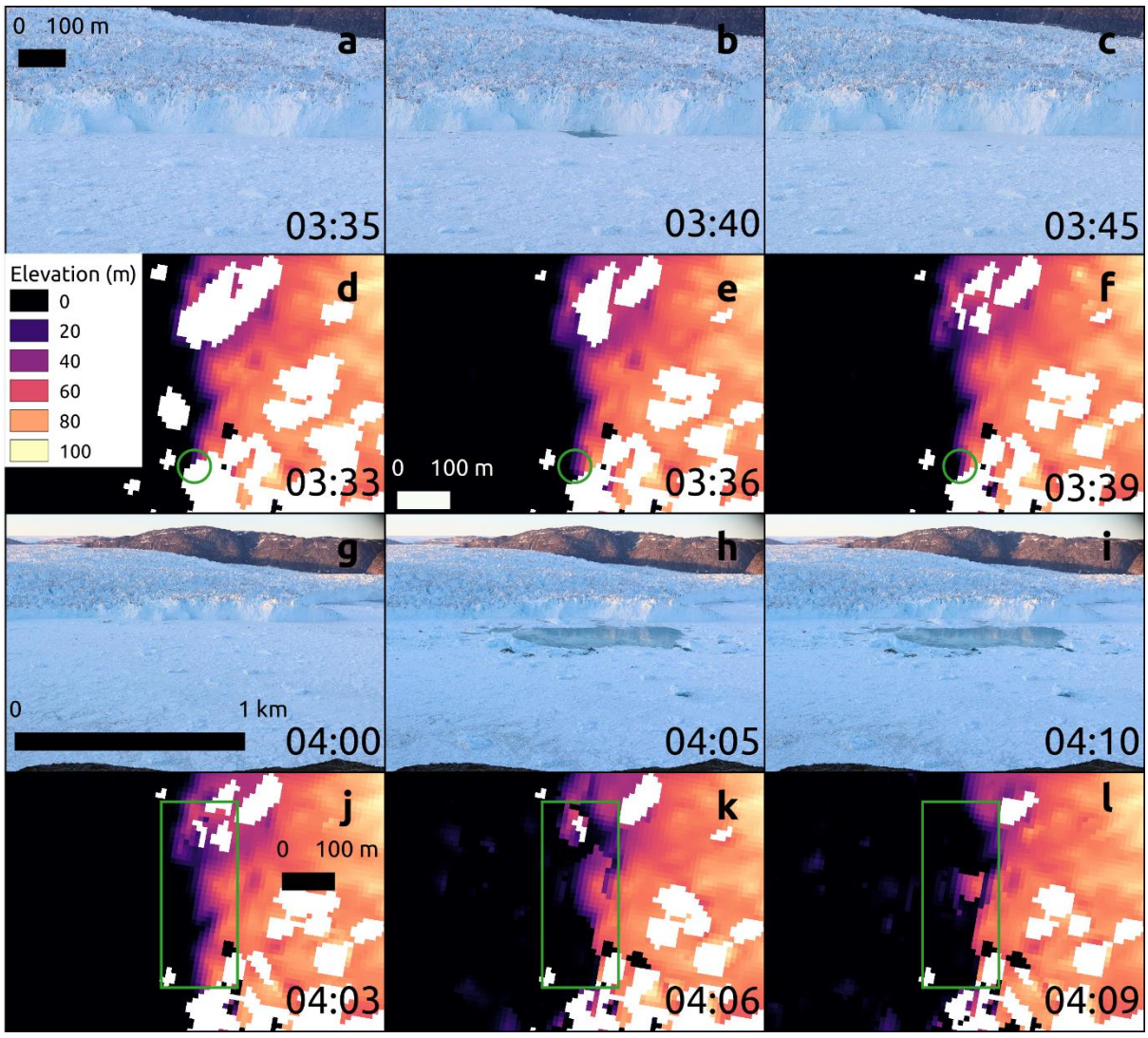

*Figure 6 – Comparison of specific calving-event detection across time-lapse and TRI datasets. Panels **a-c** show a smaller constituent calving event of the total loss in Figure 5 from time-lapse imagery; Panels **d-f** show the same event from the TRI's perspective (event denoted by green circle). Panels **g-i** show the largest constituent calving event of the loss in Figure 5 from time-lapse footage; Panels **j-l** show this event from the TRI's viewpoint (inside green box).*

Before extracting the full TRI record of calving events, we compare the TRI observations against two contemporaneous high-precision DEMs from UAV surveys separated by 12 hours and time-lapse camera images captured sequentially during this period (Figure 5). The UAV-derived DEMs (Figure 5a-c) show a distinct change in the terminus position, but cannot specify whether calving occurred as a single large event or multiple smaller events for the total ≈1,250,000 m^3 in subaerial volume loss calculated by differencing the DEMs. This is resolved by the TRI, which captured identical frontal positions (Figure 5d-f) and how terminus geometry changed (Figure 6). With data acquired every 3 minutes, the TRI record reveals a total of 48 individual calving events over the 12-hour period. Figure

6a-c and Figure 6d-f show one of the smaller constituent events, from the perspective of the camera and TRI, respectively, and Figure 6g-i and Figure 6j-l show the largest constituent event, which generated about 40% of the total subaerial volume loss detected over the 12-hour period. As can be seen, the time-lapse and TRI footage both agree on the timing of the calving events. Only 6/48 (12.5%) of the events exceeded a size of $5x10^4$ m^3 (Figure 7), but these larger events were responsible for 56% of the volume loss across the 12-hour period. The smaller events, whilst seven times more numerous, contributed less than half (44%) of the volume of ice calved.

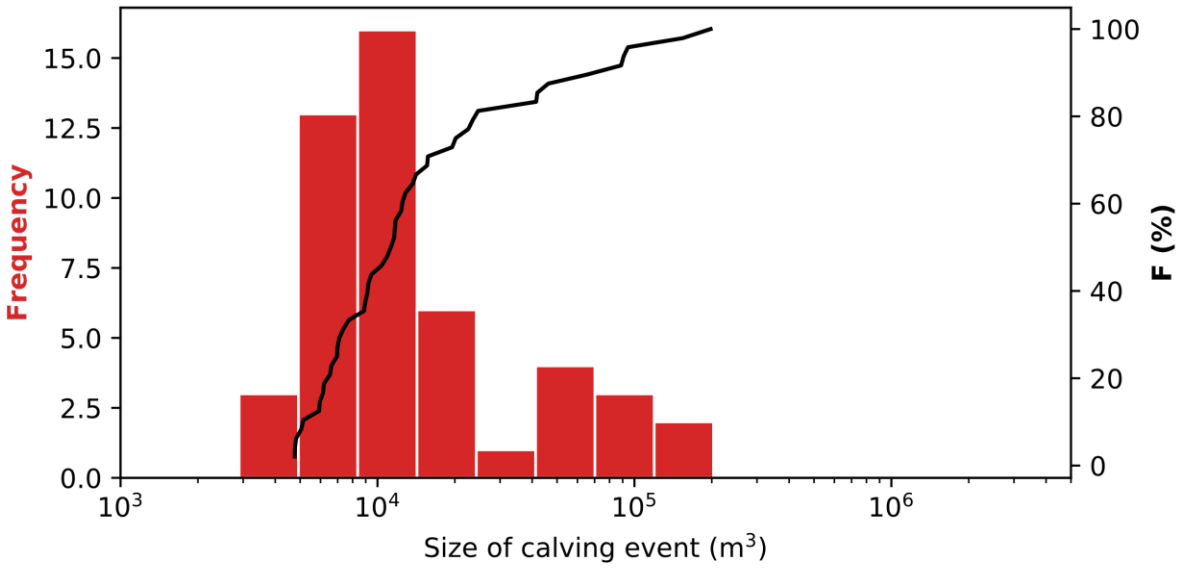

Figure 7 – Cumulative distribution function (right axis) and histogram (left axis) of frequency-magnitude relationship of single set of calving events at Store from 22:17 12/07/17 to 10:15 13/07/17. Compare with Figure 8 below. Size refers to the observed subaerial volume.

The total subaerial ice volume loss detected by differencing the two UAV DEMs is 1,266,000 m^3. When we sum up all the events within the same area detected by the TRI we obtain a total subaerial ice volume loss of 1,240,000 m^3, which is a discrepancy of only 2% compared to the independent UAV method. Assuming that the calving front remains close to vertical, and using the bed DEM shown in Figure 5g, we estimate that the accompanying submarine volume loss is 11,900,000 m^3, giving a total calving volume of 13,150,000 m^3. Given that the submarine loss is ≈9 times the subaerial loss derived from the UAV and TRI DEMs, the setting of the glacier is close to floatation.

4.5.2. Calving magnitude-frequency distribution

Over the entire three-week period of observations, we find a total of 8,026 calving events with a mean size of 48,428 m^3 (Figure 8). Two thirds of the events by frequency are under 50,000 m^3 in subaerial volume, but these only account for 15% of the total volume loss. Very large events, over

500,000 m^3 in subaerial volume, are very rare, totalling only 35 in the record, or 0.4% of total events, but are responsible for a disproportionate 8% of total volume loss. The middling third (50,000-500,000 m^3) of events by size are consequently responsible for the vast majority of total volume loss, at 77%.

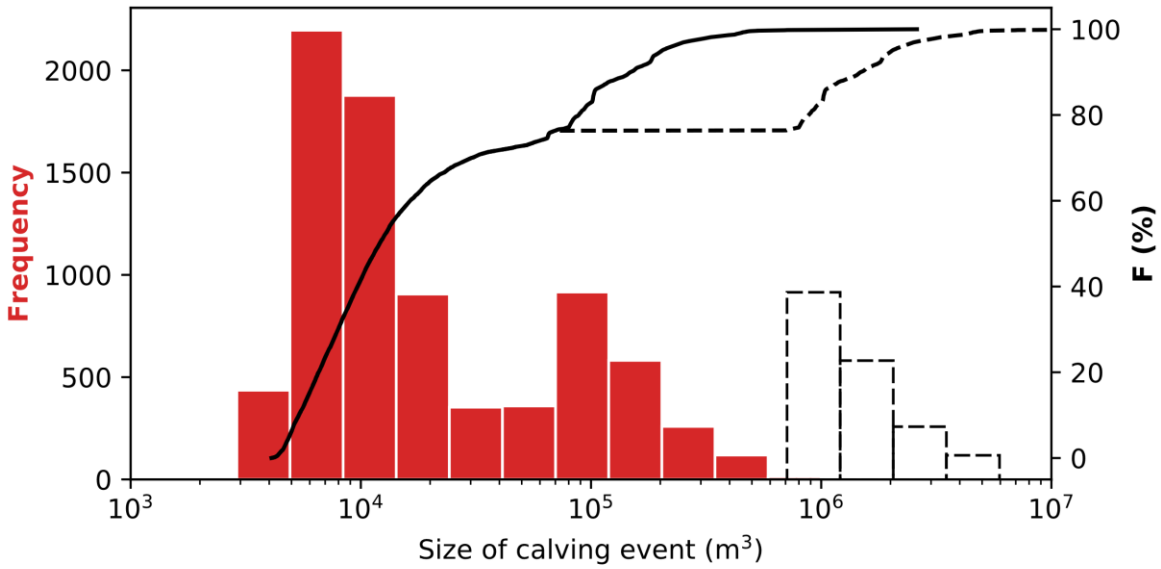

Figure 8 – Cumulative distribution function (right axis) and histogram (left axis) showing size-frequency relationship of all detected calving events observed at Store from 5th July to 27th July 2017. Dashed black bars show posited actual size of full-thickness calving events represented by the second peak in the distribution. Dashed black line shows the cumulative distribution function based on the dashed bars rather than the equivalent red bars. Compare with Figure 7 above.

4.5.3. Time-varying behaviour in calving

Considering the distribution of calving events over time (Figure 9), we observe low calving activity of <200 events per day prior to 8 July when the fjord was still frozen and filled with mélange. On the 8th, when the mélange broke up, calving activity immediately increased to 300 events, mostly driven by an increase in larger (>10^5 m^3) icebergs. From the 9th to the 14th, calving activity increases further, to ≈400 events per day, with a continued high proportion of larger events. From the 15th to the 17th, calving activity declines back to ≈300 events per day, with an especial reduction in the number of the largest (>10^6 m^3) category of events, before starting to increase again, on the 18th, with a doubling in the number of the smallest (10^3-10^4 m^3) events. Due to weather interference (high winds buffeting the TRI), there is a data gap on the 19th and 20th. However, the 10 hours of data collected on the 21st show a day of significant calving activity (Figure 9). Calving volumes peak with a value of nearly 2,000,000 m^3 on the 22nd while the daily number of events peaks on the 24th at 721, or 30 events per

hour. In general, the number and volume of calving events remain high between the 18th and 24th, though volumes are lower from the 23rd onwards.

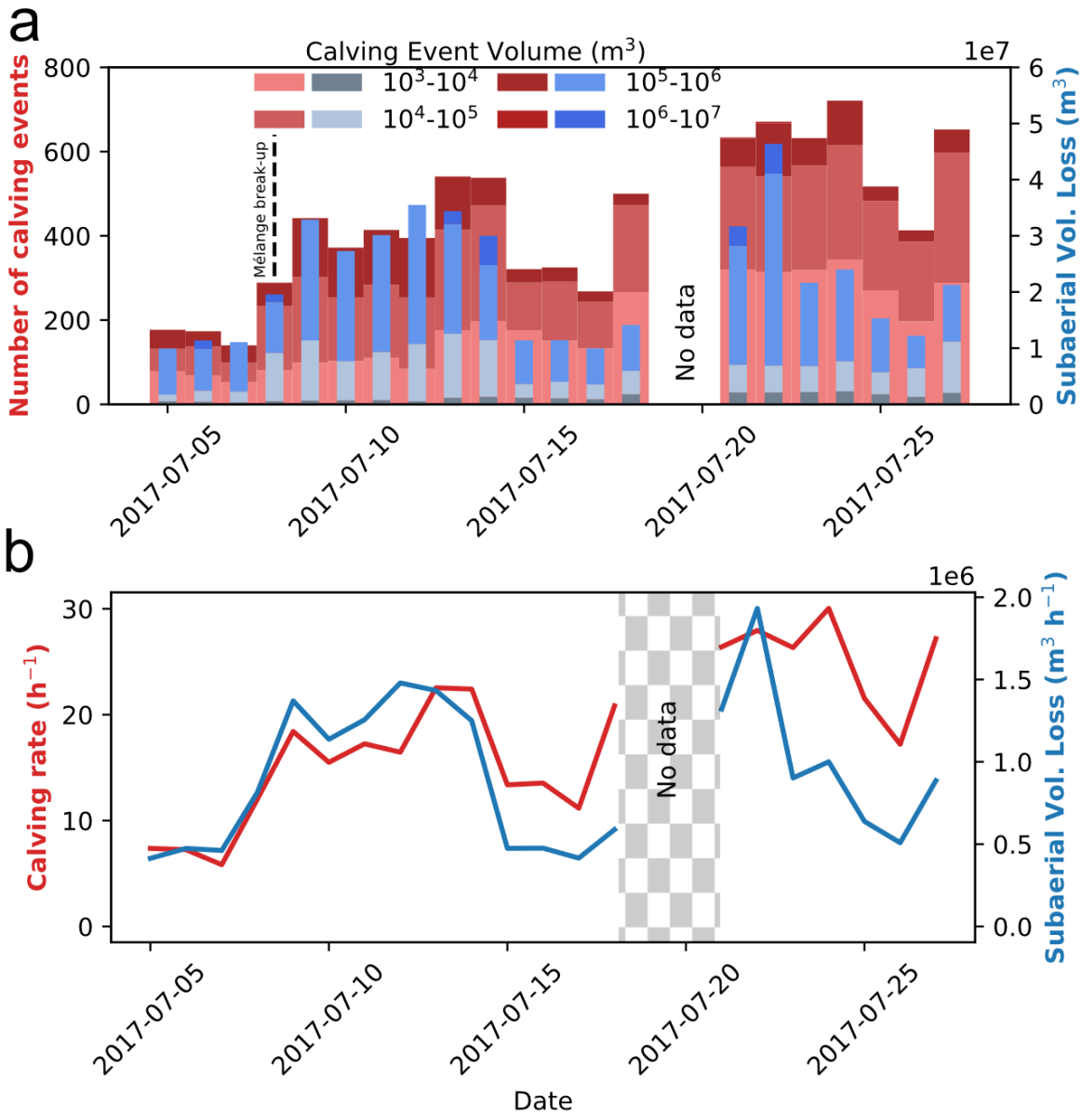

Figure 9 – Time series of calving events at Store. ***a*** *Bars stacked by volume of event. Daily counts are shown by red bars; cumulative volumes by the blue bars.* ***b*** *Hourly calving rate. Note greater calving activity from the 9th to the 14th.*

A possible trigger for calving activity is the weather or, more specifically, surface melt variations due to changes in air temperature, as greater surface melt is hypothesised to enhance the depth of surface crevasse penetration (Benn and Åström, 2018). We examine this by plotting calving counts and volumes (Figure 10) against surface melt for the Store basin, derived by integrating surface runoff from the RACMO dataset across the Store basin. Ignoring days with incomplete or no calving

data, we find correlation coefficients of 0.42 for the counts, which is significant at the 95% confidence interval, but only 0.12 for the volumes, which is statistically insignificant.

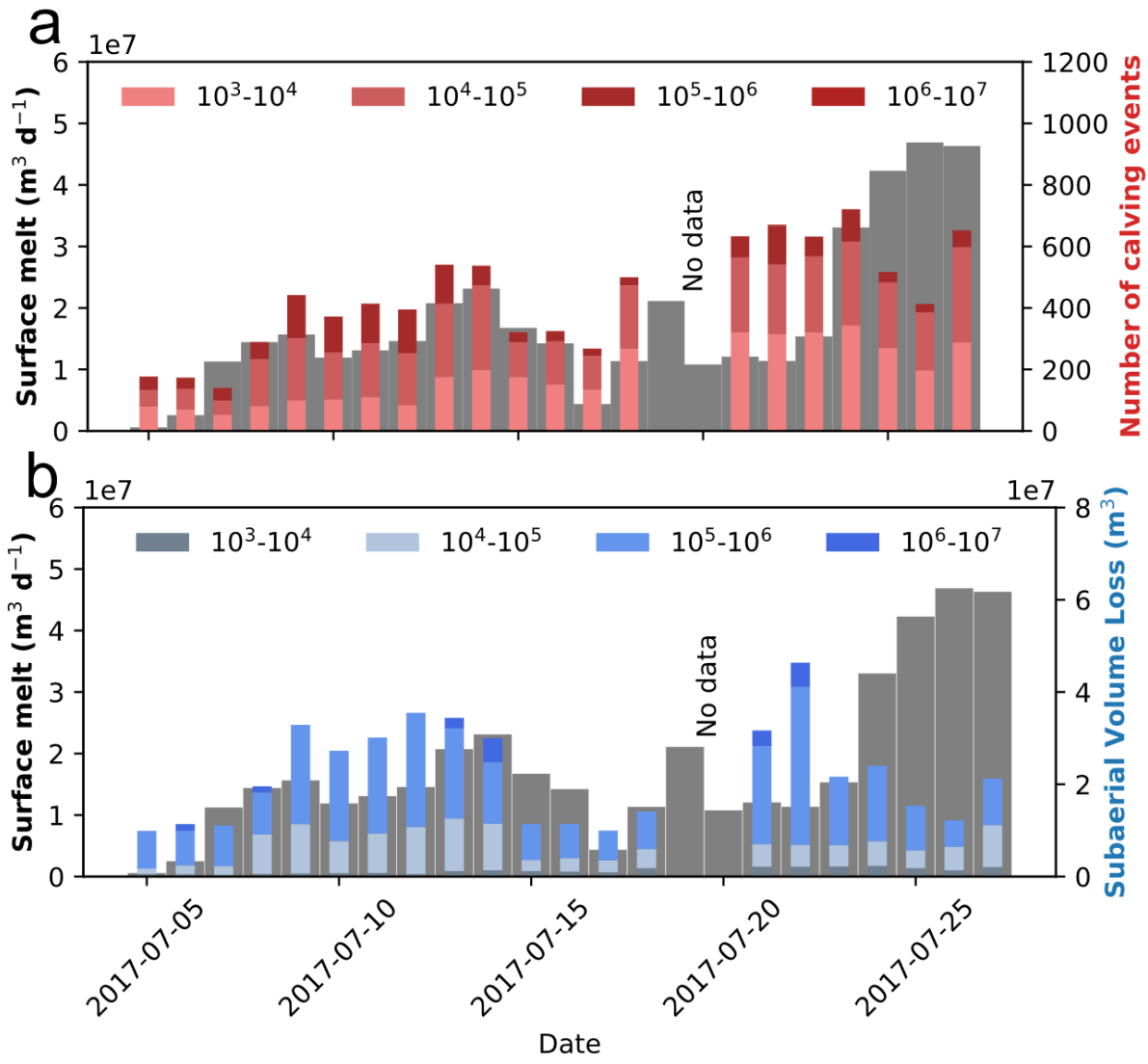

Figure 10 – Time series of calving events and surface melt derived from RACMO 2.3p2 data. ***a*** *shows calving counts (red bars) and* ***b*** *calving volumes (blue bars).*

To examine any diurnal variation in calving activity, we pick four days (Figure 11), each representative of one period of calving activity: the 6th, for the pre-mélange-break-up state of calving; the 11th, in the period of sustained higher calving following break-up; the 15th, in the following period of lower calving; and the 23rd, for the second period of higher calving.

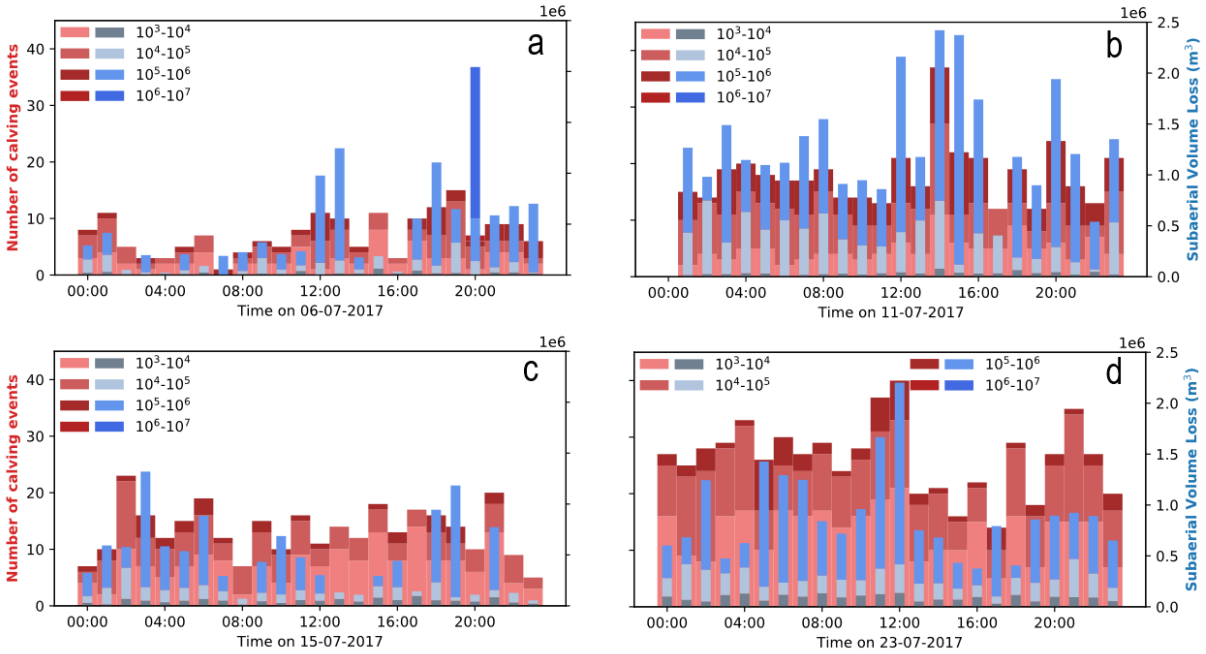

*Figure 11 – Time series of calving binned by hour from **a** 06/07/2017 (before mélange breaks up), **b** 11/07/2017 (high calving activity following mélange break-up), **c** 15/07/2017 (reduced calving activity), and **d** 23/07/2017 (renewed high calving activity).*

As Figure 11 shows, there is very little discernible consistent pattern in calving activity; the only consistent feature across all four days shown is a peak in counts and volumes at 12:00 ± 2 hours WGST. On the 6th July (Figure 11a), whilst the mélange was still intact, the midday peaks occur at 12:00 (counts) and 13:00 (volumes), with very little calving for the whole morning (only 01:00 exceeds a rate of 10 events per hour). Calving then drops off into the afternoon before reviving from 17:00 through the evening. On the 11th July (Figure 11b), after mélange break-up, we see high calving all day, with both midday peaks at 12:00, followed by another peak at 14:00. The later afternoon and evening are more variable than the morning, but calving event frequency only falls well below 15 per hour at 17:00 and 22:00. In the lull in calving activity following the post-break-up peak, represented by the 15th July (Figure 11c), calving counts show little discernible pattern, though are perhaps consistently higher in the morning than the evening; rates per hour, however, stay below 20 for nearly the whole day. Calving volumes show a clearer morning peak, midday peak (at 10:00) and then an evening peak, with reduced activity in-between these. In the final period of calving we observe, the second period of high activity, as shown for the 23rd July (Figure 11d), we see once more a clear midday peak at 12:00, with an afternoon depression in both calving counts and volumes. Evening and morning activity, though, are broadly comparable. We also investigated whether a link between the tidal cycle and calving activity could be discerned, but found no statistically significant relationship in this dataset.

4.5.4. Spatial variations in calving

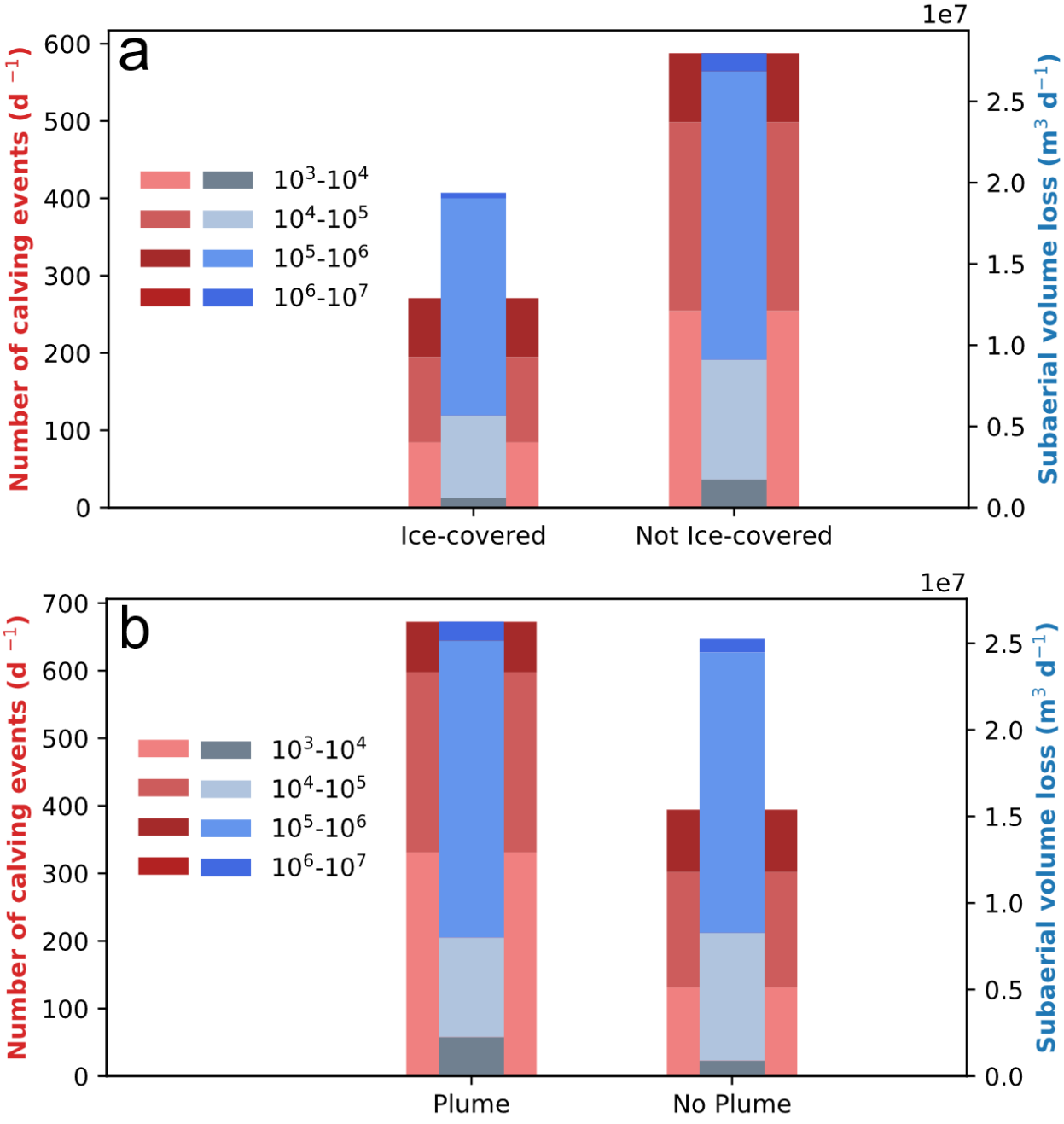

*Figure 12 – Calving event counts and volumes on average per day: **a** when mélange is present compared to when it is not. Note how mélange presence suppresses calving; and **b** when plumes are visible compared to when they are not. Note how plume presence leads to more, smaller and mid-size calving events.*

Two major factors that are hypothesised to influence calving event frequency are the presence/absence of mélange in the fjord and of active meltwater plumes fed by subglacial discharge. We assess the impact of both of these at Store by comparing calving counts and volumes for periods of mélange presence and absence and of visible plume presence and absence (Figure 12). In both cases, the counts and volumes are expressed as an average rate per day. We observe more

than a doubling in the number of calving events in the absence of mélange (from 271 events per day with mélange to 588 events without), compared to when it is present, and a concomitant 44% increase in volumes. In the presence of visible plumes, the number of calving events increases by 70%, from 395 per day to 672, but the volume loss from these events only increases very slightly, by 3%, compared to when no plumes are visible.

4.6. Discussion

4.6.1. Calving behaviour

The observed magnitude-frequency distribution of calving shows a positively skewed relationship (Figure 8): there are far more smaller events than larger ones, though the rarer larger events account for most of the volume loss. The smaller events mostly represent occurrences similar in style to that shown in Figure 6a-f, i.e. detachment of relatively small blocks of ice from the subaerial portion of the calving front that then fall into the fjord. The larger events are instead exemplified by Figure 6g-l, where entire sections of the front peel off and topple over. No large tabular-style calving events are observed here; at Store, these events usually happen on the floating southern part of the calving front and not on the grounded northern section analysed here (Todd et al., 2018). Contrary to other observations (Åström et al., 2014; Chapuis and Tetzlaff, 2014), the calving events discussed here do not follow a clear power-law distribution (Figure 8), with the cumulative distribution across the entire dataset suggesting a bimodal sequence of calving events (Figure 13). One peak is at a magnitude of the order of 10^4 m^3, with another on the order of 10^5 m^3. We hypothesise that the first peak represents the smaller calving events described above, where only a (relatively) small subaerial portion of the calving front calves. The second peak then represents the larger calving events in which a larger portion of the front breaks off. We explain the bimodal event size distribution (with a paucity of intermediate sized events) to be due to the mechanics of fracture propagation: if a fracture reaches the waterline, it will usually fill with water, which will propagate it deeper, which will further increase the water pressure in a positive feedback. It is also possible that surface fractures will intersect basal crevasses that propagate upwards from the base (Todd et al., 2018). Both of these mechanisms can generate large, full-thickness calving events. The first peak consequently represents those events where the initiating fracture does not reach the waterline, limiting calving to detachment of blocks on the subaerial region of the calving front; the second peak represents those where the fracture has reached the waterline and continued to the base, or intersected a basal crevasse, resulting in events that are an order of magnitude greater or even larger. Because our observations are limited to the subaerial portion of the front and we know the terminus is close to floatation, the larger events reported with a modal peak of 10^5 m^3 may be the

subaerial portion of events with a true modal size closer to 10^6 m^3 (as shown by dashed black lines in Figure 8). As such, intermediate events are rare, because detachment of blocks can only be so large (i.e. a few tens of metres of ice thickness across a small section of the front) whereas the large toppling of bergs can only be so small (i.e. hundreds of metres of ice thickness across a larger portion of front).

Returning to how previous calving datasets have shown a power-law distribution for the magnitude-frequency of events, we hypothesise that this is due to the relatively short duration of previous observations. The bimodality we observe here is a result of two characteristic iceberg size distributions: one being small blocks of ice falling off the front due to instability from fractures that are tens of metres deep and the other being larger bergs forming when fractures penetrate the whole ice-column. Superimposed on this bimodality is a time-varying calving behaviour (Figure 13). In the days leading up to mélange break up on the 8th, this bimodality is evident in a similar pattern to that found for the whole dataset. Thereafter, from the 8th through to the 13th, there is a higher-than-average representation of the larger class of calving events while the smaller class is under-represented, before the 14th returns to near the overall distribution. After the 14th, however, the rest of the dataset tends towards a relative under-representation of the larger events, while the smaller events are more frequent than average. Therefore, if our observations had been limited to a few days only, e.g. as shown in Figure 7, we might have concluded that a power law fitted on the slope of the cumulative distribution function would be an accurate representation of the data; yet this slope varies greatly over the period of observations (Figure 13). We therefore suggest that, to get an accurate picture of the calving distribution at a tidewater glacier, detailed observations of calving need to be maintained for at least a week, ideally for a fortnight or even longer. Shorter observational periods run the risk of missing out on aspects or distinct periods of calving behaviour or of attempting to fit a single power law to a distribution that might have multiple distinct causes, each best-represented by a single power law. In the case presented here, a separate power law, based on the variety of cumulative distribution functions we observe (Figure 13), would be needed for a) the system before mélange break-up (5th-7th), b) the system in the immediate aftermath of mélange break-up (8th-14th), and c) the system in the later post-break-up period (15th-27th) (Figure 10, Figure 13). Doing so, we find best-fit power laws with exponents of 0.53, 0.64 and 0.57, respectively, and R^2 values of 0.58, 0.73, and 0.44, respectively, suggesting that this calving dataset is mostly poorly represented by power laws, with the possible exception of the immediate post-mélange-break-up period, though, even in this period, we still observe pronounced bimodality.

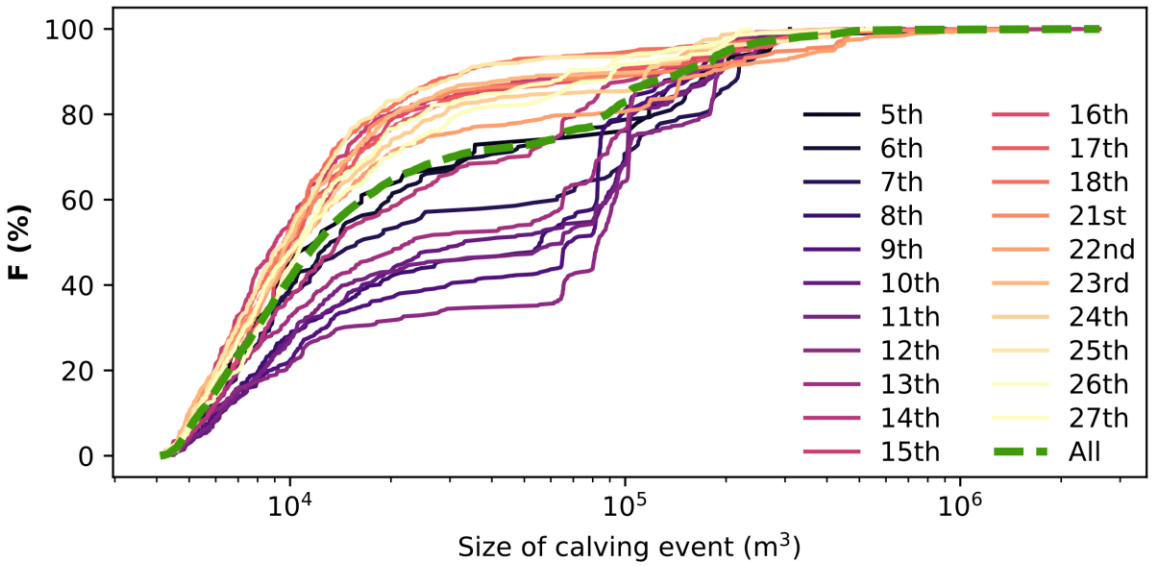

Figure 13 – Cumulative distribution function for calving events observed from 5th July to 27th July 2017, with coloured lines denoting distribution on specific days and dashed green line showing the overall distribution. Notice how days earlier in the observation period cluster below the overall average distribution, whereas those later in the period cluster above it.

4.6.2. Calving controls

The TRI record from Store provides some interesting information on the global distribution and controls on calving. We find a sustained 6-day period of higher calving activity in the aftermath of mélange break-up on the 8th July (Figure 9), with rates more than doubling compared to before break-up. Previous modelling work on Store (Todd et al., 2018) suggests this corresponds to the loss of backstress from the mélange, which provides a resisting force when the mélange is rigid. When the backstress is lost, this force disappears, facilitating crevasse propagation of sufficient depth to trigger detachment of full-thickness sections of the front (Amundson and Truffer, 2010). As such, we find the highest proportions of the largest events at this time, with the largest two categories of events (>10^5 m^3 in terms of subaerial volume and potentially >10^6 m^3 in total volume) making up an average of 33% of all events between the 9th and the 12th, inclusive, compared to an average of 24% beforehand and 11% afterwards. We then see a period of renewed calving intensity from at least the 21st to the 24th, this time predicated on smaller events, which seems to tail off on the 25th and 26th before possibly starting to pick up again on the 27th, the very last day of the record. An interesting perspective on this behaviour is provided by the theory of calving fronts as self-organised critical systems (Åström et al., 2014; Chapuis and Tetzlaff, 2014), whereby the front continually oscillates around a critical point that is determined by the environmental boundary conditions – air and water temperature, bed topography, glacier geometry, etc. Fronts that are subcritical will tend to move

towards the critical point, building up instabilities and manifesting small-scale, subdued calving behaviour. At some point, the calving front will find itself in a state of supercriticality due to a change in the environment or as it overshoots the critical point, which produces large-scale, sustained calving as the system adjusts back towards the critical point. Here, therefore, removal of the mélange can be interpreted as shifting the critical point of the system, suddenly placing the calving front of Store in a position of overshoot, and therefore supercriticality, manifested through a series of large calving events (the initial period of strong calving from the 8th-13th). The now-subcritical system then steadily re-advances towards the critical point, building up instabilities as it does so, and exhibiting small calving events (the quieter period of calving from the 14th to the 18th). Although greater calving activity is observed subsequent to this until the end of the record (the 19th to the 27th), the shape of the cumulative distribution functions (Figure 13), with a marked dominance of smaller events, suggests this is a prolongation of the subcritical phase, rather than a return to supercriticality.

This theory also helps to explain the very poor correlation found between calving event size and amount of surface melt (Figure 10). Whilst there is statistically significant correlation between surface melt and the *number* of calving events (Figure 10a), there is none between surface melt and the *volume* of events (Figure 10b). Increased surface melt should enhance fracture propagation by increasing the amount of water available for hydrofracturing at the surface, or by generating more vigorous freshwater-plume circulation at the front, leading to increased submarine melting and undercutting (O'Leary and Christoffersen, 2013) – this link is discussed further, below. Hence we would expect to find a link between surface melt and counts of calving events. Whether these fractures grow in such a way as to produce large or small calving events, however, would seem to be primarily determined by other factors, such as whether the system is in a subcritical or supercritical state.

A link between surface melt and calving activity is also observed (Figure 10), as shown by the consistent appearance of a midday peak, the most plausible explanation for which is that this time of day has the greatest amount of insolation and therefore surface melt, thus driving fracture propagation. However, this midday peak is the daily peak on only two out of the four days examined in Figure 9: the 11th and 23rd July (Figure 11b and Figure 11d); on the other two days, the daily peak occurs at 19:00-20:00 (6th July; Figure 11a) and 02:00-03:00 (15th July; Figure 11c), reinforcing the conclusion that surface melt is just one driver of calving and not necessarily the most important.

We also examine two important factors contributing to the criticality of the system (Figure 12). In accordance with the pattern of activity observed in Figure 9, we find much stronger calving activity

in the absence of mélange compared to when it is present (Figure 12a; compare Figure 9). One point worth noticing is that the largest of two observed modal peaks in calving accounts for a greater proportion (28%, representing 888 events) of the total calving count when mélange is present compared to when it is not (15%, representing 1041 events), suggesting that mélange presence preferentially suppresses smaller events, but is relatively ineffective at holding back larger events, which will calve regardless once they become sufficiently unstable.

However, a calving front exhibiting self-organised critical behaviour near its critical point should show calving activity that follows a power-law distribution with exponents in the range 1.06-1.46 (Åström et al., 2014), which we do not observe in this study. On the other hand, we do observe qualitative changes in calving behaviour between a likely subcritical calving phase (5^{th}-7^{th}; dominated by smaller events), a likely supercritical phase (8^{th}-14^{th}; dominated by larger events) and a second subcritical phase (15^{th}-27^{th}; dominated by smaller events), with the period of subcriticality representing over 2/3 of the record duration. These features are consistent with a calving front operating in a self-organised critical regime (Åström et al., 2014). It is also worth noting that, for grounded tidewater margins, which is the relevant category for the northern part of Store's calving front, the power law is expected to display an exponential cut-off for calving events with volumes over 10^4 m^3 (Åström et al., 2014). If we only consider the events below this volume threshold and repeat the power-law analysis described in Section 4.6.1, we find R^2 values of 0.83, 0.77, and 0.78, respectively. These represent a significant improvement in R^2 values for the two putatively subcritical phases and little change for the putatively supercritical phase, which is consistent with grounded calving fronts operating in a self-organised critical regime (Åström et al., 2014). The power-law exponents, however, jump to 3.66, 3.73 and 3.64 when considering events below this 10^4 m^3 threshold, which is much higher than expected. We attribute this to our processing method excluding events below 4000 m^3 in size, distorting the tail of the distribution. Therefore, we suggest that the calving front at Store exhibits behaviour that is at least qualitatively consistent with self-organised criticality and potentially provide quantitative support for this. This point also reinforces our assertion that calving behaviour changes over time and thus cannot be necessarily well-represented or modelled by a short time series of observations.

We additionally show that visible active meltwater plumes, driven by surface melt, encourage more frequent calving events (Figure 12b), possibly as a response to undercutting of the calving front, as described above. What is less intuitive is that the increase in the number of events is associated with barely any increase in the volume loss from calving. The presence of plumes in this study greatly increases the number of smaller ($<10^5$ m^3) calving events at the expense of the larger events ($>10^5$ m^3), which fall from 24% (representing 909 events) to 11% (representing 730 events) of the total

event count. We attribute this to plume-induced melting making it 'easier' for blocks and small vulnerable sections of the front to break off, removing them consecutively in a relatively high number of events before instabilities can build up in the ice and thereby reducing the frequency of large calving events. This does not mean plumes reduce the total mass loss as we are unable to observe the quantity of ice lost by plume-induced melting, or calving, taking place below the waterline. The finding does, nonetheless, highlight that the relationship between plumes and calving is not as straightforward as previously proposed (O'Leary and Christoffersen, 2013).

Also, the bimodal distribution of iceberg sizes found in this study of Store shows that classification of glaciers into types that produce either small magnitude icebergs by serac failure or large icebergs by full-thickness capsizing slabs, with Store falling in the latter category (Fried et al., 2018), may be too simplistic since both types of events are observed to occur frequently at Store. While it is possible that some glaciers will calve mostly by one mechanism and that others will calve mostly by the other, our TRI record from Store indicates that the calving mechanism inherently comprises both and that the predominant calving style can change from one type to the other over relatively short periods. This finding is a result of the extremely high resolution of the TRI, which recorded calving every 3 minutes. While our UAV investigation showed a subaerial volume loss of 1,250,000 m^3 from a frontal retreat between two surveys separated by 12 hours (Figure 6), the TRI showed this retreat was comprised of 48 individual events and that iceberg sizes varied by two orders of magnitude or more (Figure 7). This finding indicates that there are inherent limitations in the use of remotely sensed images to discern calving styles and that classification of calving glaciers may regure size-frequency distributions and assessment of probability (Figure 8, Figure 13).

4.6.3. Limitations and validation

This study has produced one of the longest records of calving from the use of a TRI. The instrument captured calving events occurring over half of the calving front of Store during three weeks in July 2017. Overall, we found a very good agreement between the volumetric loss of ice in a multitude of calving events with those estimated from the UAV-derived DEMs produced at a 0.2 m resolution (Figure 5, Figure 6). This gives us confidence that the TRI was successful in identifying calving events on the northern side of Store and that the TRI analysis has produced accurate volumetric estimates However, due to the 5-km-wide calving front, it was not possible to also survey calving taking place in the southern half of the terminus, where numerical modelling indicates the largest, tabular-style calving events are most likely to occur (Todd et al., 2018). However, our study shows that the northern terminus is very close to floatation and thus that the differences between southern half and northern half may not be so pronounced.

The data processing method for the TRI data also introduces some errors – notably, we are unable to distinguish events smaller than 4000 m^3 in volume and some events near this limit may have been erroneously excluded from the analysis. A more fundamental issue is that, obviously, the TRI only provides information on the subaerial volumes of calving events, which means the identified volumes of the larger events are only partial. As computed in Section 4.5.1, we find a nine times greater submarine calving volume than the subaerial volume from UAV and TRI DEMs for the sequence of calving events displayed in Figure 4 and Figure 5. This shows that the calving front in this location is at or very close to floatation, and hence that the observed modal peak in the subaerial calving volume of larger events represents only $1/10^{th}$ of the actual iceberg size. The modal peak of the smaller iceberg size may, however, be close to the actual volume given that these events represent relatively small blocks falling off the front.

4.7. Conclusion

We present a novel 3-week-long record of calving events at Store Glacier from a TRI survey that includes the transition from a mélange-filled proglacial fjord setting to a mélange-free environment. The record includes a total of 8,026 calving events with a mean volume of 4.8×10^4 m^3. Maximum calving event frequency peaks at 30 events per hour, or 720 per day, with an average rate of 17 events per hour, or 408 per day. This dataset suggests mélange presence preferentially suppresses smaller calving events and that mélange break-up leads to a prolonged period of higher calving activity at Store, with calving event frequency near-doubling in ice-free conditions. We assess the reliability of this dataset by making a comparison to a set of calving events independently recorded across a 12-hour period in UAV data and find a mismatch of only 2%, giving us confidence in the validity of the results presented here. With the TRI capturing calving events in high resolution, both spatially and temporally, we find a bimodal size-frequency distribution of events that reflects two specific types of calving: blocks and relatively small sections of ice breaking off the subaerial part of the terminus with a characteristic modal size of 10^4 m^3, and much larger icebergs released from full-thickness failure. While the observed modal size of the latter is 10^5 m^3, we estimate the actual volume to be closer to 10^6 m^3 since our observations capture only the subaerial portion of the terminus, which is at or near floatation. However, we find the predominant type of calving can change from small to large events over relatively short periods.

With both temporal and spatial variability in calving at Store, our observations do not support any simple power-law relationship between iceberg size and frequency. Instead, we observe a complex relationship between calving and the presence of visible meltwater plumes at the calving front. Plume presence leads to 70% more calving events, but the subaerial volume of ice detaching from

the terminus in these events only increases by 3%. We relate this to reduced support due to plume-induced melting allowing unstable ice blocks to calve earlier than they might otherwise have done. We further find little relationship between surface melt and calving volumes, though a statistically significant one between surface melt and calving counts, again indicating the complexities underlying calving behaviour.

4.8. Acknowledgements

This research was supported by the European Research Council as part of the RESPONDER project funded under the European Union's Horizon 2020 research and innovation programme (grant agreement no. 683043). SJC and TRC were supported by Natural Environment Research Council Doctoral Training Partnership studentships (NE/L002507/1), and AA by the European Union's Horizon 2020 research and innovation programme under a Marie Skłodowska-Curie grant (grant agreement no. 705215). We are grateful to the 2017 RESPONDER field team for their assistance in the field, and to Ann Andreasen and the Uummannaq Polar Institute for their kind hospitality.

5. Modelled Subglacial Hydrology of Store Glacier

'We fought far under the living earth, where time is not counted. Ever he clutched me, and ever I hewed him, till at last he fled into dark tunnels. They were not made by Durin's folk, Gimli son of Glóin. Far, far below the deepest delving of the Dwarves, the world is gnawed by nameless things. Even Sauron knows them not. They are older than he.'

-Gandalf, The Lord of the Rings, Book 3, Ch. V

This chapter presents a semi-coupled version of the model, with the full version being set out in Chapter 6. This version of the model includes 3D hydrology and proglacial plumes within a fixed glacier geometry, but neglects calving, and is intended to demonstrate the functionality of key model components within a simplified context as a stepping stone to the fully coupled model. This also provides a useful comparison for the results obtained from the fully coupled model, allowing some judgements to be made on the benefits of increased model complexity (Chapter 7.2).

The work presented in this chapter was published (Cook et al., 2020; see the reference list in this thesis for the full reference) in *The Cryosphere* and, consequently, the text of this chapter is taken directly from this publication. Co-authors provided feedback on the wording of the text and the presentation of the results, but all the work presented was undertaken by S. Cook with guidance from J. Todd, D. Slater and P. Christoffersen. S. Cook, P. Christoffersen and J. Todd designed the experiments. S. Cook also developed the model code and executed the experiments with contributions from J. Todd, P. Christoffersen and D. Slater. N. Chauché provided hydrographic data. S. Cook analysed the model outputs and wrote the manuscript, with writing contributions from all co-authors.

5.1. Abstract

We investigate the subglacial hydrology of Store Glacier in West Greenland, using the open-source, full-Stokes model Elmer/Ice in a novel 3D application that includes a distributed water sheet, as well as discrete channelised drainage, and a 1D model to simulate submarine plumes at the calving front. At first, we produce a baseline winter scenario with no surface meltwater. We then investigate the hydrological system during summer, focussing specifically on 2012 and 2017, which provide examples of high and low surface-meltwater inputs, respectively. We show that the common assumption of zero winter freshwater flux is invalid, and find channels over 1 m^2 in area occurring up to 5 km inland in winter, and that the production of water from friction and geothermal heat is sufficiently high to drive year-round plume activity, with ice-front melting averaging 0.15 m d^{-1}. When the model is forced with seasonally averaged surface melt from summer, we show a hydrological system with significant distributed sheet activity extending 65 km and 45 km inland in

2012 and 2017, respectively; while channels with a cross-sectional area higher than 1 m^2 form as far as 55 km and 30 km inland. Using daily values for the surface melt as forcing, we find only a weak relationship between the input of surface meltwater and the intensity of plume melting at the calving front, whereas there is a strong correlation between surface-meltwater peaks and basal water pressures. The former shows that storage of water on multiple timescales within the subglacial drainage system plays an important role in modulating subglacial discharge. The latter shows that high melt inputs can drive high basal water pressures even when the channelised network grows larger. This has implications for the future velocity and mass loss of Store Glacier, and the consequent sea-level rise, in a warming world.

5.2. Introduction

The Greenland Ice Sheet (GrIS) is currently losing mass at about 260 Gt a^{-1} (Forsberg et al., 2017) and this rate has been accelerating (Kjeldsen et al., 2015). Around half of this loss is tied to ice-sheet dynamics (van den Broeke et al., 2016) and the accompanying flow acceleration is partly due to tidewater outlet glaciers, which drain 88% of the ice sheet (Rignot and Mouginot, 2012). As such, understanding how these tidewater glaciers may change over time is crucial to our ability to predict the likely evolution of the GrIS in a warming climate.

One area of particular concern is the subglacial hydrology of these tidewater glaciers. Whilst there have been many studies focusing on the subglacial hydrology of land-terminating portions of the GrIS and its complex effect on the flow of the overlying ice (Chandler et al., 2013; de Fleurian et al., 2016; Christoffersen et al., 2018; Gagliardini and Werder, 2018; Meierbachtol et al., 2013; Sole et al., 2013; Tedstone et al., 2013, 2015; van de Wal et al., 2015), the hydrology of tidewater glaciers has received much less attention (e.g. Schild et al., 2016; Sole et al., 2011; Vallot et al., 2017), owing to the greater difficulty of gathering observations in the fast-flowing marine-terminating environment. Given the range of other processes operating at such glaciers, such as submarine melting, fjord circulation and calving, it is also much harder to disentangle and infer hydrological evolution from changes in surface velocity, though attempts have been made (Howat et al., 2010; Joughin et al., 2008; Moon et al., 2014). Direct basal observations on marine-terminating outlets were until recently limited to boreholes drilled near Swiss Camp and the lateral margin of Jakobshavn Isbræ (Lüthi et al., 2002). Only one study has, to date, reported direct observations from boreholes drilled along the central flowline, to the base of a marine-terminating glacier in Greenland. In that study, a persistently high basal water pressure of 93-95% of ice overburden indicates a largely inefficient basal water system 30 km inland from the calving margin at the fast-flowing and heavily-crevassed Store Glacier (Store) (Doyle et al., 2018). Yet, observed seasonal velocity fluctuations on the same

glacier are consistent with the development of a channelised basal drainage system closer to the margin (Young et al., 2019), which calls for a physical model to spatially and temporally constrain the formation of different types of basal drainage system.

Hydrological work on marine-terminating glaciers has so far focused on the subglacial discharge that drives convective plumes in the marine terminus environment, and how this process can promote calving by undercutting the glacier through submarine melting and fjord circulation (Carroll et al., 2015; Cowton et al., 2015; Fried et al., 2015; Jackson et al., 2017; Jouvet et al., 2018; Slater et al., 2018). In particular, the state of the subglacial hydrological system is thought to be a key control on the rate and spatial distribution of submarine melting, with channelised drainage favouring the highest localised melt rates, though distributed drainage may produce the highest total volume of submarine melting, with lower melt rates that affect a larger portion of the calving front (Fried et al., 2015; Slater et al., 2015). However, our observations of the near-terminus subglacial hydrological system remain extremely limited; we can only make inferences about the location and presence of subglacial channels from the presence of plumes at the fjord surface (Schild et al., 2016), subsurface incisions into the calving front (Fried et al., 2015) and oceanographic observations (Stevens et al., 2016).

Given the paucity of direct observations, insights to marine-terminating glaciers' interaction with the ocean may be found through the integration of subglacial hydrology within physically-based models of ice flow (e.g. Banwell et al., 2013; de Fleurian et al., 2014; Hewitt et al., 2012; Hoffman et al., 2016; Werder et al., 2013). So far, these models have, however, been applied largely to land-terminating catchments in Greenland or elsewhere, where validation is easier due to the availability of better observations of the hydrological system. There is, though, no fundamental reason why they should not also function effectively in a tidewater setting. On tidewater glaciers, seasonal flow variations (Moon et al., 2014) and elevation changes (Csatho et al., 2014) are observed too far inland to be explained purely by forcing at the glaciers' termini (Todd et al., 2018). With the advent of the Subglacial Hydrology Model Intercomparison Project (SHMIP) (de Fleurian et al., 2018), greater confidence in the results of these models is now possible, which provides further motivation to apply them in this novel manner. This would then provide the ability to dynamically model tidewater-glacier subglacial hydrology, allowing better prediction of plume and calving activity at the front, and ice flow inland, ultimately leading to improved constraints on future sea-level rise scenarios. In this study we therefore apply a subglacial hydrological model to a large Greenland tidewater outlet glacier with the goals of A) characterising the basal drainage system, including the extent to which it may become efficient, and B) investigating how subglacial discharge drives melting at the glacier's terminus when convective plumes develop. This study therefore couples a subglacial hydrology

model with a 1D plume model within the ice-flow model, Elmer/Ice (Gagliardini et al., 2013), in order to simulate the seasonal variation in the subglacial hydrological network of Store and the resulting plume melting.

5.3. Data and Methods

The study site (Section 5.3.1.), individual modelling components (Section 5.3.2.-5.3.4.) and their relation to each other within the model set-up (Section 5.3.5.) are described below, followed by details of the datasets used to prescribe boundary conditions (Section 5.3.6.). This paper presents coupled subglacial hydrology and plume models within a full-Stokes 3D model of Store. The subglacial hydrology model is GlaDS (Werder et al., 2013), the ice flow model is Elmer/Ice (Gagliardini et al., 2013) and the plume model is a 1D line plume (Slater et al., 2016). Each of these is described further in turn below.

5.3.1. Study site

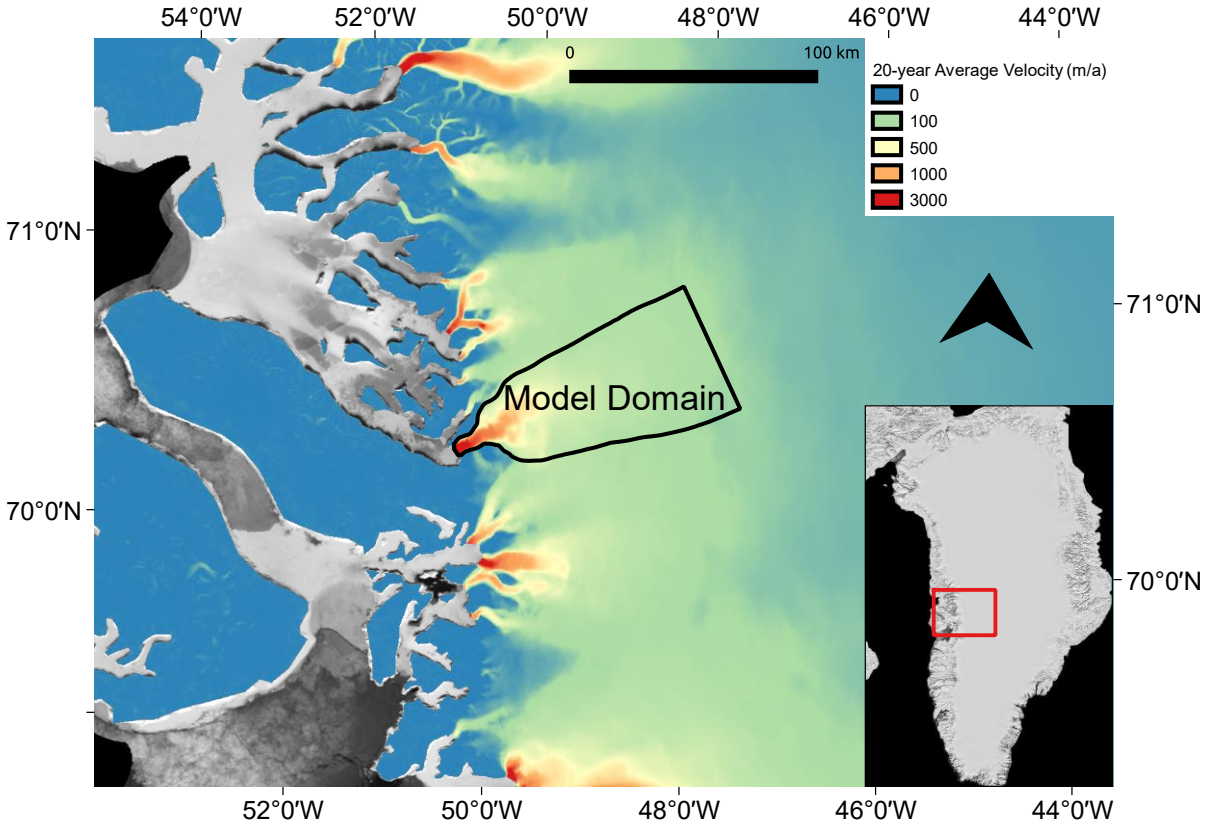

Figure 14 – Location of Store (inset) and model domain. Background shows the 20-year velocity average from the MEaSUREs dataset (Joughin et al. 2016, 2018).

Store Glacier (Store), one of the largest tidewater outlet glaciers on the west coast of Greenland (70.4°N, 50.55°W), flows into Ikerasak Fjord (*Ikerasaup Sullua*) at the southern end of the

Uummannaq Fjord system (Figure 14). The calving front is 5 km wide, with surface velocities reaching up to 6600 m a^{-1} (Joughin, 2018), and is pinned on a sill making the terminus position relatively stable despite the trunk of the glacier flowing through a deep trough extending to nearly 1000m below sea level (Rignot et al., 2015). With no observed retreat since 1985 (Catania et al., 2018), the glacier represents a stable Greenland outlet glacier and is an ideal target for modelling studies aiming to understand such glaciers, as the effects of rapid retreat do not need to be disentangled from 'natural' behaviour (e.g. Morlighem et al., 2016; Todd et al., 2018; Todd and Christoffersen, 2014; Xu et al., 2013).

5.3.2. Elmer/Ice ice-flow model

The 3D, open-source, full-Stokes, finite-element model, Elmer/Ice (Gagliardini et al., 2013), is used to simulate ice flow through solution of the Stokes equations. Elmer/Ice also provides the framework in which the other model components (below) are implemented. For a detailed description of Elmer/Ice, readers are directed to Gagliardini et al. (2013). The model presented here also builds on work applying Elmer/Ice to tidewater glaciers presented in Todd et al. (2018). The upstream limit of the model domain was taken as the 100 m a^{-1} velocity contour (Figure 14), with a boundary condition on the inflow boundary specifying observed velocity. No flow was allowed through the lateral boundaries of the domain, which also had a no-slip boundary condition applied, and a sea-pressure condition was specified on the fixed calving front, as well as on the basal boundary. A geothermal heat flux of 55 mW m^{-2} (Martos et al., 2018) was specified at the base, and ice temperature at the upper surface (including the inflow boundary) was set equal to observations. A simple Weertman-type sliding law was applied at the base, as shown in Eq. (15):

$$\tau_b = \beta u_b \tag{15}$$

Where τ_b is the basal stress, β is the basal slip coefficient, and u_b is the basal velocity.

The model mesh was refined to reach the maximum resolution of 100 m near the calving front, coarsening gradually to 2 km beyond 20 km inland. The grounding line was set to the model outflow boundary, as we do not permit the glacier to float in this study. This is not a fully realistic representation of the situation at Store, where the southern part of the terminus is floating, but a more realistic treatment would require a substantial addition in model complexity to include the relevant calving-related processes, which are not our focus here, having been investigated by Todd et al. (2018) within a similar framework at the same glacier. We consider the impact of this

simplification on our results to be negligible, with the minor exception of some aspects of the plume modelling. This impact is discussed further below.

5.3.3. GlaDS hydrology model

Modelling of Store's subglacial hydrology is achieved using the GlaDS (Glacier Drainage System) module within Elmer/Ice, an implementation of the GlaDS model (Werder et al., 2013), which participated in the SHMIP tests (de Fleurian et al., 2018) and has been developed specifically for glaciological contexts (Gagliardini and Werder, 2018; Werder et al., 2013). GlaDS simulates both a continuous sheet of water across the entire model domain, representing inefficient distributed drainage, and discrete channel elements, which can form along the edges of the mesh elements when sheet thickness locally exceeds a threshold, thereby representing efficient drainage.

GlaDS is run on a 2D mesh distinct from the 3D ice-flow mesh, but replicating the footprint of the ice-flow mesh. That is, the nodes of the hydrology mesh are distributed across the same area as the ice-flow mesh, but at a different resolution. This allows a progressively finer GlaDS mesh resolution, starting at 100 m in the lowermost 20 km of the domain and coarsening to 2 km only in the uppermost portion of the domain, beyond 100 km from the front. Hence, we obtain a detailed understanding of the hydrology in the main trunk of the glacier, without increasing the computational cost of calculating the velocity and temperature of the ice throughout the model domain. This dual-mesh approach requires interpolation of variables between the two meshes (the ice velocity and normal stress, along with the residual from the temperature solver and the position of the grounding line). Channels are not allowed to form along the boundaries of the hydrology mesh and no water flow is assumed to occur across the lateral or inflow boundaries. In addition, the hydraulic potential (ϕ) is set to 0 at the calving front (i.e. we assume the calving front is at flotation), following Eq. (16) and (17):

$$\phi = \rho_w g Z + P_w \tag{16}$$

$$P_w = \rho_w g (Z_{sl} - Z) \tag{17}$$

Where ρ_w is the density of water at the calving front (i.e. of seawater in this case), g is the gravitational constant, Z is the elevation with respect to sea level, P_w is the water pressure, and Z_{sl} is sea level. In the case where Z_{sl} is set at 0.0, as it is here, and Z is negative, which will be true for

the outflow of the subglacial hydrological system at the bottom of the calving front, it can be seen that substituting Eq. (17) into Eq. (16) will give a result of 0 for ϕ.

Water entering the hydrological system is derived from surface and basal meltwater production. Specifically, the source term for the hydrological model at each node on the mesh is the sum of basal and internal melting due to friction and strain, and surface melt. Basal and internal melting are computed from the interpolated temperature residual, while surface melt is taken from a raster of melt values, as described in Section 5.3.6. below. Because the study focuses on the hydrology of the terminus region, we make the simplifying assumption that surface melt travels straight to the bed at the point of production, which is reasonable on a heavily crevassed glacier such as Store. While some runoff in reality is routed and stored at the surface (Smith et al., 2015), supraglacial stream networks are typically much smaller in size compared to the basal system considered here.

Parameters for the hydrological model are similar to those detailed in Gagliardini and Werder (2018), and are set out in Table 3. We use a higher bedrock bump height and cavity spacing, given the observed smoother sedimentary topography of Store and the length scale over which it varies (Hofstede et al., 2018). For full mathematical details of the GlaDS model and a sensitivity analysis of the model to these parameters, readers are directed to Werder et al. (2013), and for additional details on its implementation within the Elmer/Ice framework, to Gagliardini and Werder (2018). An additional sensitivity analysis was not undertaken here as being beyond the scope of this study.

The coupling between the ice-flow model and the hydrology model in this study is only one-way – there is no feedback from the hydrological system to the overlying ice – as our intention in this study was to investigate the hydrological system in winter, its expansion in summer and how its evolving nature affects submarine melting of the calving front. A coupling of ice dynamics and hydrology is beyond the scope of this study, but will be undertaken as part of future work.

5.3.4. Plume model

For the purposes of this study, a 1D plume model based on buoyant plume theory (Jenkins, 2011; Slater et al., 2016) was implemented in Elmer/Ice. The model simulates the evolution of subglacial runoff after it emerges from the grounding line and rises towards the fjord surface, mixing turbulently with the warm surrounding fjord water and stimulating melting at the ice-ocean interface. This model has been successfully used to model proglacial plumes in studies of diverse focus (Hopwood et al., 2018; Slater et al., 2017), including within the MITgcm ocean circulation model (Cowton et al., 2015).

Table 3 – Parameters used in GlaDS model for all model runs in this study.

Description	Symbol	Value	Units
Pressure melt coefficient	c_t	$7.5 \cdot 10^{-8}$	K Pa^{-1}
Heat capacity of water	c_w	4220	J kg^{-1} K^{-1}
Sheet flow exponent	α_s	3	
Sheet flow exponent	β_s	2	
Channel flow exponent	α_c	5/4	
Channel flow exponent	β_c	3/2	
Sheet conductivity	k_s	0.0002	m s kg^{-1}
Channel conductivity	k_c	0.1	$m^{3/2}$ $kg^{-1/2}$
Sheet width below channel	l_c	20	m
Cavity spacing	l_r	100	m
Bedrock bump height	h_r	1	m
Englacial void ratio	e_v	10^{-4}	

In this study, a continuous sheet-style 'line' plume (Jenkins, 2011; Slater et al., 2016), split into coterminous segments, is simulated across the calving front. Our limited observational constraints currently support this line plume geometry as the most appropriate for use at tidewater glaciers (Fried et al., 2015; Jackson et al., 2017). Discharge at each node on the grounding line is taken as the sum of channel and distributed sheet discharge within the hydrological model GlaDS. This allows the plumes and the consequent modelled submarine melt rates across the calving front to vary dynamically as the subglacial drainage system evolves over the course of each simulation, without having to specify fixed plume locations. The drag coefficient (Cd) within the plume model was increased to 0.02, following Ezhova et al. (2018). A full description of the plume model can be found in Slater et al. (2016).

Results from the plume model are largely independent of the mesh resolution at the calving front. The input discharge and consequent submarine melt rate is calculated per metre width along the front, hence a coarser mesh will lead to more discharge at each grounding-line node. This discharge increase will, however, be spread over a larger area between nodes, so the overall input discharge and output melt rate are similar for different mesh resolutions. The frontal mesh resolution and plume segment width used on the hydrology mesh (100 m) were chosen to fit with the frontal mesh resolution on the ice mesh to minimise interpolation artefacts and also as representing a reasonable order-of-magnitude length scale for the size of subglacial channel outlets on tidewater glaciers (Fried et al. 2015; Jackson et al., 2017). We consider this to be a reasonable simplifying assumption, given

the current lack of observational constraints for the morphology of channel outlets at the calving front of tidewater glaciers.

When discussing the results of the plume model we will make use of a number of quantities which highlight different aspects of variability between our simulations. We define the 'average melt rate' as the average over all points of the subaqueous calving front and all points in time. We define the 'mean maximum melt rate' as the average over time of the maximum melt rate at any point on the calving front. We define the 'absolute maximum melt rate' as the maximum at any time and at any point on the calving front.

5.3.5. Modelling procedure

Initially, the ice flow model was run with the simple sliding law in Eq. (15) based on an initial guess at the basal slip coefficient, β, until a converged ice temperature-velocity solution was reached. We then inverted for basal friction to match satellite-derived surface velocity at Store, producing an observationally constrained steady-state temperature-velocity solution. From this starting point, a year-long hydrological simulation was run, using only basal melt, to provide an initialised state for the hydrological system as well as the ice flow. For the subsequent hydrology runs, the timestep was set to 0.1 days and all ice dynamic variables (geometry, temperature, velocity, etc.) were kept constant, given the lack of two-way coupling and our aim in conducting this study, as discussed in Section 5.3.3 above.

Subsequent to this hydrological initialisation simulation, we performed five hydrological simulations based on different scenarios as described in Table 4. Each of these scenarios ran for three months, to replicate an actual season, and all used at least basal melt as a source term for the hydrology. One simulation (Winter) was a winter simulation, with no surface melt, meaning the simulated hydrological system carried exclusively basal melt. The remaining four scenarios describe summer simulations in which the hydrological system carries surface melt in addition to basal melt. Two of these (SummerAverage12 and SummerAverage17) used a constant surface melt equal to the average during June, July and August (JJA) in 2012 and 2017, respectively, to allow a comparison between a high-melt (2012) and a low-melt (2017) year. The final two (SummerDaily12 and SummerDaily17) instead used daily values of surface melt for 2012 and 2017 to enable exploration of the differences produced in the modelled hydrological system when using realistic transient forcing, varying day to day, compared to the summer average state. Due to the fixed geometry and ice dynamics of the hydrological simulations, the basal melt term is constant across all timesteps and all simulations, as the temperature field does not evolve, allowing easier discrimination of changes in

the system caused by the addition of the surface melt in the summer simulations. The simulations are summarised in Table 4, below.

Table 4 – Summary of hydrological simulations. BM = Basal and Internal Melt; SM = Surface Melt.

Name	Season	Hydrological Source	Surface-Melt Resolution
Winter	Winter	BM	n/a
SummerAverage12	Summer 2012	BM + SM	Three-month average
SummerAverage17	Summer 2017	BM + SM	Three-month average
SummerDaily12	Summer 2012	BM + SM	Daily
SummerDaily17	Summer 2017	BM + SM	Daily

5.3.6. Data

The surface DEM used here to set the surface ice geometry in Elmer/Ice is from the ArcticDEM project, v2.0 (Porter et al., 2018), representing a composite view of the region between 2015 and 2018, and resampled to 25 m resolution. The basal DEM is taken from BedMachine v3 (Morlighem et al., 2017) at 150 m resolution and a nominal date of 2007, though this was processed further to remove errors around the terminus of Store, based on work previously conducted by the authors (Todd, 2018).

Surface melt data for input to the hydrology model are runoff values from RACMO2.3p2 at 1 km spatial resolution and daily temporal resolution (Noël, 2018). Summer averages were calculated by taking the mean of the surface melt across all days in JJA of the relevant years. The surface temperature data used as an upper-ice-surface boundary condition in the ice flow model were the average for the years 2000-2014, derived from the NASA MODIS Snow and Sea Ice Mapping Project (Hall et al., 2012, 2013). The surface velocity data used for the inversion part of the spin-up process were taken from the 20-year velocity mosaic of Greenland developed as part of the MEaSUREs project (Joughin et al., 2016, 2018). This was in order to remove the bias of any anomalous velocity patterns in any one specific year and also because sufficient good-quality velocity data for all the years looked at in this study was not available.

The temperature and salinity of the ambient fjord water, required by the plume model, were taken from conductivity-temperature-depth casts gathered in the fjord within a few kilometres of the calving front (Chauché, 2016). Different profiles (Figure 15) were used for summer (CTD cast from 02/08/2012; within 1 km of the calving front) and winter (CTD cast from 02/03/2013; 10 km from calving front). Both are the closest data to the calving front available, and are assumed to be representative of conditions at the calving front.

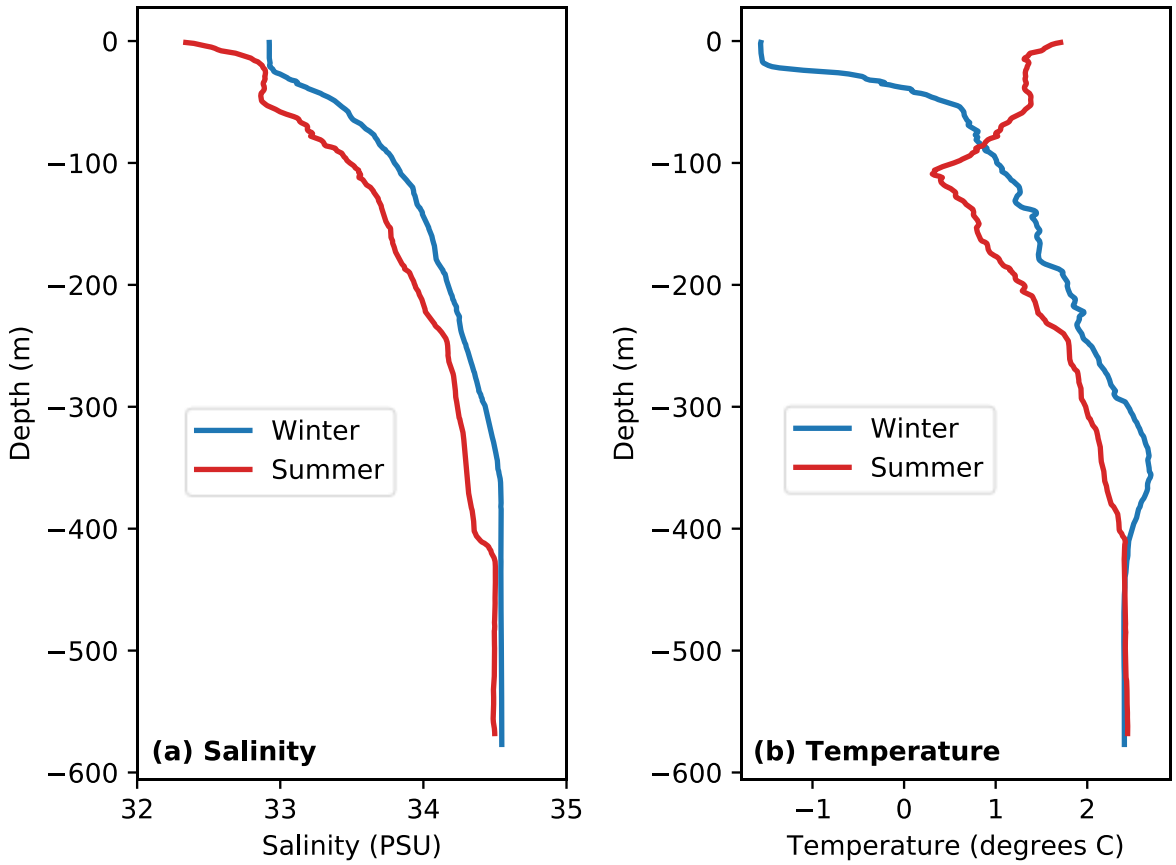

Figure 15 – Ambient fjord salinity and temperature profiles used as input to the plume model (Chauché 2016). Winter conditions from CTD cast on 02/03/13 approx. 10 km from the calving front; Summer conditions from CTD cast on 02/08/12 approx. 1 km from the calving front. (a) Salinity in winter and summer; (b) Temperature in winter and summer.

5.4. Results

The key simulation results are summarised in Table 5, with the important differences being picked out in the remainder of this section. The findings are then discussed in Section 5.5.

5.4.1. Winter baseline simulation

The results from the Winter run show a varied subglacial drainage system at Store, where channels may form even in winter when the system is fed exclusively by basal melt produced by frictional and geothermal heat (Figure 16). Channels of 1 m^2 or more in cross-sectional area, a threshold we found functions effectively as a discriminator for regions of significant channel growth, are found in a few regions extending up to 5 km inland from the terminus at the end of the model run. Smaller channels link these up and form the majority of an arborescent network with three main branches, reaching to 40 km inland (Figure 16b). Channels this small are indicative of a distributed drainage system, rather than a true channelised system. We show them in Fig 3. because they illustrate where

Table 5 – Summary of key simulation results. The channel, sheet and pressure statistics are taken from the final timestep across the entire model domain (columns marked 'End') or the timestep where maximum mean channel area in the simulation was reached (columns marked 'Max' – this occurred on timestep 60 for SummerDaily12 and timestep 74 for SummerDaily17) – for the average-forced runs, the end timestep is also the max timestep, so only figures for the end timestep are shown; the plume statistics are taken from the calving front across all timesteps. 'Area Channelised' refers to the percentage of the possible channel segments occupied by channels >1 m^2 in area.

	Winter	**SummerAverage12**	**SummerAverage17**	**SummerDaily12**		**SummerDaily17**	
	End	End	End	Max	End	Max	End
Mean channel area (m^2)	0.04	9.84	6.45	12.10	8.18	7.00	5.25
Mean channel flux ($m^3\ s^{-1}$)	$8x10^{-4}$	5.32	2.40	7.47	2.44	3.26	2.46
Area channelised (%)	0.05	12.05	6.75	15.26	10.77	8.40	6.81
Mean sheet discharge ($m^3\ s^{-1}$)	$3x10^{-4}$	0.090	0.016	0.104	0.034	0.023	0.008
Mean sheet thickness (m)	0.18	0.47	0.32	0.51	0.36	0.34	0.28
Mean effective pressure (MPa)	2.01	1.13	1.30	1.27	1.43	1.37	1.16
Mean plume melt rate ($m\ d^{-1}$)	0.15	0.68	0.50	0.65	0.65	0.50	0.50
Mean maximum plume melt rate ($m\ d^{-1}$)	0.43	4.25	3.13	3.65	3.65	3.01	3.01
Total plume melt ($m^3\ a^{-1}\ x10^{10}$)	1.26	5.85	4.29	5.95	5.95	4.36	4.36

a connected subglacial drainage system will subsequently develop. One branch of the subglacial drainage system drains the northern side of the model domain, one the southern side, and one the centre. These branches then converge into one major, central flow path that splits in two near the terminus, with one flow path exiting at the northern margin of the ice front and one at the southern margin. The pattern of discernible discharge within the distributed sheet (down to 0.0001 $m^2\ s^{-1}$) (Figure 16c) is similar, which is to be expected, as the thickness of the distributed sheet (typically up

to 1 m near the terminus, progressively dropping to below 0.1 m beyond 100 km inland) determines the location of the channels within the hydrology model.

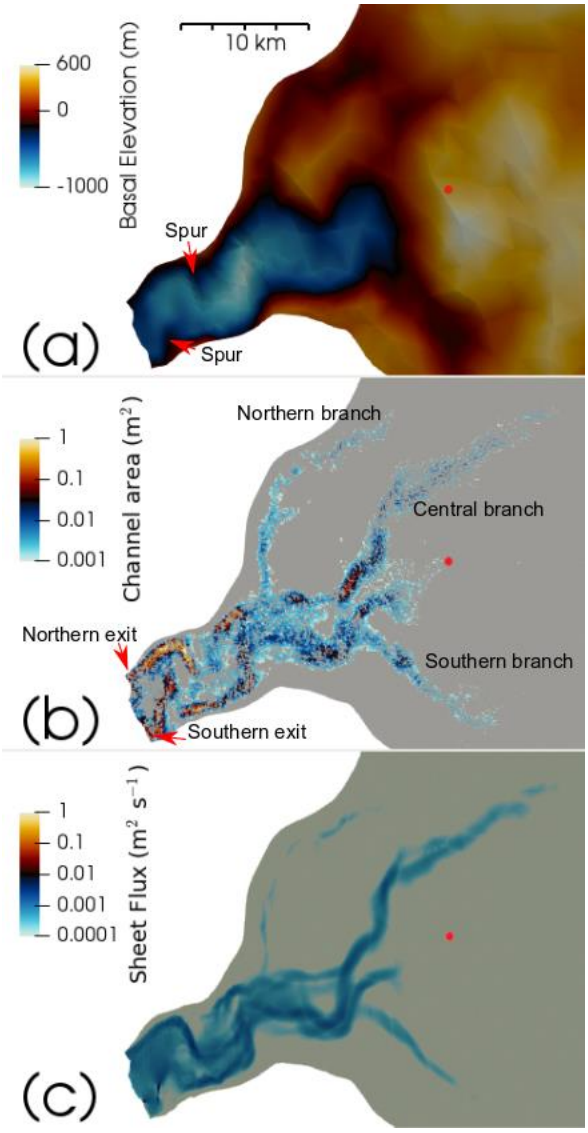

Figure 16 – Winter hydrological system at Store at end of Winter run and basal topography. (a) bed elevation; (b) channel area ; (c) sheet flux. The red dot in all panels marks the location of the S30 site from Young et al. (2019). Channels and sheet drainage pathways can be seen to largely follow the deeper parts of the bed. We have shown very small channels and low sheet discharges to fully display the existence of a connected winter drainage system.

The discharge patterns are controlled by the hydraulic potential gradient, which, as can be seen from Figure 16a, is mainly determined by the basal topography of Store and the ice thickness, with the farther-inland areas of greater hydrological activity following the deeper parts of the bed. The same can be seen nearer the terminus where the successive southward and northward bends in the drainage pathways upstream of the terminus are related to spurs of shallower bedrock jutting into the central trough from the northern and southern margins, respectively. These push the flow pathways towards the edges of the trough, compared to the more central flow paths farther inland.

In total, the input to the hydrological system from basal melt in winter amounts to 4.7×10^7 m^3 over the 92 days of the Winter simulation, or 5.96 m^3 s^{-1}, with the resulting subglacial discharge across the grounding line split 2:1 between the channels and the distributed sheet, respectively. This is sufficient to drive convective plumes and a diffuse pattern of plume-induced calving-front melting throughout the winter (Figure 17a), with a persistent diffuse plume at depth, mainly driven by discharge from the distributed sheet with occasional enhancement from channel outlets, across most of the calving front. The absolute maximum melt rate of 1.1 m d^{-1} is found at the deepest point of the calving front, where observations show that the ice becomes buoyant and floats, as shown by a marked surface depression behind the calving front denoting the flexion zone. Despite the absence of surface input, melt rates of 0.2-0.3 m d^{-1} are widespread. Overall, this leads to an average plume melt rate of 0.15

m d^{-1}, excluding the subaerial portion of the calving front, with 0.51 m d^{-1} the mean maximum melt rate. The resulting meltwater flux to the fjord from plume melting is 3.48 m^3 s^{-1}.

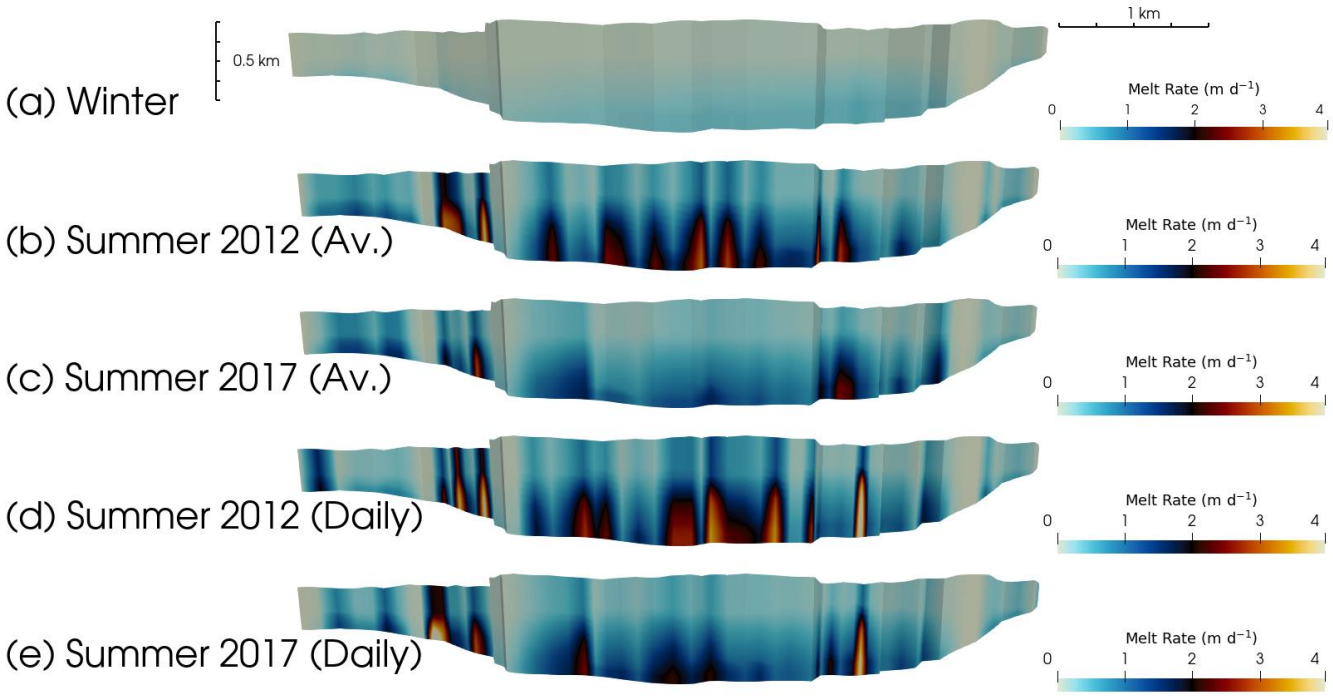

Figure 17 – Patterns of typical plume-generated frontal melt across all simulations, showing the 9th August for panels (b)-(e). (a) Winter run; (b) SummerAverage12 (average-forced) run; (c) SummerAverage17 (average-forced) run; (d) SummerDaily12 (daily-forced) run; (e) Run SummerDaily17 (daily-forced) run. North is to the left, south is to the right. Note how higher summer plume activity is concentrated into a relatively small number of localised high-melt plumes.

5.4.2. Average-forced summer hydrology and plumes

In the first set of summer simulations we forced the model with RACMO surface runoff for Store averaged over JJA in 2012 and 2017. With the addition of surface meltwater, the subglacial hydrological network is found to expand substantially (Figure 18 and Figure 19), but does not reach a steady state by the end of either simulation. In 2012 (run SummerAverage12), the number of channel elements >1 m^2 in cross-sectional area grows by three orders of magnitude through the summer. Mean channel area, meanwhile, rises by two orders of magnitude, whilst mean channel flux across all sizes of channel jumps by four orders of magnitude. In 2017, when surface melt was 63% lower than in 2012, the expansion is reduced: the number of channels >1 m^2 in area only increases by two orders of magnitude compared to winter, with mean channel area up by two orders of magnitude again, but only reaching 6.45 m^2, and mean channel flux increasing once more by four orders of magnitude, but only to 2.40 m^3 s^{-1}. As the basal hydrological system accommodates surface meltwater, the channels grow significantly in size and channels over 1 m^2 in cross-sectional area reach farther inland – up to 55 km in 2012 (Figure 18a), although less (30 km) in 2017 (Figure

18b). Discernible distributed sheet discharge pathways, meanwhile, extend up to 65 km in 2012 (Figure 19a), and growth in these is similarly reduced in 2017, to 45 km (Figure 19b). This is reflected in the mean distributed sheet discharge figures at the end of the SummerAverage12 and SummerAverage17 model runs, which show a 226-fold and 40-fold increase on the Winter run, respectively. At the same time, the mean distributed sheet thickness increases by 259% in 2012, and by 173% in 2017, compared to winter. The combined effect of these changes in the hydrological system is to reduce mean effective pressure (defined as ice overburden pressure minus water pressure) across the model domain by 44% in summer 2012 and by 35% in 2017; i.e. water pressures are higher in summer compared to winter.

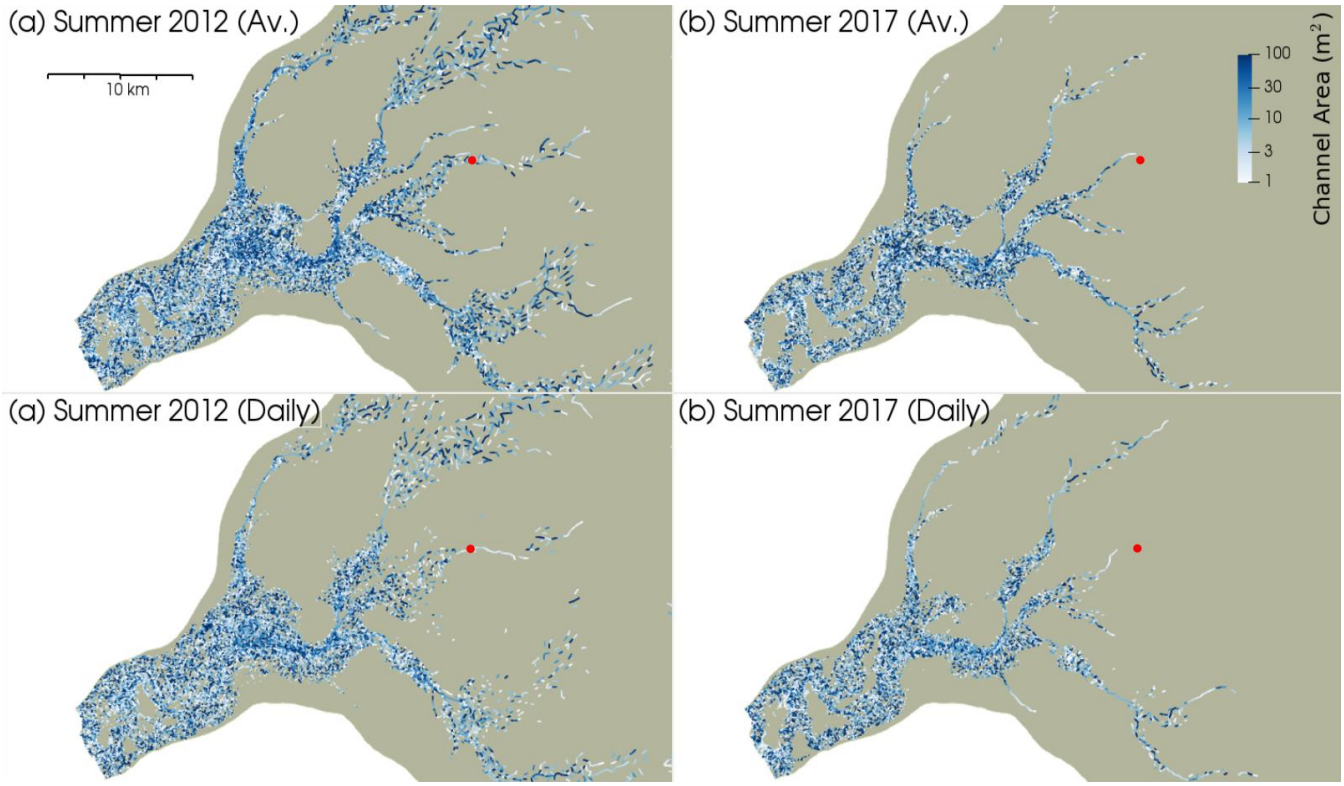

Figure 18 – Summer channel network of Store. (a) SummerAverage12 model run; (b) SummerAverage17; (c) SummerDaily12; (d) SummerDaily17 (red dot shows S30 study site from Young et al. (2019)). All the panels show the channel network at the end of the respective simulations, after three months of surface melting. The daily-forced runs show a less extensive channel network owing to declining surface melt towards the end of the melt season.

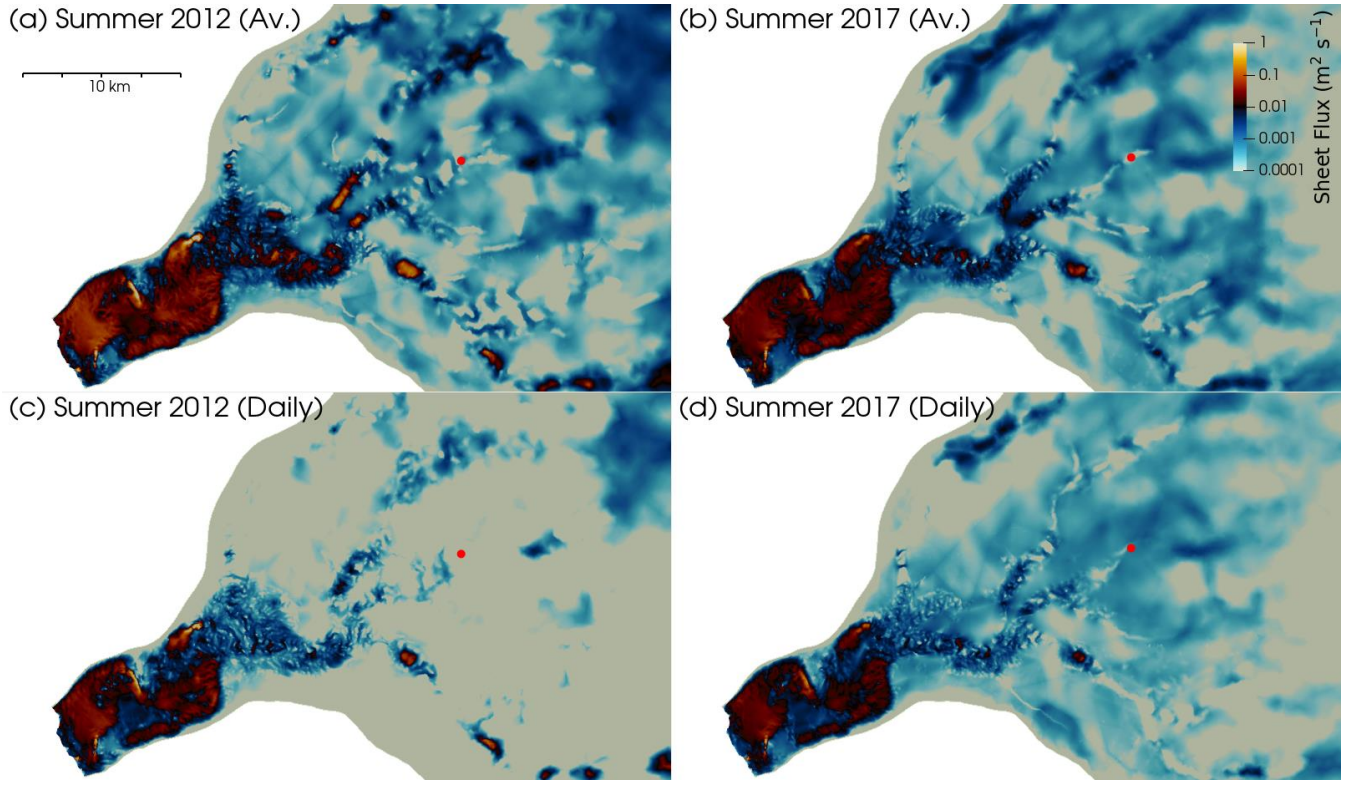

Figure 19 – Summer distributed sheet layer at Store. (a) SummerAverage12 model run; (b) SummerAverage17; (c) SummerDaily12; (d) SummerDaily17 (red dot shows S30 study site from Young et al. (2019)). All the panels show the sheet layer at the end of the respective simulations, after three months of surface melting. The daily-forced runs show a less extensive sheet owing to declining surface melt towards the end of the melt season.

Plume structure and the resulting submarine melting also differ markedly between seasons and years. In summer 2012, we find strong, channel-fed plumes that usually reach the surface spaced along the majority of the calving front, with the exception of the southern extremity (Figure 17b – the right-hand side of the terminus). In summer 2017, these stronger plumes, though still mostly reaching the surface, are more spatially restricted, appearing primarily in two regions: one on the northern side of the terminus and one around the deepest part of the calving front, where the highest melt rates are observed in winter (Figure 17c). The resulting average melt rate for 2012 is 0.68 m d^{-1}, and for 2017 it is 0.50 m d^{-1}, rising to 4.25 and 3.13 m d^{-1}, respectively, for the mean maximum melt rate. Defining long-term average melt rates for areas specifically inside strong plumes or outside of them is difficult, as the location of strong convection-driven summer plumes varies as points of discharge from the hydrological system evolve, but rates of <1 m d^{-1} for the diffuse, distributed-sheet-driven plume, and 2-4 m d^{-1} for the stronger channel-driven plumes are typical. Absolute maximum melt rates, meanwhile, reach up to 12.6 m d^{-1} for both SummerAverage12 and SummerAverage17.

5.4.3. Daily-forced summer hydrology

In the SummerDaily12 and SummerDaily17 runs we forced the model with daily values of RACMO surface runoff for Store during JJA in 2012 and 2017, respectively. Given the temporally varying nature of the surface-melt forcing, we will consider two sets of results for these runs: the end state of the simulation and the state at the maximum extent of the hydrological system. We define the latter as the time when mean channel area reaches its maximum value. Figure 18c, d and Figure 19c, d show the end states of the SummerDaily12 and SummerDaily17 runs as an illustration of how the different surface-melt forcings can lead to substantially different outcomes.

For the end state of SummerDaily12, the mean channel area drops by 17% compared to the SummerAverage12 run, and the mean channel flux drops by 54%, whilst the number of channel segments >1 m^2 in cross-sectional area drops by 11%. For the maximum state of SummerDaily12, though, the mean channel area increases by 23% compared to SummerAverage12, mean channel flux by 41%, and the channelised area by 27%. Concomitantly, the mean distributed sheet discharge and thickness at the end of the SummerDaily12 run are 63% and 25% down, respectively, compared to the SummerAverage12 run, but are 15% and 7% higher than SummerAverage12 when considering the maximum state. Overall, therefore, the change in surface-melt forcing to realistic daily totals, rather than a constant average, leads to a larger maximum drainage system extent that starts to exhibit significant decay towards the end of the melt season.

For SummerDaily17, a similar pattern is observed. At the end state of SummerDaily17, mean channel area, distributed sheet discharge and distributed sheet thickness are, respectively, 19%, 51% and 12% lower than at the end of the SummerAverage17 model run. Channel flux, along with the channelised area, show small increases of 3% and 1%, respectively, however. Considering the maximum state of the SummerDaily17 run, though, mean channel area increases by 9%, channel flux by 36%, and the area covered by channels >1 m^2 in cross-sectional area by 25%. Distributed sheet discharge and thickness similarly increase by 42% and 9%, respectively. The numerical values from which all these percentages are derived are given in Table 5, above. Similarly to 2012, therefore, we find the change in surface-melt forcing to produce a larger drainage system that then begins to decay as surface melt tails off.

Looking at the plume results for SummerDaily12 and SummerDaily17 (Figure 17d, e), both daily-forced runs show a very small decline in plume activity compared to the average-forced (SummerAverage12 and SummerAverage17) runs. In the SummerDaily12 run, the average melt rate decreases by 5% on the average melt rate for the SummerAverage12 run, and the mean maximum melt rate drops by 14%. For SummerDaily17, the average melt rate only differs by 0.1% compared to

SummerAverage17, but the mean maximum melt rate drops by 4%. The overall pattern of plume activity is broadly similar to that seen in the average-forced simulations, as can be appreciated by comparing Figure 17d and e to panels b and c, with some shift in plume locations as the different forcing leads to variations in the resulting channel networks. Absolute maximum melt rates also follow suit and decrease for both simulations, reaching 9.0 m d^{-1} for SummerDaily12, and 10.1 m d^{-1} for SummerDaily17. The total amount of melt generated by plumes, however, increases slightly in the daily-forced simulations compared to the average-forced ones, by a little under 2% in both 2012 and 2017.

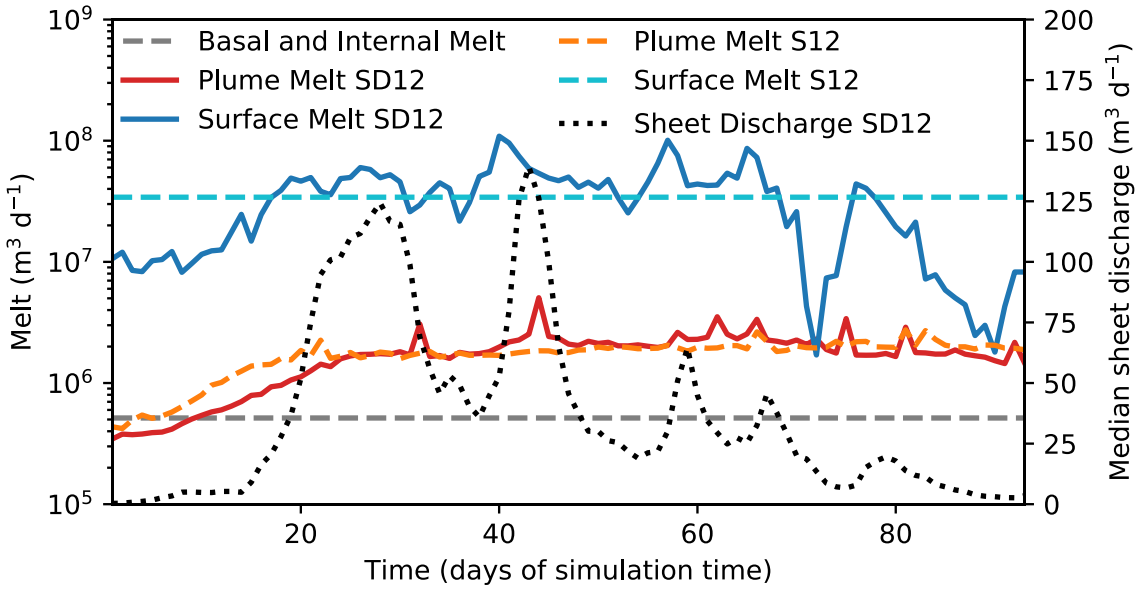

Figure 20 – Time series of melt sources in SummerDaily12 (red and blue solid lines) and SummerAverage12 (orange and light blue dashed lines) model runs. Note logarithmic y-axis. Basal and internal melt was constant across both runs and is included for comparative purposes – note how plume melt is of equal or greater importance. Median sheet discharge (dotted line; taken as the median over the whole model domain) shows response of subglacial hydrological system to surface melt, and evolution of the system towards greater channelisation over melt season.

The daily-forced simulations also allow us to examine the contributions to total melt by component over time, though the basal melt, as explained in Section 5.3.5, remains constant throughout the simulations. Surface melt in SummerDaily12 is, as would be expected, the dominant factor, being one to two orders of magnitude larger than any other source of melt during the summer (Figure 20). Plume melt, meanwhile, remains an order of magnitude greater than basal melt throughout the SummerDaily12 simulation, except for the first 20 days of the model run. Compared to the average-forced SummerAverage12 run, the more variable surface-melt input in the SummerDaily12 run also leads to greater variability in the plume melt rate. It is notable, however, that between day 72 of the model run and the end, the SummerDaily12 plume melt rate is generally equal to the

SummerAverage12 plume melt rate, despite surface-melt input being somewhat lower on occasion. Similarly, the large drop in surface melt on day 72 of the SummerDaily12 run does not show any impact on plume melt at the time or afterwards. The reasons for this will be considered further in Section 5.5, below. Sheet discharge, as a proxy for the development of the subglacial hydrological system shows a sensitive, slightly lagged response to variations in surface melt in the first half of the model run, but a much more damped response in the second half. The reasons for this will also be discussed in Section 5.5.

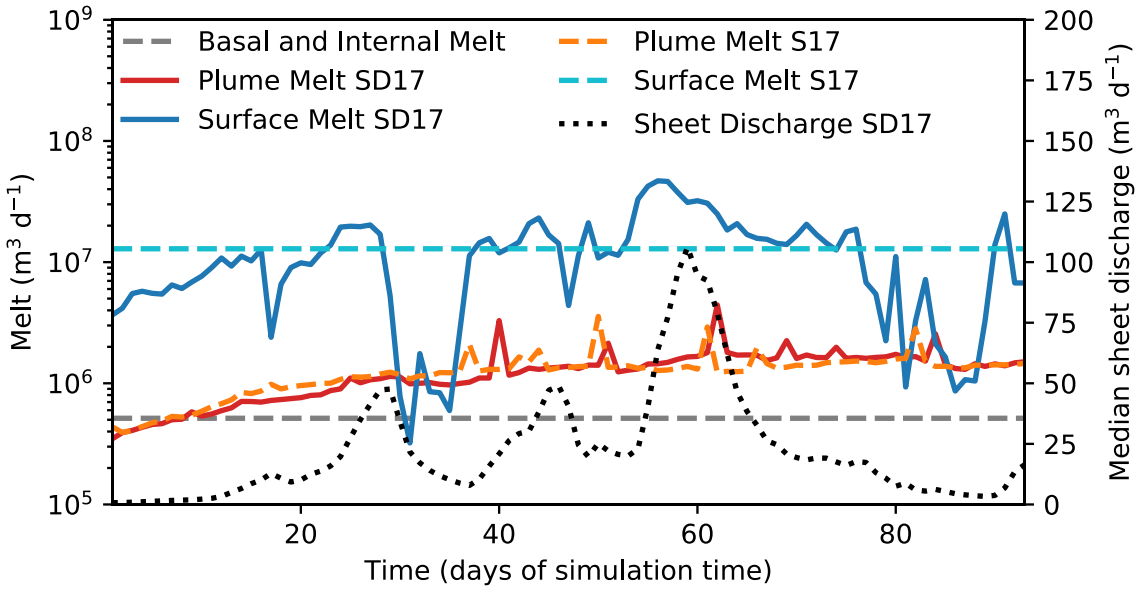

Figure 21 – Time series of melt sources in SummerDaily17 (red and blue solid lines) and SummerAverage17 (orange and light blue dashed lines) model runs. Note logarithmic y-axis. Basal and internal melt was constant across both runs and is included for comparative purposes – note how plume melt is of equal or greater importance. Median sheet discharge (dotted line; taken as the median over the whole model domain) shows response of subglacial hydrological system to surface melt, and evolution of the system towards greater channelisation over melt season.

For SummerDaily17 (Figure 21), the overall pattern is similar, but the dominance of surface melt in a cooler year is reduced, with surface melt dropping below plume melt on at least two separate occasions, and even below basal melt at one point (Day 31, equivalent to the 1st July). Plume melt still exceeds basal melt throughout, except for the first 8 days (Figure 21), underlining the importance of this mechanism even in cooler years. Similarly to summer 2012, it is also clear that, despite some periods of low surface melt in the SummerDaily17 run, the resulting plume melt rates are comparable to those from the constant-average-forced SummerAverage17 run. Again, even with a constant forcing in the SummerAverage17 run, variable plume melting is seen, further underlining how important the underlying structure of the subglacial drainage system is in determining the

resulting outflow. Unlike in 2012, however, sheet discharge remains sensitive to surface melt variations until around day 70 of the model run, exhibiting a more damped response thereafter.

5.5. Discussion

5.5.1. Winter subglacial hydrology and plume activity

This study is amongst the first to constrain the nature of evolving hydrological systems beneath fast-flowing tidewater glaciers in Greenland. When the GlaDS model and Elmer/Ice are applied to Store, we predict an active subglacial drainage system consisting of channels and a distributed sheet layer to be present even in winter, when channels exceeding 1 m^2 in cross-sectional area form up to 5 km inland from the calving front, while a distributed sheet and smaller channels extend a further 40 km inland. This is the first time to our knowledge that the existence of such a system in winter has been shown in a model and has important implications for our understanding of tidewater glacier dynamics and the ice sheet's interaction with the ocean. In contrast to previous work, which assumed zero freshwater flux into fjords outside the summer melt season and therefore for the largest part of the year (e.g. Carroll et al., 2015; Slater et al., 2018), we demonstrate that the freshwater flux within a channelised basal drainage system is in fact sufficient to drive convective plumes across the calving front, leading to localised melt rates of up to 1.1 m d^{-1} in winter at the deepest portion of the calving front, where the strongest distributed-sheet-driven plume is modelled. Averaged across the entire subaqueous portion of the calving front, this melting equates to 0.15 m d^{-1}. This is below the 1.9 ± 0.5 m d^{-1} estimated by Chauché (2016) using CTD and ADCP data gathered in winter 2012-13 as inputs to the Gade (Gade, 1979) and Motyka (Motyka et al., 2003) models of fjord circulation and melting. It should also be noted that modelled melt rates from plumes consistently underestimate observed melt rates (e.g. Sutherland et al., 2019); this is a pervasive problem in plume modelling, so it is to be expected that we find a similar result. We also model an average winter subglacial discharge of only 5.96 m^3 s^{-1}, 69% of which derives from channels and 31% from the distributed sheet. This is, as expected, at the lower range of estimates (1-72 m^3 s^{-1}) presented in Chauché (2016), so our lower melt rates are consistent with this and also with the low melt rate of 0.4 ± 0.1 m d^{-1} calculated for runoff-free simulations at Store by Xu et al. (2013). Freshwater flux into the fjord from submarine melting is 3.48 m^3 s^{-1} on average, which combined with the subglacial discharge of 5.96 m^3 s^{-1}, gives a total winter meltwater flux to the fjord of 9.44 m^3 s^{-1}. This freshwater flux may well be sufficient to drive winter-time buoyancy-driven fjord circulation, pulling warm Atlantic water towards the calving front at depth and resulting in further melting (Christoffersen et al., 2011; Mortensen et al., 2018; Straneo et al., 2010). This may be further enhanced by wind-driven circulation in autumn and early winter, when fjords are ice free and winds

are strong (Christoffersen et al., 2011). Overall, though, our results for winter at Store here suggest basal meltwater production is lower and drives less intense melting at the calving front than estimated by Chauché (2016), with higher melt rates being confined to the deeper section of the calving front. This indicates either that (i) our model may lack a process that releases additional subglacial meltwater in winter, e.g. if some of the runoff from the previous melt season went into subglacial storage before it was released (Chu et al., 2016), or (ii) that we correctly predict the release of subglacial meltwater but underestimate the resulting submarine melting, perhaps due to uncertainty in the melt rate parameterisation or due to not taking account of fjord-scale circulation (Slater et al., 2018).

Our winter run results also demonstrate the critical nature of the depth of subglacial discharge for driving plume melting. In the model results, the area of highest subglacial discharge in winter is actually towards the northern margin of the calving front (left-hand side of Figure 17), but very little plume melting is produced there. Instead, the higher melt rates are concentrated across the deepest parts of the front, where subglacial discharge is lower. This disparity can be related to the vertical profile of winter water in the fjord (Figure 15a). For water input above a depth of 300 m, which is the case for the northern margin of the calving front, the surrounding ambient water is cold and highly stratified, so that the plume quickly reaches neutral buoyancy and what ambient water it does bring into contact with the ice front has little melting potential. For the water discharged across the south-central part of the calving front, where the depth exceeds 500 m, though, the plume is mixing with warmer, less stratified water that allows it to generate significantly more melt, which will be further enhanced by the increase in thermal energy that comes with a reduced pressure-melting point. Ambient conditions are also rather constant from the grounding line up to around 350 m, where the mid-water-column thermal maximum is reached, making it easier for the plumes to rise until they hit this lower-density layer. Therefore, if warmer water is present at depths in fjords throughout the winter, we find it likely that significant melting occurs at depth in winter at tidewater glaciers in Greenland, even with limited subglacial discharge compared to summer.

5.5.2. Summer subglacial hydrology

When surface melting is incorporated in simulations of the summer melt season, the extent of both concentrated channels and distributed sheet systems grows substantially compared to winter (Figure 18 and Figure 19). Using the seasonally averaged mean surface melt between 1st June and 31st August in 2012 (run SummerAverage12), we find channels of over 1 m^2 in area extending to 55 km inland from the terminus (Figure 18a), with an active distributed sheet layer again extending a further 10 km (Figure 19a), and a resulting average freshwater flux to the fjord of 421 m^3 s^{-1}. Of the

latter, 95% comes from channel outflow and 5% from plume melting, while discharge from the distributed sheet is negligible. This shows how surface melt expanded the subglacial drainage system during the warmest summer at Store in the observational record. When the model is forced by mean surface melt for the same period in 2017 (run SummerAverage17), when surface melt was much lower (149 $m^3 s^{-1}$ compared to 395 $m^3 s^{-1}$ in SummerAverage12), close to the mean for 1981-2010, we find channels of over 1 m^2 in area reaching 30 km inland (Figure 18b) and the distributed sheet 45 km (Figure 19b). Whilst the average freshwater flux to the fjord drops by 59.7% to 170 $m^3 s^{-1}$, the relative contributions from channels (91%), plume melting (9%) and the distributed sheet (<1%) remain largely unchanged.

In this study we also examined how the basal water in our model responded when day-to-day differences in surface melt were introduced. In 2012 (run SummerDaily12), we find the daily incorporation of surface melt to produce a larger subglacial drainage system at the system's maximum extent (Figure 22a), with 27% more channels that are 23% larger on average and contain 41% more water on average than the end state of the system when we forced the model with seasonally averaged surface melt (SummerAverage12) (Figure 18a). By contrast, by the end of the SummerDaily12 simulation (Figure 18c), we find 11% fewer channels that are 17% smaller and hold 54% less water, on average, compared to the end state of SummerAverage12 (Figure 18a). For summer 2017 (run SummerDaily17), we observe a similar pattern of a larger maximum extent (Figure 22b) and smaller final extent (Figure 18d) of the hydrological system compared to that seen at the end of the average-forced 2017 run (SummerAverage17) (Figure 18b), with the exception of the number of channels and mean channel flux, which both show small increases over the final SummerAverage17 values even at the end of the SummerDaily17 run. These results for 2017 also agree well with the observations of a high-pressure distributed drainage system 30 km inland in 2014-15 reported in Doyle et al. (2018) and Young et al. (2019), towards the centre of the model domain (see Figure 16). Young et al. (2019) posited the existence of a channelised drainage system forming up to, but not beyond this point, based on observed velocity patterns from radar and GPS measurements, with a pronounced slowdown occurring at lower elevations on Store in the summer. Doyle et al. (2018), meanwhile, suggested that persistent high pressure and rapid drainage in boreholes at the site were best explained by them tapping in to an extensive distributed drainage system. Our results for summer 2017, a better comparison for observed melt in 2014-15, concur with this pattern, with significant channel growth ceasing around the 30 km mark in the region of the study site, but with a major distributed sheet drainage pathway predicted to lie in its vicinity (red circle on Figure 18d and Figure 19d).

The differences in the daily-forced runs can be linked to the variability in forcing – in the SummerDaily12 run, the last two weeks of model time have steadily decreasing surface-melt forcing, with a small up-tick for the last 3 days of the run (Figure 20). Compared to the average-forced run (SummerAverage12), it is therefore to be expected that a smaller hydrological system is found at the end of the run. A similar process is observed for summer 2017, with the drainage system in SummerDaily17 decaying as surface melt tapers off from Day 80 (equivalent to the 19th August) onwards (Figure 21). However, unlike in SummerDaily12, there are several major surface-melt spikes after this point in the SummerDaily17 run (compare the right-hand sides of Figure 20 and Figure 21), explaining why channel flux and channelised area at the end of the run do not show a drop compared to SummerAverage17. Channels start to decay, as the smaller mean channel area testifies (Table 5), but the extra surface melt keeps the system from closing down as swiftly as in summer 2012. The same idea explains the finding of lower effective pressures (and therefore higher water pressures) at the end of the SummerDaily17 run, compared to the end of the SummerDaily12 run (Table 5), despite the lower melt input in 2017. The surface-melt spikes in the last two weeks of the SummerDaily17 run (Figure 21) re-pressurise the decaying system, whereas the smoother tapering off in SummerDaily12 (Figure 20) means the decaying drainage system remains at over-capacity and keeps water pressures lower. This interpretation is reinforced by the evolution of sheet discharge in the two summers. In 2012, the strong response to surface melt variations in the first half of the model run shows a predominantly distributed hydrological system with most water transiting through the sheet; the more damped response in the second half shows the formation of a predominantly channelised system where water is preferentially routed through the efficient channels rather than the inefficient sheet. The lagged nature of the sheet's response, however, means it is not possible to see how it responds to the increased melt at the very end of the SummerDaily12 run. In 2017, the pattern of sheet drainage response shows widespread channelisation was not established until towards day 70 (9th August), but was maintained until the end of the model run, as there is little response of sheet drainage to the surface melt fluctuations from day 80 (19th August) onwards.

Looking at the maximum extent of the hydrological system in the daily-forced runs (Figure 22, Table 5), it is important to note the dynamism this reveals in the drainage system of Store. For SummerDaily12, maximum extent is reached on Day 60 (equivalent to July 30th) of the model run, with little growth after day 45 (15th July); for SummerDaily17, on Day 75 (equivalent to August 14th), levelling off from day 63 (2nd August), according with the onset of widespread channelisation shown by the sheet discharge time series (Figure 20, Figure 21) as described above. Within a month, these systems, which are substantially larger than those achieved by the end of the average-forced

SummerAverage12 and SummerAverage17 runs (Table 5), die back considerably as melt inputs drop. Of particular interest is also the timing of maximum system extent versus that of maximum melt input. For SummerDaily12 (Figure 20), the maximum melt input is achieved on Day 40 (equivalent to 10th July) of the run, with another very similar peak at Day 57 (27th July). For SummerDaily17 (Figure 21), the melt peak is Day 56 (26th July). What this suggests is twofold: first, that there is a lag of around 20 days for the full impacts of peak melt to feed through the entire subglacial system, including temporary storage and slow flow in the distributed sheet, and second, that one day of higher melt, i.e. a peak, is less important for building an extensive channelised drainage system than a sustained period of higher melt. The importance of storage is further exhibited by the strong correlation we find between it and surface melt – 0.67 for SummerDaily12 and 0.77 for SummerDaily17 – indicating that much of the excess meltwater on high-melt days is impounded for a time, rather than transiting the subglacial drainage system. Note that, for both daily-forced runs, the maximum system extent occurs near the end of a period of sustained higher surface melt and is not replicated by similar shorter periods of higher melting that happen earlier or later in the melt season.

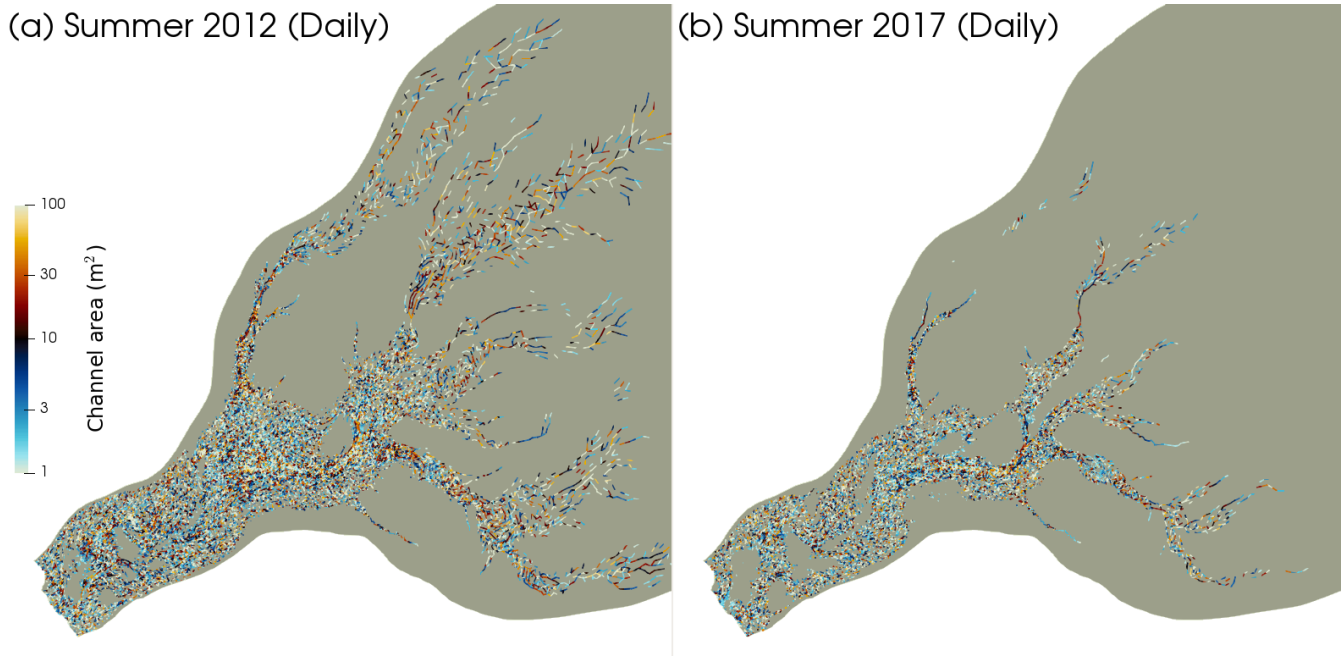

Figure 22 – Maximum extent of channelised subglacial drainage in (a) SummerDaily12 run on July 31st and (b) SummerDaily17 run on August 14th. It is instructive to compare these two panels with panels (c) and (d) of Figure 18 to show the variability of the channelised system over a melt season.

5.5.3. Summer plume activity

Turning to how these seasonal changes in the subglacial drainage system impact plume activity at the calving front, an interesting outcome is that the average melt rate in the SummerAverage17

model run is more than double that found in the Winter simulation, while the mean maximum melt rate is over six times higher (Table 5). Similarly, in SummerAverage12, the average melt rate is nearly four times greater than in Winter, whereas the mean maximum melt rate is nearly eight times higher (Table 5). Clearly, the much greater freshwater flux in either summer compared to winter is preferentially enhancing maximum melt rates compared to average melt rates. The explanation lies in the changing structure of the hydrological system: the greater degree of channelisation in summer leads to larger, more localised plumes at the expense of the more diffuse, primarily distributed-sheet-discharge-driven plume extending the length of the calving front. In other words, the extra water is preferentially concentrated by channels at a few points, rather than being spread out evenly over the entire width of the front. This is borne out by Figure 17, where several substantial localised plumes are visible in summer (panels b-e), instead of a more uniform strengthening of the winter melting pattern (panel a) across the entire front. The larger, more localised plumes in summer drive much more melting in their immediate vicinity, hence the higher modelled maximum melt rates in summer, but leave the remaining calving front comparatively less affected by plume-induced melting, reducing their impact on the modelled average rates. The latter is corroborated by Slater et al. (2015), with respect to the relative impacts of distributed and channelised drainage systems on plume melt rates. This pattern would also serve to promote calving by enhancing localised concentrated melting from plumes, creating a more indented and less stable calving front, as posited by Todd et al. (2019) with regards to calving behaviour at Store. Todd et al. (2019) further suggest that this pattern could be enhanced by longer or warmer summers, a suggestion supported by our findings in this study of greater plume activity in the warm summer 2012 compared to the cool summer 2017 (Figure 17).

This enhancement in plume melting is slightly reduced in both daily-forced runs (SummerDaily12 and SummerDaily17) (Figure 17d, e), though much more noticeably with regard to the mean maximum than the average rate, which we relate to the greater variability of meltwater forcing reducing the activity and lifespan of the largest plumes compared to the average-forced runs (SummerAverage12 and SummerAverage17). Overall, though, the pattern of greater localised melt driven by channel formation remains strong in the daily-forced runs. Identifying whether more rapid, more focused channel-driven melting or slower, more diffuse distributed-sheet-driven melting is more important for calving and glacier dynamics is currently a subject of debate and one we hope to investigate in future work, though, as described above, recent work by Todd et al. (2019) suggests the former, which promotes high localised melting and calving-front instability, is of greater importance. It is also important to note that our mean maximum plume melt rates for all summer simulations (Table 5) accord well with the observed summer melt rate at Store of 3.4 ± 0.7 m d^{-1}

from Chauché (2016), measured using side-scan sonar in summer 2012, and with other modelling studies for Greenlandic glaciers (Xu et al., 2013).

This slight reduction in concentration of melt in the largest plumes in the daily-forced runs also explains the very slight increase in total plume-induced melting (on the order of 2%) found compared to the average-forced runs, as the marginal favouring of the distributed sheet-driven plume spreads higher melt rates over a larger area. However, the difference is very small, and suggests that, if operating glacial hydrological models at longer temporal and/or larger spatial scales, averaged inputs yield similar outputs to daily-resolution data. Whether this remains the case in a fully-coupled simulation would be an interesting target for future work.

The summer plume results also reinforce the point made in Section 5.5.1, above, about the importance of the depth of the grounding line for plume activity. There are many areas of strong plume melt towards the centre of the calving front (Figure 17, Figure 23), where subglacial discharge is quite low (Figure 18, Figure 19, Figure 22), but the warmer, more saline water at the greater depths (>400 m) reached in this region of the front (Figure 15) still allow high plume melting to occur without needing much meltwater input. Conversely, despite higher meltwater discharges nearer the margins, the relatively shallow fjord depth and, therefore, colder, fresher ambient conditions (Figure 15) limit the amount of melting the resulting plumes can achieve. From our model results, consequently, it is clear that the presence and location of warm, saline water in the fjord is equally important for generating plume melt as is sustained subglacial meltwater discharge, in line with buoyant plume theory (Jenkins, 2011; Slater et al., 2016).

A further possibility for validation is provided by the location of the plumes: visible plumes at Store have been observed persistently about 2 km in from the southern margin of the terminus (i.e. about one third in from the right of Figure 17) and intermittently in the northern embayment (a similar distance in from the left of Figure 17) (Ryan et al., 2015). Our model predicts the intermittent northern plumes well, but does not produce a persistent plume at the observed location on the southern half of the terminus. Rather, the modelled plumes are more mobile and do not persistently

occupy one location, with several hotspots of plume activity in the southern half of the terminus (Figure 23). The reasons for this are considered in Section 5.5.5, below.

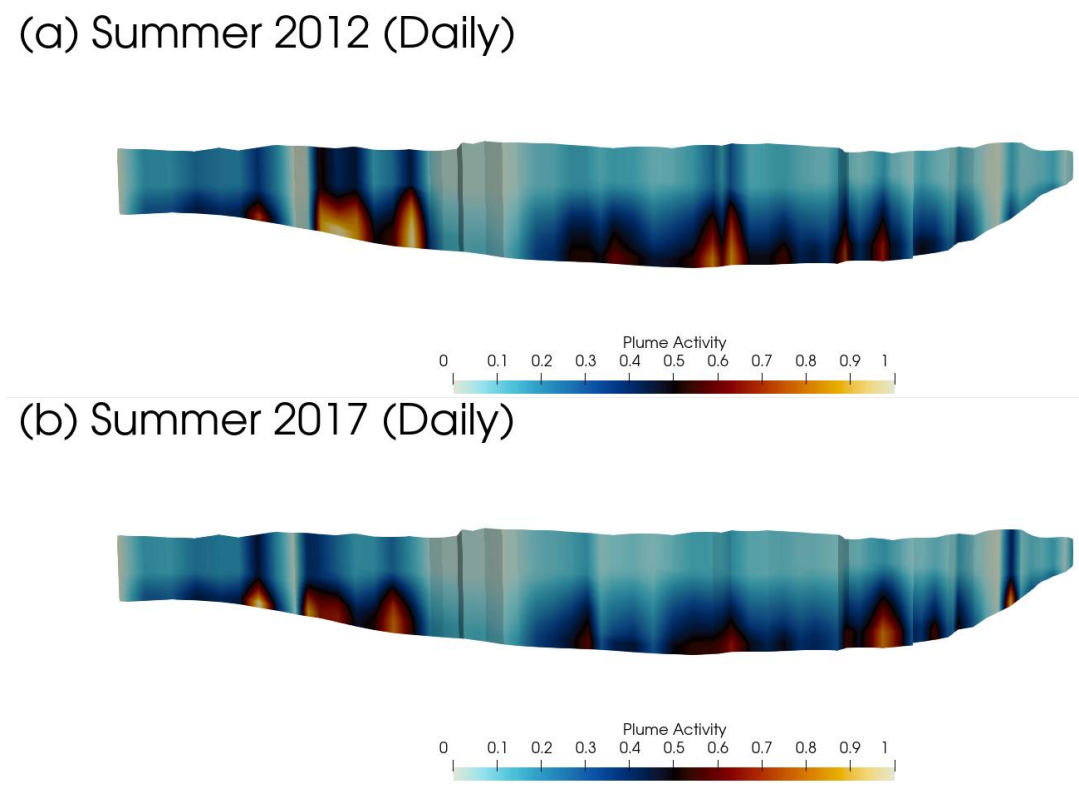

Figure 23 – Heat map of plume activity in (a) SummerDaily12 and (b) SummerDaily17 simulations. Areas with a value of 1 show the highest mean plume melt rates across the entire length of the model run; areas with a value of 0 show no plume activity at any point.

The relationship between plume activity and surface-melt variability is also critical to simple parameterisations of submarine melting. Many studies based on buoyant plume theory or high-resolution ocean modelling show a sublinear relationship between subglacial runoff and submarine melting, that is submarine melt rate is proportional to runoff raised to some power 0.25-0.9 (Jenkins, 2011; Slater et al., 2016; Xu et al., 2013). However, when considering surface melting, many studies assume a direct relationship between this and subglacial discharge, and, consequently plume melting (e.g. Carroll et al., 2016; Mankoff et al., 2016; Stevens et al., 2016; Slater et al., 2019). A scatter plot of surface melting versus submarine melting for our SummerDaily17 simulation does not, though, show a strong relationship of this form (Figure 24). Linear regression suggests surface melting explains only 21% of variability in plume melting (39% for 2012). We therefore propose that the structure of the subglacial drainage system and the associated water storage play a crucial role in mediating and smoothing water delivery to the calving front, such that variation in plume activity is only partially relatable to peaks and troughs in surface meltwater production. This mediating role of the hydrological system appears in this case to obfuscate a simple relationship between surface

and plume melt. This chimes with the important role assigned to subglacial and englacial water storage by the outcomes of the SHMIP process (de Fleurian et al., 2018).

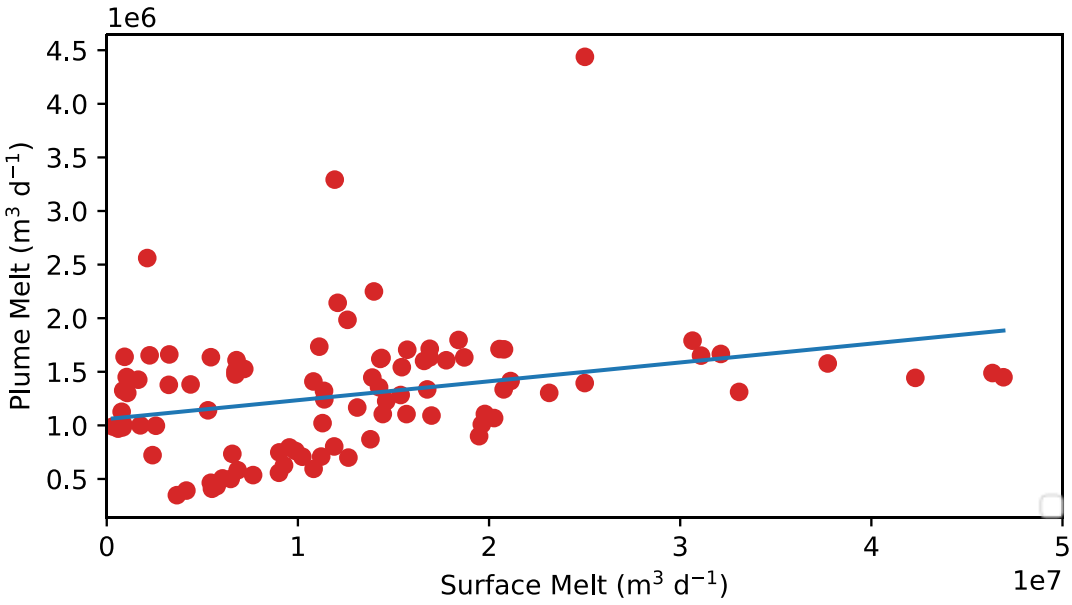

Figure 24 – Scatter plot of surface melt versus plume melt for SummerDaily17 run, showing low correlation. The line of best fit is shown in blue.

5.5.4. Implications for glacier dynamics

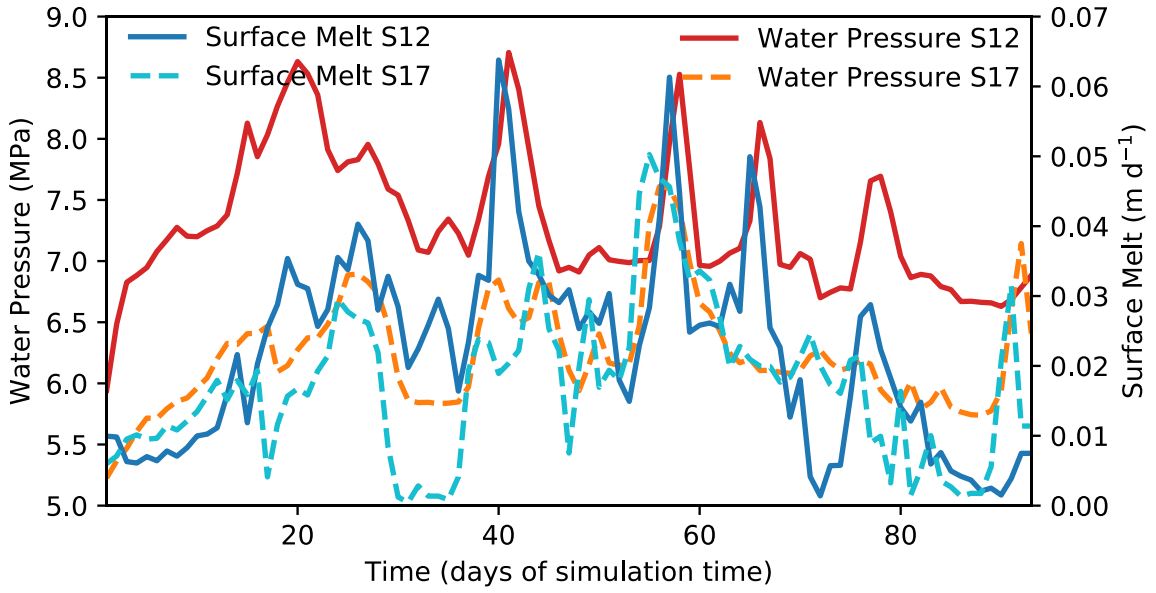

Figure 25 – Time series showing comparison between average water pressure (left axis) and surface melt (right axis) for SummerDaily12 (solid lines) and SummerDaily17 (dashed lines) model runs. Note the correlation between surface melt and water pressure.

Although daily-scale changes in surface melt are poorly correlated with plume activity at the calving front, they do show a close relationship with other aspects of the hydrological system. This is shown by Figure 25, which displays the domain-averaged water pressure versus the domain-averaged surface melt for the SummerDaily12 and SummerDaily17 runs. Peaks in surface melt are lagged by peaks in water pressure, usually by one day of model time, throughout the simulation. The correlation coefficient is 0.67 for SummerDaily12 and 0.77 for SummerDaily17, confirming the strength of this relationship.

One final point of interest is that, despite the greatly increased channelisation evident in the SummerAverage12 and SummerAverage17 model runs compared to the Winter run, modelled effective pressures decrease (i.e. modelled water pressures increase) in summer compared to winter, contrary to expectation (Meierbachtol et al., 2013). Given that we are not coupling the hydrology to the ice flow in this study, we will not address the implications for the flow of Store, save to make two brief points. The first is that modelled effective pressures are higher (i.e. modelled water pressures are lower) in the SummerDaily12 and SummerDaily17 runs than in the SummerAverage12 and SummerAverage17 runs, which suggests that the much lower effective pressures found in the latter runs are partly an artefact of the seasonally averaged surface-melt forcing. The second is that, looking at the maximum extent of the hydrological system in the SummerDaily12 run, we find lower effective pressures (i.e. higher water pressures) than for the maximum extent of the SummerDaily17 run, despite having a larger and more extensive low-pressure channel network. This perhaps indicates that even the record levels of melt in 2012 were unable to generate a low-pressure channel system of sufficient extent to evacuate all the water efficiently. If there is a melt threshold at which a fully efficient subglacial drainage system can develop at Store, it must therefore likely be at a level of melt not yet reached. Investigating what effect these hydrological changes have on ice dynamics at Store will be a focus of future work

5.5.5. Limitations and future work

One limitation of this study is the lack of two-way coupling between ice flow and subglacial hydrology, the fixed ice geometry and absence of calving processes. This simplification was used to allow us to focus purely on the evolution of the subglacial hydrological system under different forcings, inside a state representative of the long-term state of Store, and greatly reduced the computational cost of the study. Given four decades of stability of Store (Rignot et al., 2015), we also feel this is a reasonable simplification to make. Consequently, we have focused our discussion on the structure and behaviour of the hydrological system, rather than speculating as to the likely impacts of this behaviour on ice flow, which would require a fully coupled study to investigate.

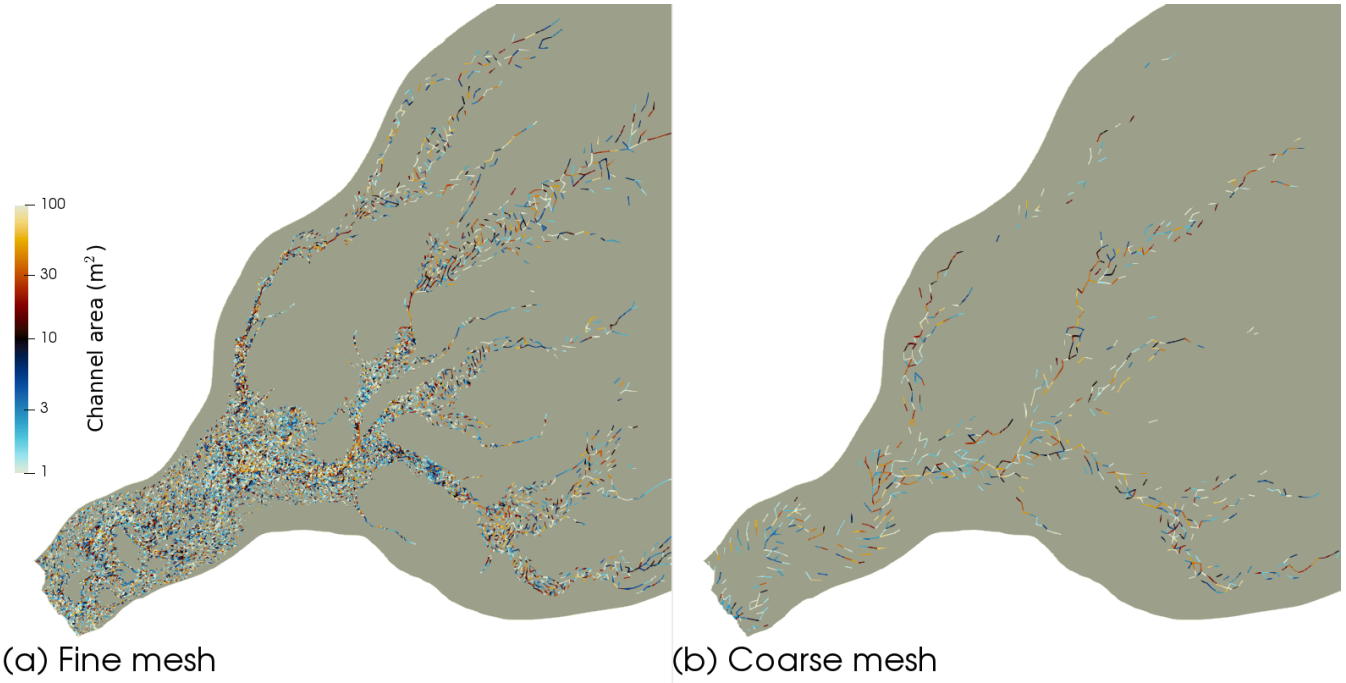

Figure 26 – Comparison of hydrological model results for different mesh resolutions. (a) The standard, fine mesh described in Section 5.3.3.; (b) a coarser, 500 m-resolution mesh. Note that the overall layout of the channel network is virtually identical between the two.

As can be seen from the description in Section 5.3.3., the hydrological model results are also ultimately dependent on the mesh. We consider that the fine resolution of the mesh throughout the area of high water flux obviates this problem. Figure 26 further shows a comparison between the results from the hydrological model for the SummerAverage12 simulation – Figure 26a shows the results on the standard mesh used for all simulations and described in Section 5.3.3.; Figure 26b shows the same results calculated on a mesh of constant 500 m resolution. As can be clearly observed, the overall pattern of the channel network remains similar between the two meshes, though, evidently, the detail of which individual channel segments are most important varies, as there are simply far fewer flow paths available on the coarser mesh. Overall, this gives us confidence that the pattern of our findings is robust, though it does caution against over-interpreting the fine details. This is further supported by the mesh dependency analysis undertaken by Werder et al. (2013) for GlaDS, which shows little variation in results in the presence of realistic topography.

Another model limitation is the simplified grounding line, which impacts our plume results. In reality, the area of high plume activity at the deepest part of the calving front (Figure 17, Figure 23) might form one single plume that would reach the surface, an effect that the model would likely reproduce with a more realistic grounding line. The model also shows a tendency for the plume activity in that region to migrate towards the centre of the calving front over the course of the simulation, which is also likely due to the simplified grounding line used in this study. Both these effects occur because

the observed grounding line for the deeper, southern side of the terminus is a kilometre or so inland from the calving front. Even though it is small, this floating section could interrupt the water flow from the southern part of the terminus towards the centre (Figure 18) and therefore shift the area of modelled enhanced plume activity back to its observed position and concentrate the discharge more stably. With the simplified setup in this study, the hydrological system oscillates between several potential stable states in the region of low hydraulic gradient immediately behind the calving front, similar to behaviour inferred from seismic observations on similar regions in real glaciers (Vore et al., 2019). We have therefore generally confined our discussion of plume melt to average values, which are less dependent on any one specific pattern of plume activity, rather than over-interpreting such patterns. Including a full representation of the grounding line to mitigate these issues and be able to realistically investigate how plume discharge locations move over time will be part of our future work on this model.

Finally, the plume model relies on several poorly-known parameters, which result in a high degree of uncertainty around the resulting melt rates. In particular, the heat and salt transfer coefficients, which determine the rate at which heat is transferred from the ocean to the ice, are very poorly constrained. This results from the extreme difficulty of directly observing submarine melt rate at tidewater glaciers simultaneously with all of the other factors affecting submarine melting, such as fjord conditions and circulation, and grounding-line subglacial hydrology. Until better observations are available to place constraints on models, the absolute values of melt rates in studies such as this should be viewed with caution. On the other hand, relative comparisons of melting, for example from location to location on a calving front (Figure 17) or between two seasons or time periods (Table 5) are more robust with regards to this uncertainty. It is also our hope that models such as ours will help to reduce these prevalent uncertainties on melting through improving understanding of near-terminus subglacial hydrology. A similar problem applies to the parameters used for GlaDS – observational difficulties mean they are currently poorly constrained, but we hope to improve this by undertaking a full validation exercise, through comparison with an independently derived dataset of calving events at Store, upon the completion of development of a coupled ice-hydrology-plume-calving model, which is the focus of our future work.

5.6. Conclusion

We present the first coupled hydrology-plume model applied to a tidewater glacier in Greenland, allowing us to investigate aspects of the subglacial hydrology of Store Glacier critical to ice dynamics and calving-front melting that are poorly constrained by existing observations and models. We demonstrate that the implementation of the GlaDS hydrological model within the Elmer/Ice

modelling suite shows promise in realistically recreating the observed behaviour of the subglacial drainage system of Store (Chauché, 2016; Doyle et al., 2018; Young et al., 2019), giving us greater confidence in its use as a predictive tool.

By modelling the seasonal changes in the subglacial hydrology of Store, we explore how discharge drives convective plumes that melt the submerged portion of the terminus. We find an active subglacial drainage system, with small channels and a distributed sheet extending up to 45 km inland in winter, which drives substantial plume activity across the calving front, with localised melt rates of up to 1.1 m d^{-1}. This means the freshwater flux is non-zero in winter, at 5.96 m^3 s^{-1}, which contrasts with assumptions of zero winter freshwater flux at tidewater glaciers in previous work. In summer, when surface melt is incorporated as an input to the drainage system, the drainage system extends up to 65 km inland, the distance inland that surface melting occurs, though significant channelisation only reaches up to 55 km. The more-developed channel system intensifies the activity of large plumes at the front, thereby raising the maximum rate of plume-induced melting to 12.6 m d^{-1}. However, the concentration of water in fewer larger channels also leaves a large portion of the calving front exposed to only a weak plume, such that average plume melt rates increase by a much smaller factor compared to winter.

Overall we find plume melting to increase the freshwater flux into the fjord by 58% in winter, when the basal drainage system predominantly carries water produced by friction at the bed. In summer, when the basal drainage system also carries surface melt, plume melting increases the freshwater flux by only about 5%, on average, although it represents a higher absolute value. Overall, we find the freshwater flux to be 9.44 m^3 s^{-1} in winter, with contributions of 42% and 58% from basal meltwater production and plume-induced melting, respectively. In summer 2012, the contributions were 95% from surface and basal meltwater production and 5% from plume melting; and in 2017 91% and 9%, respectively.

We also demonstrate that peaks in surface melt are not well-correlated with peaks in plume melt, nor are they the dominant force in determining the maximum extent of the subglacial hydrological system, which is instead defined by longer periods of sustained melting. Finally, we show that basal water pressures in our model were higher during the record warm summer in 2012 compared to 2017 when surface conditions were close to the decadal average. Modelled effective pressures therefore suggest that the high melt inputs in 2012 did not form a fully efficient subglacial drainage system even though the latter extended 55 km inland. This indicates that channel formation may not fully negate the lubricating effects of high melt on ice flow. Future work will aim to couple ice flow

and calving with the hydrology in order to simulate the dynamic effects of changes in water inputs and plume melting.

5.7. Acknowledgements

The research was supported by the European Research Council under the European Union's Horizon 2020 Research and Innovation Programme. The work is an output from grant agreement 683043 (RESPONDER). SJC also acknowledges financial assistance in the form of a studentship (NE/L002507/1) from the Natural Environment Research Council. The authors thank Marion Bougamont, Tom Cowton and Thomas Zwinger for productive discussions, as well as Olivier Gagliardini for support with numerical and Brice Noël who provided the RACMO data. DEMs provided by the Polar Geospatial Center under NSF-OPP awards 1043681, 1559691, and 1542736. DS acknowledges funding from NSF OPP-1418256.

6. Fully Coupled Investigation of Store Glacier

'As they came to the gates Círdan the Shipwright came forth to greet them. Very tall he was, and his beard was long, and he was grey and old, save that his eyes were keen as stars; and he looked at them and bowed, and said: "All Is now ready."'

-The Lord of the Rings, Book 6, Ch. IX

This chapter presents a set of experiments undertaken using the fully coupled ice-flow-calving-subglacial-hydrology-plume model, an uncoupled version of which is presented in Chapter 5.

The work presented in this chapter has been written up for submission to the *Journal of Geophysical Research: Earth Surface*, and, as such, the text of this chapter is taken directly from the prepared manuscript. A methods section is therefore included, which recapitulates some of the more detailed information in Chapters 3 and 5. References to Cook et al. (2020) refer to the published paper included as Chapter 5 in this thesis. All work presented in this chapter was undertaken by S. Cook with guidance from J. Todd and P. Christoffersen. J. Todd and P. Christoffersen provided feedback on the wording of the text and the presentation of the results. S. Cook, P. Christoffersen and J. Todd designed the experiments. S. Cook also developed the model code and executed the experiments with contributions from J. Todd, P. Christoffersen. S. Cook analysed the model outputs and wrote the manuscript.

6.1. Abstract

We present the first fully coupled model of a tidewater glacier, incorporating ice flow, calving, subglacial hydrology and plume melting, and apply it to Store Glacier, Greenland. We simulate a year of high melt (2012) and a year of low melt (2017) to examine differences in the behaviour of the glacier in these two scenarios. We validate the model by comparison to a range of observations gathered at Store Glacier, and compare its results for the hydrological system to those derived from a previous study using a simpler model. We find that the model is generally consistent with observations and makes clear the importance of terminus velocity as a large-scale control on calving event frequency. We also show the high temporal variability of calving and the consequent difficulty of deriving a simple calving law without long-term observational datasets. In terms of modelled hydrology, we find results consistent with previous work, but which highlight the importance of the ice-velocity-hydrology feedback in suppressing channel growth under thicker ice inland and in driving changes in terminus behaviour, including calving. We suggest that 2012 marks a melt threshold at which Store Glacier begins to exhibit a fully channelised drainage system at the terminus, but that this can be countered by higher water pressures and velocities inland. Overall, we

show the spatially variable nature of the coupled ice-hydrology system and its importance in determining the behaviour of the terminus and thus calving. The fully coupled nature of the model allows us to also demonstrate the likely lack of any hydrological or ice-dynamic memory at Store, with both years showing very similar glacier states at the end of the runs.

6.2. Introduction

The Greenland Ice Sheet (GrIS) is currently experiencing mass loss of 286±20 Gt a^{-1}, of which 44% is due to discharge from tidewater glaciers (Mouginot et al., 2019). Such glaciers drain 88% of the GrIS (Rignot and Mouginot, 2012), making their dynamical behaviour an important target of study when assessing the current and future state of the GrIS. The GrIS is now contributing nearly 1 mm a^{-1} to sea-level rise (IPCC, 2019), a significant increase from a stable state 40 years ago (Mouginot et al., 2019); hence, predicting this future behaviour and the ensuing change in sea level is only becoming more urgent.

However, Greenlandic tidewater glaciers present a challenging environment, leaving many important processes poorly understood. The thickness (typically hundreds of metres or more) and speed (often several kilometres a year) of the ice make access to the basal environment very difficult; only a couple of studies have reported direct borehole observations of the base from such glaciers (Doyle et al., 2018; Lüthi et al., 2002) and studies of their subglacial hydrology (e.g. Schild et al., 2016; Sole et al., 2011; Vallot et al., 2017) and basal conditions (e.g. Hofstede et al., 2018) are far fewer in number than on land-terminating portions of the ice sheet (e.g. Davison et al., 2019; Sole et al., 2013; Tedstone et al., 2015, 2013; Williams et al., 2020). This means characterisation of the physical basal properties and subglacial hydrology of Greenlandic tidewater glaciers is very limited. At the same time, observations of behaviour and morphology at the calving front are also limited, both in Greenland and globally, due to the dangerous and inaccessible nature of the environment, meaning calving and submarine-melt processes are also poorly constrained by the available data. Recent work has started to improve this situation (e.g. Cassotto et al., 2018; Jackson et al., 2019, 2017; Sutherland et al., 2019; Vallot et al., 2019; Xie et al., 2019), particularly with regards to observations of meltwater plumes at the calving front (e.g. Hewitt, 2019; Jackson et al., 2019, 2017; Jouvet et al., 2018; Slater et al., 2018), but, overall, many aspects of tidewater glaciers remain under-observed and poorly characterised.

Computer modelling provides an avenue for ameliorating this lack of direct observations and for predicting the future behaviour of Greenland's tidewater glaciers, but the complexity of these systems has made it difficult to implement realistic fully coupled models. Simulating calving is particularly challenging, as the development of a simple calving law, if one is achievable, remains

elusive (Benn et al., 2017a; Benn and Åström, 2018), requiring the use of computationally expensive full-Stokes, 3D models to reproduce calving with any degree of realism (Todd et al., 2018, 2019). Introducing and coupling subglacial hydrology and meltwater plumes, perhaps the two most important additional and under-observed sets of processes, to such models adds a further layer of computational complexity, meaning that attempts to simulate the full tidewater-glacier system have hitherto only studied selected processes in an uncoupled manner in order to keep the computation time within reasonable limits (Vallot et al., 2018). Such models are also difficult to validate, owing to the number and variety of input datasets meaning that finding a fully independent validation dataset is not necessarily straightforward.

However, growth in computational power means that developing and running a fully coupled model of a tidewater glacier is no longer impractical, allowing greater insight into the behaviour of these systems. This study therefore presents a fully coupled model of ice flow, calving, subglacial hydrology and convective meltwater plumes within the 3D, full-Stokes Elmer/Ice modelling suite, with application to Store Glacier (henceforth referred to as Store) in west Greenland. Validation of the model is undertaken by comparison to observational evidence from Store. This paper builds on the calving model presented in Todd et al. (2018), with the addition of subglacial hydrology and convective plumes, as presented in Cook et al. (2020), to develop a fully coupled model of Store that includes the primary glaciological processes and simulates the resulting glacier behaviour, revealing the complex coupled nature of Store.

6.3. Data and Methods

The study site (Section 6.3.1), model set-up (Section 6.3.2) and overall modelling procedure (Section 6.3.3) are described below. Details are included on how the individual model components are coupled within the overall framework of Elmer/Ice (Gagliardini et al., 2013) and how the model was spun up.

6.3.1. Study Site

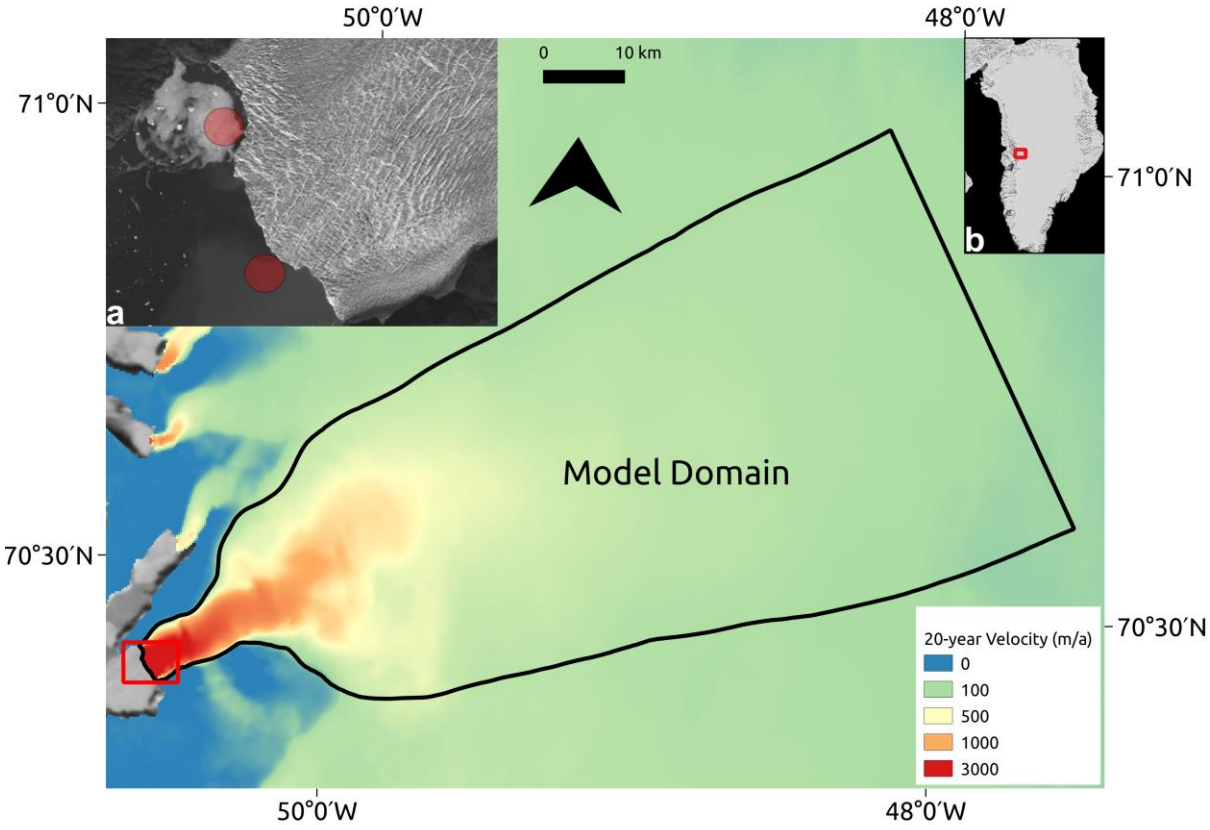

*Figure 27 – Model domain of Store (main image). Background shows the 20-year velocity average from the MEaSUREs dataset (Joughin et al. 2016, 2018). Inset **a** shows a zoomed-in view of the terminus (red rectangle in main image). Red circles show approximate areas of observed surfacing plumes. Background shows Landsat view of Store. Inset **b** shows Store's location (red rectangle) in Greenland. Background image from MODIS.*

Store (*Sermeq Kujalleq*), one of the largest tidewater outlet glaciers on the west coast of Greenland (70.4°N, 50.55°W), flows into Ikerasak Fjord (*Ikerasaup Sullua*) at the southern end of the Uummannaq Fjord system (Figure 27). The calving front is 5 km wide, with surface velocities reaching up to 6600 m a^{-1} (Joughin, 2018). The terminus is pinned between narrow fjord walls and a sill on the sea floor, making the terminus position relatively stable despite the trunk of the glacier flowing through a deep trough extending to nearly 1000 m below sea level (Rignot et al., 2015). With no observed retreat since 1985 (Catania et al., 2018), the glacier represents a stable Greenland outlet glacier and is an ideal target for modelling studies aiming to understand the 'natural' state of a tidewater glacier, i.e. one that is currently in a stable terminus position. Store could, however, retreat rapidly should increasing melt force the terminus backwards from its current pinning point (Catania et al., 2018).

6.3.2. Model set-up

In this study, we use the open-source, 3D, full-Stokes Elmer/Ice modelling suite (Gagliardini et al., 2013), which includes the GlaDS hydrological model (Werder et al., 2013). Cook et al. (2020) described the coupled use of GlaDS and a 1D plume model to investigate the subglacial hydrology of Store, with only unidirectional coupling with the overlying ice. We build on that study by the addition of the calving model detailed in Todd et al. (2018) and the implementation of two-way coupling between the overlying ice and the subglacial hydrology. Hence, our model effectively couples ice flow with evolving hydrological drainage, convective plumes driven by subglacial freshwater discharge, undercutting of the terminus and calving, providing coupling between all the components and an evolving glacier geometry. Model components, parameters, meshes and boundary conditions are the same as detailed in Cook et al. (2020), but are detailed below for ease of reference. A schematic representation of the major model components is shown in Figure 28.

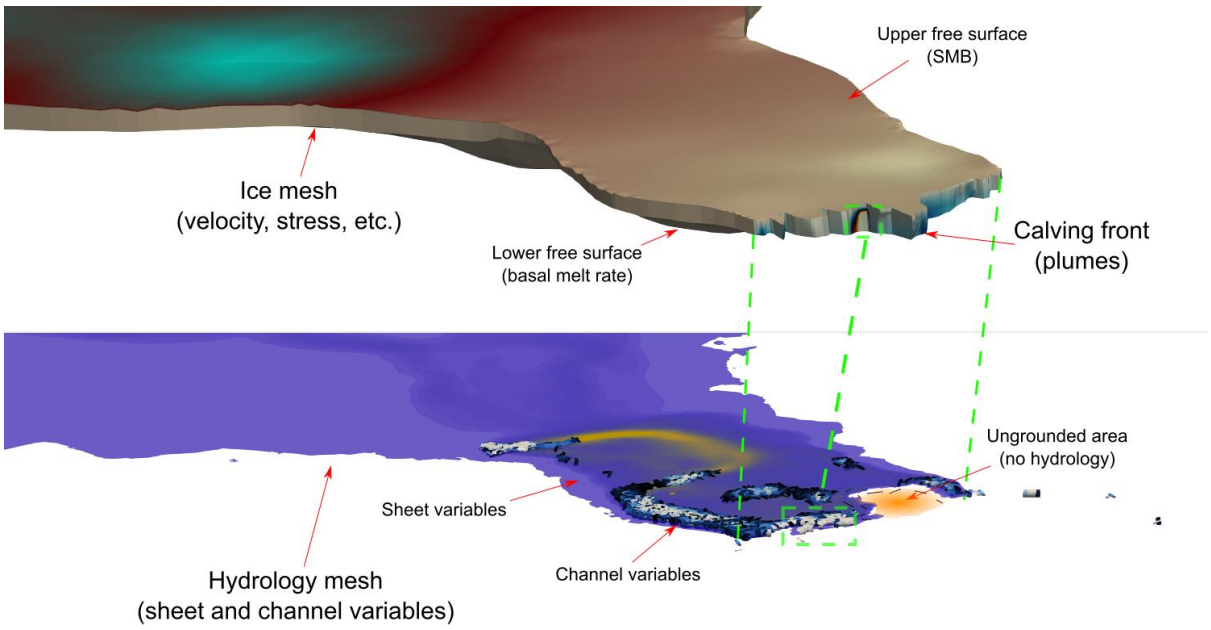

Figure 28 – Schematic of the Store Glacier model domain in Elmer/Ice with surface mass balance and terminus melting (top mesh), and sheet discharge and channel area (bottom mesh) shown in colour. Green dotted lines show points of correspondence on the two meshes. Note the dotted green rectangles that show an example of a plume simulated at the calving front and the channels simulated on the hydrology mesh that are feeding it; these channels line up with areas of simulated higher sheet discharge. The extended mesh domain of the hydrology mesh is to ensure that the hydrology can track the glacier terminus if it advances.

6.3.2.1. Ice flow and calving model

This study uses the 3D, full-Stokes ice-flow model Elmer/Ice (Gagliardini et al., 2013), implementing calving as described by Todd et al. (2018, 2019). The upstream limit of the model domain is taken as

the 100 m a^{-1} velocity contour, and a boundary condition specifying observed velocity is imposed on the inflow boundary. A no-slip condition is imposed on the lateral boundaries, and flow is also prevented through these boundaries. To allow better and more realistic representation of glacier flow near the terminus, we apply a Glen enhancement factor of 6.0 along observed shear lines on the lower trunk where ice flows into the sea, and a sea-water pressure condition was imposed on the calving front and its base.

The glacier terminus is allowed to float where the ice thickness is small enough to permit it, which makes the simulation of the grounding line more realistic than in our previous study (Cook et al., 2020). The addition of this set of processes also means that three free surfaces are present and allowed to evolve throughout each simulation. The upper free surface is subject to a surface mass balance (SMB) accumulation flux (which may be negative, representing ablation) boundary condition, varying daily to provide realistic mass forcing for the model. This is taken from RACMO 2.3p2 data (van Wessem et al., 2018). The bottom free surface consists of any parts of the glacier terminus that have become ungrounded, and to which a seasonally varying basal melt rate of 2.3 m d^{-1} in winter and 4.2 m d^{-1} in summer is applied, following Todd et al. (2018).

We also apply an ice mélange forcing as back pressure to the calving front. Following Todd et al. (2018), the mélange is deemed to develop on 1st February and last until 29th May in 2012 and 8 July in 2017, when it was observed to break out. The backstress provided by the mélange is applied with a constant value of 45 kPa over a thickness of 75 m, which is less than the 120 kPa assumed by Todd et al. (2018), but in good agreement with the backstress estimated by Walter et al. (2012) for Store and also the intermediate forcing scenario described by Todd et al. (2019).

The ice mesh was refined to reach the maximum resolution of 100 m near the calving front, coarsening gradually to 2 km beyond 20 km inland. More detail on the mesh is provided in Cook et al. (2020). Finally, the frontal free surface is allowed to advance and retreat with variations in ice flux and calving, as well as being forced by the melt rates applied from the implementation of a convective plume model as described in Cook et al. (2020) and summarised below.

6.3.2.2. Subglacial hydrology

Store's subglacial hydrology is modelled using the GlaDS (Glacier Drainage System) module within Elmer/Ice. Full details of the model are available in Werder et al. (2013), and its implementation in this context is detailed in Cook et al. (2020). GlaDS simulates an inefficient sheet drainage layer and an efficient channelised network (Figure 28), allowing the drainage to evolve as meltwater inputs change. Switching between the two types of drainage is triggered by localised concentrations of water in the sheet.

GlaDS is run on a separate 2D mesh distinct from the 3D ice-flow mesh, but replicating its footprint. This allows a finer GlaDS mesh resolution, starting at 100 m in the lowermost 20 km of the domain and coarsening to 2 km only in the uppermost portion of the domain, beyond 100 km from the front. In terms of boundary conditions, channels are not allowed to form along any of the boundaries of the hydrology mesh and no water flow is assumed or permitted to occur across the lateral or inflow boundaries. As in Cook et al. (2020), the hydraulic potential (ϕ) is set to 0 at the calving front (i.e. we assume the calving front is at flotation), following Eq. (18) and (19):

$$\phi = \rho_w g Z + P_w \tag{18}$$

$$P_w = \rho_w g (Z_{sl} - Z) \tag{19}$$

Where ρ_w is the density of water at the calving front (i.e. of seawater in this case), g is the gravitational constant, Z is the elevation with respect to sea level, P_w is the water pressure, and Z_{sl} is sea level. In the case where Z_{sl} is set at 0.0, as it is here, and Z is negative, which will be true for the outflow of the subglacial hydrological system at the bottom of the calving front, it can be seen that substituting Eq. (19) into Eq. (18) will give a result of 0 for ϕ.

Boundary conditions are also applied to all fjord-connected ungrounded areas setting all hydrological variables to 0, as water that reaches these areas has left the grounded subglacial hydrological system that GlaDS models and entered the fjord. Water pressure, however, is set equal to Eq. (19). Input to the hydrological system is provided using surface runoff data from RACMO 2.3p2 (van Wessem et al., 2018).

The parameters for GlaDS are those from Cook et al. (2020) and are shown in Table 6. The sensitivity of GlaDS to these parameters is explored in Werder et al. (2013) and is not considered further here as it is beyond the scope of this study.

6.3.2.3. Plume model

The plume model used in this study is based on buoyant plume theory (Jenkins, 2011; Slater et al., 2016) and is identical to the 1D model used and detailed in Cook et al. (2020). The model simulates a continuous sheet-style 'line' plume across the width of the calving front, split into continuous segments centred on each grounding-line node on the ice mesh. This plume geometry is supported by the limited observational data available for tidewater glaciers (Fried et al., 2015; Jackson et al., 2017).

Table 6 – Parameters used in GlaDS model for all model runs in this study.

Description	Symbol	Value	Units
Pressure melt coefficient	c_t	$7.5 \cdot 10^{-8}$	K Pa^{-1}
Heat capacity of water	c_w	4220	J kg^{-1} K^{-1}
Sheet flow exponent	α_s	3	
Sheet flow exponent	β_s	2	
Channel flow exponent	α_c	5/4	
Channel flow exponent	β_c	3/2	
Sheet conductivity	k_s	0.0002	m s kg^{-1}
Channel conductivity	k_c	0.1	$m^{3/2}$ $kg^{-1/2}$
Sheet width below channel	l_c	20	m
Cavity spacing	l_r	100	m
Bedrock bump height	h_r	1	m
Englacial void ratio	e_v	10^{-4}	

The input to the plume model is provided by subglacial discharge derived as the sum of channel and sheet discharge from GlaDS at each grounding-line node on the hydrology mesh. The resulting melt rate profiles are then applied to the frontal boundary of the ice mesh. Winter and summer data on oceanographic conditions (temperature and salinity) in the fjord are taken from conductivity-temperature-depth casts made near the calving front as described in Cook et al. (2020) (see also Figure 15).

6.3.2.4. Model coupling

In contrast to the one-way coupling used by Cook et al. (2020) to study the formation of channelised basal networks at Store, we implement a full two-way coupling between the hydrological systems and ice flow and calving, which changes the frontal geometry when icebergs break off. This coupling is achieved in three steps. Firstly, as described above, plume melt rates are applied as a forcing to the terminus of the glacier, influencing its geometry and velocity due to undercutting. Secondly, the modelled basal water pressure is used to predict the opening of basal crevasses, which play a major role in the model's calving mechanism, as described previously (Todd et al., 2018). Thirdly, a Coulomb-type sliding law (Gagliardini et al., 2007) is implemented to link ice velocities to the effective pressures in the hydrological system. This sliding law takes the form:

$$\tau_b = SN\left[\frac{\chi u_b^{-n}}{(1+a\chi^q)}\right]^{\frac{1}{n}} u_b$$

(20)

Where

$$a = \frac{(q-1)^{q-1}}{q^q}$$

(21)

And

$$\chi = \frac{u_b}{S^n N^n A_s}$$

(22)

Where S is a constant equal to the maximum bed slope of the glacier (here set to 0.9); n is a constant, typically equal to 3 (this is the constant from Glen's flow law), the value used here; q is a constant, typically equal to 1, as used here; and A_s is the sliding coefficient. The value of this coefficient was tuned to provide the best match to observed velocities, being set to 9 x 10^4 m Pa^{-3} a^{-1} beneath the terminus and up to 15 km inland, increasing to 9 x 10^5 m Pa^{-3} a^{-1} beyond 25 km inland, with a linear transition between the two values between 15 and 25 km inland. Sensitivity analysis suggested, however, that the velocity at the terminus of the glacier was relatively insensitive to the value of A_s, as all runs eventually converged towards the same velocity for a wide range of coefficients (not shown).

The model timestep was set to 0.1 days, with the GlaDS and plume models running every timestep. The less-rapidly changing variables on the ice mesh, including determination of calving events and the Stokes and temperature solutions, were only computed every day (i.e. every 10 timesteps) in order to reduce the computation time.

6.3.3. Modelling procedure

6.3.3.1. Model relaxation

Given the complexity of the fully coupled model, relaxation was undertaken in several phases (Figure 29) to allow individual model components to relax before running a fully coupled relaxation as the final step. The workflow was:

- Step 1: Steady-state simulation to obtain a converged temperature-velocity field.
- Step 2: Steady-state inversion from the results of Step 1 to obtain values for the friction coefficient at the base
- Step 3: Transient simulation lasting 10 years where the geometry of the ice was allowed to evolve, using the basal friction field from Step 2. No hydrology, plumes or calving implemented.
- Step 4: Transient simulation lasting 1 year to initialise the subglacial hydrology, using the geometry obtained from Step 3 and the friction field obtained from Step 2. GlaDS and plumes run, but are not coupled to the overlying ice. Calving is not implemented.
- Step 5: Transient simulation lasting 4 years, using the hydrological system obtained from Step 4 and the geometry from Step 3 to relax the coupled hydrology-plumes-ice system. No calving implemented.
- Step 6: Transient simulation lasting 30 years with all model components present and coupled to allow relaxation of the entire system. Calving is implemented.

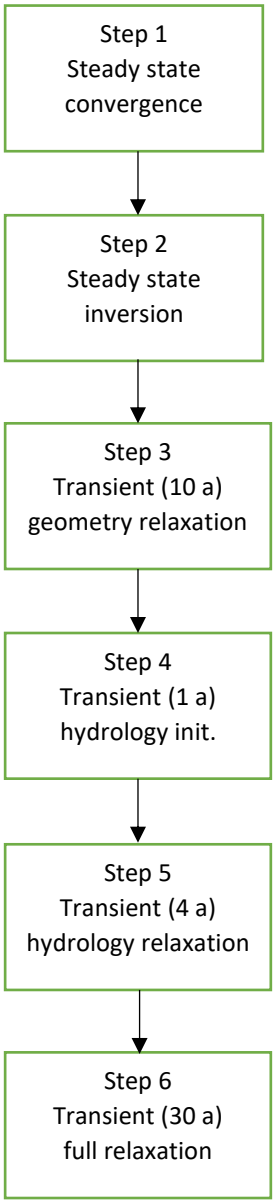

Figure 29 – Flow diagram showing model relaxation procedure in six steps.

Model relaxation steps 1-4 are the same initialisation procedure described in Cook et al. (2020). The fully coupled model (including steps 5-6) is the one described in Section 6.3.2.

6.3.3.2. Model experiments

The relaxation procedure described above was used as the basis for two one-year experiments, aiming to replicate the behaviour of Store in 2012 (a high-surface-melt year) and 2017 (a low-surface-melt year). We choose to simulate Store during these years because 2012 was the warmest year on record while 2017 was a comparatively standard year with a comparatively cool summer. We have previously examined how hydrological systems may have evolved beneath Store during these years (Cook et al., 2020), albeit with no coupling to the ice flow. In this study we explore how

glacier dynamics evolve in a fully coupled 3D full-Stokes model with time-varying basal drainage efficiency, plume-induced frontal melt, and calving. Both runs were started from the end of the last year of relaxation, so any differences between the two runs can be ascribed to the contrasting forcing, rather than dissimilar initial conditions. Experiments were forced with daily-resolution SMB and surface melt RACMO 2.3p2 data (van Wessem et al., 2018) with the assumption that runoff is delivered to the bed in the grid cell below which it was produced. Other datasets used as inputs to the model are the same as those described in Cook et al. (2020).

6.4. Results

This section summarises the key simulation results. Section 6.4.1 presents results related to the subglacial hydrology of Store, to be compared against those shown in Cook et al. (2020). Section 6.4.2 deals with the calving activity simulated by the model. Both sets of results are discussed in Section 6.5.

6.4.1. Subglacial hydrology and ice flow

6.4.1.1 Channel formation and ice-flow response

A key feature of the fully coupled model presented in this paper is the coupling between ice velocity and the underlying hydrological system. This can be seen functioning as expected in the model using results from an inland site near the limit of channel formation between May and September 2012 (Figure 30; location in Figure 31). This far inland (25 km), surface runoff is not produced until the end of May, so the thickness of the inefficient sheet (Figure 30a) and the water pressure (Figure 30b) are consequently flat before this point, with values of 0.025 m and 5.3 MPa, respectively. Velocity (Figure 30a) shows a gentle decline from 670 m a^{-1} to 620 m a^{-1} over the course of May, and there is no channelisation (Figure 30b). As surface melt begins at the end of May, water pressure increases to 7.4 MPa in the first week of June, but this has a very limited impact on velocity as melt levels are still low (<0.2 x 10^8 m^3 d^{-1}, <10 m d^{-1} locally). Velocity thus begins a slow increase, reaching 630 m a^{-1}, as the additional water is absorbed by an increase in sheet thickness to 0.115 m. A second peak in water pressure is then reached about the 20th June following a broad peak in surface melt at 0.5 x 10^8 m^3 d^{-1} (20 m d^{-1} locally), with pressure reaching 7.5 MPa, leading to velocity reaching 650 m a^{-1}, before declining to 640 m a^{-1}, as most of the water is again absorbed by a further increase in sheet thickness, to 0.16 m (from 0.11 m). Channels also begin to form at this time, but remain small and have limited impact.

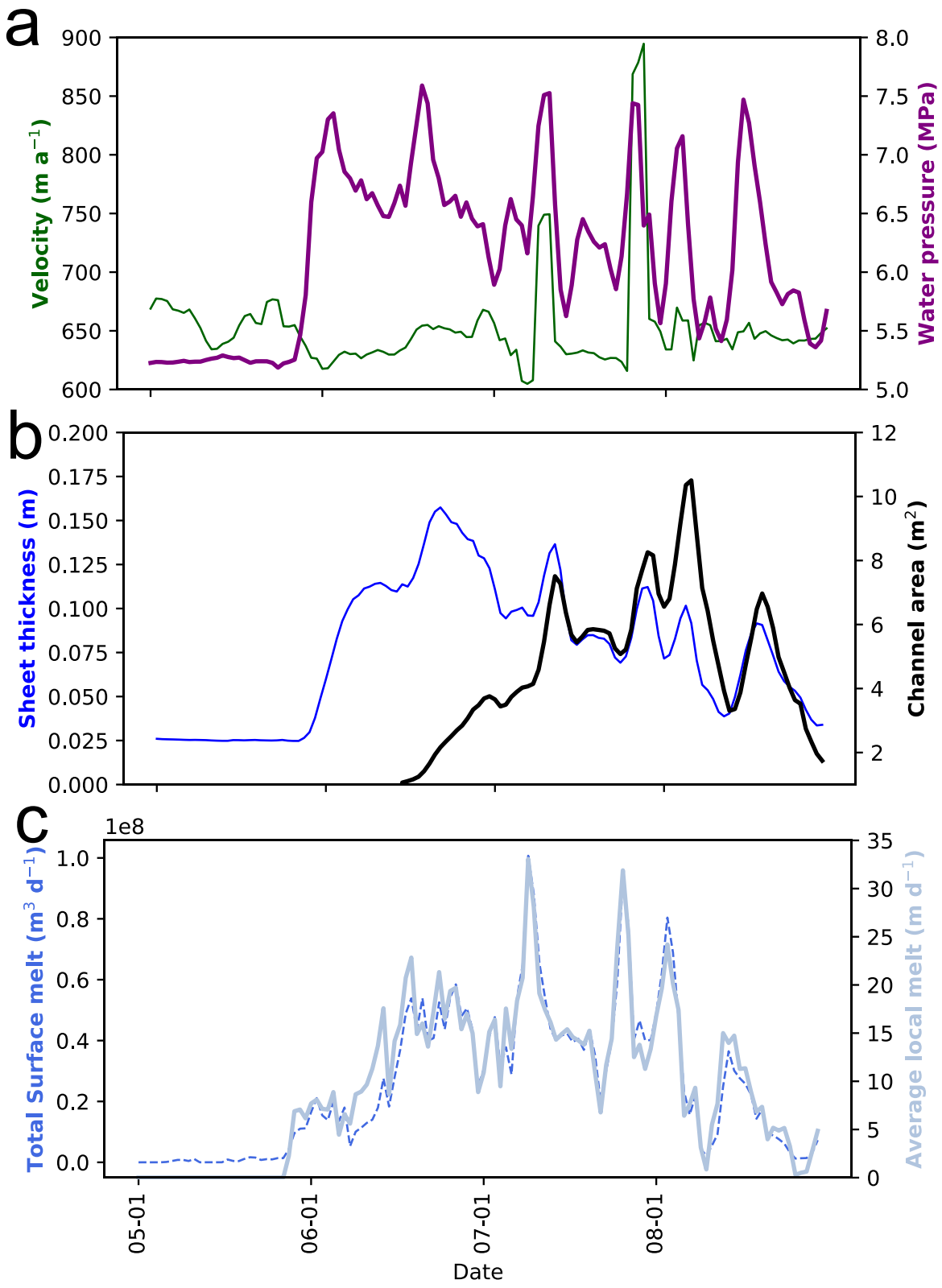

Figure 30 – Example of hydrology-velocity coupling from 25 km inland in model domain in May-September 2012 (location is shown in red box in Figure 31c). ***a*** *shows water pressure and 3-day smoothed velocity;* ***b*** *shows sheet thickness and channel cross-sectional area as proxies for the development of the inefficient and efficient drainage systems, respectively.* ***c*** *shows input to the subglacial hydrological system from RACMO 2.3p2 surface runoff data for Store as a whole and the local*

average melt rate. Note how variable the velocity response is to a given water-pressure change based on the degree of channelisation and sheet capacity in the subglacial drainage model.

Continued and higher surface runoff, producing a much sharper melt peak reaching 1.0 x 10^8 m^3 d^{-1} (34 m d^{-1} locally), leads to a third peak in water pressure, of 7.5 MPa, in the first week of July. Some of this is absorbed by a renewed increase in sheet thickness to 0.13 m, but starting from a similar base of 0.10 m, meaning that there is a much greater velocity response (a peak of 750 m a^{-1}) to the increased pressure. This saturation of the inefficient sheet drainage system also allows substantial channel growth, with average cross-sectional area exceeding 7 m^2, though this happens too late to mitigate the initial velocity response. The increased channelisation then leads to rapid drainage of the excess water in the sheet, with sheet thickness dropping to 0.07 m in the third week of July and the beginning of a declining trend in water pressure. The channels also show some decay, with average cross-sectional area falling to 5 m^2 at this point.

Two further water-pressure peaks, one at the end of July and one at the start of August (the first peaking at 7.5 MPa, the second at 7.2 MPa), then show the sophistication of the modelled hydrology. The first peak (from 0.9 x 10^8 m^3 d^{-1} of surface melt; 32 m d^{-1} locally), hitting the decaying system described above, leads to a rapid rise in sheet thickness to 0.11 m, with an increase in average channel cross-sectional area to 8 m^2, though this then again leads to rapid dewatering of the sheet. Therefore, velocity responds strongly to this first peak, reaching a seasonal maximum of 900 m a^{-1}, from which it rapidly drops to under 650 m a^{-1}. The second pressure peak (from 0.8 x 10^8 m^3 d^{-1}; 25 m d^{-1} locally), however, despite being of similar magnitude to the first, occasions a weaker velocity response (velocities stay below 670 m a^{-1}) and a smaller sheet-thickness peak (0.10 m). Instead, the average cross-sectional area of the channels rises rapidly to its seasonal high point of 10.5 m^2, leading to efficient evacuation of the excess water and explaining the reduced velocity response. Following this, sheet thickness drops to its lowest level of the summer, reaching 0.035 m (i.e., nearly returning to its pre-melt-season value) in the second week of August. Water pressure also hits a minimum of 5.4 MPa at this time as channel growth reduces pressure in the subglacial drainage system. A final water-pressure peak (7.5 MPa) in mid-August then produces a very limited velocity response, as both the sheet and the channelised system have sufficient spare capacity to accommodate the excess water from a much smaller melt peak (0.4 x 10^8 m^3 d^{-1}, 15 m d^{-1} locally).

The foregoing is to show that the model's coupling produces realistic behaviour in line with theory (Röthlisberger, 1972) and observations. Initial surface melt rapidly fills up the inefficient drainage system (the sheet in the model), leading to a large velocity response as the excess water cannot drain, and also encouraging the growth of larger channels (equivalent to the so-called 'Spring Event' on alpine glaciers (Mair et al., 2001, 2003)). Once these reach a sufficient size, they are able to drain

the bed much more efficiently, leading to water being lost from the sheet into these channels and reducing the velocity response to renewed water-input and -pressure peaks. This example also shows the importance of the degree of channelisation in controlling the model's behaviour, which will be further explored in the discussion (Section 6.5).

6.4.1.2 Channels and terminus dynamics

Having shown the fundamental validity of the velocity-hydrology coupling in the model, we present some results for the wider model domain and the terminus, where the coupling would be expected to be less evident, owing to the importance of lateral friction instead of basal friction in this environment.

Key hydrological quantities for both simulations are shown in Table 7. It is clear that the higher surface melt in 2012 (3.2×10^9 m^3 in total) compared to 2017 (1.3×10^9 m^3) leads to the development of a more extensive subglacial system consisting of larger channels, which discharge more. This peak channel size is reached on 15th July in 2012 and 4th August in 2017. At this peak, channels over 1 m^2 in area within a clear arborescent system reach 41 km inland in 2012 and 29 km in 2017 (Figure 31c, 31f). Median channel area at this peak extent in 2017 is 30% lower than in 2012, and all other variables point in the same direction: median channel flux is 46% lower, and the channelised area is 43% lower. In addition to this clearly larger channelised system in 2012, the mean sheet thickness in 2017 is 13% lower, and the mean sheet discharge is 64% lower; yet, the mean effective pressure is only 3% higher than in 2012, indicating that the expanded system in 2012 is still not sufficiently channelised overall to produce a truly efficient drainage system with low water pressures in the face of high water inputs. The greater surface-melt input in 2012 feeds through into plume melting at the terminus, which explains why the mean plume melt rate is 22% lower in 2017, whilst the mean of the daily maxima in plume melt rates is 12% lower, leading to the total volume of plume melting in 2017 being 27% lower than in 2012.

Despite this difference in peak channelised extent, though, by the end of each simulation, the subglacial hydrological system has returned to a near-identical state and extent (Figure 31a, 31d, represent this state well), with remaining channels confined to the lower 5 km of the glacier terminus. These perennial channels remain relatively large because basal meltwater is produced from frictional heat even in winter. This explains why the median channel area in winter is higher than the median value at peak extent, which includes many small channels in addition to those which are enlarged. (Table 7). Many of the quantities shown in Table 7 exhibit similar values, with the exception of median channel area and flux. While median channel area is 41% lower at the end of 2017 than in 2012, the median channel flux is 46% higher, as the larger hydrological system in

Table 7 – Summary of hydrological conditions and melt in 2012 and 2017. The channel, sheet and pressure statistics are taken from the final timestep across the entire model domain (columns marked 'End') or the timestep where maximum Area Channelised was reached (columns marked 'Peak' – this occurred on 15th July for 2012 and 4th August for 2017); the plume statistics are taken from the calving front across all timesteps. 'Area Channelised' refers to the percentage of the possible channel segments occupied by channels. Channel statistics exclude channels smaller than 1 m^2 in cross sectional area. 'Mean maximum plume melt rate' is the mean of the daily maxima in plume melt rates across the whole length of the simulation.

	2012		**2017**	
	Peak (15th July)	End	Peak (4th August)	End
Median channel area (m^2)	3.68	13.2	2.57	7.85
Median channel flux (m^3 s^{-1})	4.11	0.22	2.20	0.32
Area channelised (%)	8.03	1.39	4.57	1.42
Mean sheet discharge (m^3 s^{-1})	0.015	0.0005	0.005	0.0005
Mean sheet thickness (m)	0.13	0.08	0.11	0.07
Mean effective pressure (MPa)	1.73	2.40	1.79	2.39
Mean plume melt rate (m d^{-1})	0.34		0.27	
Mean maximum plume melt rate (m d^{-1})	4.78		4.19	
Total plume melt (m^3 a^{-1} $x10^8$)	6.46		4.69	

2012 takes longer to decay, and its more numerous, larger channels evacuate the remaining water more efficiently, resulting in less water per channel. The similarity of the sheet and pressure variables between the two years, however, suggests the hydrological systems in each year are rapidly converging towards a comparable state, indicating that the hydrological system by the end of winter is not greatly influenced by the extent to which it grew in the preceding summer.

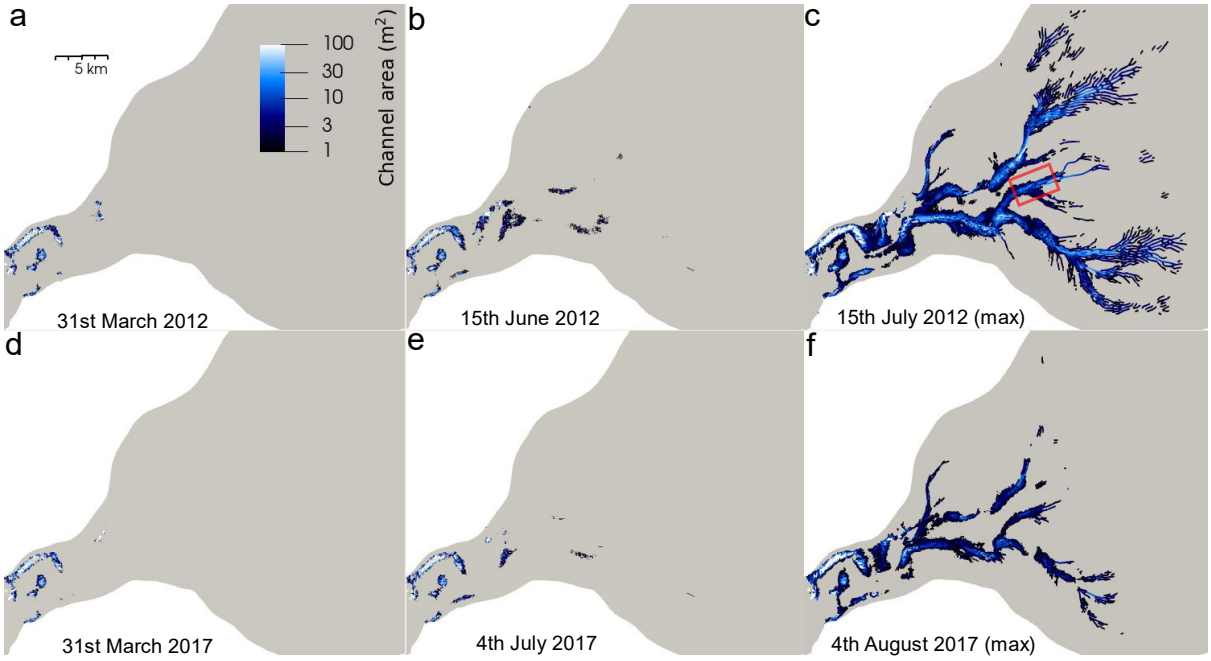

Figure 31 – Modelled subglacial channel networks at Store in 2012 and 2017. ***a*** *shows the channel extent on March 31st 2012;* ***b*** *shows the channel extent one month before peak channelisation; and* ***c*** *shows the peak channel extent in 2012 (achieved on 15th July). The red box shows the location of Figure 30 (this is also approximately the same area where water pressure records are reported by Doyle et al. (2018)).* ***d*** *shows the channel extent on March 31st 2017;* ***e*** *shows the channel extent one month before peak channelisation; and* ***f*** *shows the peak channel extent in 2017 (achieved on 4th August). Panels* ***a*** *and* ***d*** *are also representative of the channel network present at the end of their respective simulations. Note how much more extensive the network is in 2012 and how rapid growth is in the month preceding peak channelisation. Compare to Figure 16 and Figure 22.*

Considering the location and distribution of plume melting at the front further, 2012 (Figure 32a) shows two very clear sites of plume activity over the length of the simulation, a primary one on the southern side and a secondary one on the northern side, with comparatively little activity elsewhere along the submerged ice front. In 2017 (Figure 32b), the distribution of plume activity is much more uniform; the northern plume is still visible, but the southern one has disappeared. Melt undercutting is therefore much more evenly distributed in 2017, even if actual melt rates are higher in 2012 (Table 7), but with a much greater degree of spatial heterogeneity. This is because the higher degree of channelisation in 2012 (Table 7; Figure 31) leads to larger and more fixed drainage outlets at the terminus, and therefore increased localisation of large plumes and accompanying high melt rates. In 2017, these outlets are more mobile and represent a smaller contribution relative to drainage through the sheet, hence the more uniform plume activity across the front.

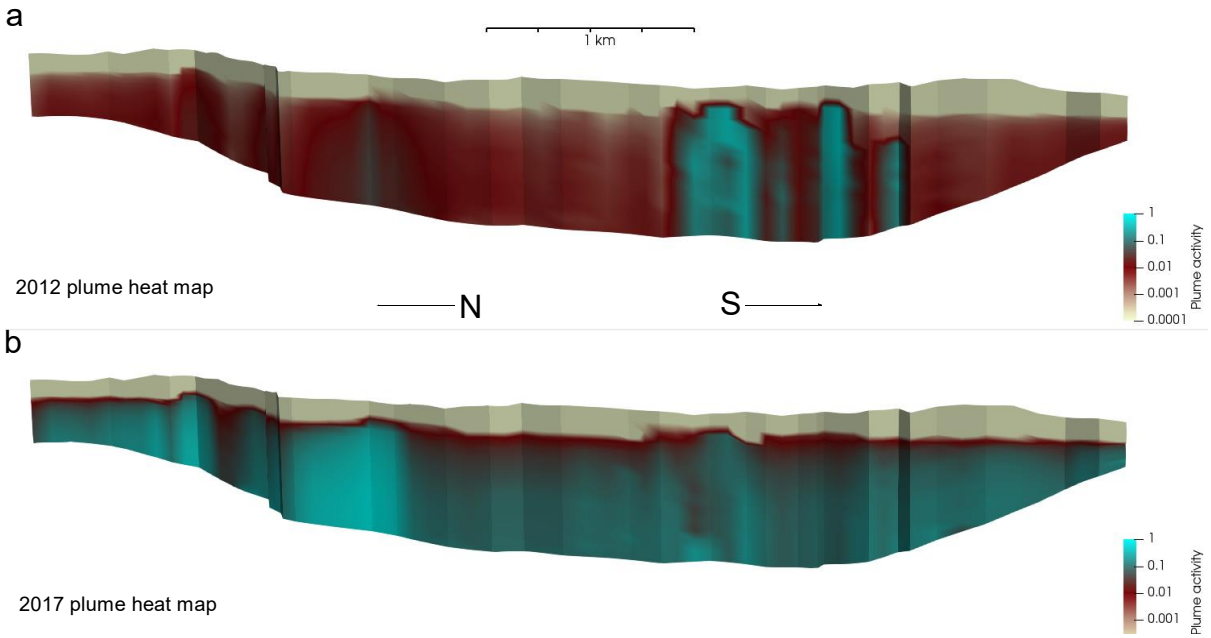

*Figure 32 – Heat map of plume activity in **a** 2012 and **b** 2017 simulations. Areas with a value of 1 show the highest mean plume melt rates across the entire length of the model run (note therefore that the index values are relative to each individual simulation and should not be taken as showing similar levels of melt between simulations); areas with a value of 0 show no plume activity at any point. North is to the left and south to the right. Note logarithmic scale and how 2017 shows much more uniform plume activity than 2012. Compare Figure 23.*

Examining the sources of different kinds of melt (Figure 33) and the consequent evolution of the subglacial drainage system, we find a minimum in channelisation of 1% towards the end of March in both years. We then see slow growth in response to early surface melt, before very rapid growth begins in the month leading up to peak extent of the channelised system. So, in 2012, the slow growth phase occurs in May, with rapid growth in June leading up to the peak (8%) on the 15th July (Figure 33a). In 2017, slow growth occurs throughout May and June, with rapid growth in July preceding the peak (4.6%) on the 4th August (Figure 33b). In particular, the sudden drop in surface melt from 2 x 10^7 m^3 d^{-1} to 3 x 10^5 m^3 d^{-1} in the last week of June in 2017 acts as a brake on the growth of the channelised system. After reaching their peaks, both years exhibit rapid decay of the channelised system in August and September, returning to pre-summer levels of channelisation (1-2%) by October. The response to variable surface-melt inputs is lagged and more pronounced before peak channelisation in both years, with a less sensitive response after peak channelisation.

Basal melt from friction across the entire 4400 km^2 area of the model domain (Figure 27) is essentially constant and identical in both years, remaining a little below 10^6 m^3 d^{-1}, whilst plume melt shows much higher variability. However, it is notable that plume melting is at or above basal melt in terms of volume, despite occurring purely on the 2 km^2 surface area of the submerged portion of the calving front, showing the importance of plume melting. Outside the summer melt

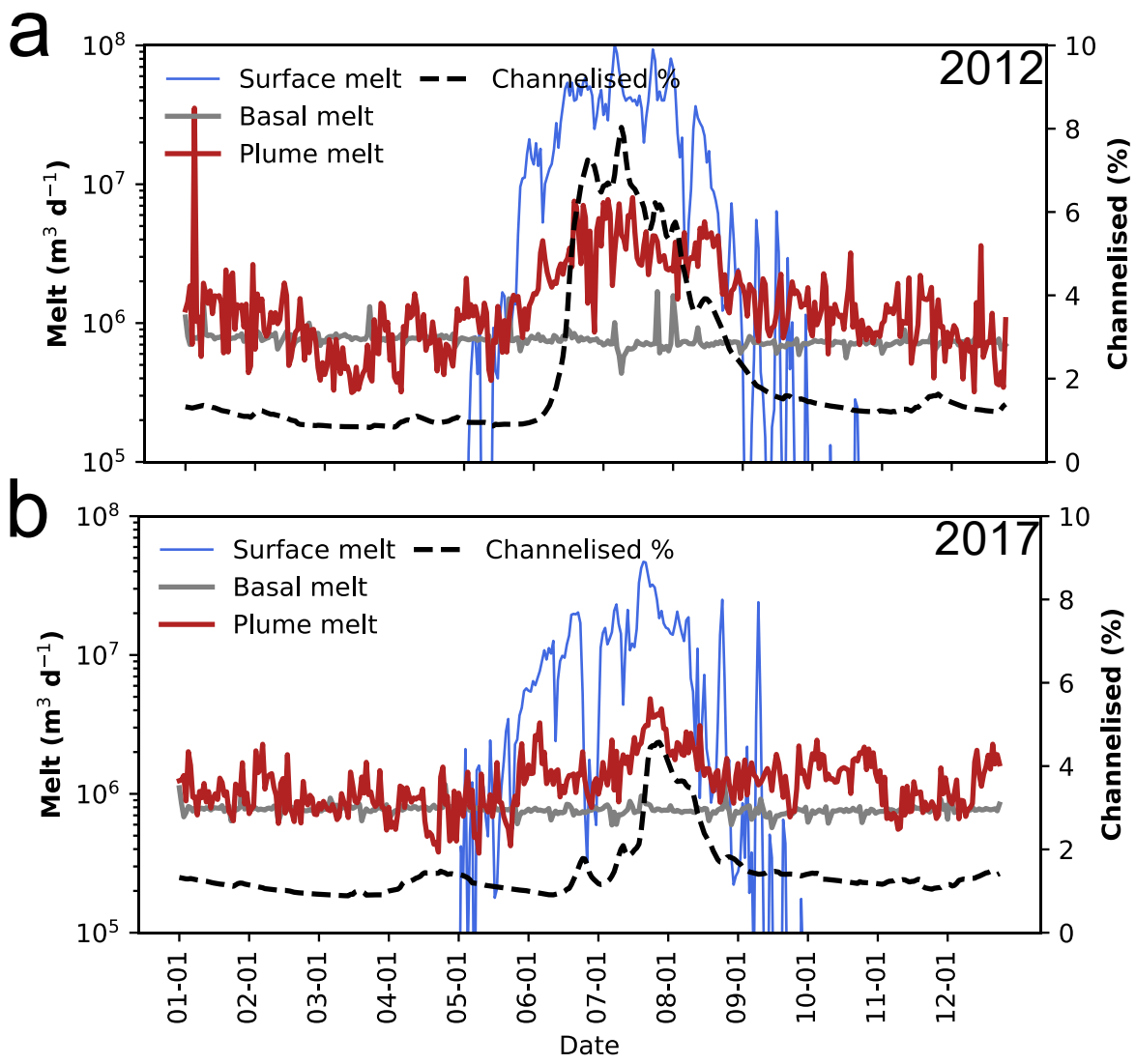

*Figure 33 – Time series of melt quantities in **a**. 2012 and **b**. 2017. The blue line shows surface melt input to the hydrological system (small values not shown); the grey line shows input to the system from melting at the ice-bed interface; the red line shows melting caused by plumes at the calving front; and the dotted black line shows the percentage of the subglacial hydrological system occupied by channels >1m² in area as a proxy for evolution of the system. Compare with Figures 20 and 21. Note how basal melt is largely constant whilst plume melting shows some seasonality. The large spike in plume melting early in 2012 is a model artefact and should not be regarded as physically meaningful.*

season, in both 2012 and 2017, plume melting is broadly equal to basal melt at around 10^6 m^3 d^{-1}. In the melt season, however, in 2012, plume melting increases by nearly an order of magnitude, staying above 3 x 10^6 m^3 d^{-1} for nearly all of June, July and August, and repeatedly peaking at 8 x 10^6 m^3 d^{-1} in June and July. In 2017, though, this summer increase is much more subdued, with a single peak at 5 x 10^6 m^3 d^{-1} on the 29th July and melt quantities otherwise at or below 3 x 10^6 m^3 d^{-1}. Conversely, the subsequent decline in plume melting back towards the 10^6 m^3 d^{-1} level as winter returns is much less evident in 2017 than 2012, with plume melt rates maintaining a higher level

through to the end of the year, as the less efficient drainage system in 2017 dewaters the bed more slowly. Outside of this general seasonal pattern of more plume melt in summer and less in winter, however, there is little relationship between surface melt and plume melt, with peaks and troughs in the former not necessarily leading to similar features in the latter. The relationship between all these factors, and how they compare to previous modelling of Store (Cook et al., 2020), will be discussed further in Section 6.5.

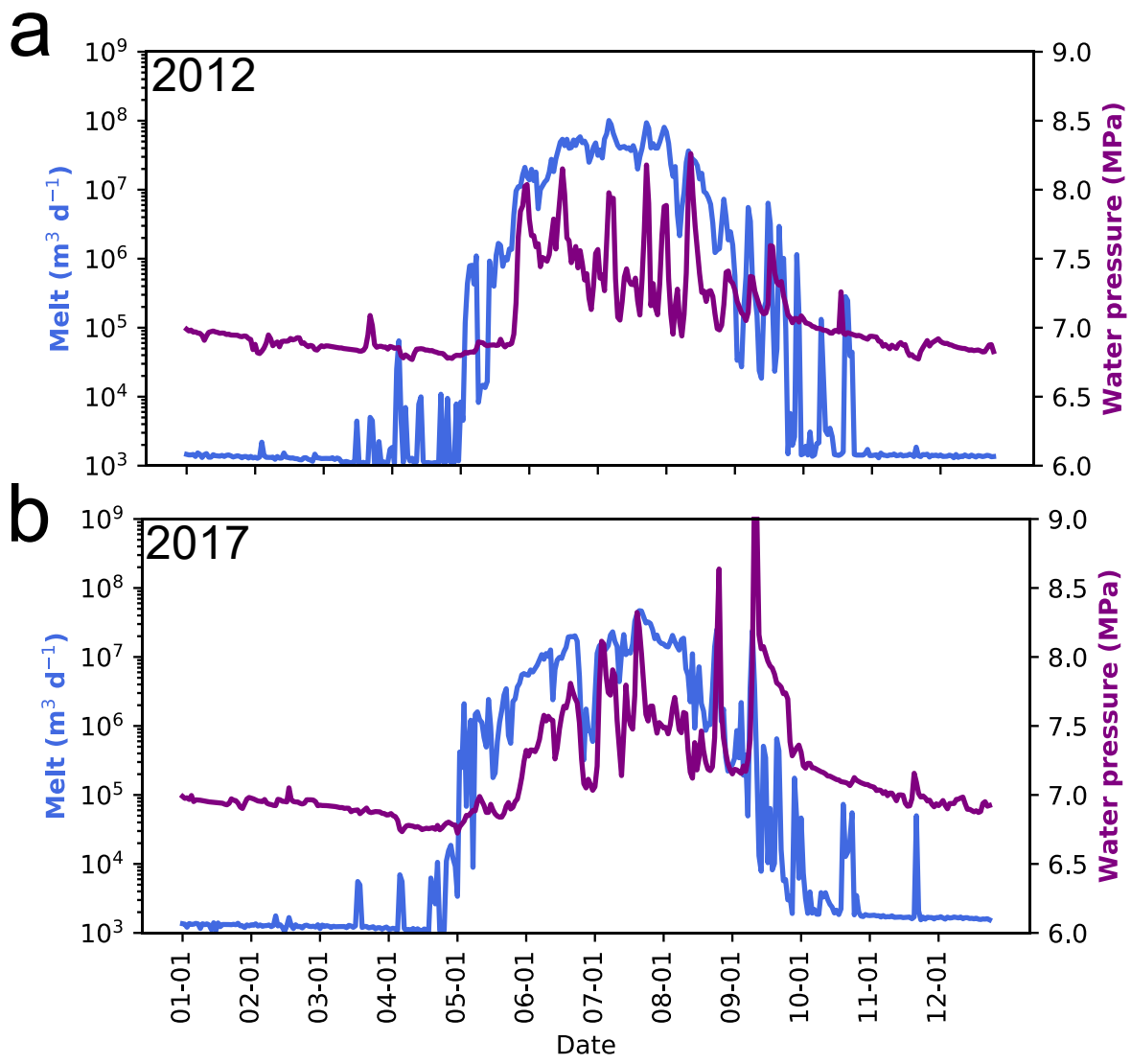

*Figure 34 – Surface melt (blue line) and domain-averaged water pressure (purple line) in **a**. 2012 and **b**. 2017 at Store. Notice how water pressure is closely linked to the surface-melt input. Compare with Figure 25.*

As the key driver of the evolution of the subglacial hydrological system, surface melt is also the key determinant of domain-averaged basal water pressure (Figure 34), with r = 0.75 between daily meltwater input and domain-averaged daily water pressure for 2012 and r = 0.61 for 2017. Water pressure shows a similar general pattern to channelisation (Figure 33): a minimum of 6.7 MPa in

March-April before the onset of surface melt, an erratic increase with peaks reaching 8.2 MPa in 2012 and 9.2 MPa in 2017 as surface melt sets in, and then a gradual decline in the final quarter of the year to below 7.0 MPa. Within that general pattern, however, there are some important differences. In 2012 (Figure 34a), there is a declining trend in water pressure from the end of May to mid-August, before increasing again through to the end of September, after which it enters the late-year general decline. In 2017 (Figure 34b), though, there is an upward trend in water pressure throughout the summer melt season until mid-August, with a very short downward trend for the second half of August, before two late surface-melt spikes push pressures up again in September, leading to a general decline from October onwards. Additionally, 2017 exhibits a much greater water-pressure response to these late-melt-season injections of surface melt than 2012, with values fluctuating by as much as 2 MPa over the course of just 4 days. This is because the less-channelised drainage system present in 2017 is less able to accommodate sudden influxes of water, leading to large water pressure spikes. In 2012, the more extensive, if decaying, channelised system can still mostly accommodate the extra water from these late-season surface-melt spikes; hence, leading to a much more muted water pressure response.

Water pressure, in turn, as shown in the previous section, is one of the main factors controlling the ice velocity inland. This relationship is less clear at the terminus, owing to the greater importance of lateral, as opposed to basal, friction in determining flow. Since the domain-averaged water pressure does not necessarily dictate the ice velocity at the terminus (Figure 35), we also consider variations in water pressure strictly beneath the terminus region (Figure 35). In 2012, basal water pressures decrease from 9 MPa at the end of May to 6 MPa at the end of September, mirroring the drop in terminus velocity. In 2017, we find basal water pressures in this near-terminus region to vary very little, with the exception of the mid-September melt-pressure spike described above. It is notable that this spike, despite its size, has very little impact on terminus velocities (Figure 35b), as it did not lead to any significant large-scale reorganisation of the subglacial hydrological system (Figure 33b) sufficient to counter the dominance of lateral friction. The declining versus unchanged water-pressure profiles in 2012 and 2017, respectively, partially explain why the corresponding velocity profiles evolved as discussed above. One feature that is not hydrologically controlled, however, is the higher April velocities seen in both years, which are instead driven by thickening of the terminus through winter and the concomitant increase in driving stress. Thickening also contributes to the increase in velocities seen at the end of the year in 2012 (Figure 35).

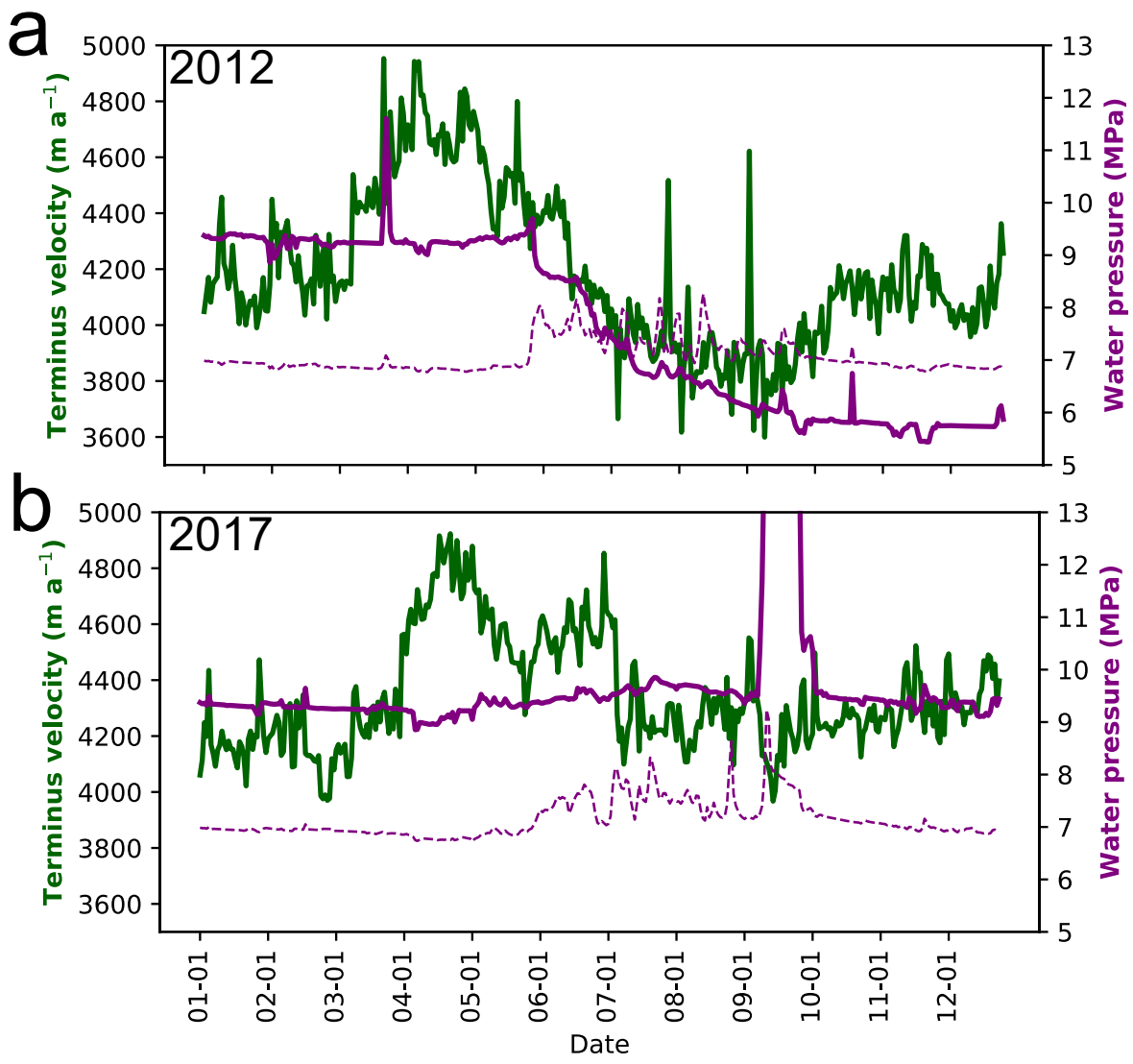

*Figure 35 – Average terminus velocity (green line), domain-averaged water pressure (dashed purple line), and near-terminus water pressure (solid purple line) at Store in **a**. 2012 and **b**. 2017. The near-terminus water pressure is the average water pressure at the bed between 4 and 10 km inland of the terminus, to remove any variations associated with (un)grounding of the front.*

6.4.2. Ice flow and calving

The modelled calving behaviour at Store is seen in Figure 36, which shows that the distribution of events in both years is quite similar, with a distinct modal peak in the 3-5 x 10^5 m^3 range. Our model produces 2,571 calving events larger than the cut-off size of 1 m^3 in 2012 and 1,677 similar events in 2017, with a mean size of 1.8 x 10^6 and 1.1 x 10^6 m^3, respectively. Of these events, 53% (2012) and 59% (2017) occur within the 10^5-10^6 m^3 interval, representing 13% and 24% of total volume loss, respectively. The largest events (>10^6 m^3) account for 29% and 22% of the total number of events in 2012 and 2017, although a much larger fraction in terms of volume: 87% and 76%, respectively.

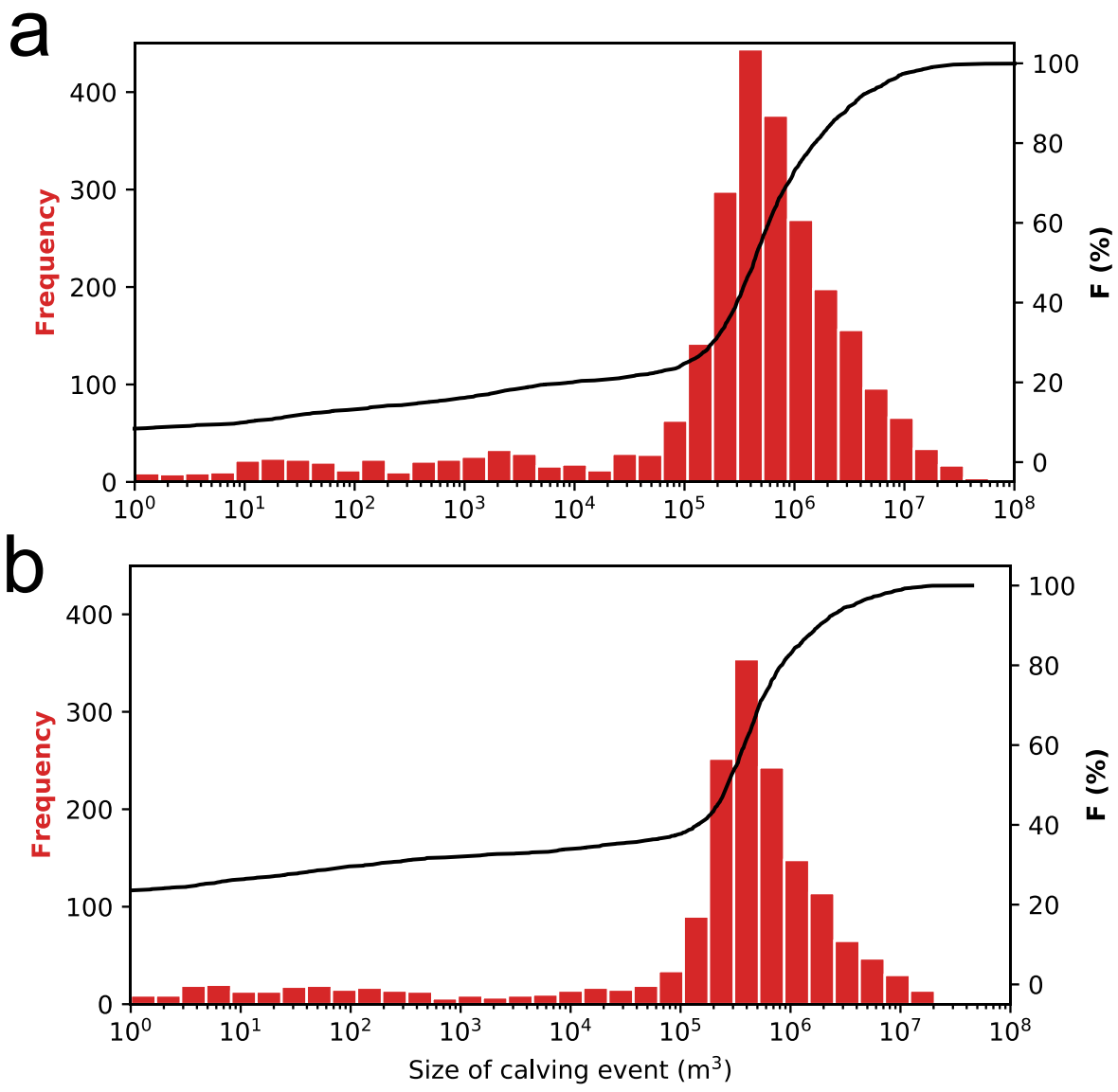

*Figure 36 – Histograms (red bars) and cumulative distribution functions of modelled calving events at Store by size in **a**. 2012 and **b**. 2017. Note similar distribution in both years.*

Both 2012 and 2017 show large day-to-day variability in their modelled calving behaviour. However, there is a similar temporal trend in both years (Figure 37): variable calving at rates of between 5 and 15 events per day in the first part of the year, which drops noticeably to below 5 events per day in the early summer (in the second week of June in 2012 and the first week of July in 2017). In 2017 (Figure 37b), this drop coincides with the observed and modelled break-up of the proglacial mélange on 8th July, but, in 2012 (Figure 37a), it occurs about three weeks after the modelled mélange break-up. The primary control on this pattern is the seasonal change in terminus velocity driven primarily by hydrology, as discussed above, with drops in velocity matching with the modelled drops in calving

activity – in 2012, velocity drops from 4300 m a^{-1} to 4100 m a^{-1}; in 2017, from 4600 to 4200 m a^{-1} (Figure 38). This interplay of velocity and calving also influences the terminus position (Figure 38) –

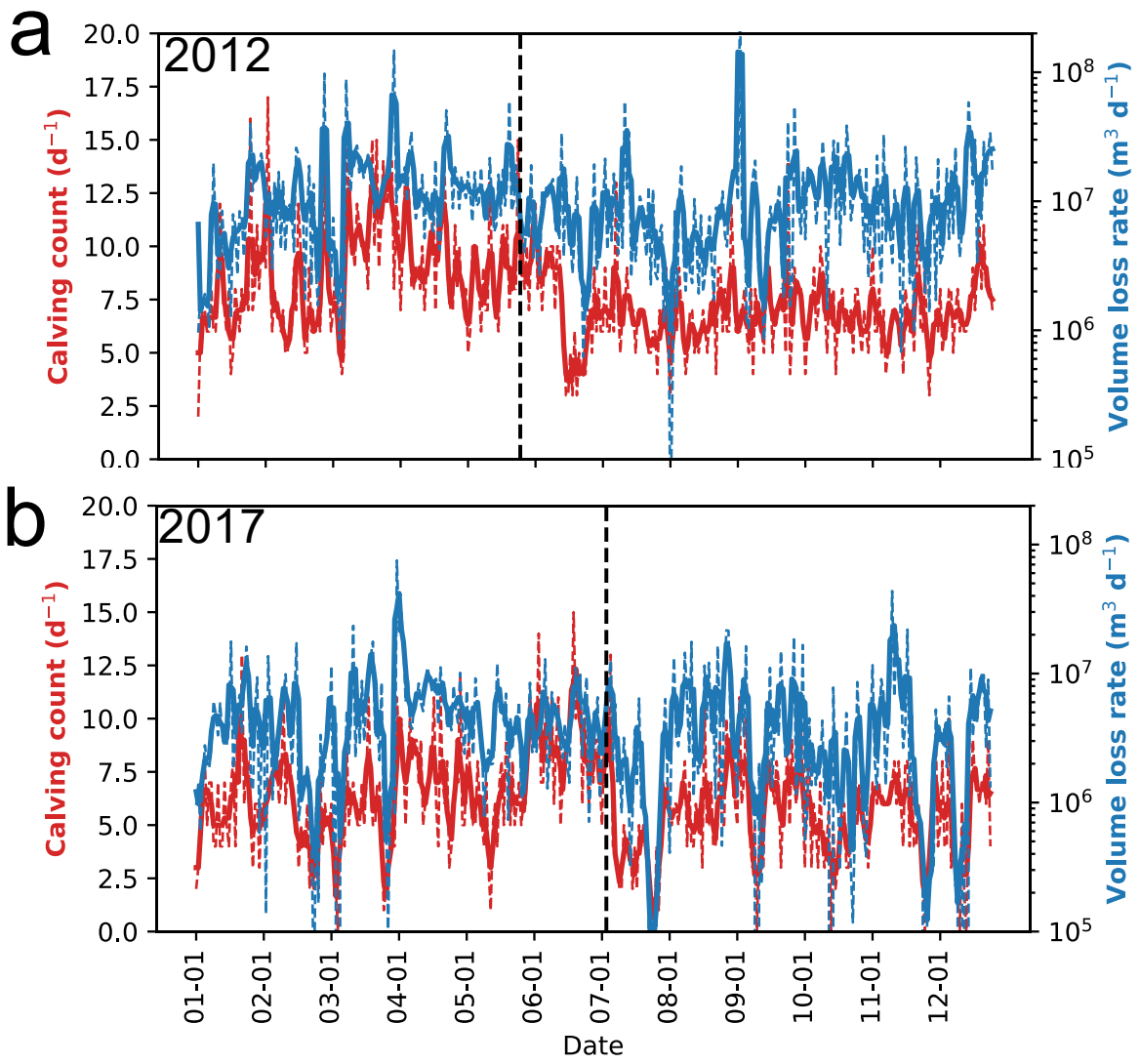

*Figure 37 – Time series of modelled calving at Store for **a**. 2012 and **b**. 2017. Red lines show the rate of calving event occurrences per day; blue lines show the volume loss rate per day. The solid lines show the 3-day moving average; the dotted lines show the actual daily totals. Vertical black lines show the timing of mélange break-up. The large volume peak in panel **a** is the result of several large calving events happening to coincide, rather than one anomalously large event.*

both years show advance in the terminus through to modelled mélange break-up. In 2012, the modelled terminus advances several kilometres until 29th May, after which it retreats as both velocity and calving event frequency decline. In 2017, the terminus advances at a slower rate throughout summer and the retreat starts in September. While calving activity drops to approximately 5 events per day on average when the melt season starts, both years show a return in activity, with around 10 events per day on average in the main summer month (July in 2012; August in 2017). Velocity continues to decline in this period in 2012, reaching a minimum of 3700 m a^{-1} in

the first week of September. The terminus position consequently retreats to a position only 1 km advanced from that at the start of the simulation, reaching this minimum at the end of November.

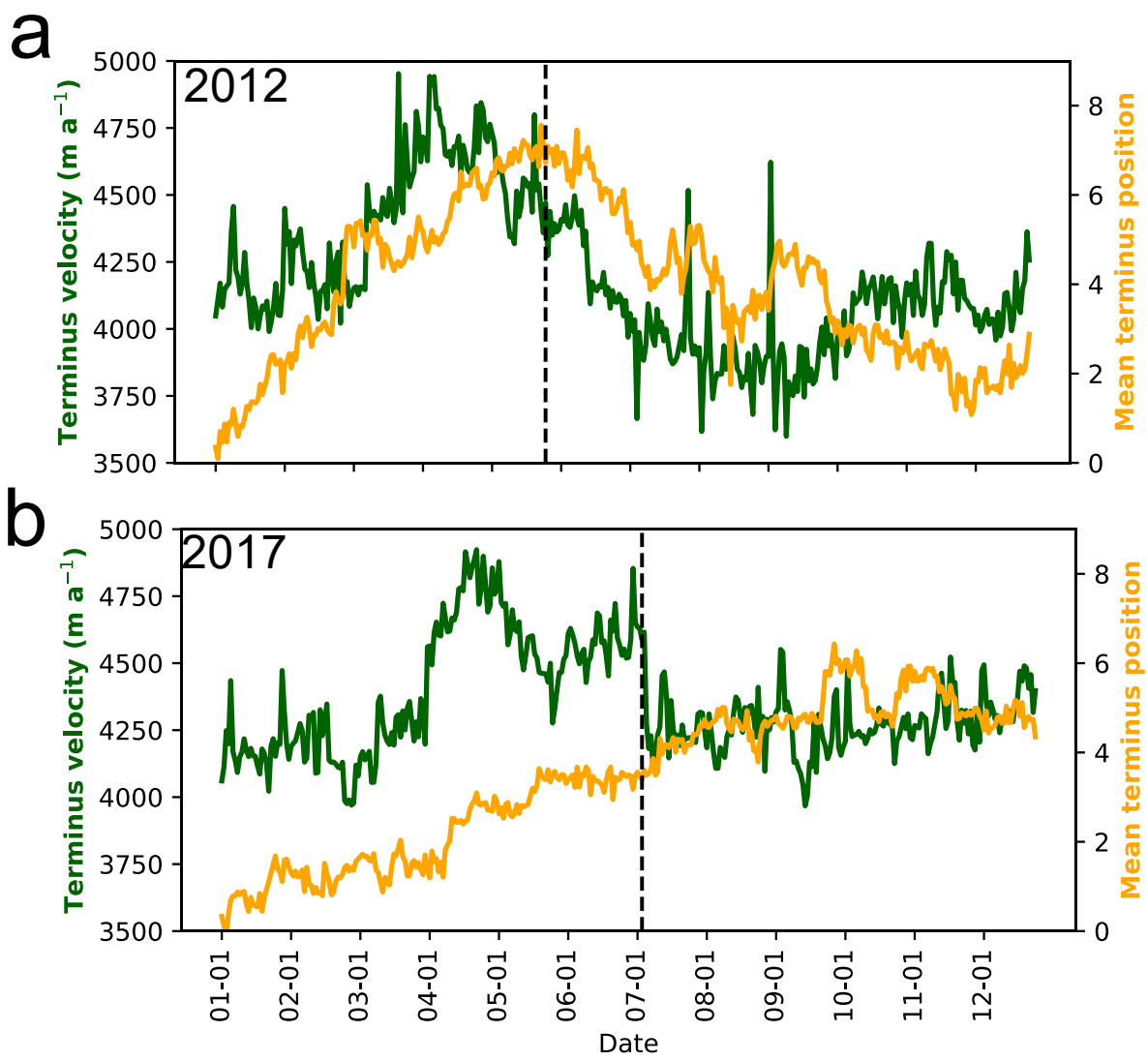

*Figure 38 – Average terminus velocity (green line) and position (yellow line) at Store in **a**. 2012 and **b**. 2017. The terminus position quantity is an average of the co-ordinates of all the points on the terminus; a higher value indicates terminus advance and a lower one retreat. The index can be read as being in units of kilometres. Note how higher velocities are associated with a lagged terminus advance and lower ones with a lagged retreat.*

In 2017, the velocity remains unchanged at around 4200 m a^{-1} with no further decline, which accounts for the less-marked drop in calving event frequency that year and the stable terminus position throughout autumn. By the end of the year, however, both simulations show an upwards trend in calving activity, moving back towards the 10-15 events per day, which can be linked to the upwards trend in velocity occurring at the same time. In both years, the ice velocity grows to around 4250 m a^{-1} which is similar to the initialised velocity in each run. As such, in 2012, a small re-advance

is seen in December, with the terminus returning to the 3-km mark. In 2017, however, the uptick is smaller and the terminus remains at its autumnal position around the 4-km threshold.

6.5. Discussion

This section discusses the results presented in the previous section. Section 6.5.1 deals with the behaviour of the fully coupled model. Section 6.5.2 then considers model limitations.

6.5.1. Fully coupled model behaviour at Store

A highly variable calving activity, with significant day-by-day and week-by-week differences in both 2012 and 2017, is a unique feature of our fully coupled model (Figure 37). Our results provide theoretical insights to the complex nature of the interaction between ice flow, terminus position, basal hydrology, plume melting and calving. The characteristic features in our model may thus inform causal relationships and behaviour, which have so far not been modelled as directly or explicitly as we do in this study. We are also able to disentangle these processes and show which are most important at Store.

The key factor within the hydrological system that controls velocity and therefore calving is the extent of channelisation (Figure 30). As noted in Section 3.1, our 2012 simulation shows a declining trend in basal water pressure in the first part of the melt season (Figure 34), from May to mid-August, suggesting that the modelled degree of channelisation is sufficient to begin the transition to a widespread efficient drainage system at Store, as has been theorised to occur elsewhere in Greenland (Davison et al., 2019; Sole et al., 2011; Sundal et al., 2011; Tedstone et al., 2015). However, the water pressure still remains higher than in winter (Table 7), with several spikes in high water pressure occurring on high-melt days (Figure 34). In 2017, by contrast, the decline in water pressures due to channel formation is much more limited (Figure 34), because channel growth and the extent of channelisation are much reduced (Table 7, Figure 31, cf. Figure 30). This limited channelisation also explains why surface-melt spikes in September in 2017 produce a much larger response in water pressure than in 2012 – the channelised system in both years has started to decay by this point (Figure 33), but the more-developed 2012 system remains better able to handle higher melt inputs and consequently dampens the pressure response. The modelled 2017 situation in September therefore has some similarities to the observed behaviour at the western margin of the GrIS in response to a week of warm, wet weather in late August-early September 2011, when unusually high surface runoff (from melt and precipitation) led to water pressure exceeding ice overburden pressure at site R13 in a borehole 13 km inland from the margin (Doyle et al., 2015). In our model, the domain-averaged water pressure remains below the ice overburden pressure in

2017, but the water pressure in the region 4-10 km behind the terminus (Figure 35), so in a similar position to the borehole of Doyle et al. (2015), exceeds ice overburden pressure (maximum modelled ice thickness in this region is 1400 m). Water pressures exceeding ice overburden pressure have been observed at Store (Doyle et al., 2020) and our model is also consistent with the persistently high basal water pressures observed in boreholes at site S30 on Store Glacier (Doyle et al., 2018). Our modelled hydrological system is further consistent with the inefficient drainage inferred at this site (Doyle et al., 2018), which is located in-between two major subglacial drainage pathways and therefore outside the main channelised network (Cook et al., 2020). The model's behaviour is therefore, overall, in good agreement with the observed hydrological behaviour of the GrIS.

This channelisation control on velocity is confined to the region where the channelised network waxes and wanes seasonally, which means it excludes the terminus region (<10 km from calving front), where channels exist continuously year-round, as well as the interior region (>40 km inland of the calving front), where channels physically cannot form. According to our model, the terminus should contain large channels with cross sectional areas on the order of hundreds of metres or more in summer (Figure 31a, 31d) and even throughout winter (Table 7). Hence, widespread channelisation extends seasonally from the terminus region when surface melt first sets in, which occurred in April in 2012. The corresponding terminus velocity peak (Figure 35) may be partly a response to pressurisation of these channels, as the winter channels receive surface melt (Figure 34a), but is principally the result of higher driving stresses due to winter accumulation thickening the terminus. Inland, however, where the channel network is not present year-round, the modelled velocity response to channelisation-controlled water pressure is clearer (Figure 30). As surface melt then increases into summer, however, the terminus velocity declines as the channel network develops and becomes increasingly efficient (Figure 31), with modelled velocity reaching a minimum in September. As the channelised system subsequently decays, velocity increases through to the end of the year, reflecting the return of a higher-pressure, more distributed system. This matches up with the Type 3 behaviour and posited cause described by Moon et al. (2014), which they observe at Store in 2012, providing further validation of the fully coupled model's ability in replicating the behaviour of Store.

The behaviour of terminus velocity in 2017, however (Figure 35b), is more reminiscent of Type 2 behaviour according to the classification of Moon et al. (2014). In this simulation, we obtain an early-melt-season (June) velocity peak at the onset of surface melt (Figure 34b), before a return to lower velocities, similar to the pre-melt velocity, unlike in 2012, where summer velocity drops below the start-of-year values (Figure 35a). The reduced model channelisation in 2017 (compared to 2012)

explains this – the initial surface melt expands the channels beneath the terminus enough to manage the increased quantities of melt, but subsequent surface melt is not enough to build a truly efficient channelised drainage system, meaning the subglacial environment, even at the terminus, remains in an intermediate, partly-channelised state that maintains higher water pressures (Figure 35) and therefore also higher ice velocities. This highlights the model's ability to reproduce the observed heterogeneous nature of tidewater-glacier behaviour, both temporally and spatially (Csatho et al., 2014; Moon et al., 2014), with two different types of glacier behaviour being modelled as a result of different SMB and surface-runoff forcing. With our modelled Store displaying key traits of two different proposed types of tidewater glacier (Moon et al., 2014), we caution against imposing overly strict classifications.

However, in both 2012 and 2017, we model an increased average water pressure across the model domain in summer, so, even when the modelled hydrology becomes truly efficient in 2012, the model domain, as a whole, is experiencing higher basal water pressures. This is due to surface melt extending inland to regions where channel development is much more limited (Figure 31c, 31f) owing to the evolving thickness of the ice. This feature of our model may explain why previous studies have observed interannual increase in ice flow in the interior of the GrIS (Doyle et al., 2014), while flow at lower elevations, where thinner ice and more efficient drainage predominate, has resulted in the opposite trend (Tedstone et al., 2015; van de Wal et al., 2008). Our model also shows that subglacial channels larger than 1 m^2 largely vanish in winter and that the state of the subglacial drainage system at the end of each simulation is nearly identical (Figure 31a, 31d; Table 7), despite large differences in the size and configuration of channels during the preceding summer season. This shows that a significant enlargement of the channelised system during the record high melt year of 2012 did not increase the basal drainage efficiency of the subsequent winter. This suggests that fast flowing tidewater glaciers like Store may not possess the long lasting channels hypothesised to stabilise the land-terminating ice margin (Sole et al., 2013; Tedstone et al., 2015), nor may they be as subject to large-scale dewatering of the bed (Hoffman et al., 2016), both due to reduced channelisation and the reduced importance of basal friction (as opposed to lateral friction) in controlling ice motion.

As a final hydrological point and related to the importance of the degree of channelisation discussed above, the major difference we find between the hydrological system modelled in this study and that generated by a simplified version of the same model (Cook et al., 2020) is that the channelised system in 2012 at its maximum extent reaches less far inland here than in the simplified model (41 compared to 55 km), though the figure for 2017 is virtually identical (29 compared to 30 km). This difference highlights the importance of including two-way ice-hydrology coupling in a model. The

more restricted inland extent of the channelised system in 2012 in this study is due to the coupling between the hydrology and ice flow allowing the higher water pressures under the thicker ice inland to feed back into higher ice velocity, generating localised thickening as ice velocities downstream drop, increasing channel closure rates and consequently suppressing channel formation. The same process operates in 2017, but there is less of an effect because there is a smaller meltwater input to grow channels, especially in the interior far inland. These results show that previous work based on hydrological models detached from ice flow (Banwell et al., 2016, 2013; Cook et al., 2020; de Fleurian et al., 2016) may have over-predicted the ability of channels to form and the extent to which channelised networks grow.

As the foregoing discussion makes clear, the fully coupled model is successful in producing realistic hydrology-velocity coupling and behaviour at Store. This then has an impact on calving at the terminus. In both 2012 and 2017, the rate of calving largely follows the terminus velocity, but both years show a pronounced early-summer drop in calving event frequency (Figure 37). In 2012, this drop occurs because of a sharp decrease in terminus velocity from 4500 m a^{-1} to 4100 m a^{-1}, which happened three weeks after the mélange broke up. In 2017, however, the velocity/calving decline and mélange break-up coincide. This shows that mélange break-up in our model is not the primary driver of the modelled change in calving event frequency, but that this change is being largely controlled by surface melt and the development of the subglacial hydrological system. This does not mean mélange break-up has no effect on calving – in 2012, it is still the case that the removal of the mélange marks the peak of overall terminus advance (Figure 38a) and, in 2017, there is an initial peak reaching 12.5 events per day immediately after mélange removal, before the subsequent decline in calving – but the fully coupled model results show that hydrology-driven velocity changes at the terminus can be equally important. This is also the case in 2017, when the hydrologically driven velocity changes at the terminus fortuitously coincidence with mélange break-up. This hydrological control was not captured in previous models of Store, either because hydrology was not a model feature (Morlighem et al., 2016; Todd et al., 2018, 2019) or because hydrology was not coupled to ice flow (Cook et al., 2020). We note, however, that mélange buttressing is applied with a back stress of 45 kPa over a thickness of 75 m in this study, whereas values of 120 kPa and 140 m were used previously by Todd et al. (2018). This difference in model set-up explains why our model shows a more subdued response to mélange formation and break-up compared to previous work (Todd et al., 2018), and we would expect mélange buttressing to make a larger contribution to the seasonal characteristics of Store if its backstress is higher than that which we have assumed here. With a more detailed study of the effect of mélange being beyond the scope of this study, we refer

to previous work in which the sensitivity of calving to variation in mélange backstress was explored (Todd et al., 2019).

Whereas previous work posited a link between plume melting and calving at Store (Todd et al., 2018, 2019), we find the hydrology-induced changes in terminus velocity to exert a stronger control on calving. This finding stems from implementation of subglacial hydrology and meltwater plumes, which makes ice velocities in the model subject to the variations in basal drainage efficiency and terminus undercutting controlled by the subglacial discharge. However, it is possible to link plume activity to individual calving events in the model, as shown in Figure 39. This displays two examples of plume activity on the northern side of the calving front. The first example (Figure 39a-e) shows the removal of a small promontory during 28th-31st March 2012, when perennial channels beneath the terminus discharge basal meltwater produced by friction alone into the fjord. This discharge forms a relatively strong plume with melt rates of 2 m d^{-1} in the vicinity of the promontory, weakening it over several days and leading to eventual calving. The second example (Figure 39f-j) shows similar behaviour at the same part of the calving front, with stronger plumes (melt rates over 3 m d^{-1}), occurring between the 15th and 18th July 2012. This sequence of events is consistent with plume-triggered calving at tidewater-glacier termini (Benn et al., 2017a), allowing us to be confident that the fully coupled model is indeed reproducing realistic tidewater-glacier behaviour. An example of this process happening at Store is shown in Figure 40.

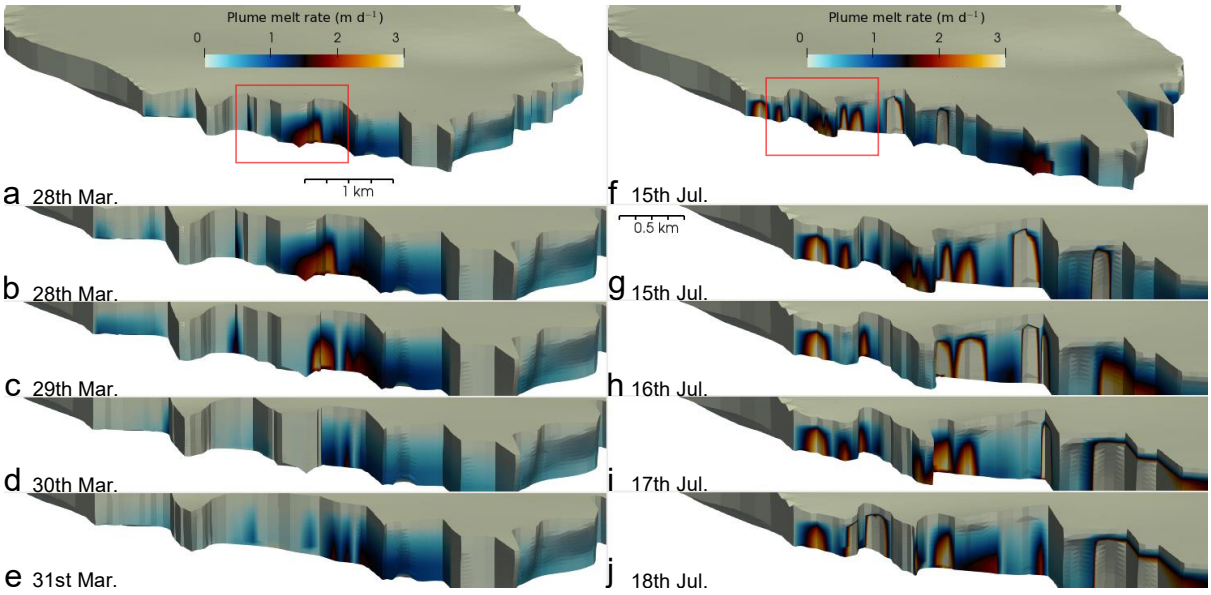

Figure 39 – Examples of plume-calving interaction in the 2012 simulation. ***a*** *shows the modelled terminus of Store on the 28th March. The red box indicates the area of interest, zoomed in on for a day-by-day view in* ***b*****-*****e*** *– see how a promontory has calved off.* ***f*** *shows a second example of this process happening in summer, with day-by-day views in* ***g*****-*****j****. Note higher plume melt rates in and around the promontory that calves.*

Considering calving-front plumes further, which are driven by the subglacial discharge from channels and lead to melting and calving at the terminus, a notable finding here is that the distribution of plume melt across the terminus is far more uniform in 2017 than in 2012 (Figure 32). This key feature in our simulations reflects the impact of reduced channelisation at the terminus, with fewer and smaller channels forming ephemeral points of discharge along the terminus in 2017. Maximum melt rates in 2012 are higher, and their impact is localised and much more concentrated; whereas the lower melt rates present in 2017 are evenly spread across the calving front. This general pattern corroborates well with Slater et al. (2015); however, we model overall higher total melt (by 28%) from the more channelised situation in 2012 compared to the more distributed case in 2017. Given total surface melt is nearly three times higher in 2012 ($3.2x10^9$ m^3) than in 2017 ($1.3x10^9$ m^3), this indicates that the increased localisation of higher melt rates does have a powerful mitigating effect on total direct melt from plumes (though not on calving caused by melt-induced destabilisation of the front). However, this mitigating effect is not sufficient to completely balance the impact of these higher melt rates, leading to more plume melting overall. This, combined with the fact that we model 53% more calving events in 2012 than 2017, tends to support the argument made by Todd et al. (2019) that higher localised plume melt rates driven by channel discharge are more important in promoting calving and affecting glacier termini than lower, but more widespread, diffuse-drainage-driven melt rates.

The location of plumes in our model are consistent with observations. In 2012 (Figure 32a), we model two clear plume hotspots, one on the northern side of the terminus and one on the southern side, that line up well with observations of surfacing plume activity at Store (Figure 27, Figure 40). In 2017, the northern plume remains a hotspot for submarine melt, but the southern plume is smaller and less stationary, changing location (Figure 32b). This shows that the modelled subglacial drainage network has a relatively fixed northern outlet and a more mobile southern outlet.

*Figure 40 – Example of observed surfacing plumes and promontory collapse (blue ellipse) at the terminus of Store from 17th July 2017. **a** shows terminus at 11:10; **b** at 12:00; and **c** at 12:50. The red boxes marked 'N' and 'S' denote plumes surfacing in the northern and southern plume hotspots, respectively; in panel **c** the southern plumes are no longer visible and the two separate northern plumes have joined up. Photo is taken from northern side of fjord looking southwards. Photo credit: A. Abellan.*

The plume melt rates found in this study reach maximum values of 14 m d^{-1}. While these maximum rates are similar in magnitude to the ice velocity of around 16 m d^{-1} at the terminus of Store, the seasonal mean values of the daily maximum melt rates are below 5 m d^{-1} in both years (Table 7). While plume melting may not be a major determinant of terminus position of fast-flowing outlets like Store (Benn et al., 2017a; Cowton et al., 2019), it is worth pointing out, however, that higher plume melt coincides with the cessation of terminus advance and, in some cases, terminus retreat in our model (Figure 38, Figure 33).

6.5.2. Limitations and future work

The foregoing discussion has shown that the fully coupled model is capable of reproducing realistic behaviour of the tidewater-glacier system at Store and of offering novel insights into its behaviour. In addition to the limitations already noted, particularly the model's under-estimation of calving generally, and smaller calving events especially, there are some additional caveats to note.

The modelled terminus velocity is slower than observed (4000-5000 m a^{-1} compared to 6000 m a^{-1}), which may contribute to the under-estimation of calving. We attribute this to limitations in the sliding law and mesh resolution used in the model, making it difficult to replicate the small-scale changes in basal properties across the relatively narrow glacier trunk. Both years also show an overall terminus advance (Figure 38); while this is realistic for the low-melt year of 2017, this is not the case for 2012. The model also has a tendency to grow a large floating ice shelf in the southern part of the terminus (an instance of this is visible in Figure 39f), which is not observed at Store in reality. This suggests the model is over-estimating the stability of floating ice, likely for the same reason it under-estimates calving generally – i.e. the lack of pre-existing crevasses. If this ice shelf were to calve realistically, this would also contribute to resolving the terminus-advance issue described above. While the work presented here shows that our model captures full-thickness icebergs realistically, the calving criterion used does not allow the simulation of small icebergs, which would be expected to form a significant portion of the total calved ice volume (Walter et al., 2020). The work presented here would thus likely by improved by incorporation of additional calving processes, such as waterline erosion and blocks of ice toppling or breaking off due to pre-existing structural weaknesses in the subaerial portion of the terminus (Mallalieu et al., 2020).

In both simulated years, we also exclude events below 1 m^3 in size from this analysis, as they represent minor mesh adjustments made by the model to maintain mesh quality and should not be interpreted as real events. These excluded events represent 10% of the total catalogue of events in 2012 and 20% in 2017.

6.6. Conclusion

We find that the fully coupled model of Store generally reproduces the observed and previously modelled behaviour of the glacier well, with all model components interacting successfully. Comparison to available observational data shows that the model is capable of reproducing a range of glacier behaviour consistent with observations. We also demonstrate the high temporal variability of calving activity and suggest that long time series of observations are required if simple-yet-accurate calving laws are to be derived. Our results further make clear that changes in the terminus velocity are the main large-scale control on calving at Store, because of the strong topographic control on terminus position. The model also reproduces the subglacial hydrological system of Store in a way that compares well with previous work on the subject. The model predicts channelised drainage systems extending 5 km inland outside the melt season, up to 29 km inland in summer 2017, and 41 km inland in summer 2012, as the inclusion of two-way hydrology-ice feedback suppresses channel formation under thicker ice inland, something not well-calculated in the simpler model. We additionally show that higher meltwater inputs lead to more channelised drainage at the terminus, and more active plumes with higher melt rates that can have a greater impact on terminus stability and calving. For 2012, we posit that a truly efficient channelised drainage system was present at Store, which led to a late-summer slowdown of the terminus, an effect not modelled in the lower-melt year of 2017. However, subglacial water pressures still increased inland in 2012, pointing to the potential for velocity declines at the terminus to be countered by velocity increases farther upstream. Overall, we show the spatially variable nature of the coupled ice-hydrology system and its importance in determining the behaviour of the terminus and thus calving. The fully coupled nature of the model allows us to also demonstrate the likely lack of any hydrological or ice-dynamic memory at Store, with both years showing very similar glacier states at the end of the runs.

6.7. Acknowledgements

The research was supported by the European Research Council under the European Union's Horizon 2020 Research and Innovation Programme. The work is an output from grant agreement 683043 (RESPONDER). SJC also acknowledges financial assistance in the form of a studentship (NE/L002507/1) from the Natural Environment Research Council. The authors thank Marion Bougamont, Tom Cowton, Donald Slater and Thomas Zwinger for productive discussions, as well as Olivier Gagliardini and Peter Råback for support with numerical modelling and Brice Noël who provided the RACMO data, and Nolwenn Chauché who provided the data for the ambient conditions in the fjord. DEMs provided by the Polar Geospatial Center under NSF-OPP awards 1043681, 1559691, and 1542736. DS acknowledges funding from NSF OPP-1418256.

7. Synthesis and Conclusion

'Sing and rejoice, ye people of the Tower of Guard,

for your watch hath not been in vain,

and the Black Gate is broken,

and your King hath passed through,

and he is victorious.'

-An Eagle, The Lord of the Rings, Book 6, Ch. V

This thesis has presented a dataset of calving activity at Store Glacier (Store) derived from a terrestrial radar interferometer (TRI) that represents a heretofore-unseen combination of length and detail for calving at a Greenlandic tidewater glacier (Chapter 4). In parallel, an uncoupled model of subglacial hydrology and plume melting at the calving front has been developed, applied to Store, and compared to sparse borehole and calving-front observations (Chapter 5). This was then used as a base for the development of a fully coupled model that includes ice flow, calving processes, subglacial hydrology and plume melting, which was applied to Store (Chapter 6). This final section summarises the findings from the previous three chapters and considers what insights these provide into the behaviour of tidewater glaciers and the performance of the model. It also validates the fully coupled model against the TRI observations, as well as comparing its results to those from the uncoupled model. An overall summary is then provided as a conclusion to this dissertation.

7.1. Model compared to observations

This section summarises the model's performance against observational data. Section 7.1.1 considers the uncoupled and fully coupled models' performance compared to observations of Store available before the dataset presented in Chapter 4 was gathered. Section 7.1.2 then evaluates how well the fully coupled model performs against this novel dataset.

7.1.1. Model compared to previous work

The uncoupled model can be validated against a few direct observations of the subglacial drainage system from boreholes (Doyle et al., 2018a) and of melting rates at the calving front (Chauché, 2016). Dealing with the borehole observations first, these recorded an active high-pressure, distributed system 30 km inland from the terminus of Store in 2014-15. The uncoupled model run for summer 2017 is the best comparator for these observations, as melt that year was more similar to 2014 and 2015 than in the high-melt year of 2012, the other simulated year. The model results

show larger channels (>1 m^2 in cross-sectional area) reaching to around the 30 km mark in 2017, with a high-pressure, distributed drainage system dominating from this point inland. This indicates that the model is generally correctly reproducing the evolution of the subglacial drainage system and suggests that our parameter choices are sensible.

Where the model does less well is in replicating observed plume melting. Winter-time melt rates are about half those found by Chauché (2016). In summer, the mean maximum plume melt rates fall within the range of observed melt from Chauché (2016) and previous modelling work (Xu et al., 2013), but the terminus-averaged melt rates are lower. However, under-estimation of plume melt rates is a consistent problem in all plume-modelling studies (e.g. Ezhova et al., 2018; Slater et al., 2016; Sutherland et al., 2019), so the results in this dissertation are part of this wider pattern, rather than being a problem specific to this model. It may also be that the freshwater flux estimated by Chauché (2016) is too high, which would lead to over-estimation of melt rates.

The spatial pattern of plume melting at the terminus may therefore offer a more useful validation of this part of the model. Plumes at Store are observed persistently surfacing on both the northern and southern sides of the terminus. The uncoupled model performs well at simulating the northern plume hotspot, but is less effective on the southern side, likely because this part of the terminus is floating, so the model's simplified grounding line makes it less able to accurately replicate what is occurring in this region.

Based on this sparse observational dataset, it therefore seems that the uncoupled model is mostly consistent with what is known about the subglacial and calving-front hydrology of Store, with inaccuracies being due to known shortcomings in all models (plume melt rates; an area of active research) or known over-simplifications in this model in particular (plume locations; better represented in the more complex model in Chapter 6).

The fully coupled model performs similarly well against these observations, and it does better reproduce the observed location of surfacing plumes, suggesting that the more realistic representation of the grounding line improved model functioning. The addition of full coupling to glacier dynamics to the model also allows us to make a comparison to the data gathered for 2012 at Store by Moon et al. (2014). We find that the model reproduces the observed velocity profile for Store well. The model also produces behaviour consistent with observations of hydrologically induced acceleration in the interior of Greenland (Doyle et al., 2014) and deceleration at lower elevations (Tedstone et al., 2015; van de Wal et al., 2008), as well as observed styles of calving (see Chapter 6.5.1).

7.1.2. Fully coupled model compared to TRI observations

The TRI observational record provides an unprecedented level of detail on the calving behaviour of a large, Greenlandic tidewater glacier. An important point to note in this section is that volumes from the TRI data are always sub-aerial calving volumes only, regardless of the actual size of the calving event, and refer to the northern half of the calving front of Store. Volumes from the model are always the full size of calving events and refer to the entire calving front.

A clear bimodal distribution of calving is found (Figure 8), with a peak in event size at 10^4 m^3 and another at 10^5 m^3, though, as the TRI can only record sub-aerial calving volume, the true location of this peak is likely to be closer to 10^6 m^3, as I show that the grounded portion of Store's calving front is very near floatation, so the volume of submarine ice is consequently nine times greater than the volume of sub-aerial ice. Volumes derived from the TRI record concord well with those from an independent set of UAV observations, and reveal that what appeared to be a single large calving event was actually composed of 48 smaller events over the 12-hour period between UAV flights (Section 4.5.1).

The TRI record also shows that there is no single clear environmental predictor of calving activity, with many factors contributing. The removal of ice mélange leads to a doubling in the number of events, and more, larger events, whilst visible surfacing plumes equate with a 70% increase in calving event frequency, but biased heavily towards smaller events, such that the observed volume loss only increases by 3% (Section 4.5.4). Surface melt has some impact on the *number* of calving events, but not on the magnitude distribution of these events (i.e. not on the *size* of each individual event). Overall, the record shows that calving behaviour at Store is extremely variable on daily and weekly timescales, and warns against classifying glaciers based on a supposed dominant calving mechanism (Fried et al., 2018). It also makes clear that deriving a simple power law for calving from a short time series of data is unlikely to be truly representative of a glacier's total calving behaviour. The record does offer some support for the theory of calving fronts as self-organised critical systems (Åström et al., 2014), however, which would explain the difficulties faced in modelling more generally of identifying simple predictors for calving.

To further validate the fully coupled model, we compare its calving results to this observational record of calving at Store. We model 113 calving events between the 5th and 27th July 2017, of which we include 86 in this analysis, as these were above the threshold of TRI detectability of 4,000 m^3 imposed by the processing method (see Chapter 4.3.3). These 86 events had a mean size of 730,000 m^3 to compare against the observational record from the TRI for the same period. The model includes events from across the terminus, not just the northern side observed by the TRI, however,

as restricting the analysis in this manner would lead to too few modelled calving events from which to draw conclusions. The distribution of events shows a major peak in the 10^5-10^6 m^3 volume range, with a small subsidiary peak at 10^4 m^3 (Figure 41). Events below 10^5 m^3 represent only 10% of the modelled calving events and less than 1% of the total volume loss. The largest events (>10^6 m^3) represent a further fifth of the modelled total, and 61% of the total volume loss, meaning that the major peak between 10^5 and 10^6 m^3 accounts for 70% of the total catalogue and 40% of losses by volume.

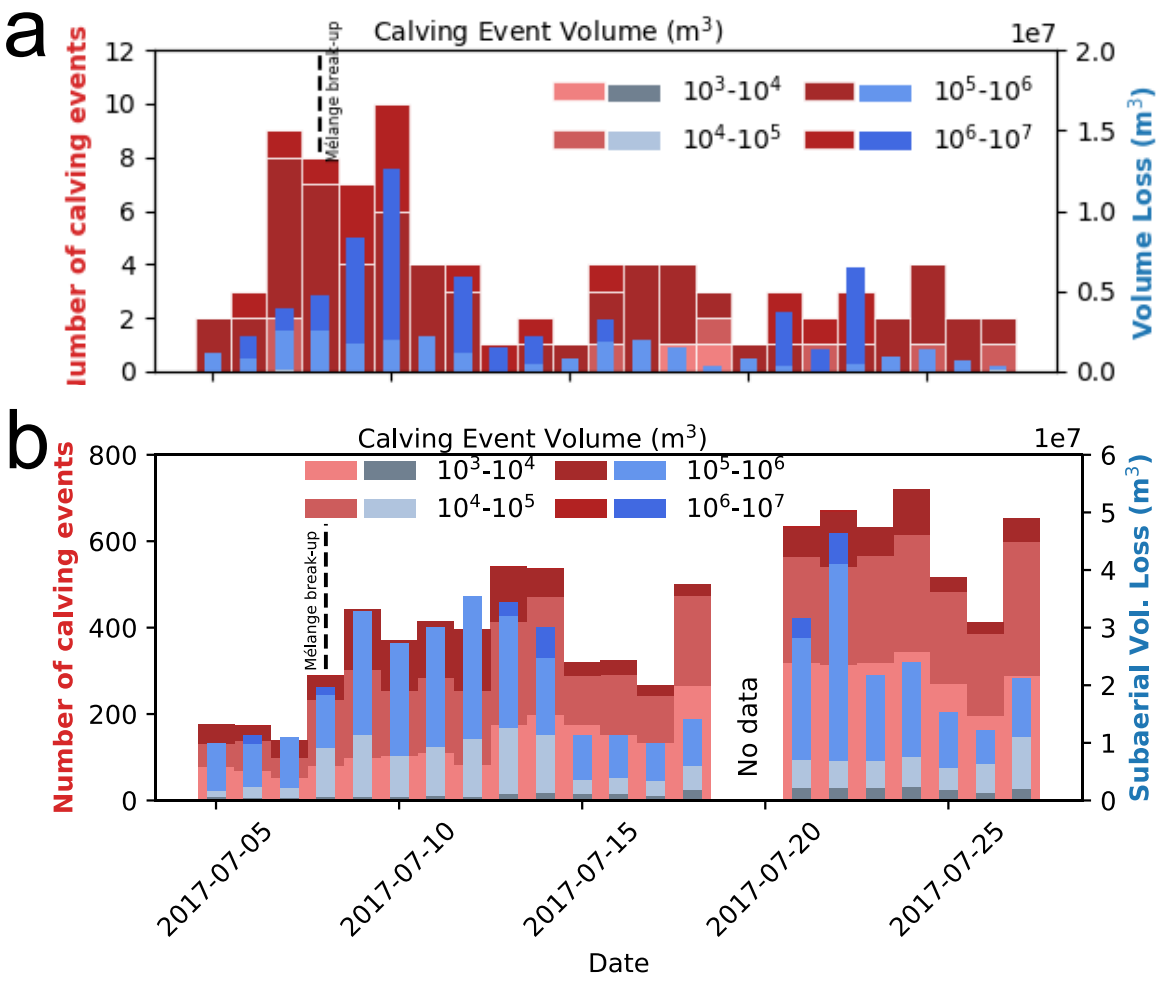

*Figure 41 – **a** Time series of modelled calving events at Store between 5th and 27th July 2017. **b** Time series of observed calving events over same period as **a**, taken from Chapter 4, showing northern half of calving front and subaerial volumes only. Bars stacked by volume of event. Daily counts are shown by red bars; cumulative volumes by the blue bars. Vertical black line shows timing of mélange break-up. Note that events below 4,000 m³ in size are not shown.*

In terms of temporal distribution of the modelled calving events (Figure 41a), there is a clear peak in calving activity in and around mélange break-up, simulated to have occurred on the 8th July, as in the observed TRI record. Particularly, calving volumes and the number of the largest category of events

(10^6-10^7 m^3) are at their highest in the two days following mélange removal, with both counts and volumes peaking on the 10th July. These two days see 7/19 of these largest calving events occurring, representing 25% of the total volume loss for the entire three-week period. The model also produces a smaller cluster of stronger calving activity from the 21st-23rd July, where five more largest-category events occur, representing a further 15% of the total volume loss.

Qualitatively the fully coupled model is in overall good agreement with the observed calving behaviour of Store (Chapter 4). The two clusters of modelled higher volume loss (Figure 41a) – the first on the 9th-10th July and the second on the 21st-23rd – with reduced calving in-between, are consistent with equivalent observed periods of increased calving activity from the 9th to the 14th and 21st to 22nd, with a quieter period in-between (Figure 41b). The model also reproduces the preponderance of larger calving events in the aftermath of mélange break-up as observed. This indicates the model captures some of the most fundamental drivers of calving behaviour at Store, although not all, as we discuss below.

The mean modelled calving event is an order of magnitude larger than the observed equivalent, which is to be expected, as the modelled volumes are the total calved volume, whereas the observed volumes are purely the sub-aerial portion of this. The 1:10 ratio between modelled total calving volume and the observed sub-aerial fraction is consistent with Store's terminus being either fully afloat (southern end) or close to floatation (northern end). However, it is notable that the number of modelled events – 86 – is two orders of magnitude smaller than the observed number of events – 8,026 – and that the model is particularly unable to reproduce the observed peak of smaller events in the 10^3-10^4 m^3 volume range. The larger events with a peak in the 10^5-10^6 m^3 range are, on the other hand, in good overall agreement with the true magnitude of large observed events, clustered around a similar volumetric range (Chapter 4). This indicates that our model captures full-thickness icebergs with a good degree of realism, but that it does not capture the smaller icebergs, which are observed to break off the glacier as well. We consider this disagreement to be the result of the calving criterion in our model, which is based on full-thickness calving events caused by crevasses (surface or basal) penetrating the entire thickness of the ice. It thus lacks the inclusion of other processes that may contribute to calving, including slabs of ice which topple or fall off when pre-existing fractures weaken the subaerial part of the terminus.

This validation exercise also reinforces the point made in Chapter 4 about the danger of deriving a power law for glacier calving from a short time series of observations. Indeed, looking at the three-week observational period described in Chapter 4, the model results suggest that this is a particularly unrepresentative period of calving for Store in that year (Figure 37b), with the third-

highest day of modelled calving occurring at the start of the record, before heading into the start of a three-week slump in calving activity that culminates in a calving minimum at the end of July. Consequently, attempting to define 'normal' calving activity and using that to derive any kind of general law would seem impractical without a month or more of observations, so that some sort of longer-term average can be calculated.

On balance, consequently, it is clear that the model is capturing the majority of the underlying physics well, but is missing some process(es) of particular relevance to smaller calving events. The most likely candidate is the absence of any kind of ice damage or crevasse memory in the model, with crevasses only opening if the local stress balance permits it, and subsequently closing and being 'forgotten' as the stress regime changes with ice flow. Calving events will clearly be greatly facilitated by the presence of these existing weaknesses in the ice, explaining the model's global under-estimation of calving, particularly its under-representation of smaller events. This is because the detachment of small blocks these smaller events represent is a failure mechanism more reliant on pure fracturing, and less on calving-front processes such as buoyancy or plume melting, which are included in the model.

7.2. Fully coupled versus uncoupled model

The uncoupled model shows that Store's subglacial drainage system, and the meltwater plumes it feeds, remain active throughout the winter, with channels extending up to 5 km inland, fed only by basal melt. When hydrology and glacier dynamics are uncoupled, in summer, these channels extend up to 55 km (2012) and 30 km (2017) inland, driving much higher plume activity at the calving front. One factor the model makes particularly clear is that the depth of subglacial meltwater discharge is critically important to the strength of the resulting plume. At Store, even large volumes of melt discharged into the relatively cool water at depths of 300 m or less lead to little melting, while even small discharges at greater depths can mix in the warmer ambient fjord water and achieve higher melt rates (Section 5.5.1). It is therefore probable that deep-grounded tidewater glaciers in Greenland experience high continuous submarine melt from plumes (up to or exceeding 1 m d^{-1} in places), even in winter. The uncoupled model also makes it clear that plume melt is not well-correlated with surface melt, with storage in the subglacial hydrological system acting to decouple one from the other; and that several days of high surface melt are required to expand and channelise subglacial drainage systems effectively. Individual high-melt days lead to water pressure spikes, but are not sufficient to cause widespread channelisation.

In terms of the general subglacial hydrological configuration of Store, incorporating the subglacial hydrological model, GlaDS, into the fully coupled model produces a very similar set of results to

those seen in the uncoupled model, including those described above. The general pattern of channel growth in both winter (compare Figure 31a, 31d in Chapter 6 with Figure 16b in Chapter 5) and summer (compare Figure 31c, 31f in Chapter 6 with Figure 22 in Chapter 5) – the 'peak' states reported in Chapter 6 are directly comparable with those labelled 'max' in Chapter 5; the 'end' states in Chapter 6 are also a good proxy for the 'Winter' simulation in Chapter 5. Although Chapter 6 is based on a fully coupled model, we find the response of the hydrological system to surface-melt inputs to be broadly similar to that seen in Chapter 5 (compare Figure 33 in Chapter 6 with Figure 20 and Figure 21 in Chapter 5), with channelisation (Figure 33) and water pressure (Figure 34) showing a strong dependency on the timing of spikes and troughs in the surface-melt input. The correlation coefficients of 0.75 and 0.61 for the relationship between surface melt and water pressure in 2012 and 2017, respectively, in the fully coupled model compare favourably with the coefficients of 0.67 and 0.77 for the JJA melt period in Chapter 5. This indicates that the accommodation of surface meltwater in the basal drainage system is not significantly altered when hydrology and ice flow are coupled. We also find a similar lack of relationship in the fully coupled model between surface melting and plume melting as seen in the uncoupled model – for the JJA period in Chapter 6, we find that a linear regression suggests surface melt explains only 8% of the variability in plume melt in 2012, and 27% in 2017, values which are broadly similar with those in Chapter 5.

One area where there is a clear, physically based difference between the subglacial drainage system in the fully coupled model compared to the uncoupled model, though, is with regards to the maximum extent of channelisation in the high-melt year of 2012. In the uncoupled model, channels over 1 m^2 in cross-sectional area grow up to 55 km inland; in the fully coupled model, they reach only 41 km. This is the result of the two-way coupling between the ice and the hydrology suppressing channel growth as velocities and water pressures increase under the influence of rising surface melt, leading to localised ice thickening, as farther-downstream areas slow down due to increasing channelisation. This effect is absent from the uncoupled model. In the low-melt year of 2017, though, very little difference in drainage system extent is observed, as there was insufficient melt to form channels far enough inland that this feedback exerts a major control on their formation and growth. This suppression of channels inland accords well with that expected from observations and theory (Dow et al., 2015; Meierbachtol et al., 2013), suggesting that the fully coupled model is performing markedly better in these regions than the uncoupled model.

The other important difference between the two models is with regards to plume-melt locations. For 2012, the fully coupled model produces two plume-melting hotspots that line up very well with the observed locations of surfacing plumes at Store, indicating that over-simplification of the grounding line was the key barrier to accurately simulating these in the uncoupled model. In 2017, however,

the fully coupled model fails to reproduce the observed southern plume, suggesting that this drainage pathway is of secondary importance in the model compared to its northern equivalent. Based on the observed size of the surfacing plumes, this seems to be incorrect – more water is discharged in the south than in the north – and is most likely due to inaccuracies in the basal DEM creating small changes in the near-flat hydraulic potential of the terminus region (Vore et al., 2019). These then cause the model to unrealistically favour the northern drainage route.

Therefore, from a purely hydrological point of view, the fully coupled model is unlikely to be necessary, unless simulations are being conducted for thicker ice in the accumulation zone of an ice sheet, or plume locations need to be modelled to a high degree of accuracy. A simplified simulation will produce a good approximation of a glacier's subglacial drainage system if that is the only output required. However, the fully coupled model does provide several novel insights into the overall functioning of the whole tidewater-glacier system, which is covered in the next section.

7.3. The behaviour of tidewater glaciers

The uncoupled and fully coupled models both show a good overall correspondence to the limited observational evidence for the subglacial hydrology of Store, whilst the fully coupled model is mostly qualitatively consistent with the validation dataset, if not quantitatively. This represents a step change in the coupled modelling of tidewater glaciers, with this dissertation marking the first time both subglacial hydrology and calving have been included and coupled in the same model; the fact that the model also produces results that bear up well in the face of reality is a strong argument for its essential validity. However, to be considered worthwhile, both the uncoupled and fully coupled models need to show some novel insights into tidewater-glacier behaviour. This is especially the case given the complexity and computational expense of the model. Re-running the relaxation for the fully coupled model (see Section 7.2), now I have it all set up, would likely take two months of computer time; the final fully coupled experiments each took 7-10 days of computer time. Clearly, the use case for the fully coupled model needs to be strong to justify such computational expense.

As discussed above, it is already clear that the interaction between hydrology and ice flow in the fully coupled model results in a significantly better simulation of the subglacial hydrology in inland regions under thicker ice and in accurately specifying plume locations, compared to the uncoupled model, which does not feature these interactions. Where the model really excels, however, is in showing up the intricate inter-dependencies of the whole tidewater-glacier system. The results show that terminus velocity is clearly the main large-scale control on calving, but that this terminus velocity is very much dependent on surface-melt driven changes in the configuration of the subglacial hydrological network. The fully coupled model also makes clear the unusualness of the

validation period in 2017 – at the start of the record, the model records its third-highest calving day, before entering a three-week period of the lowest modelled calving all year. This underscores the point raised above about the difficulty of basing calving laws on short observational datasets.

The fully coupled model also allows some further key hydrological-ice dynamic points to be investigated. A major outcome of the model results is that the fewer, larger, more channelised plumes in 2012 are a central factor in causing greater numbers of calving events and in driving terminus retreat in the summer; a retreat not seen with the more evenly distributed plume melting of 2017. This has been theorised previously (Todd et al., 2019), but having it appear unprompted in a physically based model is a powerful indication that it may be a real effect. If so, this would have implications for tidewater-glacier stability across Greenland and elsewhere, as warmer future climates should lead to more melt and more channelised subglacial drainage systems.

The fully coupled model also implies that there is a channelisation threshold at Store within the range of current melt levels. In 2012, the terminus shows a velocity profile indicative of complete channelisation; in 2017, this is not the case, so the threshold at which the terminus becomes fully channelised lies somewhere between the two cases. Water pressures, overall, though, across the entire model domain, increase in summer in both modelled years, showing that this fully channelised system is limited to the lower reaches of the glacier, even in 2012. The terminus may slow down, but inland areas will consequently speed up in high-melt years, leading to localised thickening; a pattern similar to that seen in the land-terminating parts of the ice sheet (Davison et al., 2019), but modelled for the first time on a tidewater glacier here.

The simulation of the full glacier system additionally allows me to consider how far the entire system shows any memory of high melt, i.e. how far the effects of one extreme year persist into the following year(s) and condition future ice behaviour. There has been some suggestion that this is the case for the land-terminating margins of the GrIS (Tedstone et al., 2015), but the fully coupled model shows little evidence of this occurring at Store. The end state of the glacier in 2012 and 2017 is very similar, with the exception of a slightly retreated terminus in 2012, which looks to be re-advancing such that it would have reached the same position as 2017 before the next melt season began. The underlying mechanism for this behaviour (i.e. a memory effect) in south-west Greenland has been suggested to be dewatering of poorly connected areas of the bed (Hoffman et al., 2016); it is likely that the faster flow and thicker ice of tidewater glaciers, and the consequent greater basal water production mean that this dewatering mechanism is less applicable in these environments. For Store, at least, it therefore seems likely that several years of melt at least equal in magnitude to 2012 would be required to force it to begin retreating. Store's stability, however, is a product of its

topographic setting; this stability should therefore not be looked for at similar glaciers elsewhere in Greenland, but will be very dependent on local factors.

If there is one point that re-appears time and again in this dissertation, however, it is that tidewater glaciers are extremely complex environments that defy simple classification. Both the TRI dataset and the model results show how variable calving is and how basing any kind of classification or law on short datasets of calving observations is challenging. The model results also show how dynamic all elements of the system are and how closely and sensitively they inter-link, which can make any kind of approximation ineffectual, certainly on shorter timescales. It is likely that smaller tidewater glaciers are more amenable to simplification, however, as their slower flow and smaller size would reduce the degree of variability observed on a glacier as fast and large as Store.

Overall, therefore, the fully coupled model simulates Store with a worthwhile degree of accuracy, without having been calibrated specifically for this glacier (the only exception being the sliding coefficient in the sliding law, which has been tuned for Store). This indicates that the model has managed to largely capture the underlying physical processes that lead to the observed behaviour of tidewater glaciers. It has also shown that it is capable of providing useful new information on the functioning of these systems, which suggests there is a use case for it, despite its computational expense.

In terms of further work on the model, the foregoing discussion has made clear that the main second-order process not yet included in the model is the lack of ice damage or crevasse memory in any form, which is the main reason for the inaccurate terminus advance. Attempts have been made to include ice-damage schemes in models previously (Duddu and Waisman, 2013; Krug et al., 2014), but it would lead to further model complexity and computational expense. However, if computational power were to continue to improve, making the problem more tractable, this would be an interesting avenue to pursue. An improved model of mélange evolution and break-up would also be an intriguing addition, but this would require full simulation of at least part of the fjord, so is perhaps a bridge too far for the moment. And, of course, it would be interesting to apply the model to other glaciers, in Greenland or elsewhere, to see how far it successfully reproduces their behaviour.

7.4. Summary

This dissertation presents i) a three-week dataset of calving behaviour at Store Glacier, Greenland (Store), obtained using a terrestrial radar interferometer (TRI); ii) an uncoupled finite-element model of 2D subglacial hydrology and 1D plume melting applied to Store; and iii) a fully coupled 3D finite-

element model of ice flow, calving, subglacial hydrology and plume melting applied to Store and validated against the TRI dataset.

The TRI dataset provides a record of calving at a large Greenlandic tidewater glacier of unprecedented length and detail. It shows 8,026 calving events happening at Store in the three weeks from 5th to 27th July 2017, forming a bimodal distribution with a mean iceberg size of 48, 428 m^3, and with one peak at 10^4 m^3 (representing subaerial detachment of small blocks of ice) and another at 10^5 m^3 (representing full-thickness failures, meaning that this latter peak is likely nearer 10^6 m^3 because the TRI only records sub-aerial ice volumes). Comparing one 12-hour period to an independent UAV dataset shows only a 2% mismatch in calving volumes. I show that mélange break-up leads to a doubling of the number of calving events and that mélange presence preferentially suppresses small events, whilst the presence of visible meltwater plumes is associated with a 70% increase in calving event frequency, though only a 3% increase in volume loss, meaning that plumes preferentially promote smaller events. Higher surface melt, meanwhile, is associated with a larger number of calving events, but not a higher mass loss. Generally, the TRI record shows the highly variable nature of calving at Store and the difficulty of using a short time series of observations to derive any kind of meaningfully representative calving law. The record also shows some evidence for the calving front of Store being classed as a self-organised critical system, which would further underline the difficulties of finding simple predictors for its behaviour. Overall, the dataset indicates velocity (strongly linked to calving-front location) is the key determinant of calving activity, with environmental factors modulating this, but not dominating, which fits with the observations that the termini of calving glaciers tend to exist at certain stable points (as is the case at Store) where velocity and calving are able to balance (e.g. Catania et al., 2018; Rignot et al., 2016).

In parallel to the TRI dataset, I develop and apply a 2D subglacial-hydrology model (GlaDS) (Gagliardini and Werder, 2018; Werder et al., 2013) and a coupled 1D plume model (based on buoyant plume theory) (Jenkins, 2011; Slater et al., 2016) to Store. This represents the first time a coupled hydrology-plume model has been applied to a Greenlandic tidewater glacier. I show that GlaDS functions well in modelling Store's subglacial hydrological system, based on the limited observational evidence available, and demonstrate that this system remains active all year, including throughout winter, with plumes capable of producing melt rates of up to 1.1 m d^{-1} present, driven by a largely distributed drainage system extending to 45 km inland. In winter, significant channels (>1 m^2 in cross-sectional area) are furthermore confined to the lower 5 km of the glacier. In summer, these larger channels extend 55 km inland in a high-melt scenario (2012) and 30 km inland in a low-melt one (2017), driving plume melt rates of up to 12.6 m d^{-1} in the locality of large channel outlets (cf Chauché, 2016). I also show that there is little relationship at the day or week scale between

surface melt inputs to the hydrological system and plume melt outputs from it, and that individual peak days of surface melt are the main driver of hydrological system evolution, which is instead determined by longer-term periods of high or low melt input. I further suggest that the subglacial hydrological system, even at its largest extent in 2012, is incapable of fully evacuating the water at the base, leading to an overall increase in basal water pressures in summer despite increased channelisation.

Combining these two strands of development, I then develop and apply a 3D, fully coupled finite-element model of ice flow, calving, subglacial hydrology and plume melting to Store, and validate it against the TRI dataset. I show that the model qualitatively reproduces the calving behaviour of Store well, but quantitatively under-estimates it, particularly in regard to smaller calving events. The model also reinforces the point about the difficulty of establishing what 'normal' calving of a tidewater glacier looks like, and consequently finding a simple calving law. The coupled nature of the model allows me to demonstrate that hydrology-induced velocity changes at the terminus are the major large-scale control on calving behaviour and activity at Store. The coupled model produces similar hydrological results to the uncoupled model, but with some key areas of difference: principally that channel growth is suppressed under thicker ice inland, limiting the extent of the channel network to 40 km in summer 2012; and better localisation of plume-melt locations, owing to improved simulation of the grounding line. I further show that melt in 2012 allowed the terminus to fully channelise and slow down, but that this was still not sufficient to reduce basal water pressure and velocities inland, mirroring the situation observed in the land-terminating parts of the GrIS; in 2017, however, this channelisation did not occur, providing bounds on a threshold for terminus channelisation at Store. Unlike the land-terminating parts of the ice sheet, on the other hand, I additionally demonstrate that Store appears to have little hydrological or dynamic memory of even a high-melt year such as 2012, and posit this is because of greater water production at the bed, making dewatering mechanisms less viable.

Looking forward, the clear priority for further development of the fully coupled model presented here is some method to incorporate ice damage and pre-existing crevasses to facilitate calving at the terminus, as well as a more realistic approach towards the effect of mélange on the terminus. The former is chiefly a computational issue that will mainly be stymied by numerical technicalities; the latter has some elements of this, but would also be greatly assisted if more observational datasets of the typical thickness, rigidity and evolution of mélange in a range of tidewater settings were available. Additionally, more comprehensive observations of calving over a period of weeks or months at a range of tidewater glaciers would greatly assist in developing and validating calving models similar to the one presented in this dissertation. Given that the modelling undertaken in this

dissertation would have been unthinkable a decade before I started this PhD, and barely possible even 5 years before I started, I feel it likely that such modelling challenges will be overcome in the next decade, which would be a great boon to glaciology.

8. References

Ahlkrona, J., Lötstedt, P., Kirchner, N. and Zwinger, T.: Dynamically coupling the non-linear Stokes equations with the shallow ice approximation in glaciology: Description and first applications of the ISCAL method, J. Comput. Phys., 308, 1–19, doi:10.1016/j.jcp.2015.12.025, 2016.

Amundson, J. M. and Truffer, M.: A unifying framework for iceberg-calving models, J. Glaciol., 56(199), 822–830, doi:10.3189/002214310794457173, 2010.

Andrews, L. C., Catania, G. A., Hoffman, M. J., Gulley, J. D., Lüthi, M. P., Ryser, C., Hawley, R. L. and Neumann, T. A.: Direct observations of evolving subglacial drainage beneath the Greenland Ice Sheet, Nature, 514(7520), 80–83, doi:10.1038/nature13796, 2014.

Arthern, R. J., Hindmarsh, R. C. A. and Williams, C. R.: Flow speed within the Antarctic ice sheet and its controls inferred from satellite observations, J. Geophys. Res. Earth Surf., 120(7), 1171–1188, doi:10.1002/2014JF003239, 2015.

Aschwanden, A., Fahnestock, M. A., Truffer, M., Brinkerhoff, D. J., Hock, R., Khroulev, C., Mottram, R. and Khan, S. A.: Contribution of the Greenland Ice Sheet to sea level over the next millennium, Sci. Adv., 5(6), eaav9396, doi:10.1126/sciadv.aav9396, 2019.

Åström, J. A., Riikilä, T. I., Tallinen, T., Zwinger, T., Benn, D., Moore, J. C. and Timonen, J.: A particle based simulation model for glacier dynamics, The Cryosphere, 7(5), 1591–1602, doi:10.5194/tc-7-1591-2013, 2013.

Åström, J. A., Vallot, D., Schäfer, M., Welty, E. Z., O'Neel, S., Bartholomaus, T. C., Liu, Y., Riikilä, T. I., Zwinger, T., Timonen, J. and Moore, J. C.: Termini of calving glaciers as self-organized critical systems, Nat. Geosci., 7(12), ngeo2290, doi:10.1038/ngeo2290, 2014.

Banwell, A., Hewitt, I., Willis, I. and Arnold, N.: Moulin density controls drainage development beneath the Greenland ice sheet, J. Geophys. Res. Earth Surf., 121(12), 2015JF003801, doi:10.1002/2015JF003801, 2016.

Banwell, A. F., Willis, I. C. and Arnold, N. S.: Modeling subglacial water routing at Paakitsoq, W Greenland, J. Geophys. Res. Earth Surf., 118(3), 1282–1295, doi:10.1002/jgrf.20093, 2013.

Benn, D. I. and Åström, J. A.: Calving glaciers and ice shelves, Adv. Phys. X, 3(1), 1513819, doi:10.1080/23746149.2018.1513819, 2018.

Benn, D. I., Cowton, T., Todd, J. and Luckman, A.: Glacier Calving in Greenland, Curr. Clim. Change Rep., 1–9, doi:10.1007/s40641-017-0070-1, 2017a.

Benn, D. I., Åström, J., Zwinger, T., Todd, J., Nick, F. M., Cook, S., Hulton, N. R. J. and Luckman, A.: Melt-under-cutting and buoyancy-driven calving from tidewater glaciers: new insights from discrete element and continuum model simulations, J. Glaciol., 1–12, doi:10.1017/jog.2017.41, 2017b.

Bougamont, M., Christoffersen, P., Hubbard, A. L., Fitzpatrick, A. A., Doyle, S. H. and Carter, S. P.: Sensitive response of the Greenland Ice Sheet to surface melt drainage over a soft bed, Nat. Commun., 5, 5052, doi:10.1038/ncomms6052, 2014.

Bougamont, M., Christoffersen, P., Price, S. F., Fricker, H. A., Tulaczyk, S. and Carter, S. P.: Reactivation of Kamb Ice Stream tributaries triggers century-scale reorganization of Siple Coast ice flow in West Antarctica, Geophys. Res. Lett., 42(20), 8471–8480, doi:10.1002/2015GL065782, 2015.

Broeke, M. R. van den, Enderlin, E. M., Howat, I. M., Kuipers Munneke, P., Noël, B. P. Y., Berg, W. J. van de, Meijgaard, E. van and Wouters, B.: On the recent contribution of the Greenland ice sheet to sea level change, The Cryosphere, 10(5), 1933–1946, doi:https://doi.org/10.5194/tc-10-1933-2016, 2016.

Carroll, D., Sutherland, D. A., Shroyer, E. L., Nash, J. D., Catania, G. A. and Stearns, L. A.: Modeling Turbulent Subglacial Meltwater Plumes: Implications for Fjord-Scale Buoyancy-Driven Circulation, J. Phys. Oceanogr., 45(8), 2169–2185, doi:10.1175/JPO-D-15-0033.1, 2015.

Cassotto, R., Fahnestock, M., Amundson, J. M., Truffer, M., Boettcher, M. S., De La Peña, S. and Howat, I.: Non-linear glacier response to calving events, Jakobshavn Isbræ, Greenland, J. Glaciol., 1–16, doi:10.1017/jog.2018.90, 2018.

Catania, G. A., Stearns, L. A., Sutherland, D. A., Fried, M. J., Bartholomaus, T. C., Morlighem, M., Shroyer, E. and Nash, J.: Geometric Controls on Tidewater Glacier Retreat in Central Western Greenland, J. Geophys. Res. Earth Surf., 123(8), 2024–2038, doi:10.1029/2017JF004499, 2018.

Chandler, D. M., Wadham, J. L., Lis, G. P., Cowton, T., Sole, A., Bartholomew, I., Telling, J., Nienow, P., Bagshaw, E. B., Mair, D., Vinen, S. and Hubbard, A.: Evolution of the subglacial drainage system beneath the Greenland Ice Sheet revealed by tracers, Nat. Geosci., 6(3), 195–198, doi:10.1038/ngeo1737, 2013.

Chapuis, A. and Tetzlaff, T.: The variability of tidewater-glacier calving: Origin of event-size and interval distributions, J. Glaciol., 60(222), 622–634, doi:10.3189/2014JoG13J215, 2014.

Chapuis, A., Rolstad, C. and Norland, R.: Interpretation of amplitude data from a ground-based radar in combination with terrestrial photogrammetry and visual observations for calving monitoring of Kronebreen, Svalbard, Ann. Glaciol., 51(55), 34–40, doi:10.3189/172756410791392781, 2010.

Chauché, N.: Glacier-Ocean interaction at Store Glacier (West Greenland). Ph. D. Aberystwyth University, 2016.

Chauché, N., Hubbard, A., Gascard, J.-C., Box, J. E., Bates, R., Koppes, M., Sole, A., Christoffersen, P. and Patton, H.: Ice–ocean interaction and calving front morphology at two west Greenland tidewater outlet glaciers, The Cryosphere, 8(4), 1457–1468, doi:10.5194/tc-8-1457-2014, 2014.

Christoffersen, P., Mugford, R. I., Heywood, K. J., Joughin, I., Dowdeswell, J. A., Syvitski, J. P. M., Luckman, A. and Benham, T. J.: Warming of waters in an East Greenland fjord prior to glacier retreat: mechanisms and connection to large-scale atmospheric conditions, The Cryosphere, 5(3), 701, 2011.

Christoffersen, P., Bougamont, M., Hubbard, A., Doyle, S. H., Grigsby, S. and Pettersson, R.: Cascading lake drainage on the Greenland Ice Sheet triggered by tensile shock and fracture, Nat. Commun., 9(1), 1064, doi:10.1038/s41467-018-03420-8, 2018.

Chu, W., Schroeder, D. M., Seroussi, H., Creyts, T. T., Palmer, S. J. and Bell, R. E.: Extensive winter subglacial water storage beneath the Greenland Ice Sheet, Geophys. Res. Lett., 43(24), 12,484-12,492, doi:10.1002/2016GL071538, 2016.

Chudley, T. R., Christoffersen, P., Doyle, S. H., Abellan, A. and Snooke, N.: High-accuracy UAV photogrammetry of ice sheet dynamics with no ground control, The Cryosphere, 13(3), 955–968, doi:https://doi.org/10.5194/tc-13-955-2019, 2019.

Cook, S. J., Christoffersen, P., Todd, J., Slater, D. and Chauché, N.: Coupled modelling of subglacial hydrology and calving-front melting at Store Glacier, West Greenland, The Cryosphere, 14(3), 905–924, doi:https://doi.org/10.5194/tc-14-905-2020, 2020.

Cowton, T., Slater, D., Sole, A., Goldberg, D. and Nienow, P.: Modeling the impact of glacial runoff on fjord circulation and submarine melt rate using a new subgrid-scale parameterization for glacial plumes, J. Geophys. Res. Oceans, 120(2), 796–812, doi:10.1002/2014JC010324, 2015.

Cowton, T. R., Todd, J. A. and Benn, D. I.: Sensitivity of tidewater glaciers to submarine melting governed by plume locations, Geophys. Res. Lett., 0(ja), doi:10.1029/2019GL084215, 2019.

Csatho, B. M., Schenk, A. F., Veen, C. J. van der, Babonis, G., Duncan, K., Rezvanbehbahani, S., Broeke, M. R. van den, Simonsen, S. B., Nagarajan, S. and Angelen, J. H. van: Laser altimetry reveals complex pattern of Greenland Ice Sheet dynamics, Proc. Natl. Acad. Sci., 111(52), 18478–18483, doi:10.1073/pnas.1411680112, 2014.

Cuffey, K.M. and Paterson, W.S.B.: The physics of glaciers. Academic Press, 2010.

Das, S. B., Joughin, I., Behn, M. D., Howat, I. M., King, M. A., Lizarralde, D. and Bhatia, M. P.: Fracture Propagation to the Base of the Greenland Ice Sheet During Supraglacial Lake Drainage, Science, 320(5877), 778–781, doi:10.1126/science.1153360, 2008.

Davison, B. J., Sole, A. J., Livingstone, S. J., Cowton, T. R. and Nienow, P. W.: The influence of hydrology on the dynamics of land-terminating sectors of the Greenland Ice Sheet, Front. Earth Sci., 7, doi:10.3389/feart.2019.00010, 2019.

De Andrés, E., Slater, D. A., Straneo, F., Otero, J., Das, S. and Navarro, F.: Surface emergence of glacial plumes determined by fjord stratification, , doi:10.5194/tc-2019-264, 2020.

van Dongen, E., Jouvet, G., Walter, A., Todd, J., Zwinger, T., Asaji, I., Sugiyama, S., Walter, F. and Funk, M.: Tides modulate crevasse opening prior to a major calving event at Bowdoin Glacier, Northwest Greenland, J. Glaciol., 1–11, doi:10.1017/jog.2019.89, 2019.

Dow, C. F., Kulessa, B., Rutt, I. C., Doyle, S. H. and Hubbard, A.: Upper bounds on subglacial channel development for interior regions of the Greenland ice sheet, J. Glaciol., 60(224), 1044–1052, doi:10.3189/2014JoG14J093, 2014.

Dow, C. F., Kulessa, B., Rutt, I. C., Tsai, V. C., Pimentel, S., Doyle, S. H., van As, D., Lindbäck, K., Pettersson, R., Jones, G. A. and Hubbard, A.: Modeling of subglacial hydrological development following rapid supraglacial lake drainage, J. Geophys. Res. Earth Surf., 120(6), 2014JF003333, doi:10.1002/2014JF003333, 2015.

Dow, C. F., McCormack, F. S., Young, D. A., Greenbaum, J. S., Roberts, J. L. and Blankenship, D. D.: Totten Glacier subglacial hydrology determined from geophysics and modeling, Earth Planet. Sci. Lett., 115961, doi:10.1016/j.epsl.2019.115961, 2019.

Doyle, S. H., Hubbard, A., Fitzpatrick, A. A. W., van As, D., Mikkelsen, A. B., Pettersson, R. and Hubbard, B.: Persistent flow acceleration within the interior of the Greenland ice sheet, Geophys. Res. Lett., 41(3), 2013GL058933, doi:10.1002/2013GL058933, 2014.

Doyle, S. H., Hubbard, A., van de Wal, R. S. W., Box, J. E., van As, D., Scharrer, K., Meierbachtol, T. W., Smeets, P. C. J. P., Harper, J. T., Johansson, E., Mottram, R. H., Mikkelsen, A. B., Wilhelms, F., Patton, H., Christoffersen, P. and Hubbard, B.: Amplified melt and flow of the Greenland ice sheet driven by late-summer cyclonic rainfall, Nat. Geosci., 8(8), 647–653, doi:10.1038/ngeo2482, 2015.

Doyle, S. H., Hubbard, B., Christoffersen, P., Young, T. J., Hofstede, C., Bougamont, M., Box, J. E. and Hubbard, A.: Physical Conditions of Fast Glacier Flow: 1. Measurements From Boreholes Drilled to the Bed of Store Glacier, West Greenland, J. Geophys. Res. Earth Surf., 123(2), 324–348, doi:10.1002/2017JF004529, 2018.

Doyle, S., Hubbard, B., Christoffersen, P., Bougamont, M., Law, R., Chudley, T., Prior-Jones, M., and Schoonman, C.: Subglacial water pressure records from a fast-flowing outlet glacier in Greenland, EGU General Assembly 2020, Online, 4–8 May 2020, EGU2020-7271, https://doi.org/10.5194/egusphere-egu2020-7271, 2020.

Duddu, R. and Waisman, H.: A nonlocal continuum damage mechanics approach to simulation of creep fracture in ice sheets, Comput. Mech., 51(6), 961–974, doi:10.1007/s00466-012-0778-7, 2013.

Enderlin, E. M., Howat, I. M., Jeong, S., Noh, M.-J., van Angelen, J. H. and van den Broeke, M. R.: An improved mass budget for the Greenland ice sheet, Geophys. Res. Lett., 41(3), 2013GL059010, doi:10.1002/2013GL059010, 2014.

Evans, D. J. A., Livingstone, S. J., Vieli, A. and Ó Cofaigh, C.: The palaeoglaciology of the central sector of the British and Irish Ice Sheet: reconciling glacial geomorphology and preliminary ice sheet modelling, Quat. Sci. Rev., 28(7–8), 739–757, doi:10.1016/j.quascirev.2008.05.011, 2009.

Everett, A., Kohler, J., Sundfjord, A., Kovacs, K. M., Torsvik, T., Pramanik, A., Boehme, L. and Lydersen, C.: Subglacial discharge plume behaviour revealed by CTD-instrumented ringed seals, Sci. Rep., 8(1), 13467, doi:10.1038/s41598-018-31875-8, 2018.

Ezhova, E., Cenedese, C. and Brandt, L.: Dynamics of three-dimensional turbulent wall plumes and implications for estimates of submarine glacier melting, J. Phys. Oceanogr., doi:10.1175/JPO-D-17-0194.1, 2018.

Favier, L., Durand, G., Cornford, S. L., Gudmundsson, G. H., Gagliardini, O., Gillet-Chaulet, F., Zwinger, T., Payne, A. J. and Le Brocq, A. M.: Retreat of Pine Island Glacier controlled by marine ice-sheet instability, Nat. Clim. Change, 4(2), 117–121, doi:10.1038/nclimate2094, 2014.

de Fleurian, B., Gagliardini, O., Zwinger, T., Durand, G., Le Meur, E., Mair, D. and Råback, P.: A double continuum hydrological model for glacier applications, The Cryosphere, 8(1), 137–153, doi:10.5194/tc-8-137-2014, 2014.

de Fleurian, B., Morlighem, M., Seroussi, H., Rignot, E., van den Broeke, M. R., Kuipers Munneke, P., Mouginot, J., Smeets, P. C. J. P. and Tedstone, A. J.: A modeling study of the effect of runoff variability on the effective pressure beneath Russell Glacier, West Greenland, J. Geophys. Res. Earth Surf., 121(10), 2016JF003842, doi:10.1002/2016JF003842, 2016.

de Fleurian, B., Werder, M. A., Beyer, S., Brinkerhoff, D. J., Delaney, I., Dow, C. F., Downs, J., Gagliardini, O., Hoffman, M. J., Hooke, R. L., Seguinot, J. and Sommers, A. N.: SHMIP The subglacial hydrology model intercomparison Project, J. Glaciol., 1–20, doi:10.1017/jog.2018.78, 2018.

Flowers, G. E.: Modelling water flow under glaciers and ice sheets, Proc R Soc A, 471(2176), 20140907, doi:10.1098/rspa.2014.0907, 2015.

Forsberg, R., Sørensen, L. and Simonsen, S.: Greenland and Antarctica Ice Sheet Mass Changes and Effects on Global Sea Level, Surv. Geophys., 38(1), 89–104, doi:10.1007/s10712-016-9398-7, 2017.

Fried, M. J., Catania, G. A., Bartholomaus, T. C., Duncan, D., Davis, M., Stearns, L. A., Nash, J., Shroyer, E. and Sutherland, D.: Distributed subglacial discharge drives significant submarine melt at a Greenland tidewater glacier, Geophys. Res. Lett., 42(21), 2015GL065806, doi:10.1002/2015GL065806, 2015.

Fried, M. J., Catania, G. A., Stearns, L. A., Sutherland, D. A., Bartholomaus, T. C., Shroyer, E. and Nash, J.: Reconciling drivers of seasonal terminus advance and retreat at thirteen central west Greenland tidewater glaciers, J. Geophys. Res. Earth Surf., 0(ja), doi:10.1029/2018JF004628, 2018.

Fürst, J. J., Durand, G., Gillet-Chaulet, F., Tavard, L., Rankl, M., Braun, M. and Gagliardini, O.: The safety band of Antarctic ice shelves, Nat. Clim. Change, 6(5), 479–482, doi:10.1038/nclimate2912, 2016.

Gagliardini, O. and Werder, M. A.: Influence of increasing surface melt over decadal timescales on land-terminating Greenland-type outlet glaciers, J. Glaciol., 1–11, doi:10.1017/jog.2018.59, 2018.

Gagliardini, O., Cohen, D., Råback, P. and Zwinger, T.: Finite-element modeling of subglacial cavities and related friction law, J. Geophys. Res. Earth Surf., 112(F2), F02027, doi:10.1029/2006JF000576, 2007.

Gagliardini, O., Zwinger, T., Gillet-Chaulet, F., Durand, G., Favier, L., de Fleurian, B., Greve, R., Malinen, M., Martín, C., Råback, P., Ruokolainen, J., Sacchettini, M., Schäfer, M., Seddik, H. and Thies, J.: Capabilities and performance of Elmer/Ice, a new-generation ice sheet model, Geosci. Model Dev., 6(4), 1299–1318, doi:10.5194/gmd-6-1299-2013, 2013.

Gagliardini, O., Brondex, J., Gillet-Chaulet, F., Tavard, L., Peyaud, V. and Durand, G.: Brief communication: Impact of mesh resolution for MISMIP and MISMIP3d experiments using Elmer/Ice, The Cryosphere, 10(1), 307–312, doi:10.5194/tc-10-307-2016, 2016.

Gillet-Chaulet, F., Gagliardini, O., Seddik, H., Nodet, M., Durand, G., Ritz, C., Zwinger, T., Greve, R. and Vaughan, D. G.: Greenland ice sheet contribution to sea-level rise from a new-generation ice-sheet model, The Cryosphere, 6(6), 1561–1576, doi:10.5194/tc-6-1561-2012, 2012.

Gillet-Chaulet, F., Durand, G., Gagliardini, O., Mosbeux, C., Mouginot, J., Rémy, F. and Ritz, C.: Assimilation of surface velocities acquired between 1996 and 2010 to constrain the form of the basal friction law under Pine Island Glacier, Geophys. Res. Lett., 2016GL069937, doi:10.1002/2016GL069937, 2016.

Gladstone, R. M., Warner, R. C., Galton-Fenzi, B. K., Gagliardini, O., Zwinger, T. and Greve, R.: Marine ice sheet model performance depends on basal sliding physics and sub-shelf melting, The Cryosphere, 11(1), 319–329, doi:10.5194/tc-11-319-2017, 2017.

Gong, Y., Zwinger, T., Cornford, S., Gladstone, R., Schäfer, M. and Moore, J. C.: Importance of basal boundary conditions in transient simulations: case study of a surging marine-terminating glacier on Austfonna, Svalbard, J. Glaciol., 1–12, doi:10.1017/jog.2016.121, 2016.

Gong, Y., Zwinger, T., Åström, J., Altena, B., Schellenberger, T., Gladstone, R. and Moore, J. C.: Simulating the roles of crevasse routing of surface water and basal friction on the surge evolution of Basin 3, Austfonna ice cap, The Cryosphere, 12(5), 1563–1577, doi:10.5194/tc-12-1563-2018, 2018.

Hall, D. K., Comiso, J. C., DiGirolamo, N. E., Shuman, C. A., Key, J. R. and Koenig, L. S.: A Satellite-Derived Climate-Quality Data Record of the Clear-Sky Surface Temperature of the Greenland Ice Sheet, J. Clim., 25(14), 4785–4798, doi:10.1175/JCLI-D-11-00365.1, 2012.

Hall, D. K., Comiso, J. C., DiGirolamo, N. E., Shuman, C. A., Box, J. E. and Koenig, L. S.: Variability in the surface temperature and melt extent of the Greenland ice sheet from MODIS, Geophys. Res. Lett., 40(10), 2114–2120, doi:10.1002/grl.50240, 2013.

Hewitt, I. J.: Subglacial Plumes, Annu. Rev. [online] Available from: https://ora.ox.ac.uk/objects/uuid:5670898b-df2c-4de5-804a-0ba1c8e5677e/download_file?file_format=pdf&safe_filename=plumes.pdf&type_of_work=Journal+article (Accessed 11 June 2019), 2019.

Hewitt, I. J., Schoof, C. and Werder, M. A.: Flotation and free surface flow in a model for subglacial drainage. Part 2. Channel flow, J. Fluid Mech., 702, 157–187, doi:10.1017/jfm.2012.166, 2012.

Hoffman, M. J., Andrews, L. C., Price, S. A., Catania, G. A., Neumann, T. A., Lüthi, M. P., Gulley, J., Ryser, C., Hawley, R. L. and Morriss, B.: Greenland subglacial drainage evolution regulated by weakly connected regions of the bed, Nat. Commun., 7, doi:10.1038/ncomms13903, 2016.

Hofstede, C., Christoffersen, P., Hubbard, B., Doyle, S. H., Young, T. J., Diez, A., Eisen, O. and Hubbard, A.: Physical conditions of fast glacier flow: 2. Variable extent of anisotropic ice and soft basal sediment from seismic reflection data acquired on Store Glacier, West Greenland: Subglacial patches of Store Glacier, J. Geophys. Res. Earth Surf., doi:10.1002/2017JF004297, 2018.

Hopwood, M. J., Carroll, D., Browning, T. J., Meire, L., Mortensen, J., Krisch, S. and Achterberg, E. P.: Non-linear response of summertime marine productivity to increased meltwater discharge around Greenland, Nat. Commun., 9(1), 3256, doi:10.1038/s41467-018-05488-8, 2018.

How, P., Schild, K., Benn, D., Noormets, R., Kirchner, N., Luckman, A., Vallot, D., Hulton, N. and Borstad, C.: Calving controlled by melt-under-cutting: detailed calving styles revealed through time-lapse observations, Ann. Glaciol. [online] Available from: https://doi.org/10.1017/aog.2018.28 (Accessed 31 October 2018), 2018.

Howat, I. M., Box, J. E., Ahn, Y., Herrington, A. and McFadden, E. M.: Seasonal variability in the dynamics of marine-terminating outlet glaciers in Greenland, J. Glaciol., 56(198), 601–613, doi:10.3189/002214310793146232, 2010.

Hubbard, A.: High-Resolution Modeling of the Advance of the Younger Dryas Ice Sheet and Its Climate in Scotland, Quat. Res., 52(1), 27–43, doi:10.1006/qres.1999.2055, 1999.

Iken, A.: The Effect of the Subglacial Water Pressure on the Sliding Velocity of a Glacier in an Idealized Numerical Model, J. Glaciol., 27(97), 407–421, doi:10.3198/1981JoG27-97-407-421, 1981.

Iken, A. and Bindschadler, R. A.: Combined measurements of Subglacial Water Pressure and Surface Velocity of Findelengletscher, Switzerland: Conclusions about Drainage System and Sliding Mechanism, J. Glaciol., 32(110), 101–119, doi:10.3198/1986JoG32-110-101-119, 1986.

IPCC Special Report on the Ocean and Cryosphere in a Changing Climate [H.-O. Pörtner, D.C. Roberts, V. Masson-Delmotte, P. Zhai, M. Tignor, E. Poloczanska, K. Mintenbeck, A. Alegría, M. Nicolai, A. Okem, J. Petzold, B. Rama, N.M. Weyer (eds.)]. In press. 2020.

Jackson, R. H., Shroyer, E. L., Nash, J. D., Sutherland, D. A., Carroll, D., Fried, M. J., Catania, G. A., Bartholomaus, T. C. and Stearns, L. A.: Near-glacier surveying of a subglacial discharge plume: Implications for plume parameterizations, Geophys. Res. Lett., 44(13), 6886–6894, doi:10.1002/2017GL073602, 2017.

Jackson, R. H., Nash, J. D., Kienholz, C., Sutherland, D. A., Amundson, J. M., Motyka, R. J., Winters, D., Skyllingstad, E. and Pettit, E.: Meltwater intrusions reveal mechanisms for rapid submarine melt at a tidewater glacier, Geophys. Res. Lett., n/a(n/a), doi:10.1029/2019GL085335, 2019.

Jenkins, A.: Convection-Driven Melting near the Grounding Lines of Ice Shelves and Tidewater Glaciers, J. Phys. Oceanogr., 41(12), 2279–2294, doi:10.1175/JPO-D-11-03.1, 2011.

Joughin, I.: MEaSUREs Greenland Monthly Ice Sheet Velocity Mosaics from SAR and Landsat, Version 1. Boulder, Colorado USA. NASA National Snow and Ice Data Center Distributed Active Archive Center. doi: https://doi.org/10.5067/OPFQ9QDEUFFY, 2018.

Joughin, I., Das, S. B., King, M. A., Smith, B. E., Howat, I. M. and Moon, T.: Seasonal Speedup Along the Western Flank of the Greenland Ice Sheet, Science, 320(5877), 781–783, doi:10.1126/science.1153288, 2008.

Joughin, I., Smith, B. E. and Howat, I. M.: A complete map of Greenland ice velocity derived from satellite data collected over 20 years, J. Glaciol., 64(243), 1–11, doi:10.1017/jog.2017.73, 2018.

Joughin, I., Smith, B., Howat, I. and Scambos, T.: MEaSUREs Multi-year Greenland Ice Sheet Velocity Mosaic, Version 1. Boulder, Colorado USA. NASA National Snow and Ice Data Center Distributed Active Archive Center. doi: https://doi.org/10.5067/QUA5Q9SVMSJG, 2016.

Joughin, I., Shean, D. E., Smith, B. E. and Floricioiu, D.: A Decade of Variability on Jakobshavn Isbrae: Ocean Temperatures Pace Speed Through Influence on Mélange Rigidity, The cryosphere, 14(1), 211–227, doi:10.5194/tc-14-211-2020, 2020.

Jouvet, G., Weidmann, Y., Seguinot, J., Funk, M., Abe, T., Sakakibara, D., Seddik, H. and Sugiyama, S.: Initiation of a major calving event on the Bowdoin Glacier captured by UAV photogrammetry, The Cryosphere, 11(2), 911–921, doi:https://doi.org/10.5194/tc-11-911-2017, 2017.

Jouvet, G., Weidmann, Y., Kneib, M., Detert, M., Seguinot, J., Sakakibara, D. and Sugiyama, S.: Short-lived ice speed-up and plume water flow captured by a VTOL UAV give insights into subglacial hydrological system of Bowdoin Glacier, Remote Sens. Environ., 217, 389–399, doi:10.1016/j.rse.2018.08.027, 2018.

Kamb, B.: Sliding motion of glaciers: Theory and observation, Rev. Geophys., 8(4), 673–728, doi:10.1029/RG008i004p00673, 1970.

Khazendar, A., Borstad, C. P., Scheuchl, B., Rignot, E. and Seroussi, H.: The evolving instability of the remnant Larsen B Ice Shelf and its tributary glaciers, Earth Planet. Sci. Lett., 419, 199–210, doi:10.1016/j.epsl.2015.03.014, 2015.

Khazendar, A., Fenty, I. G., Carroll, D., Gardner, A., Lee, C. M., Fukumori, I., Wang, O., Zhang, H., Seroussi, H., Moller, D., Noël, B. P. Y., Broeke, M. R. van den, Dinardo, S. and Willis, J.: Interruption of two decades of Jakobshavn Isbrae acceleration and thinning as regional ocean cools, Nat. Geosci., 12(4), 277, doi:10.1038/s41561-019-0329-3, 2019.

King, M. D., Howat, I. M., Jeong, S., Noh, M. J., Wouters, B., Nöel, B. and van den Broeke, M. R.: Seasonal to decadal variability in ice discharge from the Greenland Ice Sheet, Cryosphere Discuss., 1–28, doi:10.5194/tc-2018-177, 2018.

Kjeldsen, K. K., Korsgaard, N. J., Bjørk, A. A., Khan, S. A., Box, J. E., Funder, S., Larsen, N. K., Bamber, J. L., Colgan, W., van den Broeke, M., Siggaard-Andersen, M.-L., Nuth, C., Schomacker, A., Andresen, C. S., Willerslev, E. and Kjær, K. H.: Spatial and temporal distribution of mass loss from the Greenland Ice Sheet since AD 1900, Nature, 528(7582), 396–400, doi:10.1038/nature16183, 2015.

Kleman, J., Hättestrand, C., Borgström, I. and Stroeven, A.: Fennoscandian palaeoglaciology reconstructed using a glacial geological inversion model, J. Glaciol., 43(144), 283–299, doi:10.3198/1997JoG43-144-283-299, 1997.

Konovalov, Y. V.: Inversion for basal friction coefficients with a two-dimensional flow line model using Tikhonov regularization, Res. Geophys., 2(2), 11, doi:10.4081/rg.2012.e11, 2012.

Krug, J., Weiss, J., Gagliardini, O. and Durand, G.: Combining damage and fracture mechanics to model calving, The Cryosphere, 8(6), 2101–2117, doi:10.5194/tc-8-2101-2014, 2014.

Larour, E., Utke, J., Csatho, B., Schenk, A., Seroussi, H., Morlighem, M., Rignot, E., Schlegel, N. and Khazendar, A.: Inferred basal friction and surface mass balance of the Northeast Greenland Ice Stream using data assimilation of ICESat (Ice Cloud and land Elevation Satellite) surface altimetry and ISSM (Ice Sheet System Model), The Cryosphere, 8(6), 2335–2351, doi:10.5194/tc-8-2335-2014, 2014.

Liu, W., Xie, S.-P., Liu, Z. and Zhu, J.: Overlooked possibility of a collapsed Atlantic Meridional Overturning Circulation in warming climate, Sci. Adv., 3(1), e1601666, doi:10.1126/sciadv.1601666, 2017.

Lliboutry, L.: General Theory of Subglacial Cavitation and Sliding of Temperate Glaciers, J. Glaciol., 7(49), 21–58, doi:10.3198/1968JoG7-49-21-58, 1968.

Luo, H., Castelao, R. M., Rennermalm, A. K., Tedesco, M., Bracco, A., Yager, P. L. and Mote, T. L.: Oceanic transport of surface meltwater from the southern Greenland ice sheet, Nat. Geosci., 9(7), 528–532, doi:10.1038/ngeo2708, 2016.

Lüthi, M., Funk, M., Iken, A., Gogineni, S. and Truffer, M.: Mechanisms of fast flow in Jakobshavns Isbræ, Greenland, Part III: measurements of ice deformation, temperature and cross-borehole conductivity in boreholes to the bedrock, J. Glaciol., 48(162), 369–385, 2002.

MacAyeal, D. R.: A tutorial on the use of control methods in ice-sheet modeling, J. Glaciol., 39(131) [online] Available from: http://www.igsoc.org:8080/journal/39/131/igs_journal_vol39_issue131_pg91-98.pdf (Accessed 4 January 2016), 1993.

Mahaffy, M. W.: A three-dimensional numerical model of ice sheets: Tests on the Barnes Ice Cap, Northwest Territories, J. Geophys. Res., 81(6), 1059–1066, doi:10.1029/JC081i006p01059, 1976.

Mair, D., Nienow, P., Willis, I. and Sharp, M.: Spatial patterns of glacier motion during a high-velocity event: Haut Glacier d'Arolla, Switzerland, J. Glaciol., 47(156), 9–20, doi:10.3189/172756501781832412, 2001.

Mair, D., Willis, I., Fischer, U. H., Hubbard, B., Nienow, P. and Hubbard, A.: Hydrological controls on patterns of surface, internal and basal motion during three "'spring events'": Haut Glacier d'Arolla, Switzerland, J. Glaciol., 49(167), 555–567, doi:10.3189/172756503781830467, 2003.

Mallalieu, J., Carrivick, J. L., Quincey, D. J., Smith, M. W. and James, W. H. M.: An integrated Structure-from-Motion and time-lapse technique for quantifying ice-margin dynamics, J. Glaciol., 63(242), 937–949, doi:10.1017/jog.2017.48, 2017.

Mallalieu, J., Carrivick, J. L., Quincey, D. J. and Smith, M. W.: Calving Seasonality Associated With Melt-Undercutting and Lake Ice Cover, Geophys. Res. Lett., 47(8), e2019GL086561, doi:10.1029/2019GL086561, 2020.

Martos, Y. M., Jordan, T. A., Catalan, M., Jordan, T. M., Bamber, J. L. and Vaughan, D. G.: Geothermal heat flux reveals the Iceland hotspot track underneath Greenland, Geophys. Res. Lett., 0(ja), doi:10.1029/2018GL078289, 2018.

Maxwell, D., Truffer, M., Avdonin, S. and Stuefer, M.: An iterative scheme for determining glacier velocities and stresses, J. Glaciol., 54(188), 888–898, 2008.

McMillan, M., Leeson, A., Shepherd, A., Briggs, K., Armitage, T. W. K., Hogg, A., Kuipers Munneke, P., van den Broeke, M., Noël, B., van de Berg, W. J., Ligtenberg, S., Horwath, M., Groh, A., Muir, A. and Gilbert, L.: A high-resolution record of Greenland mass balance, Geophys. Res. Lett., 43(13), 2016GL069666, doi:10.1002/2016GL069666, 2016.

Mcnabb, R. W., Hock, R., O'Neel, S., Rasmussen, L. A., Ahn, Y., Braun, M., Conway, H., Herreid, S., Joughin, I., Pfeffer, W. T., Smith, B. E. and Truffer, M.: Using surface velocities to calculate ice thickness and bed topography: a case study at Columbia Glacier, Alaska, USA, J. Glaciol., 58(212), 1151–1164, doi:10.3189/2012JoG11J249, 2012.

Meierbachtol, T., Harper, J. and Humphrey, N.: Basal Drainage System Response to Increasing Surface Melt on the Greenland Ice Sheet, Science, 341(6147), 777–779, doi:10.1126/science.1235905, 2013.

Moon, T., Joughin, I., Smith, B., van den Broeke, M. R., van de Berg, W. J., Noël, B. and Usher, M.: Distinct patterns of seasonal Greenland glacier velocity, Geophys. Res. Lett., 41(20), 2014GL061836, doi:10.1002/2014GL061836, 2014.

Morlighem, M., Rignot, E., Seroussi, H., Larour, E., Ben Dhia, H. and Aubry, D.: Spatial patterns of basal drag inferred using control methods from a full-Stokes and simpler models for Pine Island Glacier, West Antarctica, Geophys. Res. Lett., 37(14), n/a-n/a, doi:10.1029/2010GL043853, 2010.

Morlighem, M., Bondzio, J., Seroussi, H., Rignot, E., Larour, E., Humbert, A. and Rebuffi, S.: Modeling of Store Gletscher's calving dynamics, West Greenland, in response to ocean thermal forcing, Geophys. Res. Lett., 43(6), 2016GL067695, doi:10.1002/2016GL067695, 2016.

Morlighem, M., Williams, C. N., Rignot, E., An, L., Arndt, J. E., Bamber, J. L., Catania, G., Chauché, N., Dowdeswell, J. A., Dorschel, B., Fenty, I., Hogan, K., Howat, I., Hubbard, A., Jakobsson, M., Jordan, T. M., Kjeldsen, K. K., Millan, R., Mayer, L., Mouginot, J., Noël, B. P. Y., O'Cofaigh, C., Palmer, S., Rysgaard, S., Seroussi, H., Siegert, M. J., Slabon, P., Straneo, F., van den Broeke, M. R., Weinrebe, W., Wood, M. and Zinglersen, K. B.: BedMachine v3: Complete Bed Topography and Ocean Bathymetry Mapping of Greenland From Multibeam Echo Sounding Combined With Mass Conservation, Geophys. Res. Lett., 44(21), 11,051-11,061, doi:10.1002/2017GL074954, 2017.

Mortensen, J., Rysgaard, S., Arendt, K. E., Juul-Pedersen, T., Søgaard, D. H., Bendtsen, J. and Meire, L.: Local coastal water masses control heat levels in a West Greenland tidewater outlet glacier fjord, J. Geophys. Res. Oceans, 0(ja), doi:10.1029/2018JC014549, 2018.

Mosbeux, C., Gillet-Chaulet, F. and Gagliardini, O.: Comparison of adjoint and nudging methods to initialise ice sheet model basal conditions, Geosci Model Dev, 9(7), 2549–2562, doi:10.5194/gmd-9-2549-2016, 2016.

Mouginot, J., Rignot, E., Scheuchl, B., Fenty, I., Khazendar, A., Morlighem, M., Buzzi, A. and Paden, J.: Fast retreat of Zachariae Isstrom, northeast Greenland, Science, 350(6266), 1357–1361, doi:10.1126/science.aac7111, 2015.

Mouginot, J., Rignot, E., Bjørk, A. A., van den Broeke, M., Millan, R., Morlighem, M., Noël, B., Scheuchl, B. and Wood, M.: Forty-six years of Greenland Ice Sheet mass balance from 1972 to 2018, Proc. Natl. Acad. Sci., 201904242, doi:10.1073/pnas.1904242116, 2019.

Nienow, P. W., Sole, A. J., Slater, D. A. and Cowton, T. R.: Recent Advances in Our Understanding of the Role of Meltwater in the Greenland Ice Sheet System, Curr. Clim. Change Rep., 3(4), 330–344, doi:10.1007/s40641-017-0083-9, 2017.

Nye, J. F.: Water Flow in Glaciers: Jökulhlaups, Tunnels and Veins, J. Glaciol., 17(76), 181–207, doi:10.3198/1976JoG17-76-181-207, 1976.

O'Leary, M. and Christoffersen, P.: Calving on tidewater glaciers amplified by submarine frontal melting, The Cryosphere, 7(1), 119–128, doi:10.5194/tc-7-119-2013, 2013.

Palmer, S., Shepherd, A., Nienow, P. and Joughin, I.: Seasonal speedup of the Greenland Ice Sheet linked to routing of surface water, Earth Planet. Sci. Lett., 302(3–4), 423–428, doi:10.1016/j.epsl.2010.12.037, 2011.

Passalacqua, O., Gagliardini, O., Parrenin, F., Todd, J., Gillet-Chaulet, F. and Ritz, C.: Performance and applicability of a 2.5-D ice-flow model in the vicinity of a dome, Geosci Model Dev, 9(7), 2301–2313, doi:10.5194/gmd-9-2301-2016, 2016.

Pattyn, F., Schoof, C., Perichon, L., Hindmarsh, R. C. A., Bueler, E., de Fleurian, B., Durand, G., Gagliardini, O., Gladstone, R., Goldberg, D., Gudmundsson, G. H., Huybrechts, P., Lee, V., Nick, F. M., Payne, A. J., Pollard, D., Rybak, O., Saito, F. and Vieli, A.: Results of the Marine Ice Sheet Model Intercomparison Project, MISMIP, The Cryosphere, 6(3), 573–588, doi:10.5194/tc-6-573-2012, 2012.

Pętlicki, M. and Kinnard, C.: Calving of Fuerza Aérea Glacier (Greenwich Island, Antarctica) observed with terrestrial laser scanning and continuous video monitoring, J. Glaciol., 62(235), 835–846, doi:10.1017/jog.2016.72, 2016.

Petra, N., Zhu, H., Stadler, G., Hughes, T. J. R. and Ghattas, O.: An inexact Gauss–Newton method for inversion of basal sliding and rheology parameters in a nonlinear Stokes ice sheet model, J. Glaciol., 58(211), 889–903, doi:10.3189/2012JoG11J182, 2012.

Podgórski, J., Pętlicki, M. and Kinnard, C.: Revealing recent calving activity of a tidewater glacier with terrestrial LiDAR reflection intensity, Cold Reg. Sci. Technol., 151, 288–301, doi:10.1016/j.coldregions.2018.03.003, 2018.

Porter, C., Morin, P., Howat, I., Noh, M., Bates, B., Peterman, K., Keesey, S., Schlenk, M., Gardiner, J., Tomko, K., Willis, M., Kelleher, C., Cloutier, M., Husby, E., Foga, S., Nakamura, H., Platson, M., Wethington, M., Williamson, C., Bauer, G., Enos, J., Arnold, G., Kramer, W., Becker, P., Doshi, A., D'Souza, C., Cummens, P., Laurier, F., Bojesen, M.: "ArcticDEM", https://doi.org/10.7910/DVN/OHHUKH, Harvard Dataverse, V2, 2018.

Price, S. F., Payne, A. J., Howat, I. M. and Smith, B. E.: Committed sea-level rise for the next century from Greenland ice sheet dynamics during the past decade, Proc. Natl. Acad. Sci., 108(22), 8978–8983, 2011.

Rignot, E. and Mouginot, J.: Ice flow in Greenland for the International Polar Year 2008-2009: ICE FLOW GREENLAND 2009, Geophys. Res. Lett., 39(11), n/a-n/a, doi:10.1029/2012GL051634, 2012.

Rignot, E., Fenty, I., Menemenlis, D. and Xu, Y.: Spreading of warm ocean waters around Greenland as a possible cause for glacier acceleration, Ann. Glaciol., 53(60), 257–266, doi:10.3189/2012AoG60A136, 2012.

Rignot, E., Fenty, I., Xu, Y., Cai, C. and Kemp, C.: Undercutting of marine-terminating glaciers in West Greenland, Geophys. Res. Lett., 42(14), 5909–5917, doi:10.1002/2015GL064236, 2015.

Rignot, E., Fenty, I., Xu, Y., Cai, C., Velicogna, I., Cofaigh, C. ó, Dowdeswell, J. A., Weinrebe, W., Catania, G. and Duncan, D.: Bathymetry data reveal glaciers vulnerable to ice-ocean interaction in Uummannaq and Vaigat glacial fjords, west Greenland, Geophys. Res. Lett., 43(6), 2667–2674, doi:10.1002/2016GL067832, 2016.

Rippin, D., Willis, I., Arnold, N., Hodson, A., Moore, J., Kohler, J. and Björnsson, H.: Changes in geometry and subglacial drainage of Midre Lovénbreen, Svalbard, determined from digital elevation models, Earth Surf. Process. Landf., 28(3), 273–298, doi:10.1002/esp.485, 2003.

Röthlisberger, H.: Water Pressure in Intra- and Subglacial Channels*, J. Glaciol., 11(62), 177–203, doi:10.3198/1972JoG11-62-177-203, 1972.

Rutt, I. C., Hagdorn, M., Hulton, N. R. J. and Payne, A. J.: The Glimmer community ice sheet model, J. Geophys. Res., 114(F2), doi:10.1029/2008JF001015, 2009.

Schild, K. M., Hawley, R. L. and Morriss, B. F.: Subglacial hydrology at Rink Isbræ, West Greenland inferred from sediment plume appearance, Ann. Glaciol., 57(72), 118–127, doi:10.1017/aog.2016.1, 2016.

Schoof, C.: Ice-sheet acceleration driven by melt supply variability, Nature, 468(7325), 803–806, doi:10.1038/nature09618, 2010.

Schuler, T., Fischer, U. H. and Gudmundsson, G. H.: Diurnal variability of subglacial drainage conditions as revealed by tracer experiments, J. Geophys. Res. Earth Surf., 109(F2), F02008, doi:10.1029/2003JF000082, 2004.

Seale, A., Christoffersen, P., Mugford, R. I. and O'Leary, M.: Ocean forcing of the Greenland Ice Sheet: Calving fronts and patterns of retreat identified by automatic satellite monitoring of eastern outlet glaciers, J. Geophys. Res. Earth Surf., 116(F3), F03013, doi:10.1029/2010JF001847, 2011.

Shapero, D. R., Joughin, I. R., Poinar, K., Morlighem, M. and Gillet-Chaulet, F.: Basal resistance for three of the largest Greenland outlet glaciers, J. Geophys. Res. Earth Surf., 121(1), 2015JF003643, doi:10.1002/2015JF003643, 2016.

Shepherd, A., Ivins, E., Rignot, E., Smith, B., van den Broeke, M., Velicogna, I., Whitehouse, P., Briggs, K., Joughin, I., Krinner, G., Nowicki, S., Payne, T., Scambos, T., Schlegel, N., Geruo, A., Agosta, C., Ahlstrøm, A., Babonis, G., Barletta, V. R., Bjørk, A. A., Blazquez, A., Bonin, J., Colgan, W., Csatho, B., Cullather, R., Engdahl, M. E., Felikson, D., Fettweis, X., Forsberg, R., Hogg, A. E., Gallee, H., Gardner, A., Gilbert, L., Gourmelen, N., Groh, A., Gunter, B., Hanna, E., Harig, C., Helm, V., Horvath, A., Horwath, M., Khan, S., Kjeldsen, K. K., Konrad, H., Langen, P. L., Lecavalier, B., Loomis, B., Luthcke, S., McMillan, M., Melini, D., Mernild, S., Mohajerani, Y., Moore, P., Mottram, R., Mouginot, J., Moyano, G., Muir, A., Nagler, T., Nield, G., Nilsson, J.,

Noël, B., Otosaka, I., Pattle, M. E., Peltier, W. R., Pie, N., Rietbroek, R., Rott, H., Sørensen, L. S., Sasgen, I., Save, H., Scheuchl, B., Schrama, E., Schröder, L., Seo, K.-W., Simonsen, S. B., Slater, T., Spada, G., Sutterley, T., Talpe, M., Tarasov, L., Jan van de Berg, W., van der Wal, W., van Wessem, M., Vishwakarma, B. D., Wiese, D., Wilton, D., Wagner, T., Wouters, B., Wuite, J. and The IMBIE Team: Mass balance of the Greenland Ice Sheet from 1992 to 2018, Nature, 1–1, doi:10.1038/s41586-019-1855-2, 2019.

Shreve, R. L.: Movement of Water in Glaciers*, J. Glaciol., 11(62), 205–214, doi:10.3198/1972JoG11-62-205-214, 1972.

Slater, D., Nienow, P., Sole, A., Cowton, T., Mottram, R., Langen, P. and Mair, D.: Spatially distributed runoff at the grounding line of a large Greenlandic tidewater glacier inferred from plume modelling, J. Glaciol., 1–15, doi:10.1017/jog.2016.139, 2017.

Slater, D. A., Nienow, P. W., Cowton, T. R., Goldberg, D. N. and Sole, A. J.: Effect of near-terminus subglacial hydrology on tidewater glacier submarine melt rates, Geophys. Res. Lett., 42(8), 2861–2868, doi:10.1002/2014GL062494, 2015.

Slater, D. A., Goldberg, D. N., Nienow, P. W. and Cowton, T. R.: Scalings for Submarine Melting at Tidewater Glaciers from Buoyant Plume Theory, J. Phys. Oceanogr., 46(6), 1839–1855, doi:10.1175/JPO-D-15-0132.1, 2016.

Slater, D. A., Straneo, F., Das, S. B., Richards, C. G., Wagner, T. J. W. and Nienow, P.: Localized plumes drive front-wide ocean melting of a Greenlandic tidewater glacier, Geophys. Res. Lett., 0(ja), doi:10.1029/2018GL080763, 2018.

Smith, L. C., Chu, V. W., Yang, K., Gleason, C. J., Pitcher, L. H., Rennermalm, A. K., Legleiter, C. J., Behar, A. E., Overstreet, B. T., Moustafa, S. E., Tedesco, M., Forster, R. R., LeWinter, A. L., Finnegan, D. C., Sheng, Y. and Balog, J.: Efficient meltwater drainage through supraglacial streams and rivers on the southwest Greenland ice sheet, Proc. Natl. Acad. Sci., 112(4), 1001–1006, doi:10.1073/pnas.1413024112, 2015.

Sole, A., Nienow, P., Bartholomew, I., Mair, D., Cowton, T., Tedstone, A. and King, M. A.: Winter motion mediates dynamic response of the Greenland Ice Sheet to warmer summers, Geophys. Res. Lett., 40(15), 3940–3944, doi:10.1002/grl.50764, 2013.

Sole, A. J., Mair, D. W. F., Nienow, P. W., Bartholomew, I. D., King, M. A., Burke, M. J. and Joughin, I.: Seasonal speedup of a Greenland marine-terminating outlet glacier forced by surface melt–induced changes in subglacial hydrology, J. Geophys. Res. Earth Surf., 116(F3), doi:10.1029/2010JF001948, 2011.

Solgaard, A. M., Messerli, A., Schellenberger, T., Hvidberg, C. S., Grinsted, A., Jackson, M., Zwinger, T., Karlsson, N. B. and Dahl-Jensen, D.: Basal conditions at Engabreen, Norway, inferred from

surface measurements and inverse modelling, J. Glaciol., 1–13, doi:10.1017/jog.2018.45, 2018.

Stevens, L. A., Straneo, F., Das, S. B., Plueddemann, A. J., Kukulya, A. L. and Morlighem, M.: Linking glacially modified waters to catchment-scale subglacial discharge using autonomous underwater vehicle observations, The Cryosphere, 10(1), 417–432, doi:https://doi.org/10.5194/tc-10-417-2016, 2016.

Stevens, L. A., Hewitt, I. J., Das, S. B. and Behn, M. D.: Relationship between Greenland Ice Sheet surface speed and modeled effective pressure, J. Geophys. Res. Earth Surf., 0(ja), doi:10.1029/2017JF004581, 2018.

Stocker, T. F., Qin, D., Plattner, G. K., Tignor, M., Allen, S. K., Boschung, J., Nauels, A., Xia, Y., Bex, B. and Midgley, B. M.: IPCC, 2013: climate change 2013: the physical science basis. Contribution of working group I to the fifth assessment report of the intergovernmental panel on climate change, 2013.

Stokes, C. R. and Tarasov, L.: Ice streaming in the Laurentide Ice Sheet: A first comparison between data-calibrated numerical model output and geological evidence, Geophys. Res. Lett., 37(1), L01501, doi:10.1029/2009GL040990, 2010.

Straneo, F., Hamilton, G. S., Sutherland, D. A., Stearns, L. A., Davidson, F., Hammill, M. O., Stenson, G. B. and Rosing-Asvid, A.: Rapid circulation of warm subtropical waters in a major glacial fjord in East Greenland, Nat. Geosci., 3(3), 182–186, doi:10.1038/ngeo764, 2010.

Strozzi, T., Werner, C., Wiesmann, A. and Wegmuller, U.: Topography Mapping With a Portable Real-Aperture Radar Interferometer, IEEE Geosci. Remote Sens. Lett., 9(2), 277–281, doi:10.1109/LGRS.2011.2166751, 2012.

Sundal, A. V., Shepherd, A., Nienow, P., Hanna, E., Palmer, S. and Huybrechts, P.: Melt-induced speed-up of Greenland ice sheet offset by efficient subglacial drainage, Nature, 469(7331), 521–524, doi:10.1038/nature09740, 2011.

Sutherland, D. A., Jackson, R. H., Kienholz, C., Amundson, J. M., Dryer, W. P., Duncan, D., Eidam, E. F., Motyka, R. J. and Nash, J. D.: Direct observations of submarine melt and subsurface geometry at a tidewater glacier, Science, 365(6451), 369–374, doi:10.1126/science.aax3528, 2019.

Tedstone, A. J., Nienow, P. W., Sole, A. J., Mair, D. W. F., Cowton, T. R., Bartholomew, I. D. and King, M. A.: Greenland ice sheet motion insensitive to exceptional meltwater forcing, Proc. Natl. Acad. Sci., 110(49), 19719–19724, doi:10.1073/pnas.1315843110, 2013.

Tedstone, A. J., Nienow, P. W., Gourmelen, N., Dehecq, A., Goldberg, D. and Hanna, E.: Decadal slowdown of a land-terminating sector of the Greenland Ice Sheet despite warming, Nature, 526(7575), 692–695, doi:10.1038/nature15722, 2015.

Todd, J.: A 3D Full Stokes Calving Model for Store Glacier, West Greenland. Ph. D. University of Cambridge, 2016.

Todd, J. and Christoffersen, P.: Are seasonal calving dynamics forced by buttressing from ice mélange or undercutting by melting? Outcomes from full-Stokes simulations of Store Glacier, West Greenland, The Cryosphere, 8(6), 2353–2365, doi:10.5194/tc-8-2353-2014, 2014.

Todd, J., Christoffersen, P., Zwinger, T., Råback, P., Chauché, N., Benn, D., Luckman, A., Ryan, J., Toberg, N., Slater, D. and Hubbard, A.: A Full-Stokes 3D Calving Model applied to a large Greenlandic Glacier, J. Geophys. Res. Earth Surf., 2017JF004349, doi:10.1002/2017JF004349, 2018.

Todd, J., Christoffersen, P., Zwinger, T., Råback, P. and Benn, D. I.: Sensitivity of a calving glacier to ice–ocean interactions under climate change: new insights from a 3-D full-Stokes model, The Cryosphere, 13(6), 1681–1694, doi:https://doi.org/10.5194/tc-13-1681-2019, 2019.

Truffer, M.: The basal speed of valley glaciers: an inverse approach, J. Glaciol., 50(169), 236–242, 2004.

Vallot, D., Pettersson, R., Luckman, A., Benn, D. I., Zwinger, T., Pelt, W. J. J. V., Kohler, J., Schäfer, M., Claremar, B. and Hulton, N. R. J.: Basal dynamics of Kronebreen, a fast-flowing tidewater glacier in Svalbard: non-local spatio-temporal response to water input, J. Glaciol., 1–13, doi:10.1017/jog.2017.69, 2017.

Vallot, D., Åström, J., Zwinger, T., Pettersson, R., Everett, A., Benn, D. I., Luckman, A., van Pelt, W. J. J., Nick, F. and Kohler, J.: Effects of undercutting and sliding on calving: a global approach applied to Kronebreen, Svalbard, The Cryosphere, 12(2), 609–625, doi:10.5194/tc-12-609-2018, 2018.

Vallot, D., Adinugroho, S., Strand, R., How, P., Pettersson, R., Benn, D. I. and Hulton, N. R. J.: Automatic detection of calving events from time-lapse imagery at Tunabreen, Svalbard, Geosci. Instrum. Methods Data Syst., 8(1), 113–127, doi:https://doi.org/10.5194/gi-8-113-2019, 2019.

Vore, M. E., Bartholomaus, T. C., Winberry, J. P., Walter, J. I. and Amundson, J. M.: Seismic Tremor Reveals Spatial Organization and Temporal Changes of Subglacial Water System, J. Geophys. Res. Earth Surf., 0(ja), doi:10.1029/2018JF004819, 2019.

Voytenko, D., Dixon, T. H., Holland, D. M., Cassotto, R., Howat, I. M., Fahnestock, M. A., Truffer, M. and De La Peña, S.: Acquisition of a 3 min, two-dimensional glacier velocity field with

terrestrial radar interferometry, J. Glaciol., 63(240), 629–636, doi:10.1017/jog.2017.28, 2017.

Wagner, T. J. W., Straneo, F., Richards, C. G., Slater, D. A., Stevens, L. A., Das, S. B. and Singh, H.: Large spatial variations in the flux balance along the front of a Greenland tidewater glacier, The Cryosphere, 13(3), 911–925, doi:https://doi.org/10.5194/tc-13-911-2019, 2019.

van de Wal, R. S. W., Boot, W., Broeke, M. R. van den, Smeets, C. J. P. P., Reijmer, C. H., Donker, J. J. A. and Oerlemans, J.: Large and Rapid Melt-Induced Velocity Changes in the Ablation Zone of the Greenland Ice Sheet, Science, 321(5885), 111–113, doi:10.1126/science.1158540, 2008.

van de Wal, R. S. W., Smeets, C. J. P. P., Boot, W., Stoffelen, M., van Kampen, R., Doyle, S. H., Wilhelms, F., van den Broeke, M. R., Reijmer, C. H., Oerlemans, J. and Hubbard, A.: Self-regulation of ice flow varies across the ablation area in south-west Greenland, The Cryosphere, 9(2), 603–611, doi:10.5194/tc-9-603-2015, 2015.

Walder, J. S.: Hydraulics of Subglacial Cavities, J. Glaciol., 32(112), 439–445, doi:10.3198/1986JoG32-112-439-445, 1986.

Walter, A., Lüthi, M. P. and Vieli, A.: Calving event size measurements and statistics of Eqip Sermia, Greenland, from terrestrial radar interferometry, The Cryosphere, 14(3), 1051–1066, doi:10.5194/tc-14-1051-2020, 2020.

Walter, J. I., Box, J. E., Tulaczyk, S., Brodsky, E. E., Howat, I. M., Ahn, Y. and Brown, A.: Oceanic mechanical forcing of a marine-terminating Greenland glacier, Ann. Glaciol., 53(60), 181–192, doi:10.3189/2012AoG60A083, 2012.

Werder, M. A., Hewitt, I. J., Schoof, C. G. and Flowers, G. E.: Modeling channelized and distributed subglacial drainage in two dimensions, J. Geophys. Res. Earth Surf., 118(4), 2140–2158, doi:10.1002/jgrf.20146, 2013.

Werner, C., Strozzi, T., Wiesmann, A. and Wegmuller, U.: A Real-Aperture Radar for Ground-Based Differential Interferometry, in IGARSS 2008 - 2008 IEEE International Geoscience and Remote Sensing Symposium, vol. 3, p. III-210-III–213., 2008.

van Wessem, J. M., Berg, W. J. van de, Noël, B. P. Y., Meijgaard, E. van, Amory, C., Birnbaum, G., Jakobs, C. L., Krüger, K., Lenaerts, J. T. M., Lhermitte, S., Ligtenberg, S. R. M., Medley, B., Reijmer, C. H., Tricht, K. van, Trusel, L. D., Ulft, L. H. van, Wouters, B., Wuite, J. and Broeke, M. R. van den: Modelling the climate and surface mass balance of polar ice sheets using RACMO2 – Part 2: Antarctica (1979–2016), The Cryosphere, 12(4), 1479–1498, doi:https://doi.org/10.5194/tc-12-1479-2018, 2018.

Williams, J. J., Gourmelen, N. and Nienow, P.: Dynamic response of the Greenland ice sheet to recent cooling, Sci. Rep., 10(1), 1–11, doi:10.1038/s41598-020-58355-2, 2020.

Willis, I., Lawson, W., Owens, I., Jacobel, B. and Autridge, J.: Subglacial drainage system structure and morphology of Brewster Glacier, New Zealand, Hydrol. Process., 23(3), 384–396, doi:10.1002/hyp.7146, 2009.

Wood, M., Rignot, E., Fenty, I., Menemenlis, D., Millan, R., Morlighem, M., Mouginot, J. and Seroussi, H.: Ocean-induced melt triggers glacier retreat in Northwest Greenland, Geophys. Res. Lett., 0(ja), doi:10.1029/2018GL078024, 2018.

Xie, S., Dixon, T. H., Voytenko, D., Holland, D. M., Holland, D. and Zheng, T.: Precursor motion to iceberg calving at Jakobshavn Isbræ, Greenland, observed with terrestrial radar interferometry, J. Glaciol., 62(236), 1134–1142, doi:10.1017/jog.2016.104, 2016.

Xie, S., Dixon, T. H., Holland, D. M., Voytenko, D. and Vaňková, I.: Rapid iceberg calving following removal of tightly packed pro-glacial mélange, Nat. Commun., 10(1), 3250, doi:10.1038/s41467-019-10908-4, 2019.

Xu, Y., Rignot, E., Fenty, I., Menemenlis, D. and Flexas, M. M.: Subaqueous melting of Store Glacier, west Greenland from three-dimensional, high-resolution numerical modeling and ocean observations, Geophys. Res. Lett., 40(17), 4648–4653, doi:10.1002/grl.50825, 2013.

Young, T. J., Christoffersen, P., Doyle, S. H., Nicholls, K. W., Stewart, C. L., Hubbard, B., Hubbard, A., Lok, L. B., Brennan, P., Benn, D. I., Luckman, A. and Bougamont, M.: Physical conditions of fast glacier flow: 3. Seasonally-evolving ice deformation on Store Glacier, West Greenland, J. Geophys. Res. Earth Surf., 0(ja), doi:10.1029/2018JF004821, 2019.

Zhan, Z.: Seismic noise interferometry reveals transverse drainage configuration beneath the surging Bering Glacier, Geophys. Res. Lett., doi:10.1029/2019GL082411, 2019.

Zhang, T., Price, S., Ju, L., Leng, W., Brondex, J., Durand, G. and Gagliardini, O.: A comparison of two Stokes ice sheet models applied to the Marine Ice Sheet Model Intercomparison Project for plan view models (MISMIP3d), The Cryosphere, 11(1), 179–190, doi:10.5194/tc-11-179-2017, 2017.

Zwally, H. J., Abdalati, W., Herring, T., Larson, K., Saba, J. and Steffen, K.: Surface Melt-Induced Acceleration of Greenland Ice-Sheet Flow, Science, 297(5579), 218–222, doi:10.1126/science.1072708, 2002.